Novel Techniques for Dopant Profile Monitoring

Thesis submitted by

Nikolaos E. Porfiris

for the degree of

Doctor of Philosophy

Edinburgh Microfabrication Facility,
Department of Electrical Engineering,
University of Edinburgh,
Scotland.

December 1992

Abstract

Ion implantation and subsequent dopant activation are two of the most important fabrication steps for VLSI and ULSI circuits. The need for on-line monitoring of those steps is imperative due to the tighter tolerances being imposed by the reduction in geometries and the increase of wafer dies and wafer diameters. Knowledge of the distribution of the implanted ions with depth, both before and after activation, is crucial in the control of device performance. The aim of this project was to develop a novel approach to obtain fast and accurate implant profiles, suitable for on-line monitoring.

In the new approach, the Pattern Etch Transfer (PET) technique is used to create a number of rectangular trenches of increasing depth into silicon, by use of a single photolithography step. The trenches are first patterned into photoresist by variation of the exposure time for each trench. Reactive Ion Etching (RIE) is then used to transfer those trenches into silicon, by a simultaneous etch of photoresist and the Si substrate. Implant damage, dopant profiles and carrier profiles can then be obtained from measurements performed on the flat silicon surface at the bottom of each trench.

Experiments were performed to obtain better depth resolution (75 Å), minimize the induced-damage levels and achieve high accuracy and repeatability. In the PET technique measurements are performed at neighbouring trenches, therefore the resulting depth profile includes an error associated with the implant variation across the wafer. The effect of the implant profile variation across the wafer was seperately assessed by use of a second method, the two-dimensional Reactive Ion Etching technique. This method is not suitable for fast monitoring since RIE is used to successively strip thin layers of Si (75 Å) across the whole wafer. Etch rate variations across the wafer were measured and minimized in order to accurately determine the depth from the initial Si surface. At each depth a two-dimensional sheet resistance mapping was obtained. Two-dimensional implant profiles across the wafer can thus be acquired and 3σ limits of the carrier concentration values at each depth can be obtained. Therefore, the limiting curves that are evaluated

from the two-dimensional RIE technique define the upper and lower margins for the implant profile curve obtained by the PET technique.

The PET technique provides a platform for the application of most of the existing implant characterization techniques. Preliminary experiments revealed the suitability of the stripping methods for monitoring of sheet resistance, optical constants and thermal-waves with depth.

Differential Hall measurements were used as the benchmark test for the assessment of carrier concentration profiles obtained by the four-point probe measurements in combination with the PET structure and the two-dimension RIE technique. Damage profiles were acquired by use of ellipsometry and thermal-waves inside the PET trenches. Secondary Ion Mass Spectroscopy and SUPREM IV simulation results were used as the benchmark for dopant profiles. Shallow implants for the source/drain junctions of the 1.2μm CMOS process and high dose BF_2 double implants were monitored. Theoretical predictions were used to explain the resulting dopant, damage and carrier concentration profiles.

The thesis also contains a critical review of ion implantation theory, problems and the most important existing monitoring and profiling techniques.

Acknowledgements

I would like to express my gratitude to my supervisor, Professor John M. Robertson, for his excellent guidance throughout the project, his valuable comments and above all for providing me with a very good training in scientific thinking, arguments flow and report writing.

I am also deeply thankful to my second supervisor, Dr. Robert Holwill, for his critical comments, pieces of advice and suggestions he offered me.

I am grateful to Dr Anthony Walton for his advice on the simulation packages and to Mr Alan Gundlach for his comments and suggestions on fabrication matters. I am also deeply thankful to all the EMF stuff for their kind assistance, frinedship and cooperation; particularly I would like to thank Dr J. M. T. Stevenson, Dr Les Hayworth, Mr Brian Neilsen, Mr Alec Ruthven and Mr Mike Fairgrieve for their help and advice. I am also thankful to all my friends and collegues in EMF for their support and the pleasant working environment they created during my stay in Edinburgh.

I am grateful to SERC for awarding me a scholarship and sponsoring me.

Finally, I would like to thank my parents and all my family members for their continuous support and encouragement throughout my research work.

To my parents

Table of Contents

Chapter 1

Introduction

1.1 Implantation as a production process

Ion implantation is one of the most versatile and pervasive technologies in modern integrated circuit (IC) fabrication. The major reason for the successful application of ion implantation in IC process technology is the accuracy and uniformity with which dopants can be introduced into a silicon wafer. However, dose inaccuracies and excessive non-uniformities may still occur and may lead to out-of-specification devices. Deficiencies in performance become especially important in applications such as the fabrication of complex dynamic random access memories (DRAMs), which require certain transistors to have closely matched threshold voltages.

Equipment calibration is another key issue which aggravates the problem of device control. The existence of multiple product fabrication lines or the use of certain parts of a fab-line for the production of different devices results in a continuous need for equipment calibration at the desired values for each particular process. The desire for increased productivity continues to drive the introduction of larger wafer size. However, productivity gains from the use of larger area wafers need to be balanced against the contradictory requirements for tighter uniformity of device characteristics. The combination of the high cost of ion implanters with the increasing number of ion implantation steps in sub-micron processes

has, therefore, an impact on the process cost. A number of strategic options are available for production control of implantation:

1. Maintain single product fabrication lines.

2. Dedicate an implanter for each implant step of the production process.

3. Exclusive use of outside implant services with performance specification.

4. Establish inter-implanter calibration, checks of dose uniformity and accuracy and a coherently sustained process control program to assess implanter performance and malfunctions.

The first option is not compatible with the increased competition in all semiconductor markets and the product diversification requirements that those markets impose. The second option requires huge capital investment with an uncertain rate of return (especially in the competitive market conditions and the recession that exists today). The third option can reduce the capital tied up in equipment but is not particularly effective for yield improvement. The wafer specifications, the contamination levels, the time required, the volume of production and the lack of a technology base are its main drawbacks. The fourth option seems to be the only way out of the problem and needs more thorough analysis.

1.2 Strategies for implant control

Control of ion implantation and associated annealing processes may be approached from three different viewpoints: the equipment suppliers (ion implanter manufacturers), the users (process engineers and machine operators) and the fab coordinators (production and manufacturing engineers). Each of those groups has developed an independent strategy to achieve better implanter performance within the constraints of the business priorities that they face.

1.2.1 The equipment suppliers' strategy

Manufacturers of implantation systems are trying to meet the challenge of providing the required processing capability while minimizing the side effects which may be inherent in the system design or operation. Improved implanters incorporating better charge neutralization schemes, enhanced cooling without wafer flexing, low particulate performance guarantees, improved beam purity and stability, increased dose accuracy and uniformity, fully automated set-up and self-diagnostic tools are setting higher standards in the overall system specifications.

The inherent synergy of ion implantation and annealing on IC production necessitates an equivalent improvement of the annealing equipment. In rapid thermal processing equipment, the increase in the number of manufacturers, the variety of configurations of heating elements, improved chamber design and the effort to accurately measure and control temperature uniformity within the chamber are indicative of the level of maturity reached in this technology.

1.2.2 The process characterization strategy

The task of the process engineers is to monitor the implant step performance with respect to device performance targets. Their strategy, which is focused on ensuring good implantation quality, has been based at the following principles:

1. Select the ion implantation-dependent device parameters to monitor during production.

2. Develop appropriate measurement techniques to monitor those parameters and tackle any performance problems.

3. Optimize the measurement techniques for accuracy, resolution, precision and turn-around time.

1.2.3 The manufacturing strategy

A volume integrated circuit fabrication process is much more than the sum of the separate process steps. Dopant profiles change with subsequent heat treatments, physical and electrical variables all have tolerances that combine in different proportions for different device parameters and all processes must be managed to give high yield, low cost and short process cycles. This is the promise of computer integrated manufacturing (CIM) and the technologies are being rapidly developed for application to IC production.

The manufacturing view-point combines many of the conclusions based on machine or engineering data as follows:

1. Collect machine performance data within the production scheduling context.

2. Develop an automated and systematic way of collecting and storing data from control wafers or from test sites on production wafers.

3. Develop methods to convert raw data into usable information, eg. averages, standard deviations, model parameters, contour plots, 3-dimensional plots, etc.

4. Implement all of the above steps on the manufacturing line with appropriate training for all levels of staff.

1.3 Failings of the traditional control strategies

1.3.1 Equipment suppliers

One of the major design features of later generations of implantation machines is the extensive use of internal sensors, coupled to adaptive control mechanisms, so that control by direct intervention of the operator or process engineer is no longer needed. Examples of internal monitors include direct dose measurements, sensors

for particles, surface charge and wafer temperature. Although much progress has been made in solving problems associated with the machine-wafer interaction eg charge neutralization solutions, enhanced cooling without wafer flexing, improved beam purity and reduced cross-contamination, major areas of concern remain:

1. Different generations of equipments are still in use in fab-lines so availability or compatibility of equipment upgrades is problematic. However, retrofitting the existing implanters rather than purchasing new systems can prove a good compromise between the amount of capital investment required and the yield improvement on wafers of increasing size and decreasing linewidths [1].

2. Conco mitant development of device processing and equipment improvement reveals problems that were not evident in the past.

   Such a problem can be illustrated by the following example which occurs when the ion beam is raster-scanned over the polysilicon gate electrode (over the SiO_2 gate dielectric). The charge build-up that occurs in the polysilicon layer (due to the ion beam and the emitted secondary electrons) causes a voltage difference between the Si substrate and the gate electrode. Shrinking device geometries reduce the oxide thickness to 100 Å or less. Normally the excess charge is removed by tunneling through the oxide layer; the resulting gate oxide degradation being annealed out during the subsequent dopant activation step. However, inhomogeneities and small defects that are present in such a thin oxide can lead to an increased current flow between the electrode and the oxide and catastrophic breakdown of the gate oxide may occur. The use of the electron flow gun does not eliminate the problem since an excess negative potential would lead to exactly the same catastrophic result. Therefore, the complex relationship between oxide thickness, beam current and electron flood current can severely reduce device yield.

3. Advanced processing and product development activities are usually set up on pilot lines and are then transferred to production lines. Ideally the implantation machines that are purchased for the production lines should be ordered with tighter performance specifications than those used for the pilot

line development. This is required by the problems that are encountered in the advanced, scaled processes. Particulate contamination levels is an example of such a problem originating from decreasing feature and circuit size. However, machine puchases cannot keep pace with the continuous process improvements imposed by the market competition or the tight specification limits determined by the customer requirements on customized or Application Specific Integrated Circuit (ASIC) production lines. This can have a severe impact on the yield. In these cases, pre-control monitoring can prove invaluable in keeping the process variation within the process specification limits.

The above areas of concern indicate that machine improvements on their own are unlikely to be sufficient to provide the degree of process control that is needed for increased parametric yield of sub-micron devices.

1.3.2 Processing limitations

The process engineer is required to accurately control the processing scheme so that the product meets the circuit designer specifications. In order to achieve this target at acceptable yield and reliability, he must investigate the sensitivity of the process variables and try to keep them to a minimum. Traditional statistical process control strategy aims to provide a process diagnostic tool. As such, it should indicate failure at the earliest possible stage and save the company from continuing to work on out-of-spec products. The input process parameters that are monitored by the existing techniques (eg dose, energy, anneal temperature) are only indirectly related to the final device performance characteristics. Such a relation which is revealed by the use of simplified physical models, can prove insufficent for accurate prediction of the device performance since it does not take into account particular process step characteristics (eg degree of channeling at the tail of the implant profile). This can be illustrated in the following example for the threshold adjustment implant.

The threshold voltage (V_t) of a MOS transistor is determined by ion implantation and is a crucial parameter that must be bounded by well-defined specification limits. The value of V_t depends on process parameters such as the implanted dose, the implant energy, the oxide thickness, the annealing time and temperature. It is also linked to quantities such as the effective dose implanted in Si and the degree of dopant activation which are indirectly controlled by the process specifications. By use of SUPREM III [1] the effect of energy and dose variation on the threshold voltage shift for a boron implanted n-channel MOS transistor (140 Å gate oxide thickness) was investigated and the simulation results are presented in fig. 1–1. Although the threshold voltage shift for the energy and dose used are qualitatively expected, severe differences might occur with experimental results [2]. The effect of the implant energy and dose variation on threshold voltage sensitivity is also depicted in fig. 1–1 for an implant energy of 40 keV and a dose of 3×10^{11}ions/cm^2. The sensitivity of V_t to dose variation is about 3 times higher than the sensitivity for the equivalent percentage change in energy. However, the simulation results underestimate the threshold voltage variation. The reason can be graphically represented in fig. 1–2. Only the part of the activated implant profile that resides inside the depletion region contributes to the threshold voltage shift [3]. Large process variations can lead to large implant profile shifts. Existence of channelling tails can also have a significant effect on the threshold voltage shift. Accurate determination of the depth and shape of the profile is thus required.

The insufficiency of the gathered data is due to the nature of the parameters that are being monitored. Parameters such as sheet resistance, optical constants and modulated reflectance that can be successfully monitored do not give the necessary information that could be used to predict if the specific devices would be operative within the specifications. Such information could be ideally extracted from the as-implanted and electrical profile distributions. Traditional monitoring is based on the inherent 'averaging' procedure of parameters such as sheet resis-

---

[1]SUPREM III is a full process simulator, trademark of Technology Modelling Associates (TMA).

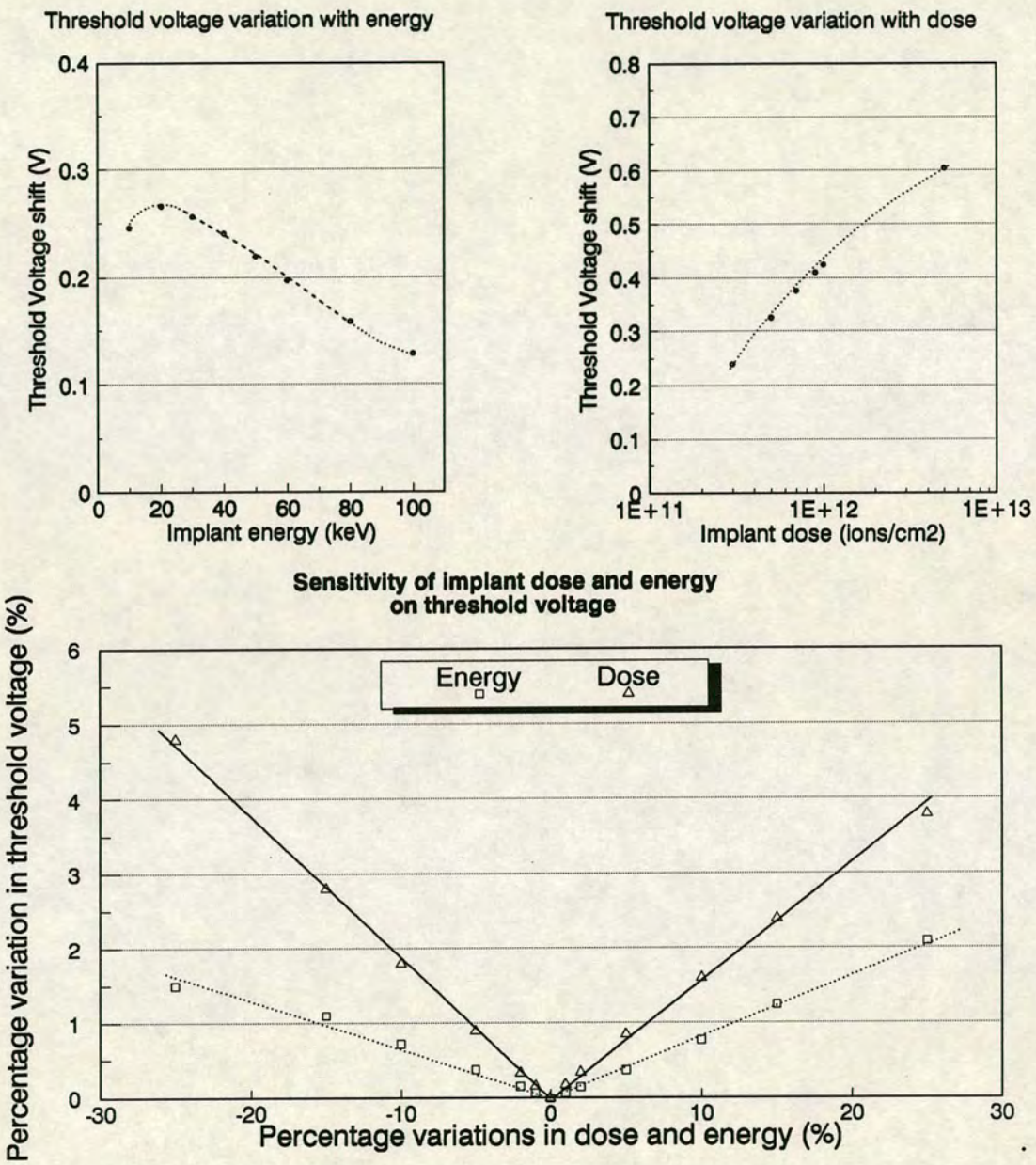

Figure 1–1: Simulated threshold voltage shift over a range of implant energies and doses for an n-channel device with a gate oxide of 140 Å. The third graph indicates the sensitivity that dose and energy variations can have on the threshold voltage. The nominal energy and dose values for the sensitivity results were 40keV and 3×10^{11}ions/cm^2, and a variation up to 25 % took place below and above those values.

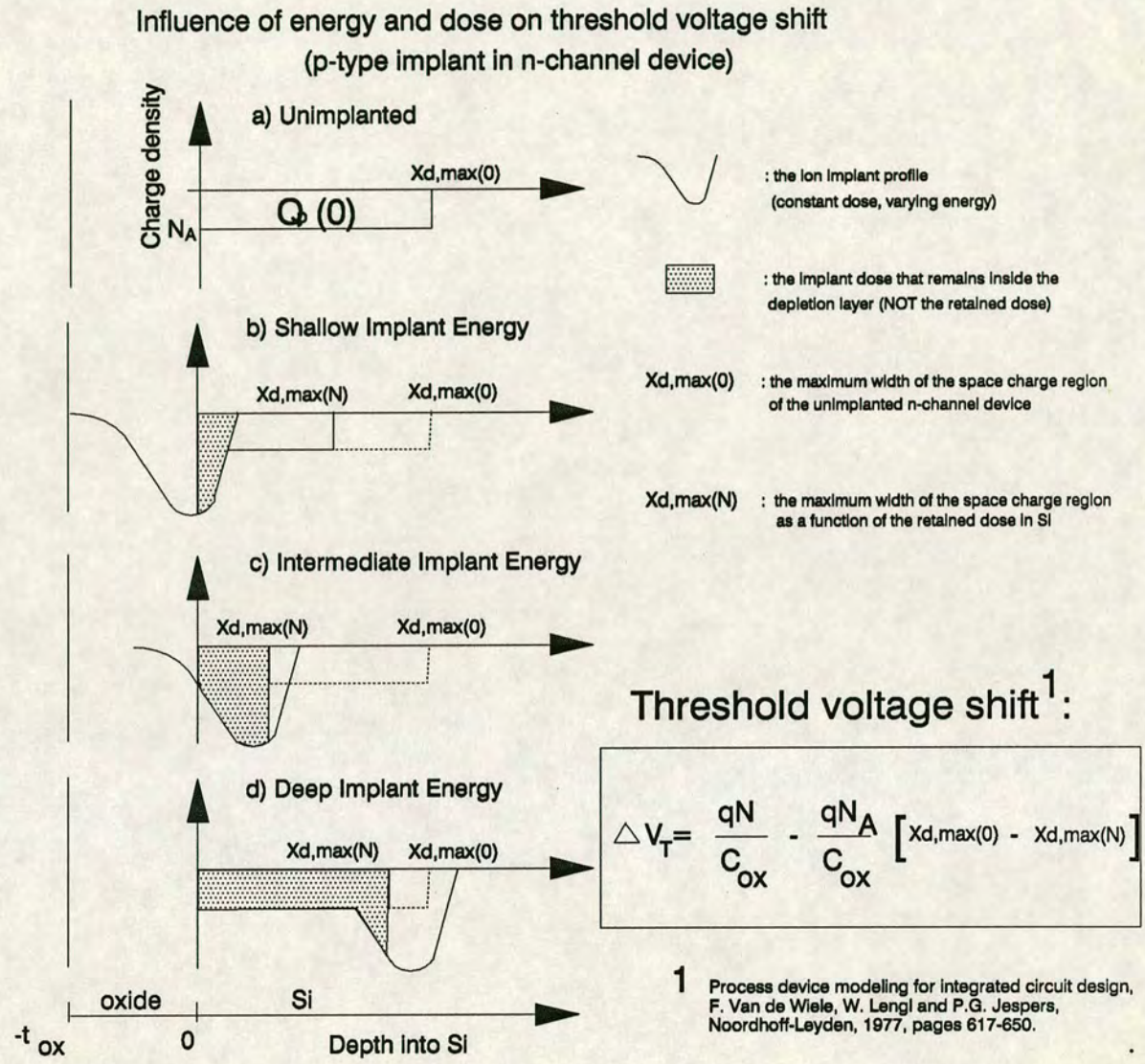

Figure 1–2: The charge distributions in the surface depletion layers of unimplanted (a) and boron ion-implanted (b,c,d) n-channel MOS transistor are depicted. The implantation energies are around 20, 80 and 150 keV for graphs b, c and d respectively. The maximum width of the depletion layer decreases rapidly with the increase of the implant dose that remains inside the depletion layer (from Xd,max(0) to Xd,max(N).

tance and optical constants over a certain depth in silicon. The contributions to the 'average' monitored value from each depth, depends on the parameter monitored and on the ion type, damage or carrier concentration at the specific depth. It is therefore expected that the peak concentration contribution will dominate in the sheet resistance monitoring (see section 3.5.2) and that the optical constant value would be dependent on the damage created close to the surface (see chapter 7). Effects such as channelling and reverse current leakage(due to the presence of defects in the near-junction region) cannot be effectively monitored by use of the traditional techniques, since they occur away from the surface and at low dopant concentration regions. Ironically, within-spec electric device operation crucially depends on the non-occurence of such side-effects. The need for a new on-line implant profiling technique therefore emerges. Information obtained by implant profiles can make use of models linking process parameters to final device performance characteristics to give more accurate and efficient device yield forecasts.

1.3.3 Manufacturing factors

The central thrust in today's manufacturing is to discover key variables in product and process design, examine their individual and combinatory contribution to process variations and define the key process tolerances so that the process width can be well-inside the specification width. Therefore, process design for manufacturability is the key objective. The manufacturing engineer has to ensure that the process is and remains manufacturable.

His main decisions, in the case of ion implantation, are equipment cost, throughput, implanter allocation to process steps, manufacturing cycle time, process repeatability and reliability and process flexibility (eg ability switch from one implant species to another in order to reduce the number of implanter machines required and at the same time avoid increased setup times and cross-contamination effects). He must also define, tune and control the manufacturing tolerances of the process parameters of each individual process step. The only tools to help him in those

decisions are a properly designed Computer Aided Manufacturing (CAM) system, experimental design and process modeling.

The database of the CAM system can indicate at which stage of the process the problem exists. Experimental design can then be used to explore the process parameter sensitivities. However, the link of those parameters to the final design parameters is complex and depends on subsequent processing. Process simulation models [4] can be used for setting up initial process and equipment tolerances. However, the intrinsic simplifications of the models are not appropriate for the tight design tolerances control of ULSI devices. Real-time measurement is needed to be fed to those models. As was indicated in the processing limitations example, process key variables (eg dose, energy) may not be sufficient for providing the data needed for the models. Once more the requirement for an appropriate fast, accurate, real-time implant profiling technique emerges.

1.4 ULSI specifications for implantation

1.4.1 Process requirements

The recent trend from VLSI to ULSI, may be observed in the evolution of memory technology from the 1Mbit DRAM (1.3 μm) towards the 16Mbit DRAM (0.5 μm). In the fabrication of these submicrometer devices, ion implantation is one of the critical process steps. This is a consequence of the steady increase of the number of implantation steps in VLSI and ULSI processing lines. From the threshold adjustment and field implants of the 1970 s, today's CMOS twin-tub technologies use implantation pervasively with applications such as n-well, p-well, channel stop, threshold adjustments for both p- an n- channel devices, Lightly-Doped-Drain (LDD) implants, polysilicon gate electrode doping, n^+ and p^+ source and drain implants. Leading edge twin-well processes use 12 implants. If Large Angle Tilt Implant Drains (LATIDs) and Large Angle Tilt Implanted Punch-through Stoppers (LATIPS) take the place of the LDD implants for deep-submicron CMOS processes (16 and 64 Mb DRAM processes), the number of implants can exceed

15. Some indicative dose and energy ranges for those applications are depicted in fig. 1–3.

Ideally, process development in a pilot line should ensure a robust process for transfer to volume production. Qualitatively this involves analysis of all features that contribute to tolerances of device parameters and the algebra that is appropriate to the combination of those distributions. A design for manufacturability (DFM) approach would ideally set high C_p and C_{pk} values. However, for the continuously shrinking submicron devices the evolving problems are due to a complex interaction of fundamental physical principles (ie the short channel stability of the threshold voltage). From the other side the increasing wafer sizes impose tighter tolerances. Therefore, satisfactory solutions are increasingly difficult to obtain and the machines might be pushed to operate at their limits for those critical implants. The process mean can thus drift and the product can be out-of-specs due to the low C_{pk} value imposed by the tighter process specification limits and the loose process control (due to those critical problems). On-line pre-control of the implant profile is thus necessary to ensure that the existing process variation will not have a significant effect on yield.

1.4.2 Critical problems of ion implantation for small geometries

1.4.2.1 Shallow junction formation

Formation of shallow junctions has initiated the release of a plethora of papers. Low energy BF_2 implants, implantation through a thin oxide layer, preamorphization implants by Si^+ followed by low energy BF_2^+ implantation and RTA [5] or Ge^+ followed by a 6keV BF_2 implant [6] are very difficult to precisely and repeatably control in a manufacturing environment. Even the slightest increase of the amorphization implant energy, due to implanter malfunction, may result in a drastic increase of the junction leakage current [7]. Source and drain leakage current are directly related to memory retention time and therefore defect structures that undergo RTA anneal have to be monitored. Besides, commercial

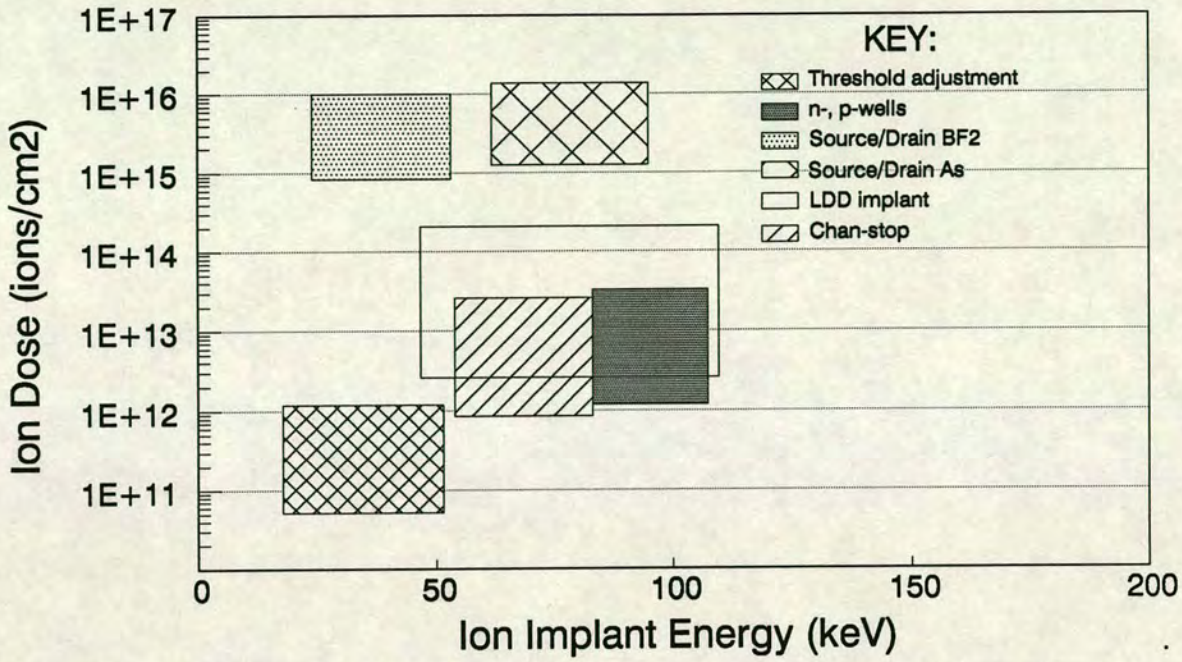

Figure 1–3: The different type of implants for a CMOS process with some typical dose and energy ranges employed.

implanters with a satisfactory high beam current for implant energies below 10keV are rare. Only a doping profile monitoring method can reveal such a problem at that process stage. It is thus obvious that the electrical characteristics of the junctions are of prime importance and profile monitoring should also take place after the one- or two- stage annealing process. Unfortunately, as will be shown later in section 3.5.2, sheet resistance monitoring is not sufficent. A phenomenon like channelling in the low concentration area(profile tail) does not contribute significantly to any measurement based on total dose so a depth profiling technique is required. Furthermore, the simultaneous occurence of multiple problems within the implant and annealing cannot be easily identified by the existing surface monitoring techniques (sheet resistance, ellipsometry).

1.4.2.2 Lateral spread of implanted ions, beam shadowing effects

As they approach their rest point, implanted ions suffer lateral scattering which broadens both damage and atomic profiles. The magnitude of the straggle is close to the range straggle value (ΔR_p) [8]. Precise control of lateral impurity profiles of the order of $\mathbf{0.01\mu m}$ is required especially in the fabrication of delicate device structures such as LDDs (light doped drain) in small size MOSFETs [9, 10]. For self-aligned source and drain ion implantation which is defined by the gate, spreading of the lateral profile can take place. This is due to the combined effect of the gate thickness and mask edge slope when the substrate is tilted from the incident ion direction. This effect can reduce the dopant volume concentration at the geometric edge of the mask by up to 50 % and affects the performance characteristics of small geometry devices. Therefore, the degree of this shadowing effect in LDDs and other structures(eg vertical wall implants of trench capacitors by tilting and rotating the wafer during implantation) has to be assessed on-line with a technique having a high spatial resolution.

1.4.2.3 Non-uniformity due to implant angle variation

In order to create LDD structures or impurity doping of trench side walls(used as capacitors or isolation trenches), slant incidence and rotation of the wafers during implantation is a solution [6]. The need for vertical walls has recently increased due to the development of three-dimensional type device structures for higher performance ULSIs [11]. A graph summarizing some of the implant applications performed at various angles of incidence and dose levels can be found in fig. 1–4.

The amount of angular variation depends on the method used in the ion implanter to spread the ions uniformly over the wafer surface [12]. The variation of device yield at various parts of the wafer due to variation of the implant angle (and the associated non-uniformity in channeling effect) has deleterious effects on the overall device yield. The new technical issues to be solved are the exact control of the device pattern orientation with respect to the ion incident direction, the continuous change in crystal orientation of the substrate with respect to the implant

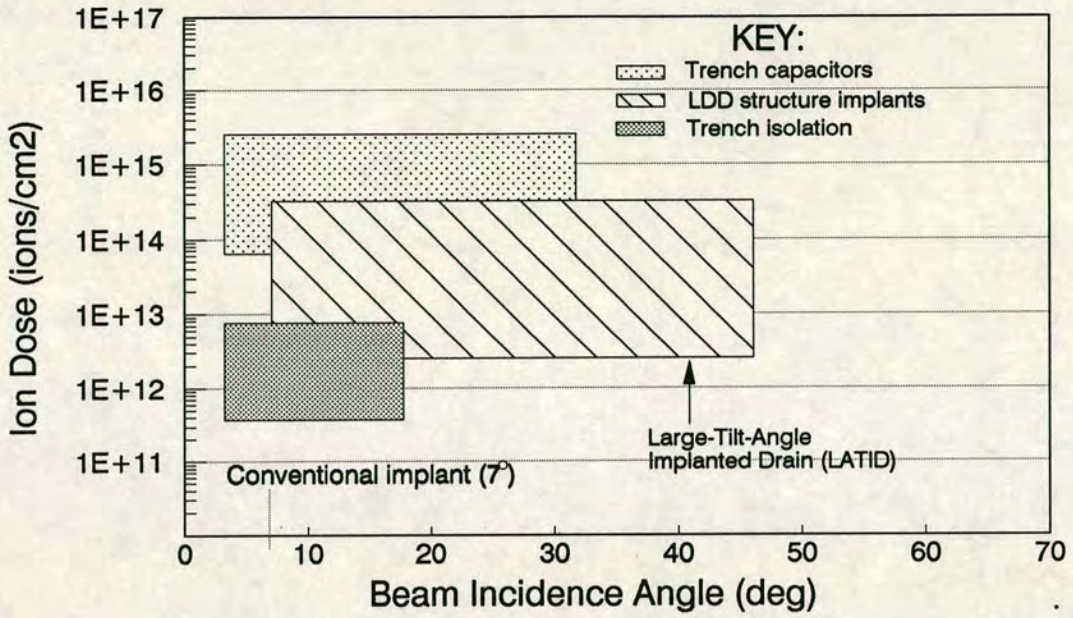

Figure 1–4: Some of the main applications of tilted angle implants at the typical dose ranges employed. Dose values can extend sometimes outside the typical ranges depicted on the graph for custom processes.

incidence direction (due to the wafer rotation), the mechanical difficulty in wafer handling for large tilt angles of implantation and the reflection and recoil of ions from the mask and oxide edges or inside the narrow steep trench. Therefore, selectable angles that remain constant across the whole wafer should be the machine manufacturer's objective to improve yields. Until this target is achieved, precise measurements of dopant profiles across and along the trench walls and across the LDD emerge as major pre-control requirements.

1.4.2.4 Hot-electron resistant structures

Since geometrical structure, channel length and the electrical field distribution close to the drain edge have been shown to be critical in the electrical device performance, emphasis has been given to the development of a variety of structures with specially designed drain regions [13]. In order to reduce hot-electron injection into the gate oxide, the peak-electric field near the gate must be reduced. Graded drain, lightly doped drain (LDD) and doubly doped drain (DDD) structures are

among the variety of structures used for reducing the hot-electron effect by use of tip [14] and spacer [15] technologies.

1.4.2.5 Silicide formation

Silicides can be used to form shallow junctions of low sheet resistivity. These metal compounds can be formed by reaction of a metal (eg W, Ti) with the underlying silicon substrate or polysilicon layer or by co-deposition of metal and Si, followed by a heat treatment. For the fabrication of such shallow doped underlayer structures, silicide formation can take place before, during or after the doping process step. The resulting profile depends on the implanted impurity ions, the smoothness of the silicide-silicon interface, the existence of an oxide layer on the Si surface before the silicide formation and the profile redistribution mechanisms during the heat treatment. On-line characterisation is needed for those profiles since obtaining smooth silicide-silicon interface and controlling the degree of redistribution are critical points and at the same time difficult to control.

1.4.2.6 MeV implants

High energy (MeV) implantation is an extension of the technique for deeper penetration of the ions. The main advantage is that it leaves the near-surface region relatively un-altered and defect-free and this has made it very attractive for advanced device technologies. The main range of applications can be seen in figure 1–5. Development of practical implanters has now been initiated, therefore on-line characterization of the MeV implanted layers will be required in the near future.

1.4.2.7 New technologies

One of the most important limiting factors in IC manufacturing with continuously decreasing device dimensions is the concurrently diminishing process thermal budget (and the overall hot processes budget). It has been speculated (simulation results based on experimental data models) [16] that the current ion implantation

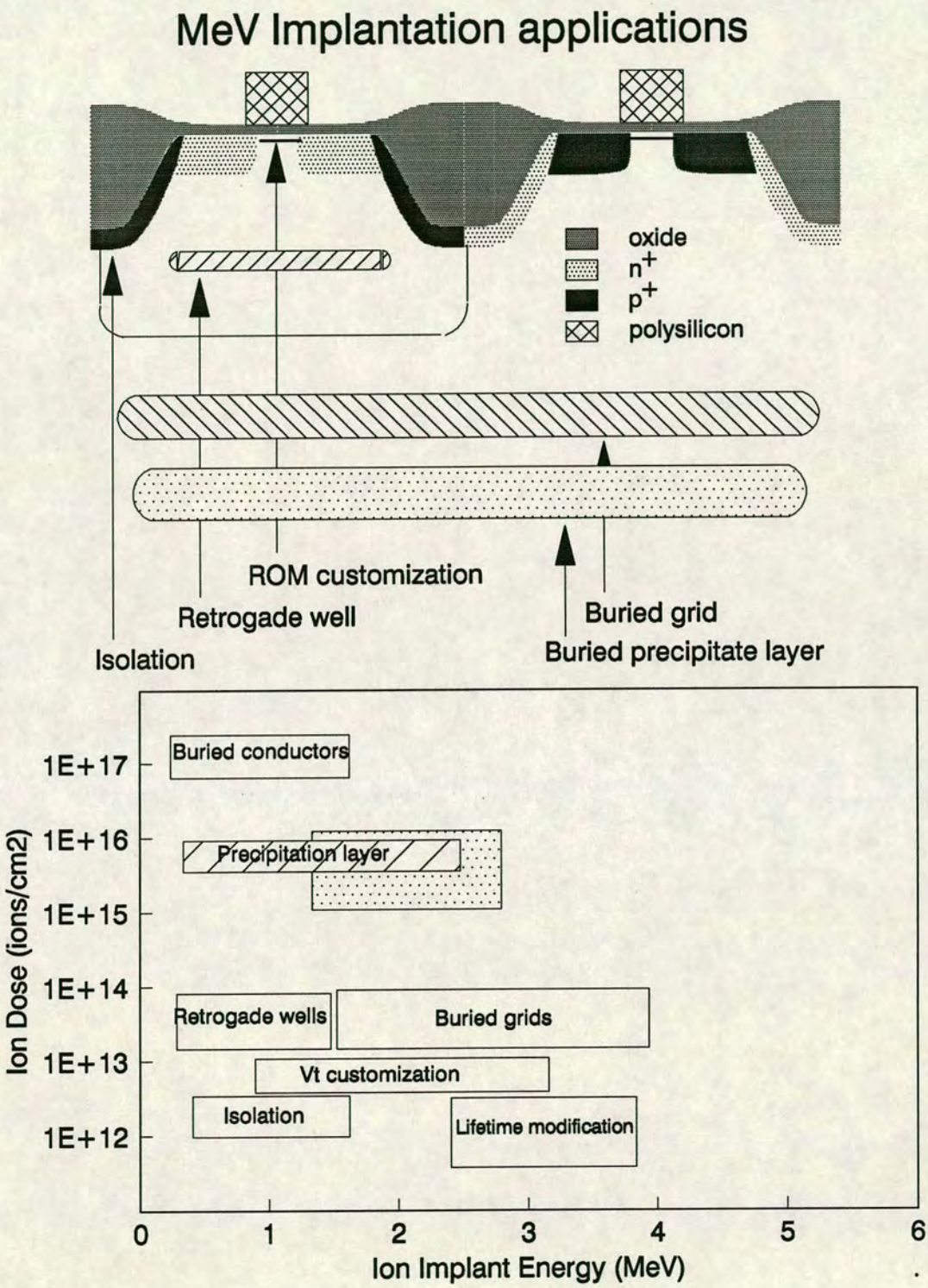

Figure 1–5: Some of the main applications of MeV implants are being displayed in the upper part of the figure. The typical energy and ion dose ranges employed for those implant applications are depicted in a chart.

technology may not be practical for scaled 0.25 μm technology due to implantation damage-assisted diffusion of dopants. Hyper-shallow junction formation (junction depths around 60nm) [17], very low energy (less than 1keV) implantation [18] are among the tools used for extending junction formation technology to the ultrashallow layers by ion implantation (USLI) regime. Plasma immersion ion implantation is another emerging technique. Although those techniques are far from production, the development of an on-line implant profile monitoring would be necessary for characterizing such ultra shallow implanted layers. Depth resolution and measurement accuracy would be the technique prerequisites.

1.5 Requirements for improved on-line profiling techniques

The emerging production control problems and requirements described earlier cannot be met by the existing monitoring tools. A new profiling technique to meet the increasing technology requirements must be developed for on line monitoring. The new measurement tool thus requires good resolution of the measured quantity and absolute accuracy. Its spatial resolution should be easily adjusted on the scale of typical implant depths for the various applications. Fast measurements and the minimum number of extra process steps are requirements directly imposed by the desire for short process and time cycles on the production lines. The traditional sequence of layer stripping and parameter measurements in order to reveal the depth variation of the monitored parameter (and thus a depth profile) would be ineffective due to the time and processing involved. A completely new concept is needed. At the same time it would be beneficial if the new method could take advantage of the whole range of the existing monitoring methods.

The strategy that was adopted in this project was:

1. To actively review and experimentally assess as many profiling methods as possible.

2. Develop a new approcah for on-line profiling (PET structure).

3. Compare the new technique against the existing methods and assess both its capabilities and limitations for implant profile characterization.

Bibliography

[1] T. Carducci and B. Hardegen. Ion implanter upgrade improves IC yields. *Microelectronics Manufacturing Technology*, 14(1):64–66, 1991.

[2] F. Van de Wiele, W. Lengl, and P. G. Jespers. *Process device modelling for integrated circuit design.* Noordhoff-Leyden, 1977.

[3] O. Kudoh, K. Nakamura, and M. Kamoshida. Implant dose profile dependence of electrical characteristics of ion-implanted transistors. *Journal of Applied Physics*, 45(10):4514–4519, 1974.

[4] P. H. Singer. Process modelling and simulation. *Semiconductor International*, (1):74–80, 1987.

[5] M. Miyake, T. Kobayashi, S. Horiguchi, K. Iwadate, and K. Kurihara. Subquarter-micrometer p-channel MOSFETs with 8nm S/D junctions. In *Symposium on VLSI Technology, Digest of Technical Papers*, page 91, May 1987.

[6] T. Tokuyama. Critical problems of ion implantation in processing small geometry integrated devices. *Nuclear Instruments and Methods in Physics Research*, B37/38:744–748, 1989.

[7] M. C. Ozturk, J. J. Wortman, C. M. Osburn, A. Ajmera, G. A. Rozgoni, E. Frey, W. K. Chu, and C. Lee. Optimization of the germanium preamorphization conditions for shallow-junction formation. *IEEE Transactions on Electron Devices*, ED-35:659, 1988.

[8] H. Matsamura and S. Furukawa. Theoretical considerations in lateral damage distribution formed by ion implantation. *Japanese Journal of Applied Physics*, 14:1783, 1975.

[9] S. Furukawa, H. Matsumura, and H. Ishiwara. Theoretical considerations on lateral spread of implanted ions. *Japanese Journal of Applied Physics*, 11:134, 1972.

[10] T. Tokuyama. Trends in ion implantation in silicon VLSI technology. *Nuclear Instruments and Methods in Physics Research*, B19/20:299–306, 1987.

[11] M. Current. Recent trends in ion implantation. Lecture in the IIT90 conference seminars.

[12] R. E. Kaim. Improved VLSI device yields through control of implant angle. *Solid State Technology*, (2):103–107, 1990.

[13] J. J. Sanchez, K. K. Hsueh, and T. A. DeMassa. Drain-engineered hot-electron-resistant device structures. *IEEE Transactions on Electron Devices*, ED-36(6):1125–1132, 1989.

[14] S. Ogura, P. Tsang, W. Walker, D. Critchlow, and J. Shepard. Design and characteristics of the lightly doped drain-source (LDD) insulated gate field-effect transistor. *IEEE Transactions on Electron Devices*, ED-27:1359–1367, 1980.

[15] S. Ogura, P. Tsang, W. Walker, D. Critchlow, and J. Shepard. Elimination of hot-electron gate by the lightly doped drain-source structure. *IEDM Tecnical Digest*, pages 654–656, 1981.

[16] R. B. Fair and G. A. Ruggles. Thermal budget issues for deep submicron ULSI. *Solid State Technology*, (5):107–113, 1990.

[17] S. N. Hong, G. A. Ruggles, J. J. Paulos, and J. J. Wortman. Device performance of shallow junction PMOSFETs fabricated using low-energy ion

implantation of B and BF_2 into crystalline and Ge preamorphized silicon. *Electronic Letters*, 25(16):1100, 1989.

[18] S. N. Hong, G. A. Ruggles, J. J. Paulos, and J. J. Wortman. Formation of ultrashallow $p^+ - n$ junctions by low-energy boron implantation using a modified ion implanter. *Applied Physics Letters*, 53(18):1741, 1988.

Chapter 2

Ion Implantation and annealing

2.1 Objective

This chapter is a very concise summary of ion implantation and annealing theory. Numerous references covering all aspects of the subject exist (machine design, ranges theory,implant theory and modelling). However, the aim of the chapter is to reveal the following features of the process:

1. The nature of residual damage after ion implantation is a strong function of ion implantation and substrate variables.

2. The way that the different amorphous states that the substrate can have after ion-implantation at various doses, energies and substrate temperatures affect the annealing behavior and electrical recovery of the dopants.

The material presented is further restricted to information necessary to theoretically support the experimental results of subsequent chapters.

2.2 Ion Implantation

2.2.1 Introduction

Ion implantation is a doping technique for semiconductor materials. Traditionally, doping was achieved by diffusion from gas or solid sources at high temperature but these processes suffer from disadvantages such as lack of uniformity and difficulty to produce shallow abrupt junctions [1]. By comparison, ion implantation is a non-equilibrium process where dopant atoms are inserted into the solid by violent use of their excess kinetic energy. An ion beam is swept over the wafer surface in high vacuum and the areas to be implanted are defined by a masking layer such as photoresist. Ion implantation has now become the most important doping technique for ICs. The main reasons are listed below:

- It produces extremely reproducible and homogeneous doping profiles. Good control of the dopant environment can be achieved throughout the process.
- It is compatible with silicon planar technology (since masking layers can be photoresist, oxides or nitrides).
- Since it is a non-equilibrium process, the amount of dopant can exceed the solid solubility limit at the implant temperature.
- Is a low temperature process although annealing is necessary to restore crystallinity.

2.2.2 Ranges of ions and stopping processes

If fast, charged particles strike a solid, different processes take place which slow down the impinging particle and simultaneously damage the solid [2]. Those are:

1. Inelastic impacts with:
   (a) bound electrons leading to ionization
   (b) nuclei leading to nuclear reactions, excitations or bremsstrahlung

(c) bound electrons

2. Elastic impacts with atoms leading to partial transfer of kinetic energy.

3. Cerenkov radiation emission.

Nuclear stopping predominates at low energies and high atomic numbers (but electron stopping is still significant), while electronic stopping dominates completely for high energies and low atomic numbers.

Different theories have been developed to explain the stopping procedure. In the LSS theory [3] the total energy loss per unit distance travelled is equal to the sum of the nuclear and electronic losses. The stopping power S [1] [4], of implanted ions through nuclear collisions is described as a sum of independent two-body elastic collisions. The electronic stopping is calculated assuming a free electron gas. Calculations for this theory have been performed by several authors [5] and the results have been published in the form of tables.

In Biersack theory [6] the process of slowing down the implanted ions is described by a diffusion model. One can represent the directions of ion motion by polar and azimuthal angles ψ and θ and depict them on a unit sphere. Since the direction of the motion changes at random with each collision, the stochastic motion on the unit sphere is governed by a diffusion process such as Brownian motion.

Monte Carlo calculations for the determination of the implant profiles can be used to define the solution of transport equations [7, 8]. Both the spatial distribution of energy deposited and the particle distribution can be calculated [9].

---

[1] The stopping power is related to energy loss by the expression $S = \frac{1}{N}\frac{dE}{dx}$ where N denotes the number of target atoms /cm^3

2.2.3 Range distributions

According to the classical LSS theory as well as the Biersack approach, the range profiles of implanted impurity distributions are given by symmetrical Gaussian distributions (therefore the projected range R_p and projected straggle ΔR_p implant parameters [10] can be evaluated). However, experiments [11] have shown that dopant profiles possess tails and are skewed in both crystalline and amorphous silicon. Therefore, both theories were extended to incorporate four moments of the range distributions for many ion-target combinations [12]. For slightly assymetrical profiles the third moment is sufficient to obtain a good profile description [13] and the two joint half-Gaussian evaluated profile is accurate. However, the Pearson IV distribution employing the first four moments is the most useful for the analytical representation of an implanted profile [14, 15].

The LSS theory is of limited accuracy in the prediction of dopant depth distributions for shallow junctions. The model on which the LSS calculations of implanted depth distributions is based treats the substrate as an amorphous medium. Since in most cases, shallow implants are performed in crystalline Si (preamorphization implants are the exception) the LSS theory assumption does not hold true. The Pearson IV distribution [2] provides an excellent representation of the doping profile of B^+ implants while for BF_2^+ implants the Gaussian distribution is more appropriate [17].

---

[2]The regions of validity of the Pearson IV distributions and the accuracy of the 4 moments of the matching curves are described in [16].

2.3 Ion implantation damage and electrical activation

2.3.1 Introduction

Just after the implant process step, the implanted area will be highly disordered (possibly even amorphous) with most of the dopant ions occupying non-electrically active sites in the silicon lattice. The electrical behavior after implantation is therefore dominated by deep-level electron and hole traps, which capture carriers and make the resistivity and leakage currents high. Annealing is the process step required to repair lattice damage, place the dopant atoms in substitutional sites where they will be electrically active and thus recover carrier mobility. The shape of the carrier concentration profile is affected during the annealing stage [18] and by other high temperature process steps in the fabrication sequence. The final implant profile shape, which is crucial for the device performance within specifications, depends on a number of inter-related parameters. A closer investigation of annealing mechanisms will be presented in the following sections. The derivation of conclusions from the experimental results will be based on the effect of those mechanisms.

2.3.2 The nature of ion implantation damage

Annealing results depend on the nature of the residual damage which depends on the dopant type, the implantation dose, the implantation energy, the dose rate, the substrate temperature and the atomic mass of the substrate. As the mass of the implanted ions increases, the dose required to transform the crystalline material to amorphous decreases [10]. Therefore the best approach would be to distinguish between the different types of damage caused by different types of ions and doses. The distinction between light and heavy ions is done with respect to the mass of the Si atom. The dose level division is only qualitative since the

energy of the ions influences the dose at which a particular defect occurs; higher energy ions at a lower dose can have the same effect as that of low energy at a higher dose. As the energetic ions penetrate the solid, they collide with both the electrons and the nuclei of the target. The energy lost in electronic exitations ultimately appears as heat. The remaining energy of the primary ions goes into atomic displacement. This displacement constitutes the ion implantation damage. It is created as Frenkel pairs [19] of vacancies and interstitials. The number of those pairs is given by

$$[n] = k\frac{E_D}{2E_d} \tag{2.1}$$

where E_D is the remaining energy, k is the displacement efficiency(typically about 0.8) and E_d is the displacement threshold energy(around 15eV for Si) [20]. The interstitials and vacancies accumulate as a function of implanted dose and an amorphous phase transition has been shown to occur at a critical damage energy $\mathbf{E_D}$ of 12eV/atom or $6.0\text{x}10^{23}\text{eV/cm}^3$ for silicon[21]. This value was determined at 4° K, where annealing effects are negligible [22]. At higher temperatures, mobility of interstitials and vacancies becomes high enough that they annihilate each other or they form dislocation loops. Ions having mass equal to or higher than that of ^{51}Sb can produce amorphous regions directly. For the lighter ions, overlap of damage regions produced by several ions is required since each ion deposits less eV per atom than the threshold value for amorphization.

1. LIGHT IONS

   Light ions produce simple defects that cluster in the form of dislocation loops [23].

   - LOW DOSES

     The small mass of the ions is responsible for clouds of point defects which are not close to each other due to the low dose. Due to cascading effects they form damage clusters with a mean diamater about 5nm.

     After annealing an agglomeration of the point defects leads to the formation of dislocation loops.

- MEDIUM DOSES

  The effect of an increased dose is an increase in the density of point defects. At the same time formation of small amorphous zones and dislocation loops takes place. The effect of annealing is again the formation of additional dislocation loops [24].

- HIGH DOSES

  The dose increase has an impact on the density of the clusters. During annealing the increased number of dislocation loops tends to agglomerate. In the area near the projected range of the implanted ion where the density of the dislocation loops is the highest, formation of dislocation networks takes place due to the interaction of the dislocation loops.

2. HEAVY IONS

Heavy ions produce amorphous cascades [21, 25].

- LOW DOSES

  The bigger ion mass is related to the larger amount of momentum transfer to the substrate atoms which are being displaced from their lattice sites. Point defects and damage clusters are being created in the implanted Si. Because of the low dose the amorphous clusters are isolated.

  During annealing solid phase epitaxial regrowth (SPE) of the amorphous material takes place. The result is a re-crystallized, defect-free Si substrate with a very small number of isolated dislocation loops.

- MEDIUM DOSES

  The increased dose creates an amorphous layer which extends over and under the peak of the implanted dopant profile. The amorphous layer is more dense than for lower doses and its thickness depends on the number of implanted ions [26, 27]. This amorphous zone does not extend up to the surface since the impinging ions undergoinelasticcollisions as they first enter the substrate. During those collisions no momentum

transfer takes place. For greater depths, the ions possess less energy and they undergo elastic scattering collisions with the Si atoms. By knocking out the target atoms from their lattice sites interstitial point defects are formed. Those defects are more pronounced at the extreme of range of the implanted atoms.

Solid phase epitaxial regrowth of the amorphous layer takes place during annealing. It proceeds simultaneously starting from the two amorphous-crystalline interfaces and continuing until the two interfaces meet each other. The presence of that plane of implanted atoms is the origin of the plane of dislocation loops appearing around the middle of the previous amorphous zone. A second plane of dislocation loops that appears after annealing at the depth of the second interface, is attributed to the agglomeration of the 'end of range' interstitial dislocation loops.

- HEAVY DOSES

  The amorphous layer thickness increases with increased dose and extends towards the surface. Above a threshold dose which is critically determined by the dose rate and the substrate temperature the implanted part of the semiconductor is completely amorphized.

  During annealing solid phase epitaxial regrowth occurs into the amorphous material(see the following section). After re-crystallization of the material we have only the existence of the 'end of range' dislocation loops [28].

The recrystallization of the amorphous layer is a very important process which plays primary role for ULSI junction implants.

2.3.3 Solid phase epitaxial regrowth

Only if amorphous layers are formed can SPE growth provide an efficient mechanism of annealing. SPE growth is a thermally activated process and can be described by the Arrhenius expression [29]

$$V = V_0 \exp(-E_a/kT) \tag{2.2}$$

where E_a is the activation energy
k is the Boltzman constant
T is the temperature involved
V is the SPE growth rate
V_0 a constant that depends on the crystallographic orientation of the interface and on the doping type

According to [23] the interface velocity V_0 is 8.5nm/min for (100) and 1nm/min for (111) interfaces for undoped Si and is 60 times higher for P and As implanted wafers. The activation energy value was measured around 2.35 eV [23]. We expect therefore the SPE growth rate to vary :

- with dose (since it increases with dopant concentration) [21].
- with dopant species [30].
- with substrate crystallographic orientation (highest for $< 100 >$) [31].
- with depth, since it should show a maximum near the average projected range of the ions where maximum concentration occurs.

Annealing of loops occurs via a dislocation climb and glide mechanism. If the loop is located within twice its diameter from the surface, it glides to the surface and is annealed out. The substrate acts as a seed for the crystal growth, therefore the SPE-grown layers have exactly its orientation. TEM micrographs can be used to show the evolution of crystallization. Time resolved reflectivity is a technique used to determine the SPE rate quantitatively, but it does not provide direct information on dopant precipitation and interface structure [32]. The SPE growth state can be assessed by use of a combination of sheet resistance and ellipsometric measurements of the refractive index and extinction coefficient of the implanted wafer.

2.3.4 Annealing methods

The idea of thermal treatment after ion bombardment in order to bring the system closer to its equilibrium state is as old as ion implantation itself [18] . However the increasing demands of semiconductor technology have initiated research into a lot of different heat treatment methods. The critical parameter for characterizing the different types of annealing is temperature profile broadening. The difference in profile broadening between furnace anneal and Rapid Thermal Annealing for a high dose boron implant is depicted in 2–1.

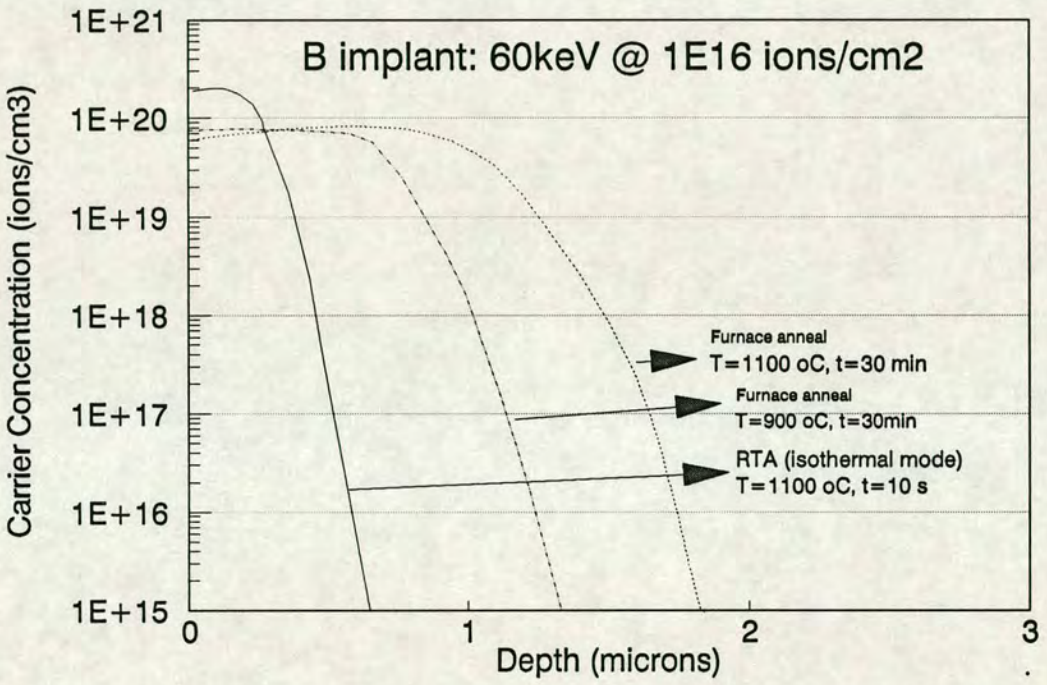

Figure 2–1: The profile broadening depends on the annealing technique used.

It is given by $\sqrt{2D^*\tau}$ where D^* is the heat diffusivity and τ is the time available for diffusion. The heat diffusivity is a function of temperature.

On the basis of time of the specimen' s anneal, four regimes of operation can be identified:

1. Furnace annealing.

   In order to retain the advantage of the lowest possible temperature processing, annealing in furnaces for times starting from 30 min and temperatures

from 900 °C has been traditionally used. Depending on the process requirements, desired degree of activation and maximum allowed dopant diffusion, the time and temperature conditions can vary over a large range of values. A number of references can be found in [10, pages 142-143].

2. Rapid isothermal annealing.

   For Si specimens, rapid thermal annealing can involve times from 5s and temperatures in the 500 - 1200 °C range. For 5s at 1100 °C the thermal diffusion distance is about 1cm. Therefore, wafers of 500 μ m thickness are uniformly heated. For an amorphous region with a maximum thickness of 1 μm, the SPE regrowth is completed in less than 1ms (from the moment the critical temperature for recrystallization is exceeded) and the rest of the time is used in removing the dislocation loops. For the above conditions the profile broadening is less than 500 Å.

3. Adiabatic annealing.

   Nanosecond pulses of energy from lasers or electron beams are used. The energy is transferred to the target in less than 1ns and is used to heat and melt thin layers of materials. Despite the large temperature gradients involved, the short duration of the anneal does not allow nucleation of thermal-stress-induced dislocations. Melting proceeds even under the implanted layer and therefore 'defect-free' annealing is obtained [33, 34]. Some of its disadvantages are the rapid dopant redistribution within the molten layer and thermal non-matching between different structures or materials.

4. Thermal flux annealing.

   A continuous wave (cw) laser or electron beam is used for heating. The temperature profile broadening is about 200 Å, therefore ion-implanted layers are uniformly heated. The times involved are just enough for SPE growth so dislocation loops with the same Burger vectors coalesce to form larger dislocation areas. Another disadvantage is the increased thermal stresses compared to adiabatic annealing. The main advantage of the method is the negligible concentration profile broadening.

2.3.5 Choice of Annealing Method

As lateral device dimensions decrease with increasing need for circuit complexity and speed, junction depths and layer thicknesses are also reduced. The generation of those junctions with the required dimensions, characteristics and repeatability is not possible with the equipment and processes currently used in VLSI production facilities [35]. The need for small thermal budgets - to minimize dopant redistribution - and the simultaneous need for complete electrical activation cannot be achieved by furnace anneal. Furthermore, sideways dopant scattering under the gate electrode can reach unacceptable levels and can shrink the channel length for CMOS transistors. There is a widely shared belief in industry, [36,37], that RTP has not widely replaced furnace anneal due to the fact that it does not demonstrate a significant process or quality advantage for current technology. However, the new device technologies are going to require it [36,38]. Rapid Thermal Anneal (RTA) is the most promising tool in semiconductor technology to circumvent problems arising from reduced device dimensions. Its system-specific limitations of temperature uniformity and temperature control [39] will, however, reduce the device yield whenever the technique is implemented on the manufacturing lines. The requirement for pre-control measurements on production lines will thus become a necessity, until the processes are fully under control [3] (with technology improvements). The conflicting ULSI requirements of minimum dopant penetration and minimum defect formation can best be met by the combined use of optimized ion implantation (appropriate choice of ion, energy, dose, temperature) and RTA for annealing [28,40]. Since the objective of this project is the development of a fast, pre-control method for ULSI production line implant profile monitoring, RTA in the isothermal mode must be used as the annealing method.

---

[3]Process control will be gained when, for example, the process C_p and C_{pk} values start to approach the target values of 2 and 1.5 respectively.

2.4 Dopant behaviour

The behaviour of an ion implanted species differs from the diffusion doped species in the following three aspects:

1. The ion implantation induced crystal damage influences the diffusion rate.
2. The as-implanted impurity concentration is not limited by the solid solubility of the dopant in silicon since it is a non-equilibrium procedure.
3. A considerable fraction of the implanted dopant resides at interstitial sites.

During annealing, redistribution of the implants will occur due to thermal diffusion which can be adequately described by Fick's laws. The diffusion coefficient (for a solid diffusion process) is given by :

$$D(T) = D_0 \exp(-Q/kT) \tag{2.3}$$

which is similar to 2.2. In the case of implantation we expect the thermal diffusion to be time-dependent due to the fact that defects are released during annealing and may, thus, enhance it. It is therefore necessary to investigate the behaviour of each dopant- type during annealing and have an insight into the way that anneal temperature and time affect its shape [4].

2.4.1 Boron/Boron Fluoride

2.4.1.1 Anneal process parameters and atomic diffusivity

A boron atom implanted into Si is usually found in one of several possible interstitial sites. During annealing it diffuses out of the intestitial sites to available

---

[4]Extensive experimental results on the effect of anneal temperature on phosphorus implant at various dose levels are recorded in literature. However, they are not included in this summary since P implants have not been treated in this project.

substitutional ones so the activation should depend on the concentration of vacancies and self-interstitials in Si [41] . The desired activation can be manipulated through the use of three process variables:

1. *Temperature* The vacancy concentration is a function of the ambient temperature [19]. By increasing the annealing temperature and thus increasing the vacancy concentration we increase the number of activated B atoms.

2. *Time* The time required for the activation of a single B atom is the time for mutual diffusion of the closest B atom and vacancy towards each other. However, the existence of other defects in a damaged substrate which annihilate vacancies is the competing mechanism for activation.

3. *Cooling rate* Quenching (rapid cooling rate) by suddenly lowering the high annealing temperature 'freezes' the dopants in their location [42] . On the other hand the high concentration of vacancies at the higher temperature is preserved during the quenching time. They therefore continue their movement towards the Si surface (even though their velocities are reduced due to quenching) and activate boron atoms nearer to the surface.

Experiments, [43,44], verify that those parameters that determine the bulk generation rate and lifetime of vacancies and self-interstitials, determine shallow junction properties as well.

2.4.1.2 Reverse annealing effect

The effective surface concentration of the implanted layer can be estimated by measuring the sheet-resistance Hall-coefficient $R_{s,eff}$ [14, page 15]. If we plot the effective surface concentration of the charge carriers versus the annealing temperature of silicon [14], we can see that $R_{s,eff}$ increases with annealing temperature up to around 550 °C due to removal of lattice disorder. In the 550-800 °C regime a decrease occurs in some cases. This reverse annealing effect is due to interactions of substitutional boron with defects that are released from the damaged regions.

The decrease of substitutional boron has been measured by channelling techniques [45]. As mentioned in [23] for B implants above the critical dose for amorphization, no reverse annealing takes place. The above observations are presented in fig. 2–2 In the temperature range of reverse annealing, rod shaped crystallographic defects elongated in $< 100 >$ directions dominate.

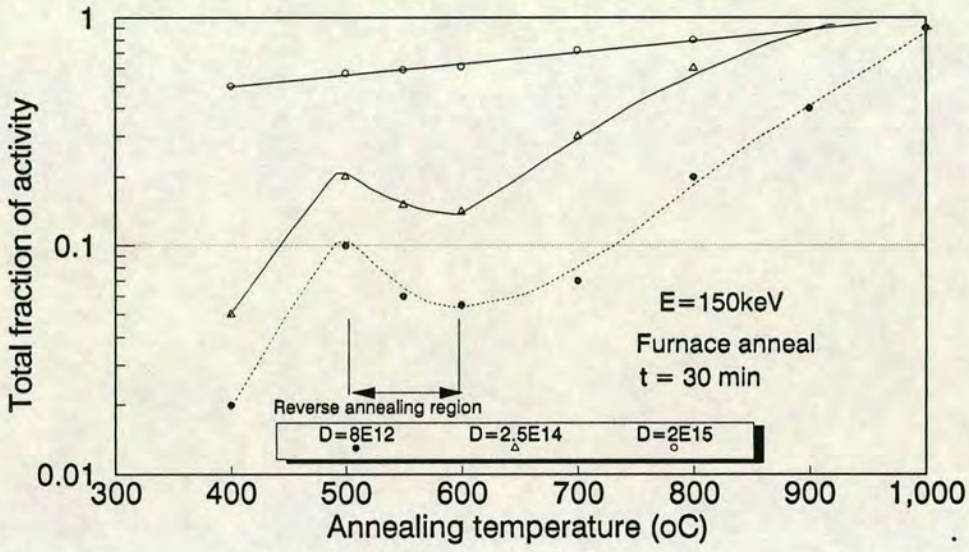

Figure 2–2: The reverse annealing effect

With increasing temperature the rod structure coarsens and elongated intersitial dislocation loops and Frank loops appear. Although the structure of the rod effects is not completely known, it was shown [23] that their shrinking is controlled by the diffusivity of B in Si. This implies that they contain B or are boron precipitates. The existence of precipitates and their dissolution during heat treatment above 800 °C further implies that the concentration in solid solution is limited to the equilibrium solubility of B at the annealing temperature. For temperatures above 800 °C we have a further decrease of the effective sheet resistance, with an activation energy around 5eV (corresponding to the energy needed for formation and migration of a vacancy) [46]. A schematic representation of the reverse annealing effect is depicted in 2–2 where the degree of activation for different temperature regimes and different doses reveals the above mechanism.

2.4.1.3 Temperature and time effects on concentration profiles

The problem is fully discussed in section 9.4.1.4 for the case of BF_2^+ implants and RTA annealing. The influence of the furnace annealing process parameters on the sheet resistance and carrier concentration profiles can be found in [14, pages 69-85].

2.4.1.4 Profile broadening during annealing

Profile broadening during annealing is determined by three types of boron atom behaviour, each with its own mobility characteristics.

1. *Clustering mechanism of boron precipitates.*

   From the profiles obtained after annealing, a relatively immobile boron fraction exists in the high boron concentration region. After annealing at temperatures in the 700-1000 °C regime, an increase of the boron concentration is observed at the mean depth of the implanted ions whereas in the neighbouring regions there is a decrease [14]. There is therefore a tendency for boron to diffuse to areas of high concentration where it precipitates. The proposed mechanism [47] suggests two stages.

   - Firstly, silicon interstitials created during implantation displace substitutional boron as they are mobilized during annealing. This decrease of substitutional boron after annealing at 600 °C was verified experimentally [48], [45].
   - Secondly, it is suggested that at high concentrations the interstitials will precipitate in cluster formation. This supposition is sustained by TEM observations [49, 50] where the increasing annealing temperatures change the granular appearance of boron-implanted silicon into linear and loop defects which are correlated with precipitates. The above effect is very pronounced at high implant doses where the maximum boron concentration is higher than the boron solubility limit at the annealing temperature.

2. *Interstitial-type increased diffusion rate (at low anneal temperatures): Fast profile broadening.*

   At the beginning of the anneal process the mobile boron fraction shows a fast diffusion effect. This is a dose-dependent effect. At lower doses it appears to occur at 700 °C whereas at the higher doses it occurs at around 800 °C. From the proposed mechanisms the most probable is the one that assumes that this effect is due to the diffusion of boron interstitials formed during implantation or during annealing by the displacement of substitutional boron by silicon interstitials [14, pages 81-83]. It must be noted that the initial profile broadening is temperature-dependent.

3. *Substitutional-type, decreased diffusion rate: Slow profile broadening.*

   After the initial broadening a substitutional-type diffusion prevails and the diffusion rate is slowed down. The diffusion rate is highly concentration-dependent [14].

2.4.2 Arsenic

2.4.2.1 Sheet resistance variation during annealing

If an isothermal anneal takes place, we can have differences in the behaviour of the sheet resistance for different implant doses. In order to verify this behaviour, the variation of sheet resistance with annealing temperature and implant dose was investigated. The experimental results of the sheet resistance variation with annealing temperature is depicted in fig. 2–3 for 3 different implant dose levels. The dose levels were selected to be below, around and above the equilibrium solid solubility regimes. All implants were carried at an energy of 40keV on a Lintott III series implanter. An ADDAX Rapid Thermal Annealer has been used for the experiment. The duration of the isothermal anneal was 10s. This time duration was found to be adequate for activating the dopants and at the same time minimizing the inevitable profile redistribution. The variation of sheet resistance

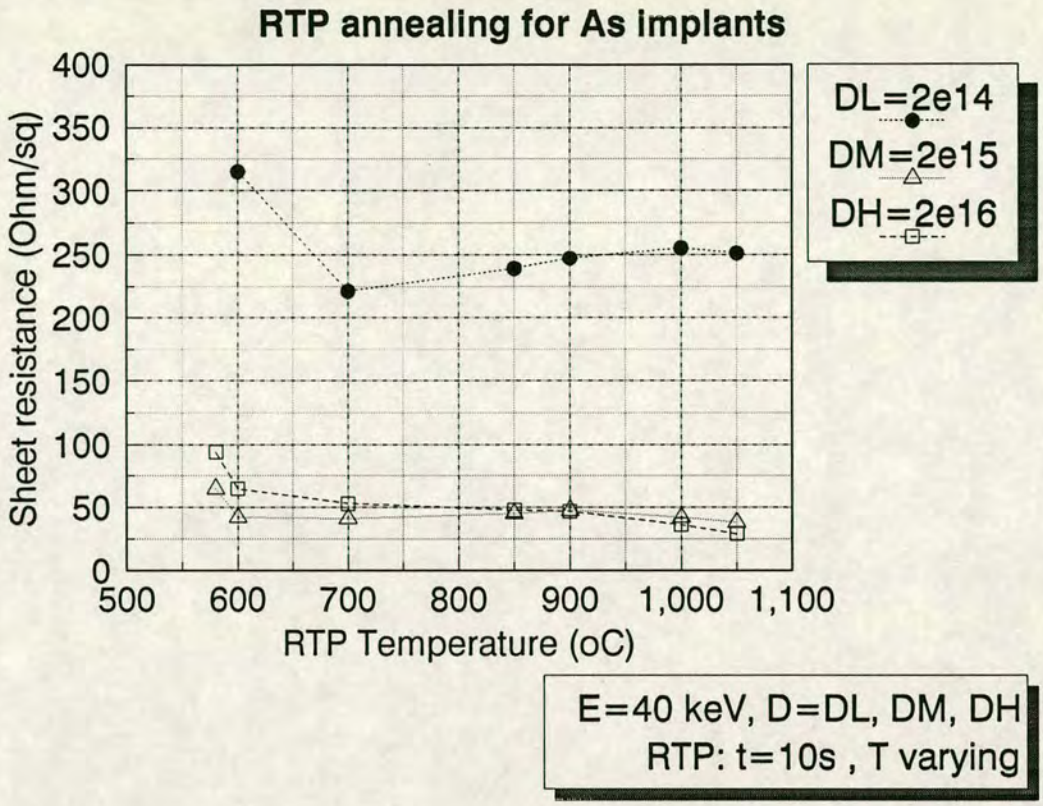

Figure 2–3: Variation of sheet resistance with RTA annealing temperature for 3 different dose levels (low :DL, medium :DM and high :DH) for As implants.

with time was not examined but the general trends of sheet resistance variation with time can be found in [51].

For all doses a low temperature anneal step leads to recrystallization of the amorphous layer and therefore to a rapid decrease in the sheet resistance. This effect can be seen in fig. 2–3 in the 580 to 700 °C temperature regime. For the low and medium dose levels, sheet resistance displays a slight increase with temperature, after recrystallization has taken place. This can be attributed to arsenic clustering near the near peak region. This leads to a partial deactivation and, therefore, an increase in the measured sheet resistance. At higher temperatures, the increased mobility at the peak concentration regime dominates over the clustering effects and sheet resistivity decreases.

The above effect is not observed in the high dose curve. The electrical activity

at high doses is rather complicated [18, page 103]. Near the solid solubility limit many dopants partially coalesce. Impurities with high segregation coefficients, such as As, P and Sb redistribute during high temperature treatments to develop a concentration gradient at the interface (this is because the rate at which the impurity is moving towards the Si bulk is higher than the rate transported away by diffusion) [52]. Implanted impurities are pushed out at the interface during low temperature annealing (recrystallization) because of the impurity segregation at the moving amorphous-crystal boundary during regrowth [53, page 131]. An impurity redistribution is therefore expected at those temperatures. At higher temperatures, implanted As atoms precipitate into the dislocation loops during annealing. For prolonged annealing times those loops climb to the surface [54] and carry with them As atoms at a rate faster than As can diffuse away. Therefore, a pileup of implanted As atoms develops near the surface but only for high dose implants. This phenomenon does not permit deactivation in the near-peak area which would lead to an increase in sheet resistance for high dose implants.

The variation of the sheet resistance with annealing time for As implants is discussed in [51]. No sheet resistance measurements can be performed prior to a 10s RTA. The main reason for such behaviour is the time needed for the temperature to rise over the 500 °C barrier (into the SPE regrowth temperature regime). In order to avoid this effect, a 5s pre-heat to 500 °C is always used before the actual annealing temperature in the RTA annealing recipe. For annealing time durations less than 10s, sheet resistance decreases (the wafer approaches a single crystal state). For annealing times longer than 10s sheet resistance starts to increase again. This is due to As loss from the surface. The use of an oxide cap over the Si surface reduces the As loss.

Bibliography

[1] G. Dearnaly, J. H. Freeman, R. S. Nelson, and J. Stephen. *Ion Implantation.* North Holland, 1973.

[2] J. F. Ziegler. The stopping and range of ions in solids. In *Ion Implantation Science and Technology, Second Edition*, pages 3–63. Academic Press, 1988.

[3] J. Lindhard, M. Scharff, and H. E. Schiott. Range concepts and heavy ion ranges. *Matematisk-fysiske Meddelelser*, 33(14):1–42, 1963.

[4] T. E. Seidel. Ion implantation. In *VLSI Technology.* McGraw-Hill, 1989.

[5] J. F. Gibbons, W. S. Johnson, and S. W. Mylroie. Projected range statistics in semiconductors. 1975.

[6] J. P. Biersack. *Nuclear Instruments and Methods in Physics Research*, 182/183:199, 1981.

[7] I. B. Biersack and L. G. Haggermark. A Monte Carlo computer program for the transport of energetic ions in amorphous targets. *Nuclear instruments and Methods*, 174:257, 1980.

[8] T. L. Crandle. Analysis of ion implant processes through Monte Carlo based simulation. *Solid State Technology*, (1):43–45, 1990.

[9] M. D. Giles and J. F. Gibbons. Two-dimensional ion implantation profiles fron one-dimension projections. *Journal of the Electrochemical Society*, 132(10):2475–2478, 1985.

[10] J. L. Stone and J. C. Plunkett. Ion implantation processes in silicon. In *Impurity Doping.* North Holland Publishing Company, 1981.

[11] K. B. Winterbon. Ion implantation range and energy deposition distribution. volume 2. IFI/Plenum Press, New York, 1973.

[12] J. F. Gibbons and S. Mylroie. Estimation of impurity profiles in ion-implanted amorphous targets using joined half-gaussian distributions. *Applied Physics Letters*, 22(11):568–569, 1973.

[13] W. K. Hofker. Implantation of boron in silicon. *Phillips Research Reports, Supplements*, (8), 1975.

[14] H. Ryssel, G. Prinke, K. Haberger, K. Hoffmann, K. Muller, and R. Henkelmann. Range parameters of boron implanted into silicon. *Applied Physics*, 24:39–43, 1981.

[15] R. G. Wilson. The Pearson IV distribution and its application to ion implanted depth profiles. *Radiation Effects*, 46:141–148, 1980.

[16] M. Simard-Normandin and C. Slaby. Empirical modeling of low energy boron implants in silicon. *Journal of the Electrochemical Society*, 132(9):2218–2223, 1985.

[17] J. Gyulai. Experimental annealing and activation. In *Ion Implantation Science and Technology, Second Edition*, pages 93–163. Academic Press, 1988.

[18] N. W. Ashcroft and N. D. Mermin. *Solid State Physics.* Holt-Saunders International Editions, 1976.

[19] J. W. Corbett and J. C. Bourgoin. *Point Defects in Solids.* Plenum Press, New York, 1975.

[20] J. Narayan, O. S. Oen, D. Fathy, and O. W. Holland. Atomic structure of collision cascades in ion implanted silicon and channeling effects. *Material Letters*, 3:67, 1985.

[21] J. R. Dennis and E. B. Hale. *Journal of Applied Physics*, 49:1119, 1978.

[22] S. Mader. Ion implantation damage in silicon. In *Ion Implantation Science and Technology, Second Edition*, pages 63–92. Academic Press, 1988.

[23] C. R. Peter, J. P. de Souza, and C. M. Hasenack. Prolonged and rapid thermal annealing of boron implanted silicon. *Journal of Applied Physics*, 64:2696, 1988.

[24] J. Narayan, D. Fathy, O. S. Oen, and O. W. Holland. Structure of ion implantation damage and process of amorphization in semiconductors. *Journal of Vacuum Science and Technology, A*, 2(3):1303–1308, 1984.

[25] J. Narayan and O. W. Holland. Rapid thermal annealing of ion-implanted semiconductors. *Journal of Applied Pysics*, 56(10):2913, 1984.

[26] J. Narayan and O. W. Holland. Characteristics of ion-implantation damage and annealing phenomena in semiconductors. *Journal of the Electrochemical Society*, 131(11):2651–2662, 1984.

[27] T. O. Sedgwick. Rapid thermal processing.an integrap part of shallow junction formation. *Nuclear Instruments and Methods in Physics Research B*, B37/38:760–765, 1989.

[28] L. Csepregi, E. F. Kennedy, T. J. Gallagher, and J. W. Mayer. *Journal of Applied Physics*, 48:4234, 1977.

[29] L. Csepregi, R. P. Kullen, J. W. Mayer, and W. W. Sigmon. *Solid State Communications*, 21:1019, 1977.

[30] L. Csepregi, J. W. Mayer, and T.W. Sigmon. *Applied Physics Letters*, 29:92, 1976.

[31] G. L. Olson, J. A. Roth, L. D. Hess, and J. Narayan. *Layered structures and Interface Kinetics*. KTK Scientific Publishers, Tokyo, 1985.

[32] J. Narayan, J. Fletcher, C. W. White, and W. H. Christie. Melting phenomena and laser annealing in semiconductors. *Journal of Applied Physics*, 52:1721, 1981.

[33] C. W. White, J. Narayan, and R. T. Young. Laser annealing of ion implanted semiconductors. *Science*, 204:461, 1979.

[34] C. Russo. Rapid thermal processing - Where has it been? Where is it going? *Nuclear Instruments and Methods in Physics Research B*, B6:298–306, 1985.

[35] S. Leavitt. Rapid isothermal anneal of as implanted silicon. *Semiconductor International*, (3):64–70, 1987.

[36] S. R. Wilson and R. B. Gregory. An overview and comparison of rtp equipment: A user's viewpoint. *Materials Research Society 1986 Symposium Proceedings*, 52, 1986.

[37] S. R. Wilson, W. M. Paulson, and R. B. Gregory. Rapid Annealing Technology for future vlsi. *Semiconductor International*, (6):185–190, 1985.

[38] R. Kakoschke. Temperature problems with Rapid Thermal Processing for VLSI applications. *Nuclear Instruments and Methods in Physics Research B*, B37/38:753–759, 1989.

[39] C. Russo. Rapid thermal processing systems: Some current trends. *Microelectronics Manufacturing and Testing*, 9(6):1, 1985.

[40] R. B. Fair. Concentration profiles of diffused dopants in silicon. In *Impurity Doping*, pages 317–436. North Holland Publishing Company, 1981.

[41] K. Tempelhoff and N. Van Sung. Formation of self-disordered agglomerates in dislocation-free silicon during crystal growth. *Phys. Status Solidi A*, 70:441, 1982.

[42] T. M. Liu and W. G. Oldham. Channeling effect of low energy boron implant in (100) silicon. *IEEE Electron Devices Letters*, EDL-4:59, 1983.

[43] S. S. Cohen, J. F. Norton, E. F. Koch, and G. J. Weisel. Shallow boron-doped junctions in silicon. *Journal of Applied Physics*, 57(4):1200–1213, 1985.

[44] J. C. North and W. M. Gibson. Channeling study of boron implanted silicon. *Applied Physics Letters*, 16:126, 1970.

[45] G. Carter and W. A. Grant. *Ion Implantation of Semiconductors.* Edward Arnold Publishers Ltd., 1976.

[46] G. D. Watkins. Proc. 7th int. conf. on the physics of semiconductors(Paris-Royaumont 1964). page 97, New York, 1964. Academic Press Inc. vol.3.

[47] G. Fladda, K. Bjorkqvist, L. Eriksson, and D. Sigurd. The lattice location of boron ions implanted into silicon. *Applied Physics Letters*, 16:313, 1970.

[48] R. W. Bicknell and R. M. Allen. Electrical and electron microscope studies of annealed ion implanted silicon. *Radiation Effects*, 6:45, 1970.

[49] L. T. Chadderton and F. H. Eisen. On the annealing of damage produced by boron ion implantation of silicon. *Radiation Effects*, 7:129, 1971.

[50] S. R. Wilson, R. B. Gregory, and W. M. Paulson. Rapid isothermal anneal of as implanted silicon. *Applied Physics Letters*, 41(10):978–980, 1982.

[51] A. S. Grove. *Physics and Technology of Semiconductors.* Wiley, New York, 1967.

[52] J. S. Williams and K. T. Short. *Metastable phases by Ion Implantation.* North Holland, Amsterdam, 1982.

[53] K. Yokoto, K. Ohtsuki, S. Ishihara, and I. Kimura. Pileup of arsenic implanted into silicon with high doses at surfaces. *Nuclear Instruments and Methods in Physics Research*, B39:362–365, 1989.

Chapter 3

Ion Implantation Problems and Monitoring

3.1 Objective

Controversy about product and process requirements are commonplace in the semiconductor industry. The process and device technology interaction with the implantation equipment, through the process capability that the implanters can provide, is a key issue for increasing yield. Process control during the ion implantation and subsequent annealing steps is therefore necessary for effective IC manufacturing. The ion implant process, although inherently more reproducible than either a diffusion or epitaxial deposition, is also subject to some of the same problems as these processing steps. The subsequent annealing stage might add even more problems. Those problems will be briefly presented. Appropriate tools for validating both the implanter and the process itself exist and will be also mentioned. However, as it will be shown, process monitoring in its existing status is not adequate to monitor problems associated with incorrect dopant profile shapes. Improved impurity profile monitoring for production, evolves as the new monitoring requirement.

Due to the vast experience obtained from the developed process monitoring methods, any new technique for profile monitoring should make use of the most appropriate of the established monitoring methods.

3.2 Ion Implantation and the associated malfunctions

3.2.1 Types of Ion Implanters and their uses

Most large volume Si IC fabrication lines have at least two different implanters for routine implants of B, As and P: high current and medium current machines. Some new types of implanters (MeV implanters, high current oxygen implanters and focused ion beam implanters) have been developed for novel applications of ion implantation but have not yet been incorporated into production lines.

3.2.1.1 High current implanters

The present generation of those implanters produces 10-12 mA of P^+ and As^+ and 4-6mA of B^+ beam currents. They are batch processing machines (the batch size depends on the wafer size and the machine vendor). Mechanical scanning (high speed rotating wheel or disk) or mechanical plus magnetic scanning of the wafers alleviates the problem of the increased wafer heating at these beam powers, however, wafer cooling systems are still required. Those machines are used for implant doses in the range of 10^{13} to10^{17} ions/cm^2 and energies in the 10 to 160keV regime. Throughput depends on the dose used for the implant.

3.2.1.2 Medium dose implanters

The beam current produced is typically in the 500 to 1500 μA regime. They are serial processing machines and use an electrostatic scan system to raster the beam across the wafer. The implant dose ranges from 10^{10} to 10^{14} ions/cm^2. The energy range is in the 5 to 200 keV range. Throughput depends on the implant dose level and the ion current beam.

3.2.2 Ion Implantation malfunctions

Although ion implantation is a highly controlled method of doping semiconductors, during the implant a vast variety of errors can emerge. In Table 3–1 the type of implant errors that might appear at the various stages of the implantation are presented.

From the other side, the desire for increased productivity and the evolution of the use of larger area wafers can increase the contribution of the implantation and annealing process steps to faults. The impact of wafer size on ion implantation equipment design, throughput, dose uniformity, wafer flatness, control of wafer temperature during implant and many other technological aspects affecting process uniformity and parametric yield are obvious.

In order to present and explain the problem it is better to regroup them in terms of the causes. We can have:

1. Wafer related problems.

2. Machine related problems.

3. Human error related problems.

3.2.3 Wafer related problems

3.2.3.1 Channeling in Si

The ongoing quest for device miniaturization necessitates smaller vertical geometries and therefore shallower structures. Shallower structures require lower implant energies and less thermal redistribution. Due to the trend for shallow junctions, the ion distribution after implantation and annealing is of great importance. Incident energetic ions that are aligned with a crystal axis or plane can be steered into Si by a series of gentle collisions between the atomic planes and thus travel much deeper than their projected range. Electronic collisions provide the dominant energy loss mechanism in this phenomenon which is defined as channeling.

Ion implantation fault modes		
Fault stage	Problem origin	Problem type
1. Pre-implant	• Screen oxide thickness error • Mask error • P/R failure	• Oxide growth • Mask making • Photolithography
2. Implant set-up	• Dose selection error • Double implant • Back implant • Wrong species implant • Energy selection error	• Set-up
3. Implant mode	• Wafer surface charging • Charge exchange • Ion beam contamination • Leakage effects • Dosimeter circuitry fault • Vacuum loss faults • Ion beam contamination • Ion energy error • Broken wafer fragment shorts • Capacitively-coupled noise error • Scan lock-up • Photoresist outgassing • Secondary particles • Beam neutralization • Proximity effects due to tilt angle • Wafer heating	• Implanter malfunction
4. Post-implant treatment	• Two-step implant error • Incomplete activation • High temperature process steps	• Second implant error • Anneal treatment • Process steps

Table 3–1: Implant errors

In *axial channeling* the penetration of ions directed along crystalline channels is greater than those moving in a 'random' direction or in an amorphous solid [1]. As the energy of the ion beam is decreased the critical angle for scattering into an axial channel increases [2]. Axial channeling effects are reduced by offsetting the wafer's crystallographic axis at an angle to the incident ion beam. This offset angle must increase for reduced energies in order to minimize axial channeling. The employment of large offset angles for ion implantation has several disadvantages since:

- For masked implants with steep and high sidewalls, increased shadowing effects can be observed.
- Implantation through an angle can remove previously implanted dopant atoms.
- Increased sputtering of surface atoms can occur.
- For low dose implants dose inaccuracies might occur [3].

In *planar channeling* ions slide along crystal planes without losing much of their energy. For low energies and light ions this effect predominates. The increased depth produces deeper junctions and lower sheet resistance. Planar channelling effects can be reduced by controlling the azimuthial orientation of the wafer (wafer twist) [4]. Both effects can be reduced by implanting through a thin dielectric layer (eg oxide) or by a pre-amorphisation implant [5].

For electrostatical scan machines the principal beam angle, the angular scan and offset angles, the wafer flex angle (the wafer is flexed over a heat-sink pad for improved wafer cooling), the tilt and twist angles and the crystal orientation are the key parameters in control of planar and axial channeling effects [6, 7].

In the case of batch process implanters (disk-based) the geometry variables affecting planar channeling are the implant angle of the beam (tilt angle), the wafer orientation relative to the disc axis (twist angle), the platen doming (flex angle), the angular variation in the incident beam and the platen angle with respect to the disk spin axis [8].

There is a direct impact of both channeling effects on junction depth uniformity across the wafer. For a disk-type mechanical scan implanter, axial channeling of an 80 keV 7×10^{13}ions/cm^2 implant can exceed a 15 % variation in sheet resistance due to the above-mentioned effects [6]. For higher doses the channeling effect cannot be effectively identified and measured by sheet resistance mapping [6], although it still exists. An implant profile is needed to verify the length of the channeling tail at various wafer cites. C-V measurements on diodes fabricated across the wafer [9]are not suited for production line monitoring.

3.2.3.2 Damage introduced to Si by ion implantation

High-dose ion implantations leave residual defects in silicon which can be present even after the annealing stage, as discussed in chapter 2.

Implantation through thin layers of materials is common in IC fabrication. Those layers might be device layers (ie oxides), bevelled mask edges or contaminants that were deposited on the wafer surface. After collisions with high energy impinging ions some of those particles gain enough energy to penetrate into the semiconductor, thus creating additional damage and degrading the semiconductor material near the surface. Those particles constitute the recoil implanted species [10,11] and their maximum penetration depth does not exceed 100 Å. They can alter the measured resistivity (if they are dopants from previous implants) or create deep level traps if they are metal impurities. Due to their small concentration values they are difficult to detect by sheet resistance monitoring.

3.2.3.3 Ion-rate-arrival dependent effects

The three significant effects described below are closely related to the stopping mechanism of ions in the wafer and depend on the rate of arrival of ions on the wafer surface.

Wafer charging effects. This type of problem is particularly associated with high current implanters and high dose applications. Semiconductor implantation

involves implantation into or through insulating structures. The charge transported by the implanted ions on such structures will accumulate and develop a potential between the substrate and the surface structure [12]. The results of wafer charging can be grouped into two seperate phenomena that directly affect the final IC production yield.

Macro-charging results from the lack of good electrical return paths for certain implanted charges over the whole wafer surface. As a macroscopic effect it results in an incorrect estimate of the implanted ion dose and in the generation of a global electric field that interferes with the implanter's effort to properly distribute the ions on the wafer. Microcharging is the result of localized trapped charge in the vicinity of the dielectric structures of the IC. Those trapped charges at the insulator-conductor interface generate a high local electrical field when seperated by a thin dielectric layer. Breakdown of the insulator by this high electric field may cause explosive vaporization of the surrounding materials. The two phenomena are usually independent and the generation mechanisms are different. The magnitude of voltage required to deflect the ion beam should be in the order of hundred of volts and the charged area of centimeter dimensions while in order to destroy a MOS structure of a few square microns only several volts are required [13].

Many techniques have been suggested to negate this charging problem. Generally these neutralization methods can be categorized into "before" and "after" impact techniques. Some of the methods used to neutralize the ion charges before impact are the plasma bridge, the electron injection and the charge exchange with residual high pressure background gas [14,15]. Some proposed after-impact techniques are the electron flood [16] and the photon flood. The proposed photon flood method uses photoconductivity to increase the material conductivity and thereby short-circuit the trapped charges. The most commonly used technique is the incorporation of an electron flood gun within the ion implanter to directly neutralize the trapped surface positive charges [17,18]. In order to monitor those phenomena the most common methods used are different types of test structures, optical dosimetry and the resistive four-point probe technique.

Photoresist outgassing. The use of photoresist masking allows great processing flexibility in IC process flows. Masking thickness is energy, species and dose dependent and depends on the particular photoresist characteristics. Estimates of the required photoresist thickness for different conditions exist [19–21]. In applications encompassing higher doses or higher beam current implants a number of difficulties arise. Those include destruction or deformation of the photoresist mask due to excessive wafer heating, severe outgassing, difficulty in stripping the photoresist after high dose implants [22] and increased need for frequent cleaning residues from end-station chambers and Faraday cup assemblies. Excessively high pressures in the end-station and the beamline regions of the implanter can cause neutralization and other effects leading to overdosing and dose non-uniformities. Outgassing of the photoresist film also results in pressure increase. Initially it was thought that the wafer temperature is the most important parameter in outgassing. However, results presented at the 4th International Conf. on Ion Implantation [23], have shown that outgassing is not caused by wafer heating and that the difficulty in photoresist stripping is not a function of temperature of the wafer during the implant itself. As shown in [21,22] it is now quite clear that outgassing and the damage of the photoresist which makes it difficult to strip, are the inevitable results of ion bombardment. The mechanisms of radiation damage which cause outgassing and the formation of a carbonized layer on the top surface of the photoresist do not depend upon wafer temperature and are not significantly affected by photoresist pre-treatments. These effects are the result of the conversion of the base organic compounds into amorphous carbon [24].

Wafer heating. The temperature of the wafer during implantation increases linearly as a function of the dose [25]. The temperature is also an increasing function of the beam power. The combination of those two parameters determines the final equilibrium temperature reached (the only cooling mechanism is radiation). Since high temperatures result in photoresist degradation and non-uniform self-annealing during the ion implantation process, problems in achieving a uniformity below 1% after annealing are encountered. Wafer cooling in medium current implanters is achieved by either flexing the wafer over a domed, pliable, thermally

conductive material which is in contact with a cooled platen or by using hydrogen or nitrogen gas to transfer heat from the wafer to the cooled platen [26]. However, increased planar channeling due to wafer flexing can severely deteriorate junction depth uniformity. Beam sharing, where sequential implant segments are performed alternately on a dual end station system and the segment time is at least an order less than the thermal time constant of the wafer and cooling system, is also used.

3.2.3.4 Particle contamination

Particles on the surface of wafers can cause randomly distributed defects in photolithographic processes and in other critical steps. In the case of ion implantation this could lead to blocking the ions and therefore degrading device and circuit yield. A number of empirical yield models have been produced [27]. Particles may be deposited on wafers processed in implanters both inside and outside the end station vacuum environment. The principal source of particles is the Si wafers themselves which can generate microscopic particles chipped off from the edges of the wafer or from abrasion due to wafer handling. Wafer breakage inside the implanter, particles generated by moving parts in the vicinity of the wafer handlers [28], deposits on the walls inside the vacuum system, fragments of blisters in photoresist generated inside the implanter when the coated wafers are insufficiently cooled [29] consitute the main remaining sources of particles in the implanters. The types of forces that cause the particles to flake off and migrate onto the wafers include aerodynamic, electrostatic, centrifugal, gravitational and impact forces [30]. Good vacuum conditions and frequent clean-up can improve the contamination levels. Operating procedures to achieve the required degree of cleanliness are described in more detail in [31].

3.2.3.5 Crystal orientation

The channeling, the regrowth rate of amorphous layers and the thermal annealing of defects in Si is dependent upon the crystal orientation. This leads to differences in the implant damage and carrier depth profiles in partially annealed wafers [32].

3.2.3.6 Lateral profile spread

Implanted ions coming to rest will suffer lateral scattering, which will give rise to lateral broadening of both damage and dopant profiles.

3.2.3.7 Profile modification

Range theories and all the developed models are applicable for low dose implantations. For high dose implantations where the implanted species is no more a trace element in the Si matrix, the implanted profile is modified due to [33]:

1. Erosion of the Si surface due to sputtering
2. Swelling of the crystal lattice due to the additional atoms.
3. Loss of implanted species that are implanted near the surface region of Si due to sputtering.
4. Changes in the stopping power due to the big number of the implanted ions.
5. Segregation, precipitate growth and formation of other phases.

3.2.4 Machine related problems

3.2.4.1 Dose uniformity

There are two distinct kinds of uniformities for investigation after an implant. **Macrouniformity** involves a wafer-scale uniformity. **Microuniformity** involves the uniformity within each individual die. Both of them are equally important. The former is very useful in assessing what went wrong during the implant. The latter monitors the actual end product of a semiconductor factory. Since circuit designers base most device performance upon ratios of process-dependent variables rather than their values, it can be used to determine if a specific die will work. It must be noted that uniformity problems are machine dependent and the origins

of non-uniformity are different for the different ion beam scanning techniques as discussed in [33]. The typical uniformity specification for a modern ion implanters is less than 0.75 % for a 1σ dose variation across a single wafer and the dose level repeatability is of the same order. Doping variations in mechanical-scan implanters can arise from subtle variations in the scan velocity, failure of the stepper motor which slowly translates a spinning disk in front of the beam, failure in the microprocessor that controls those movements and many other causes which depend on the mechanical configuration of the scanning system. Some of the main factors limiting uniformity of implant with symmetrically driven electrostatic scanning plates are summarized below.

1. **Wafer tilt and implant angle.** In order to avoid channelling, wafers are normally tilted. Each scan axis has therefore a particular form of geometric distortion. The effect becomes more pronounced with increasing wafer diameter and tilt angle [34]. The effect is a geometry-induced non-macrouniformity. By the use of analogue computers associated with each axis a corrective waveform can compensate for angle tilt and wafer size [35].

   Inaccurate platen angle readouts and nonlinear deflection plate sensitivity can induce non-uniformity even if the above correction system is present. The only way to avoid such errors is to have variable control inputs from the front panel to compensate such errors after assessing 2-D implant monitor scans.

3. **Beam to scanner plates misalignment.** Misalignment of the beam center through the deflection plate gap by an amount of 1/4 the gap distance may result in uniformity variation of $2\sigma = 0.75\%$ [36].

4. **Beam noise.** Ion source instabilities cause variations in beam current, leading to ion deposition which is splotched or grainy. Since those noise modulations are not removed at their source, the only solution remaining is to average them out over an as large as possible area. This requires maximum slew rate from each scan amplifier(otherwise the averaging-out effect is lost). Tests done to prove that beam noise tends to average was demonstrated in [37].

Even the shortest implants (less than 10s) should be done with greater than 10,000 passes of the beam.

5. **Beam walkover.** Since the dose processor chooses when to start an implant while the scan controller is scanning internally, the beam position may not be at the starting position resulting in an unspecified and non-repeatable path across the wafer. A link between the two is necessary. Conventional scan controllers have beam walkovers if they are not linked to the dose processor.

6. **Microstripping.** Conventional beam scan controllers derive X and Y scan signals from a crystal oscillator. The wafer scan pattern is therefore mathematically limited to retrace its path every oscillation period. It is evident that the beam path strikes some points and misses others. This residual microstripping is inherent to scan controllers and for short implant times combined with short retracing periods the micro-uniformity is unacceptable.

7. **Beam spot size.** If we assume a spot size of a 1/20 wafer radius and allow a 50% variation in spot size, the non-uniformity produced is only 0.8% [38].

8. **Offset scan.** In most implanters, a neutral beam trap is provided by offsetting the beam line in one axis. This offset causes the distance travelled by the beam to be shorter at the maximum deflected beam and longer for the minimum deflected beam. The non-uniformity introduced by this offset depends on the scan angles and the offset angle, its effect is not small and should be compensated for optimum uniformity [39].

9. **Implant time.** The choice is related to the simultaneous solution of noise, beam walkover and microstripping problems. Scan controllers limit system throughput for low or medium doses if the optimum scan pattern is prefered.

9. **Beam neutralization.** An electrostatic-scanning system in which the neutral trap deflection plates are placed before the X and Y scanning plates may produce an underdosed area. This behaviour is due to the formation of neutral atoms within the deflection and Y-scanning plates under poor vacuum conditions.

3.2.4.2 Beam purity

Good control of the dose might be compromised by charge exchange processes within the beam and dissociation of molecular species [40]. If poor vacuum conditions exist ($> 10^{-6}$torr) in the beam line then neutralization of the high velocity ions, by electron capture from the residual gas molecules will occur. Problems similar to those of beam neutralization (mentioned earlier) may occur.

3.2.4.3 Wafer temperature

The use of high power ion beams for high dose implants (driven by the requirements for efficient implantation of large-area wafers) might lead to wafer cooling problems. Poor implanter cooling mechnisms can lead to wafer temperatures in excess of the 70°C to 100°C range. Anomalous dopant activation effects or 'in-situ' annealing can distort the implant profile [23].

3.2.4.4 Dose rate

The instantaneous current density or dose rate depends on parameters that are difficult to control. The beam spot size, the plasma ion source stability and the ion optics are among the principal sources of variation of dose rate. Variation in dose rates can affect the sample temperature and therefore the defect densities

3.2.4.5 Sputter contamination

As the ion beam strikes the spinning disk or the the wafer clamp, the ion beam aperture material will be sputtered off and deposited onto the wafer. Contamination is thus transported to the wafer [41]. Recoil implantation may drive the heavy metal or hydrocarbon contaminants deeper into the Si unless the implant is performed through a thin oxide layer(this however may lead to oxygen recoil implantation in Si).

3.2.5 Human error related problems

The use of automation combined with proper training of implant operators can reduce the 'man-made' errors. System self diagnostics and adaptive control mechanisms, which are introduced as standard in the advanced ion implanters, can be used for self-diagnostics and characterization of the implantation system itself. Automated set-up procedures are being employed in the new generation implanters. A carefully designed expert system to control the operator-machine interaction can be used in order to eliminate human errors.

3.3 Anneal malfunctions

3.3.1 Main principles of RTA

Rapid thermal annealing in the isothermal mode is done by systems characterized by an intense radiation source coupled to a thermally isolated wafer to produce a temperature increase. The wafer is subjected to the radiation field long enough to reach the steady-state temperature needed for uniform dopant activation [42]. In order to ensure proper operation of the RTA the following four principles have to be satisfied:

1. Energy has to be uniformly applied to the wafer and the energy source should heat and cool rapidly.
2. The wafer supporting device must not affect the uniformity of heating and must not conduct heat away.
3. The wafer temperature must be controlled accurately and with a closed loop during the process. The temperature measurement must also possess the shortest possible response time to temperature variations.
4. The environment of the wafer must be contamination level controlled.

If active carrier monitoring methods are used for measuring doping uniformity of implanted wafers, the anneal step malfunctions have to be investigated.

3.3.2 Machine related problems

3.3.2.1 Temperature non-uniformity

Temperature nonuniformity across the wafer and the associated problem of achieving repeatability are the subjects of main concern in RTA since they are crucial to achieving uniform energy application. Erratic dopant activation is inevitable from such a nonuniformity [43]. Unfortunately, the problems encountered with the monitoring of temperature and uniformity have not yet been solved satisfactorily.

3.3.2.2 Choice of anneal time and temperature

Incomplete dopant activation due to insufficient anneal time or low anneal temperature may lead to big variations in sheet resistance values across the wafer. This can be seen in chapter 8. Both the level of dopant activation(sheet resistance value) and the dopant distribution(sheet resistance uniformity) can be affected and lead to erroneous assessment for the implant dose uniformity. Therefore, anneal time, temperature and time-temperature ramp-up and ramp-down profile should be taken in account when assessing a sheet resistance wafer map.

3.3.2.3 Ambient gas flow

Nitrogen or argon flow are used to keep atmospheric oxygen and water vapors from entering the chamber during the anneal cycle. Turbulent gas flow might lead to thermal gradients within the annealer. Those lead to temperature gradients on the wafer surface and anneal-induced sheet resistance non-uniformities.

3.3.3 Impact of RTA implementation on production lines

RTA has been intensively studied as the most likely replacement for furnace annealing to circumvent problems arising from reduced device geometries (see the discussion in chapter 2). The main driving forces are:

1. **Reduction in high temperature processing time.** Full dopant activation with minimal redistribution makes shallow junctions and reduced geometry device structures reliable for ULSI.
2. **Reduction in overall power consumption.** By reduction of the number of furnaces required and the short time duration of the RTA process significant cuts in power consumption can be achieved.
3. **Step time reduction.** The time reduction of this step can lead to an overall process cycle-time reduction.
4. Single wafer processing mode benefit. The inherent single wafer processing mode of RTA is favored by the desire for increased productivity of IC and the concommitant trend for the use of larger area wafers.

The RTA malfunctions and lack of technology maturity, as mentioned above, have been responsible for the slow acceptance of RTA as a production tool. Therefore, the expected deterioration of performance and yield of the process from the substitution of conventional furnace anneal by RTA is the issue that **will make indispensable pre-control type of monitoring and will drive the need for a new flexible implant profile monitoring technique.** Such a tool will be needed to provide feedback about the process variation and to trace back possible problem causes within a production environment.

3.4 Implantation process control

3.4.1 Process control definition

A practical definition of process control, [44], is:

> *The measuring of particular critical variables within the manufacturing process for the purpose of:*
>
> 1. *Gathering information about the process and the processing equipment.*
> 2. *Analyzing the gathered information.*

3. Making a decision about the status of the process.

If the status is beyond specification limits or malfunctions exist, corrective action should be indicated and initiated.

3.4.2 Process control philosophies

Inspection of actual product wafers allows the user to detect implant errors within minutes after implantation. This attribute is employed to decrease processing errors, increase fab yield and lead to overall cost and quality savings.

Two predominant philosophies are competing in the fab environment [1]:

1. **System Testing.**The objective is to isolate the system (the implanter and the RTA equipment in our case) as completely as possible from all other process systems. The underlying philosophy is that if the equipment is controlled, so will the isolated process. New dosimetry systems [45,46,40,47] are being developed to control dose in terms of absolute value. Beam quality improvement is also a target for further improvement [40]. Spatial dose uniformity (especially for electrostatic ion scanning techniques) must be monitored [48] since nonuniformities below 1% must be achieved.

2. **Process Testing.** The objective is to view the physical results of the process (the implant step and the RTA step are the processes in our case) . This may be done by using test wafers or the product wafer themselves. However, it is also possible that what is being monitored might be an aggregate of other processes and environment conditions (contamination is an example).

There is no contradiction between those two methods and the use of both can ultimately be advantageous.

---

[1]Although the core of the problem is in reality epistimological the implications of it affect yield and are real.

3.4.3 Degree of process control is imposed by production environment

The different product time requirements and volume of production impose variations in the ion implant monitoring technique that would be most effective for improving yield. We can generally distinguish three categories of fab operations.

Category 1. The fab operation involves wafers of especially **high money value** but of **relative low volume** (eg military specification lots or advanced computer chips). For such cases the highest possible yield should be guaranteed and full inspection and monitoring should be carried out on these valuable wafers. Misimplanted wafers can sometimes be reimplanted and partially activated carriers can be fully activated; quality and revenue recovery can be huge, especially for the late stages of the process.

Category 2. The fab operation involves wafers of especially **high money value** of **moderate volume production**. ASIC and high-performance VLSI wafers fall in that category. Because of the medium volume of production, inspection of every wafer is not feasible. The monitoring procedure should therefore be less involved and it should be instituted on a pre-control basis, with a minimum of one wafer per cassette receiving full monitoring.

Category 3. The implant operation is that of a **full volume production** involving lots of batches. Here the finished wafer value is lower than in the previous category by at least a factor of 10. Statistical Process Control can be implemented to assure yield only when the process has been stabilized. Continually evolving processes are being transferred from the R & D environment to production. Competition imposes stringent time requirements. Therefore, the time lag between the process transfer, its stabilization and the expansion of the process capability must be minimized. A flexible and accurate technique is needed to monitor the emerging problems that can keep yield low.

It is thus obvious that although only high volume environments impose stringent requirements on the pre-control type, monitoring technique, the application

of such a technique in all three categories can be crucial for maintaining and increasing the yield.

3.4.4 Which stage of the process to monitor and the benefits

As it was discussed in chapter 1 rapid evaluation of ion implantation processing is crucial in successful IC manufacturing. The intrinsic link between implant and annealing process steps and their interaction on device characteristics implies that monitoring should take place after both process steps. This is the only way that seperate process variations can be revealed and their cause can be traced and attributed to the implanter or the RTA equipment.

The benefits from real-time process control on production wafers can be summarized to the following:

- Real-time information about the accuracy and uniformity of the implant is gathered. This information can be used to achieve a better parametric yield and device performance.

- Reduction of the process cycle time by reducing implanter idle time for testing is accomplished. Since not all implant facility problems are due to implanter-related problems, process monitoring immediately after implant can identify the equipment malfunctions from the set-up mistakes and wafer-related problems.

- A reduced test wafer cost for tracing the problem is achieved. Since the cause of the problem can be identified from a proper process control technique, the number of test wafers for machine malfunctions can be severely reduced resulting in cost savings (especially for large diameter wafer fab-lines).

- Elimination of further processing of zero-yield implanted or annealed wafers. Process errors during the set-up procedures and the input parameter selection can be recovered, if possible, in an early stage.

- Reduced partial yield loss from drifts within a batch and process errors.

The above mentioned benefits from a Statistical Process Control strategy can justify the reason why SPC is connected to device yield and quality improvements. The effectiveness of SPC relies predominately on the quality of the gathered information. The key question that therefore arises is how good is the collected information for an effective process evaluation.

3.4.5 Process control tools: the emerging requirements

Implant dose has traditionally been the quantity of interest for determining the success of the implant. Dose accuracy in terms of absolute value, repeatability from wafer to wafer and dose uniformity across the wafer have been considered the most important characteristics of any implanter. Most of the monitoring techniques have been focused on measuring those quantities of interest. However, the implant profile is the quantity that should be considered as the monitoring technique's target since that is the feature which determines device performance. This will become apparent in the rest of this chapter.

In order to make a choice of the appropriate measurement tools, the process control requirements which are strongly dependent on the advanced IC fabrication requirements have to be defined. The primary need for fast turnaround of inventory imposes testing speed as the primary requirement. Low cost, simplicity of operation, minimization of additional processing steps, simplicity of data analysis and direct relationship between measured test parameters and device performance are equally important prerequisites. The technique sensitivity should be at least an order of magnitudehigher than the levels of variation which give a significant process impact (eg less than 0.1 % sensitivity in dose for measuring 1 % dose non-uniformities). The spatial resolution and the depth resolution have to be adaptable to the different types of processes used (eg for implant depths in the range of 500 Å to more than 1μm).

3.4.6 The existing process control measurement tools

The choice of measurement tools for process monitoring has been the subject of a lot of publications [50]. Dose uniformity measurements [51] can be based on direct measures of the number of incident ions, such as electrical activity (sheet resistance, capacitance-voltage, threshold voltage, Van-der Pauw resistance) or indirect effects associated with the degree of crystal damage on semiconductors (double-implant sheet resistance, thermal-waves, ellipsometry). Therefore, any direct measurements monitor the combined effect of ion implant and annealing on the substrate[52, 53]. Glass test wafers covered with organic films, presenting changes in their optical density (Ionscan) can be also used. A brief historical development of equipment and techniques for measuring uniformity in ion implantation has been recently published [54]. In table 3.2 a comparison of the main implant monitoring techniques is dislayed.

3.4.6.1 Electrical measurements

Sheet resistance. This is a widely accepted method where the four-point probe technique (see chapter 4) is used over the wafer surface[55, 56]. The spatial resolution is limited to a few probe spacings (the closer the probe tips the better the resolution) [57]. The required precision can be below 0.1 %. The measurement averages resistance over the entire thickness of a layer confined between the surface and the junction [58]. No measurements of n on n^+ , p on p^+ epitaxial layers and implants of the same conductivity type (threshold voltage adjustment) can be performed with a four-point probe. The sheet resistance measurement range extends from 10^4 to 10^{-3} ohm/square, therefore the implant dose range can extend from 10^{12} to 10^{16}ions/cm^2. Surface passivation with sulphuric peroxide can extend the range of direct measurements to $\approx 2 \times 10^{11}$ions/cm^2 for high resistivity substrates [59].

The relative ease in measuring sheet resistance, the availability of resistivity standards for probe calibration and the existence of a series of probes for different applications make it particularly useful for real-time monitoring of processes and

TABLE 3.2: Wafer mapping techniques comparison

Tecniques/*Characteristics*	**Single I.I.R$_S$**	**Double I.I.R$_S$**	**Pulsed C-V**	**Spreading res.**	**Thermal waves**	**Ellipsometry**	**Ionscan**
Measurement type	electrical	electrical	electrical	electrical	optical	optical	optical
Quantity measured	Sheet resistance	Damage	Depletion capacitance	Spreading resistance	Crystal damage	Crystal damage	P/R damage
Species measured	active	both	active	active	both	both	both
Lateral resolution	.25mm	.25mm	5 μm	.1mm	1μm	1.5mm	3mm
Sensitivity	.7 - .8	.5 - 1.0	.7 - .8	.7 - .8	.2 - .6	.5	.2 - .6
Dose range (ions/cm^2)	$10^{12} - 10^{16}$	$10^{10} - 10^{13}$	$10^{10} - 10^{12}$	$10^{11} - 10^{17}$	$10^{10} - 10^{15}$	$10^{11} - 10^{15}$	$10^{11} - 10^{16}$
Calibration needed	no	yes	no	yes	yes	yes	yes
Relaxation time	minor	serious	minor	minor	serious	serious	serious
Substrate	opposite type	opposite type	either	same	either	either	glass+P/R
Measurement time	$\leq$ 1hr	$\leq$ 1hr	1 day	2hr	10min	$\leq$ 10min	$\leq$ 10min
Processing requirements	anneal	initial I/I + anneal	anneal + oxide + metal dots	measure before and after	none	measure before and after	measure before and after

equipment. The relationship that exists between sheet resistance and dose makes it a useful tool for monitoring dose accuracy.

Double-implant sheet resistance. A deep initial implant and anneal are given to form a conducting layer on a test wafer. The low dose to be tested is then implanted. The sheet resistance of the initial layer is increased by an amount which depends on the degree of surface damage caused by the second low dose implant. The difference of the two measured values is the monitored quantity [58,59]. The sensitivity of the technique can be selected by the choice of the dose and energy of the initial implant and decreases rapidly as the implant dose increases above 10^{13} ions/cm^2. However, the variation of the measurements with time [59,60] is an effect that must be considered when this technique is used.

An experiment was conducted to assess the technique. Boron ions were implanted at an energy of 40keV and in a 10^{11} to10^{12} ions/cm^2 dose range. The energy, dose and the annealing conditions for the first implant where optimized by use of simulations (SUPREM IV). The information about the experiment and the measurements are depicted in fig. 3–1.

Spreading resistance. The technique is explained in chapter 4. It provides carrier concentration profiles and it can be used for full-wafer mapping [56]. It possesses a good depth resolution but is impractical for on-line implementation.

Capacitance-voltage. This technique can provide precise information about the effect of low dose implants and closely represents important performance characteristics of product wafers (see also chapter 4). The measurements are normally carried out on aluminum dots formed by evaporating or sputtering aluminum through a shadow mask onto the oxide layer, followed by a sintering operation. However, because of the excessive amount of time involved, the additional processing steps and the problems of interpretation the technique is impractical for in-process control where the need for fast turnaround is paramount.

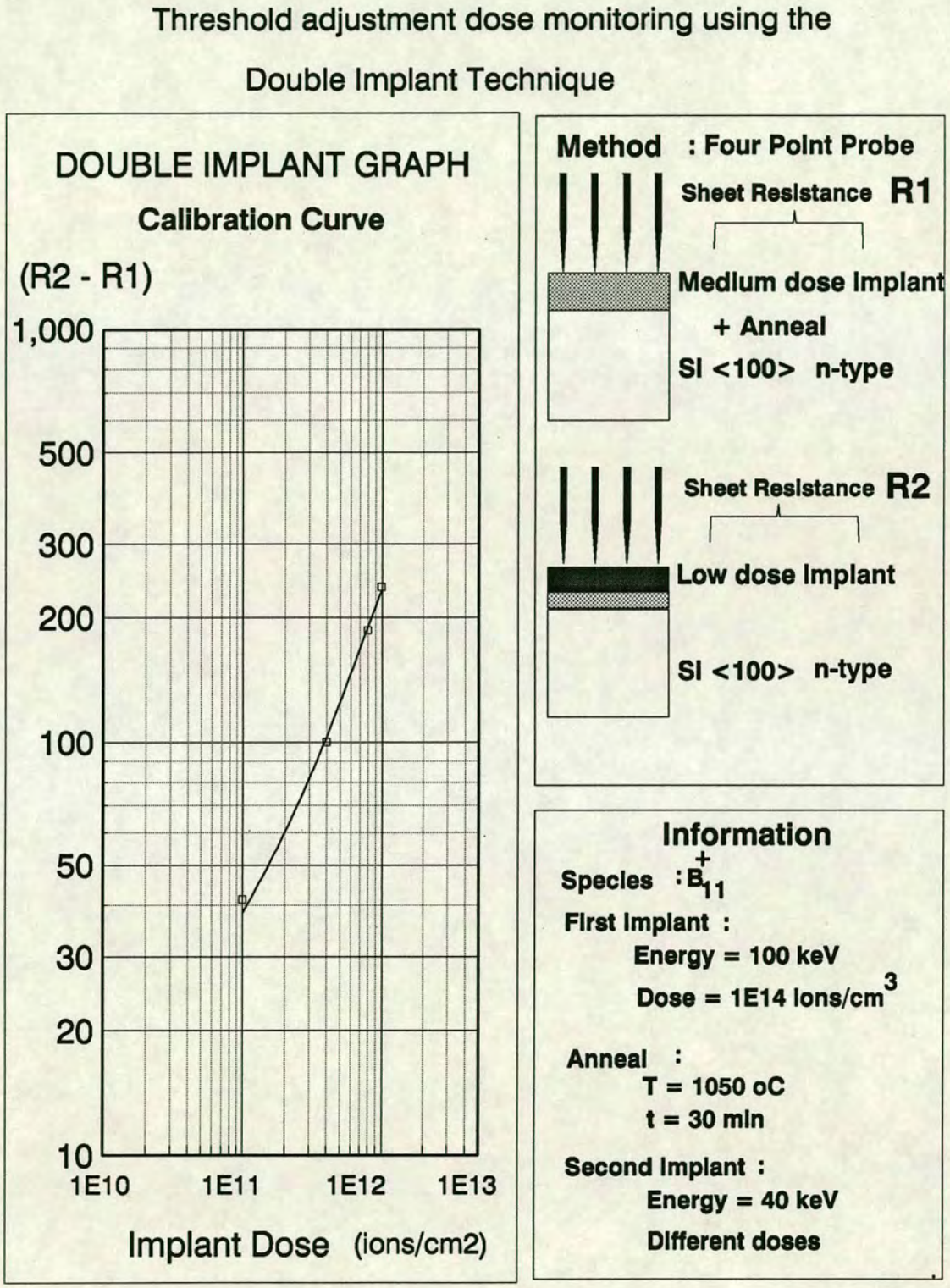

Figure 3–1: Experimental results for the double implant technique.

Device parameters. Threshold voltage, saturation current and pinch-off voltage measurements depend upon the doping concentration in the active volume of the device. Those techniques can be used for lightly doped sample monitoring. However, the remoteness of such measurements from the physical feature of interest (namely trying to estimate the electrical activity from measurement of device parameters) and the additional dependence upon inaccessible and uncontrollable geometric factors (especially for small geometries) can lead to accumulation of large errors. Therefore, precise determination of the doping level cannot be achieved.

Test patterns. Photolithography has been used to fabricate planar test structures to measure doping and doping uniformity. The good spatial resolution and the elimination of errors associated with wafer and probe tip geometry are among the advantages of the technique. However, those techniques are not suited to an industrial environment due to the required additional processing steps (photolithography, implantation for the formation of ohmic contact pads, metal deposition, thermal processing, etching). Linear resistors, Van-der-Pauw structures, Hall effect combined with Van-der-Pauw geometry structures are among the main techniques using test patterns.

3.4.6.2 Optical measurements

The main advantage of the optical methods is their 'non-contact' nature, which renders them useful for dose uniformity monitoring of production wafers. Their second advantage is that they can be used immediately after implantation and, therefore, assess the implant process before the anneal step takes place. They are all indirect techniques since they monitor damage through changes in optical constants, thermoacoustic properties or other semiconductor physical parameters. In most of those methods the measured quantities are time-dependent and must be controlled by special treatment of the implanted surfaces before the measurements or by using 'reference standard' wafers.

Ellipsometry. The technique is explained in detail in chapter 7.

Spectroscopic ellipsometry. Spectroscopic ellipsometry [61–64] (see chapter 7) can be used for implant characterization. However, it requires rather involved theoretical models and evaluation procedures. This is a drawback for routinely using the method for implantation monitoring.

Thermal-waves. Thermal wave physics is playing an ever-increasing role in the study of material parameters. Thermal waves are present whenever there exists a periodic heat generation and heat flow in a medium. From the multiple methods by which these waves can be produced and detected only higly focused laser beams can satisfy requirements such as operation in an open environment, operation without getting in contact with the wafers and obtaining images at high spatial resolution. The technique is explained in detail in 9.

Differential reflectrometry. The differential reflectometer [65] measures the spectral dependence of the normalized difference in reflectivity ($\Delta R/R$) between an unimplanted wafer (reference) and the implanted one [65]. Light coming from a monochromator is scanned between the two specimens by means of a vibrating mirror. the reflected light falls on a photomultiplier tube and the output signal is electronically processed to yield $\Delta R/R$, where $\Delta R = R_1 - R_2$ is the difference in reflectivity between the two specimens and R is the average reflectivity. A scan of photon energies from 1.5 to 6 eV is achieved in less than 3 min. It can be used for both low and high dose ranges but the sensitivity has to be increased in the low dose regime.

The method has been demonstrated to be sensitive, non-destructive, fast and requiring no special sample preparation. It can provide quantitative information on the behaviour of amorphous layers generated by ion implantation and the data evaluation is simple and straightforward [66]. It also allows a measurement of the thickness of the amorphous layer formed during the implant and an assessment of whether or not the layer is at the surface or submerged below a crystalline layer.

Ionscan. Optical dosimetry [67–69] is a technique that uses the principle of measurement of photoresist darkening due to ion beam exposure (graphitization [2]). Test wafers are fabricated by spin coating resist on transparent wafer substrates (glass wafers). Short UV exposure or baking to remove photosensitive properties must take place prior to scanning the wafer in the dosimeter (IONSCAN) and storing the background optical absorption. The wafer undergoes implantation with the rest of the product wafers. After the implant step a dosimeter scan takes place and the new values of optical absorption are subtracted from the pre-implant stored values. The net changes in optical density of the organic resin film resulting from exposure to ion implantation can be used for dose uniformity assessment [70,71].

An excellent degree of linearity exists between the difference in optical transmission and the actual dose value in the dose range from 1×10^{11} to 1×10^{14}ions/cm^2 [67]. This puts the uniformity measurement range into the area of MOS threshold adjustment implants which are very critical to good IC yield. The speed of scanning is another big advantage. However, the technique can only be used as an isolated implant monitor tool and cannot monitor the process itself. Wafer charging effects and wafer heating effects cannot be reliably monitored.

Other techniques Other methods such as optical reflectance [72,73], photoluminescence [74] and Nomarski interference contrast microscopy [75] exist, but do not satisfy the production environment requirements.

---

[2]In a general sense it can be defined to mean any of several particle collision processes which bind carbon into any relatively stable ring structure.

3.5 Insufficiency of the existing monitoring techniques

As mentionned in chapter 1, the existing monitoring techniques are insufficient for performing pre-control monitoring on the evolving industrial line needs [3]. The reasons are identified in this section.

3.5.1 Theoretical sheet resistivity-junction depth curves

In deciding if some of the design requirements (for example the junction depth for a source/drain implant) are being met, monitoring of appropriate quantities (sheet resistance or optical constants) must take place. The relation between the junction depth and the sheet resistivity has been investigated, [76]. Their product has been found to depend on the ion dose, the ion energy, the annealing conditions (temperature and therefore solubility) and the junction leakage. Although those theoretical curves can prove helpful for obtaining some insight while designing a process and chosing the appropriate process parameters, they are of limited effectiveness when a process error occurs on-line. Implanter malfunctions, channeling effects and incomplete activation can occur simultaneously and the above curves cannot distinguish their individual contributions to the error.

3.5.2 One-parameter-monitoring is insufficient

Dose accuracy requirements can vary considerably between processes and individual process steps. Irrespective of the process in use, most sensitive implants are those that control the transistor gain or switching voltage (base and emitter

---

[3]Those needs were identified to be: trend for larger area wafers, RTA implementation, increased technology demands from ion implanters, shrinking geometries and increased process complexity.

implants in bipolar devices, threshold implants in MOS devices). Any variation in dose or implant depth in those implants is directly reflected in transistor characteristics. The position of the implant peak and the shape of the profile tail determine the implant depth. It is thus obvious, that the existing monitoring for dose uniformity across the wafer is not sufficient and that the full profile must be determined for on-line control purposes. A two-dimension wafer map of the impurity profile should be identified as the long-term target. The inefficiency of the existing process monitoring tools can be nicely shown by use the following experimental example.

Let us select the sheet resistance as the wafer mapping monitoring technique. The sheet resistance measured values depend on several variables; those include the initial substrate concentration, the ion energy, the ion dose, the target temperature, the oxide thickness through which the implant took place, the anneal temperature, the anneal duration, the ambient gas and many others. The sensitivity of the process itself to each of those parameters is extremely difficult to extract since no absolute control of all those can be achieved at any instant. The final electrical characteristics produced by the implant process (profile peak level, profile peak depth, profile peak shape, profile tail shape, junction depth) determine the device characteristics and the yield. Any attempt to try to characterize this multivariable interaction with a single parameter, sheet resistance in this case, involves a risk since counterbalancing variable sensitivities might not reveal problems which can affect device performance (eg channeling). From a mathematical viewpoint, sheet resistance is inversely proportional to the integral of the carrier concentration and mobility product from the surface of the wafer to the junction depth. This effectively means that sheet resistance does not directly reflect the implanted dose (even if the solid solubility limit at the annealing temperature is not exceeded).

The inefficiency of the technique can be graphically shown in a sequence of two-dimensional maps produced at different depths in Si in figures 3.5.2, 3.5.2 and 3.5.2. The sheet resistance has been monitored at different depths, at 69 sites across each layer. A RIE step is used to etch Si in 100 to 200 Å step

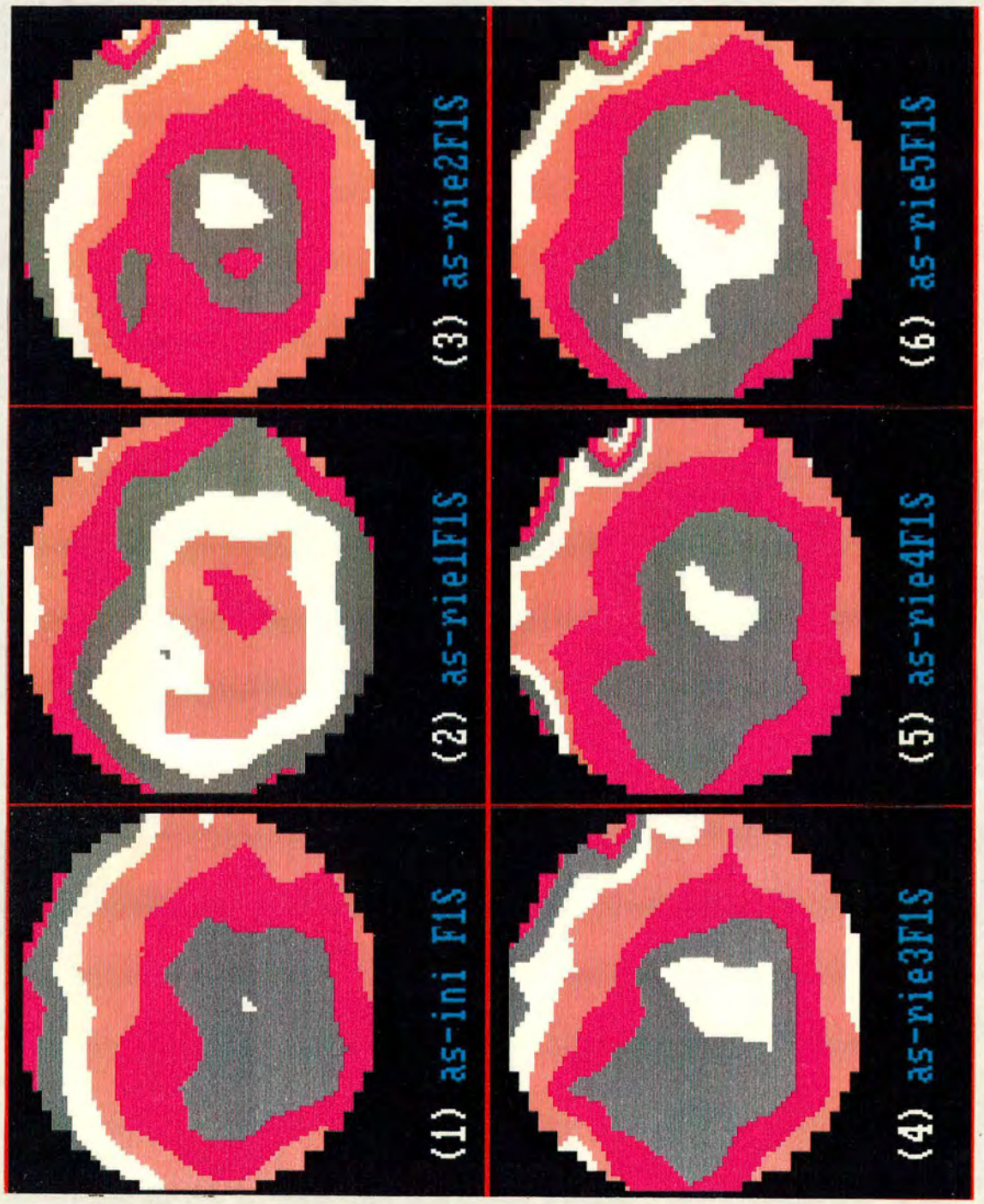

Figure 3–2: Two-dimensional sheet resistance maps for increasing depths into Si. The depths are 0, 53, 107, 161, 215 and 268 Å for graphs 1 to 6. The sheet resistance values are those of the As implant of fig.8-12.

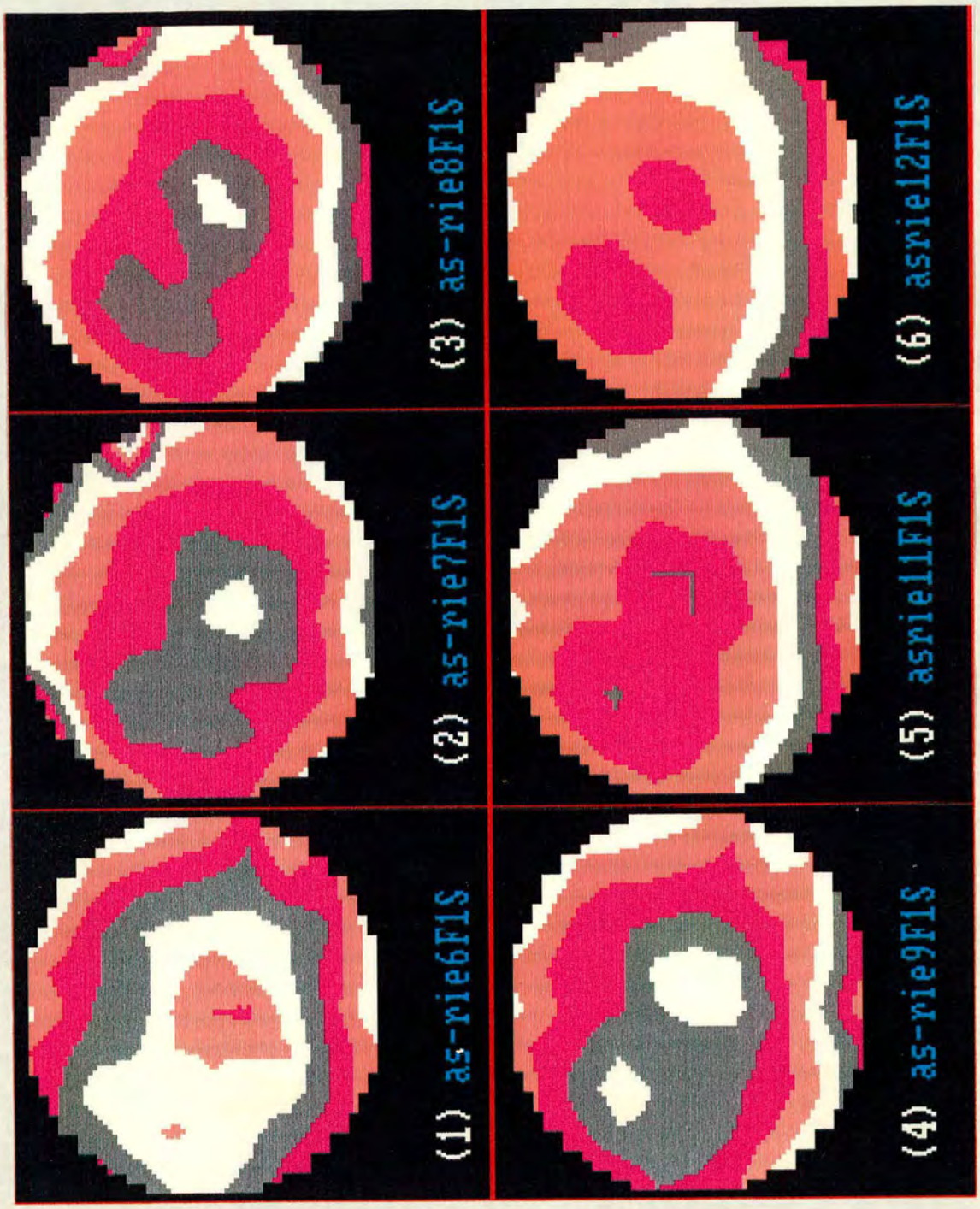

Figure 3–3: Two-dimensional sheet resistance maps for increasing depths into Si. The depths are 322, 376, 430, 483, 698 and 806 Å for graphs 1 to 6. The sheet resistance values are those of the As implant of fig.8-12.

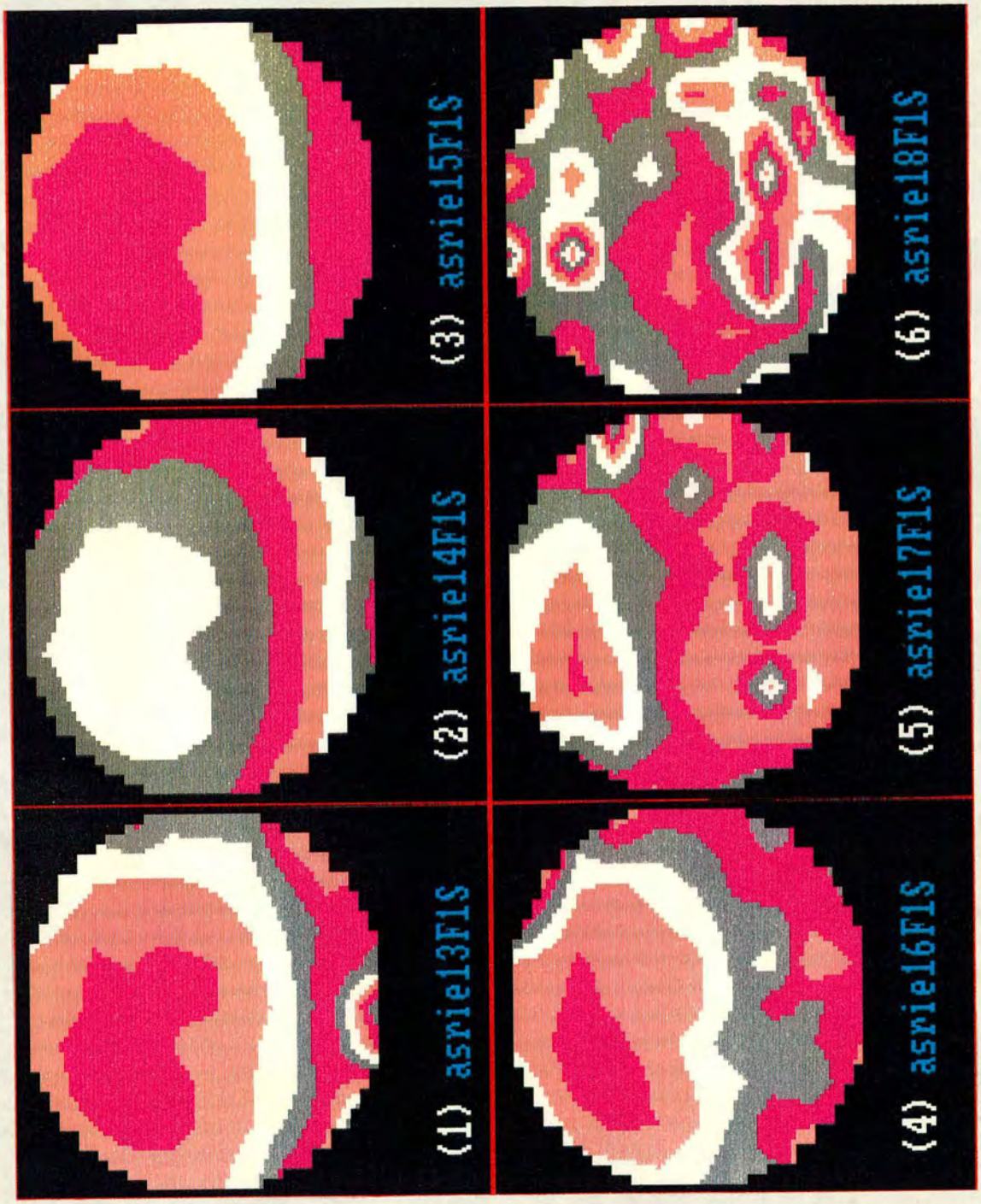

Figure 3–4: Two-dimensional sheet resistance maps for increasing depths into Si. The depths are 913, 1075, 1182, 1236, 1290 and 1397 Å for graphs 1 to 6. The sheet resistance values are those of the As implant of fig.8-12.

increments. The sheet resistance map at the surface (wafer: as-ini F1S) represents an average sheet resistance of the implanted layer measured at 69 points on the wafer surface. The above contour map is completely different from the sheet resitance uniformity map produced from sheet resistance measurements closer to the junction (wafer: asriel8 F1S) or even some of the previous 2-D maps. The inefficiency of the sheet resistant monitoring is evident. The contribution of the low concentration implanted region (eg implant profile tail) to the average sheet resistance, is obscured by the contribution of the high concentration region (eg implant profile peak). The non-uniformities of the tail-region of the implant profile can be accurately depicted only by sheet-resistance measurements

3.5.3 An example from the bipolar processes

The device speed in bipolar transistors is significantly improved by vertical scaling of the dopant profiles. Reduction of the base width and shallow emitters with junction depths less than 700 Å are thus the objectives [77]. The reduced tolerable thermal budget limit makes RTA favourable as the annealing step. However, temperature non-uniformity can introduce carrier concentration profile variations across the wafer. The exact carrier penetration depth cannot be monitored accurately by the sheet resistance method due to the reason mentioned in section 3.5.2. However, carrier penetration depth strongly affects the base charge and thus the current gain. It is therefore evident how pre-control monitoring of the wrong quantity (average sheet resistance over the whole implanted layer) can hide the effect of the implant profile tail region (which actually is the penetration depth). Ineffective pre-control (selection of the wrong technique) can thus prove disastrous on device yield (current gain out of process specs).

3.5.4 Measuring channeling effect

As it was mentioned earlier in section 3.2.3.1 channeling and the associated junction depth non-uniformities across the wafer can be effectively measured by sheet resistance measurements. However, such measurements are confined to low and

medium doses, where complete Si amorphization does not occur. For higher doses direct planar channeling effects as measured by sheet resistance mapping over a wafer decrease in proportion to the lattice damage increase with increased dose. However, at high dose and low energy implants (such as those used for the source and drain implants of MOSFETs) indirect channeling effects linked to ion scattering within the target are still a concern [3]. The inability of the sheet resistance technique to identify such effects is one more reason to develop on-line implant profiling techniques for effective process monitoring.

3.6 How profiles affect device characteristics

The evolution of processing technologies is characterized by a steady increase of the IC complexity and scaling down of the minimum dimensions. This trend implies an increased need for tight tolerances, shallow doping profiles and low defect densities. As the dimensions of ICs shrink, it becomes particularly important to determine the regions where one- and two-dimensions dopant, carrier and damage profiling should be performed after implantation and annealing steps. Device performance-within-specs would thus be confirmed at an early processing stage. The areas where profiling must take place, have to be determined for a specific process.

3.6.1 Choosing the 'process vehicle' for profile monitoring

The objective for all the above mentioned monitoring techniques is to control the implantation process so that critical transistor characteristics are within the designer's specification limits. Therefore, a 'process vehicle' for the monitoring experiments has to be determined. The choice of such a 'process vehicle' must fullfil the following requirements:

- Scaling down possibility, to submicron design rules.
- Multiple number of implants at different doses and different energies with different tolerance limits.

A twin-tub or p-well CMOS process fullfils all of the above requirements since:

- It allows scaling down in the junction depth of both n^+ and p^+ source and drain regions and in the well junction depth.
- It offers a very big number of implants at different doses and different energies (n-tub implant(phosphorus), p-tub implant(boron), p-channel threshold adjustment implant(boron), source and drain regions of p-channel implants(boron), source and drain regions of n-channel implants(arsenic)).
- It offers the possibility of independent control of the two threshold voltages of the n- and p- channel transistors and therefore needs a powerful technique for measuring dose, uniformity and the dopant profile.
- Because of the drive-in of the adjacent wells certain interesting phenomena take place (i.e. decrease of doping concentration across the border of the two wells due to compensation of the two opposite types of implants) which can affect transistor performance.

3.6.2 CMOS implant requirements

For the twin-tub CMOS process a minimum of five implants is required. The first two implants are for the n-well and p-well formation, the third is for the threshold adjustment of the p-channel transistor and the last two for the source, drain and contact regions definition for both transistors. These implants are closely related with the subsequent processing steps and with certain process parameters. Accurate control of all the doping profiles is needed, since their individual interferences on the various electrical parameters of the device can be either constructive or destructive. In order to define the tolerances for these process parameters - especially the tolerances that concern dose accuracy and doping uniformity- the contribution of each of the process parameter on the different device parameters has to be investigated. A list of the process parameters that can affect the shape of the profile during the processing and the profile characteristics that can be affected by them is presented in Table 3–3.

Process vs Affected device parameters	
Process Parameters	Device Parameters
1. N-well implantation	- junction depth of n-well
- energy	- surface concentration of n-well
- dose	- doping profile at well border
- masking oxide parameters (time, temperature)	- doping profile of n-well
- drive-in parameters	
2. P-well implantation	- junction depth of p-well
- energy	- surface concentration of p-well
- dose	- doping profile at well border
- pad oxide thickness	- doping profile of p-well
- drive-in parameters	
3. Gate oxide formation	- implant profiles redistribution
4. P/N-channel threshold adjustment	- p/n-channel threshold voltage
- energy	
- dose	
- gate oxide thickness	
5. Field oxide formation (time, temperature)	- parasitic threshold voltages under the field regions in both wells
6. N-channel S/D/C regions implant	- breakdown voltage
- energy	- junction depth
- dose	- dopant profile
7. P-channel S/D/C regions implant	- breakdown voltage
- energy	- junction depth
- dose	- dopant profile
8. Process high temperature steps (eg glass reflow, sintering)	- dopant profile redistributions
9. Design rules for specific areas (i.e. n^+ to p-well)	- Source/Drain (S/D) paracitic capacitances
	- lateral dopant profile broadening
	- active channel length

Table 3–3: List of process parameters during a twin-tub CMOS process and the doping-profile-related affected-characteristics.

From the study of the influence of the process parameters on the doping profiles (and therefore on the device parameters) the following tasks must be performed by the manufacturing and process engineers who try to achieve tighter process tolerances for improved device yields:

- Evaluation of the most crucial process parameters that can affect device performance (by experimental design experiments) and selection of tight tolerance limit levels for those process parameters (process modelling packages are a useful tool for the choice of those levels). Equipment specifications must be also taken into account for defining those levels.

- Process-run trial with the use of tight tolerance levels defined during the experimental design set-up on those crucial parameters (eg the example on threshold voltage variation in chapter 1).

- Device parameter measurements for each experimental run. The variations in dose accuracy, doping uniformity and profile shape are also recorded by use of the appropriate techniques.

- Assessment of the process parameter variation on the device characteristics based on the experimental data. Appropriate correction on tolerance levels can take place from the assessment conlusions.

- Development of a technique that can monitor quickly and accurately on a production wafer the important dopant profiles.

- Implementation of the technique for process pre-control.

Implant profile monitoring has been shown to be the most effective monitoring tool for ensuring high device yields. From the other side, pre-control measurements require an on-line monitoring technique. Since such a technique does not exist this project has been focused on developing such a technique.

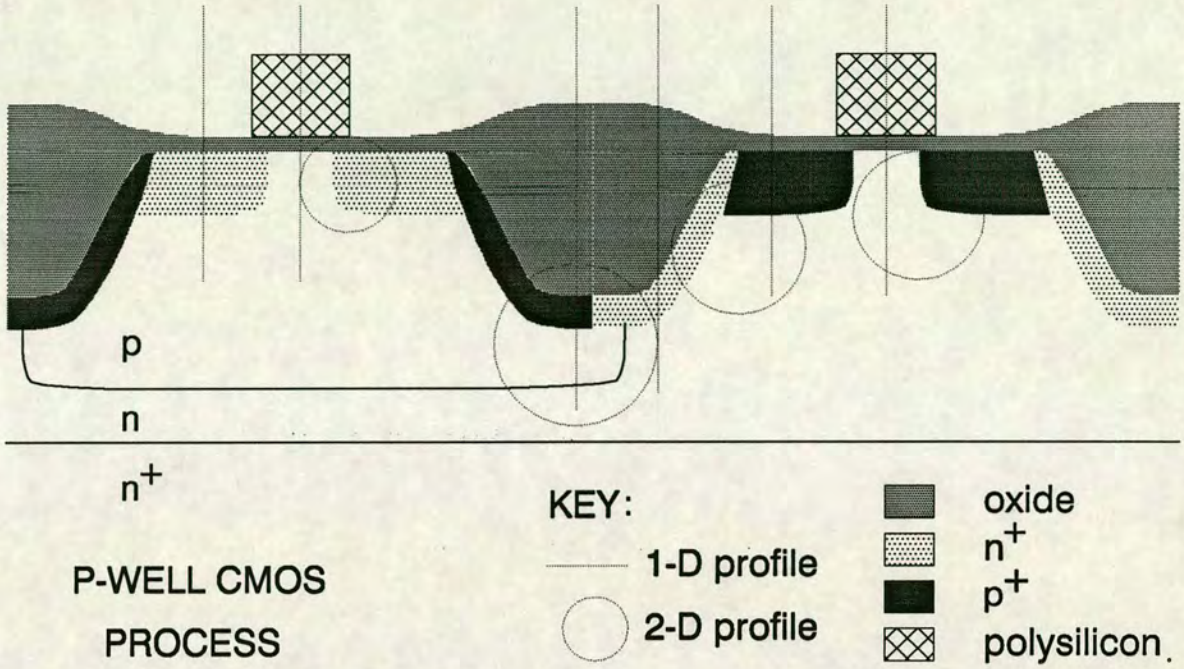

Figure 3–5: Schematic cross-section of a p-well CMOS technology indicating the areas where carrier profiling both in 1 and 2 dimensions must take place.

3.6.3 Profiling and monitoring requirements for small geometries

A schematic cross-section of a p-well CMOS technology indicating the areas where one and two dimension profiles are required can be found in fig. 3–5. Those areas are discussed in the subsequent sections.

3.6.3.1 The effect of residual localised defects in junctions

The effect of implant-induced defects on the properties of the final device are very dependent on the type of device, the type of defect and its location within the device structure. The successful control of the geometry of the final device structure is a necessary but not sufficient condition for acceptable device operation. The annealing step is closely related to the implantation step and the device electrical

characteristics. For shrinking geometries furnace anneal must give way to RTA (see section 2.3.4). Achievement of shallow junctions (through preamorphization, very low energy implants BF_2 implant or other techniques) that are defect-free is also very important. The junction position relative to the band of dislocation loops and the presence of non-gettered fluorine are the key feature in minimizing the reverse leakage current across the juction, [78]. It is thus clear that all electrically active defects must be removed from the damaged region that is located inside the device depletion layers. Since annealing step malfunctions can dramatically decrease yield, fast on-line tests of the success of both implant and anneal are needed. The development of such a technique is required.

3.6.3.2 The formation of shallow p^+ source/drain regions

The low mass of B relative to Si and the reduced ion implant energies to be used (less than 25 keV), makes it difficult to produce adequate beam currents.Channelling effects and non-uniformities are the results. Use of BF_2 at higher energies circumvents some aspects of the problem. High dose is used for such implants (over 10^{15}ions/cm^2). High surface carrier concentration is required, since a low contact resistance is desirable upon subsequent metallization. Shallow junction depths are also reponsible for high sheet resistivity values [76]. The duration and temperature of the annealing step is crucial in determining those device features. Incomplete activation in the peak area might be a severe problem. Fast profile characterization is necessary in order to assess the success of the implant at an early manufacturing stage.

3.6.3.3 The formation of shallow n^+ source/drain regions

Shallow n^+ regions may be produced by low energy As implant and annealing. The high mass of As relative to Si produces an amorphous layer in the near-surface region, thus minimizing channeling effects. A wrong selected dose or a non-uniformity during the implant might have an impact on the device electrical characteristics. The high speed of regrowth of the amorphous layer results in

an extremely high level of substitutional arsenic [80]. The major mechanism for deactivation is the As cluster formation during the annealing step [81]. Low surface carrier concntration (due to the deactivation procedure) leads to reduced device speed (by increasing the RC product). Therefore, characterization of the implant and annealing step are necessary at an early fabrication stage.

3.6.3.4 Formation of shallow p-wells

In a bulk silicon CMOS technology, the n- and p-type devices may be isolated by the use of an appropriately doped well. For submicron technologies p-wells with junction depths below 1μm are required. A combination of inert anneal and oxidizing heat treatment must be used to reduce the possibility of oxidation-induced stacking faults (OSF) growth for boron-implanted Si [80]. High junction leakage and anomalous diffusion behavior might lead to out-of-spec n-channel devices. Characterization is thus needed after the well formation.

3.6.3.5 Effect of low dose implants on device characteristics

Low dose implants ($10^{11} - 10^{13}$ions/cm^2) on product wafers cannot be monitored until the end of the manufacturing cycle to assess their success in achieving the desired electrical characteristics. Techniques for measuring the implanted dose immediately after the implant step are needed and would present a distinct advantage over the above-mentioned electrical tests. The double implant technique (see section 3.4.6.1) requires specially prepared test wafers. On the other hand the Therma-Wave technique has proved useful for a non-destructive evaluation of the implanted dose directly on production wafers [82]. The two critical electrical parameters are the drain current and the enhancement transistor voltage. Variations of 15 % in the drain current and 5 % on the threshold voltage can highly effect wafer yield and device speed [83]. A correlation between the electrical parameters versus the implant dose, through the monitoring of the Therma-Wave signal has shown very high correlation coefficents, [83]. Therefore, the thermal wave dose

measurement technique can be a powerful, real time, diagnostic tool for the tight control of low dose implants and some of the electrical device characteristics.

3.6.3.6 Two dimensional dopant profiling

The drain and source regions spread into the transistor's channel region and the boundaries between the channel stop implant, the well(s) and the source drain regions are areas in CMOS where the dimensional profiling is necessary. The first case especially might have catastrophic effects on the device characteristics since it controls the channel length. The geometrical effect of the generally used 7° tilting of the wafers with respect to the ion beam during implantation can not be neglected for down-scaled geometries. For example the overlap between the gate and the source and drain regions of MOS transistors varies by 0.06 μm for arbitrarily oriented transistors, if 0.5 μm thick polysilicon with vertical walls is used [83]. For 1 μm thick photoresist masks the offset variation between the mask edge and the implanted region edge could make things even worse. Some methods for such profiling have been developed recently [84–88]. They are not ideally suited for a manufacturing environment since they involve additional masking steps and are not easy to implement.

Bibliography

[1] B. L. Crowder, J. F. Ziegler, and G. W. Cole. *Ion Implantation in semiconductors and other materials.* Plenum, New York, 1973.

[2] G. Carter and W. A. Grant. *Ion Implantation of Semiconductors.* Edward Arnold Publishers Ltd, London, 1976.

[3] A. E. Michel. Channeling in low energy boron ion implantation. *Applied Physics Letters*, 44(4):404–406, 1984.

[4] R. Simonton and D. Kamenitsa. Channeling control in silicon (100) substrates by target orientation. *Nuclear Instruments and Methods in Physics Research*, B37/38:344-347, 1989.

[5] D. R. Zrudsky. Channeling control in ion implantation. *Solid State Technology*, (7):69–73, 1988.

[6] M. I. Current, N. L. Turner, T. C. Smith, and D. Crane. Planar channeling effects in Si (100). *Nuclear Instruments and Methods in Physics Research*, B6:336–348, 1985.

[7] N. L. Turner, M. Current, T. C. Smith, and D. Crane. Effects of planar channeling using modern ion implantation equipment. *Solid State Technology*, (2):163–172, 1985.

[8] R. B. Liebert, D. F. Downey, and V. K. Basra. Planar channeling effects in a batch process ion implanter. *Nuclear Instruments and Methods in Physics Research*, B21:391–395, 1987.

[9] M. Miyake, M. Yoshizawa, and H. Harada. Incidence angle dependence of planar channeling in boron ion implanted silicon. *Journal of the Electrochemical Society*, 130(3):716–719, 1983.

[10] T. W. Sigmon, W. K. Chu, H. Muller, and J. W. Mayer. *Ion Implantation into Semiconductors*, page 633. New York, 1975.

[11] R. A. Moline, G. W. Reullinger, and J. C. North. *Atomic Collisions in Solids*, volume 1. 1975.

[12] N. White, M. E. Mack, and G. Ryding et al. Wafer charging and beam interactions in ion implantation. *Solid State Technology*, 28(2):151–158, 1985.

[13] V. K. Basra, C. M. McKenna, and S. B. Felch. A study of wafer and device charging during high current ion implantation. *Nuclear Instruments and Methods in Physics Research*, B21:360–365, 1987.

[14] A. J. Holmes. Ion beams and ion optics. *Radiation Effects*, 44:47, 1979.

[15] J. H. Hall, H. Glawischnig, and W. Holtschmidt. Charging studies in applied materials precision implant 9000 system. *Nuclear Instruments and Methods in Physics Research*, B21:350–353, 1987.

[16] M. E. Mack, G. Ryding, and D. H. Douglas-Hamilton et al. *Nuclear Instruments and Methods in Physics Research*, B6:405, 1985.

[17] P. E. Bakeman Jr and A. F. Puttlitz. Ion implantation electron flooding requirements from a user's perspective. *Nuclear Instruments and Methods in Physics Research*, B6:399, 1985.

[18] M. L. King, S. E. Sampayan, and B. H. Hight. A method of surface charge neutralization during ion implantation. *Nuclear Instruments and Methods in Physics Research*, B21:396–399, 1987.

[19] G. Baccarani and K. A. Pickar. Range and straggle of boron in photoresist. *Solid State Electronics*, 15:239, 1972.

[20] J. F. Gibbons, W. S. Johnson, and S. W. Mylroie. *Projected Range Statistics-Seniconductors and Related Materials.* Dowden, Hutchinson and Ross Inc., Stroudsburg, PA, 2nd edition, 1975.

[21] T. C. Smith. Photoresist problems and particle contamination. In J. F. Ziegler, editor, *Ion Implantation Science and Technology*, pages 347–349. 1988.

[22] Y. Okuyama, T. Hashimoto, and T. Koguchi. High dose implantation into photoresist. *Journal of the Electrochemical Society*, 125(8):1298, 1978.

[23] T. C. Smith. Wafer cooling and photoresist masking problems in ion implantation. In *Ion Implantation:Equipment and Techniques*, volume 11 of *Springer Series in Electrophysics*, pages 196–213. Springer-Verlag, 1983.

[24] K. J. Orvek and C. Huffman. Carbonized layer formation in ion implanted photoresist masks. *Nuclear Instruments and Methods in Physics Research*, B7/8:501, 1985.

[25] P. R. Hanley. Physical limitations of ion implantation equipment. pages 3–24, 1985.

[26] M. King and P. H. Rose. Experiments on gas cooling of wafers. *Nuclear Instruments and Methods*, 189:169–173, 1981.

[27] C. H. Stapper, F. M. Armstrong, and K. Saji. Integrated circuit yield statistics. *Proc. IEEE*, 71(4):453, 1983.

[28] J. Pollock, N. Turner, R. Milgate, R. Resnek, and R. Hertel. Particulates performance of a wafer handler for serial process ion implantation. *Nuclear instruments and Methods in Physics Research*, B6:202, 1985.

[29] K. Steeples. Dose control with high power ion beams on photoresist masked targets. *Journal of Vacuum Science and Technology*, B2(1):58, 1984.

[30] D. H. Douglas-Hamilton and C. Taylor. Particles and particle transport in ion implanters. *Nuclear Instruments and Methods in Physics Research*, B6:196, 1985.

[31] T. C. Smith. Photoresist problems and particle contamination. In J. F. Ziegler, editor, *Ion Implantation Science and Technology*, pages 367–373. 1988.

[32] L. Csepregi, W. K. Chu, H. Muller, and J. W. Mayer. Regrowth behaviour of ion-implanted amorphous layers. *Radiation Effects*, 29:92, 1976.

[33] A. B. Wittkower. The effect of ion implanter design upon implant uniformity. *Solid State Technology*, 29(9):77, 1982.

[34] J. H. Freeman. *Applications of Ion Beams to Materials*, volume 28 of *Institute of Physics Conference Series*. 1976.

[35] E. McGuire. 0.1 % ultra-uniformity in electrostatically scanned ion implantation systems. *Nuclear Instruments and Methods in Physics Research*, B21:431–432, 1987.

[36] J. Keller. Beam scanning-electrostatic. *Radiation Effects*, 44:71–80, 1979.

[37] Proc. of the 7th Int. Conference on Electron and Ion Beam Science and Technology. N.Jersey, USA, 1976.

[38] N. Turner. Uniform implantation with electrostatic scanning using a target repositioning technique. *Nuclear Instruments and Methods in Physics Research*, B6:224–227, 1985.

[39] N. Turner. Improved uniformity of implanted dose by a compensated scan pattern generator. *Nuclear Instruments and Methods in Physics Research*, (189):311–318, 1981.

[40] G. Ryding. Dosimetry and beam quality. In *Ion Implantation:Equipment and Techniques*, volume 11 of *Springer Series in Electrophysics*, pages 274–290. Springer-Verlag, 1983.

[41] P. L. F. Hemment. Electrical dosimetry techniques. *Vacuum*, 29(11/12):439, 1979.

[42] C. B. Yarling. The use of RTA is a systematic ion implantation monitoring process. *Solid State Technology*, (5):252, 1985.

[43] R. Kakoschke. Temperature problems with rapid thermal processing for vlsi applications. *Nuclear Instruments and Methods in Physics Research*, B37/38:753–759, 1989.

[44] M. E. Mack. Wafer cooling, Faraday design and wafer charging. In J. F. Ziegler, editor, *Ion Implantation Science and Technology*, pages 313–344. 1988.

[45] P. Lundquist, C. McKenna, R. Brick, and P. Corey. New dosimetry system for a serial process ion implanter. *Nuclear Instruments and Methods in Physics Research*, B21:414–420, 1987.

[46] C. M. McKenna. High current dosimetry techniques. *Radiation Effects*, 44:93–110, 1979.

[47] G. Ryding and M. Farley. A new dose control technique for ion implantation. *Nuclear Instruments and Methods*, 189:295–303, 1981.

[48] N. Natsuaki, K. Ohyu, and T. Tokuyama. Spatial dose uniformity monitor for electrically scanned ion beam. *Review of Scientific Instrumentation*, 49(9):1300–1304, 1979.

[49] M. I. Current, D. S. Perloff, and L. S. Gutai. Wafer mapping techniques for characterization of ion implantation processing. In *Ion Implantation Techniques*, pages 235–254. 1982.

[50] M. I. Current and W. A. Keenan. Ion implant round robin. *Nuclear Instruments and Methods in Physics Research*, B6:418–426, 1985.

[51] W. A. Keenan, W. H. Johnson, and A. K. Smith. Advances in sheet resistance measurements for ion implantation monitoring. *Solid State Technology*, 28(6):143–148, 1985.

[52] K. Steeples. Sheet resistivity of silicon wafers implanted with a high current machine. *Nuclear Instruments and Methods in Physics Research*, B6:412–417, 1985.

[53] C. B. Yarling, W. H. Johnson, W. A. Keenan, and L. A. Larson. Uniformity mapping in ion implantation:part i. *Semiconductor International*, 34(12):57–62, 1991.

[54] D. S. Perloff, F. E. Wahl, and J. D. Reimer. Contour maps reveal nonuniformity in semiconductor processing. *Solid State Technology*, 13(2):31–36, 1977.

[55] D. S. Perloff. Dose accuracy and doping uniformity of ion implantation equipment. *Solid State Technology*, 17(2):112–120, 1981.

[56] R. G. Mazur. Mapping silicon wafers by spreading resistance. 1986.

[57] Standard method for measuring resistivity of silicon slices with a Collinear four-Point arrray. Annual Book of ASTM Standards 10.05, American Society for Testing and Materials, Philadelphia.

[58] A. K. Smith, W. H. Johnson, W. A. Keenan, M. Rigik, and R. Kleppinger. Sheet resistance monitoring of low dose implants using the double implant technique. *Nuclear Instruments and Methods in Physics Research*, B21:529–536, 1987.

[59] J. T. Chen. Monitoring low dose single implanted layers with four-point probe technology. *Nuclear Instruments and Methods in Physics Research*, B21:526–528, 1987.

[60] J. Schuur, C. Waters, J. Maneval, N. tripsis, A. Rosencwaig, M. Taylor, W. L. Smith, L. Golding, and J. Opsal. Relaxation of ion implant damage in silicon wafers at room temperature measured by thermal waves and double implant sheet resistance. *Nuclear Instruments and Methods*, B21:544–558, 1987.

[61] F. Ferrieu, D. P. Vu, C. D. Anterroches, J. C. Oberlin, S. Maillet, and J. J. Grob. Characterization of the SOI material formed by high-dose oxygen implantation using spectroscopic ellipsometry. *Journal of Applied Physics*, 62(8):3458, 1987.

[62] R. W. Collins, B. G. Yakobi, K. M. Jones, and Y. S. Tsuo. Structural studies of hydrogen-bombarded silicon using ellipsometry amd transmission electron microscopy. *Journal of Vacuum Science and Technology, A*, 4:153, 1986.

[63] P. J. McMarr, K. Vedam, and J. Narayan. Spectroscopic ellipsometry: A new tool for nondestructive depth profiling and characterization of interfaces. *Journal of Applied Physics*, 59:694, 1986.

[64] D. E. Aspnes and J. B. Theeten. Spectroscopic analysis of the interface betweeen Si and its thermally grown surface oxide. *Journal of the Electrochemical Society*, 127(6):1359–1365, 1980.

[65] R. E. Hummel. Differential reflectrometry and its application to the study of alloys, ordering, corrosion and surface properties. *Physica Status Solidi*, A76:11, 1983.

[66] R. E. Hummel, W. Xi, and D. R. Hagmann. Ion implantation damage and annealing of silicon as characterized by differential reflectrometry. *Journal of the Electrochemical Society*, 137(11):3583–3588, 1990.

[67] J. R. Golin and J. A. Glaze. High resolution dose uniformity monitoring of ion implanters, part i. *Solid State Technology*, 27(8):137–141, 1984.

[68] J. R. Golin and J. A. Glaze. High resolution dose uniformity monitoring of ion implanters, part ii. *Solid State Technology*, 27(9):289–295, 1984.

[69] J. C. Cheng and G. R. Tripp. New ion dose uniformity measurement technique. *Solid State Technology*, 26(11):143–152, 1983.

[70] J. R. Golin, N. W. Schell, and J. A. Glaze. Advanced methods of ion implant monitoring using optical dosimetry. *Solid State Technology*, 8:155–163, 1985.

[71] J. R. Golin, N. W. Schell, J. A. Glaze, and R. G. Ozarski. Latest advances in ion implant optical dosimetry. *Nuclear Instruments and Methods in Physics Research*, B21( ):542–549, 1987.

[72] S. N. Bunker, P. Siashansi, M. M. Sanfacon, and S. P. Tobin. Nondestructive analysis of silicon-on-insulator wafers. *Applied Physics Letters*, 50(26):19020, 1987.

[73] T. I. Camins and J. P. Colinge. Thickness determination of silicon-on-insulator structures. *Electronic Letters*, 22:1236, 1986.

[74] E. D. Palik and R. T. Holm. In *Nondestructive evaluation of Semiconductor materials and Devices.* 1979.

[75] S. M. Sze, editor. *VLSI Technology.* McGraw Hill, 1983.

[76] H. Mikoshiba and H. Abiko. Junction depth versus sheet resistivity in BF_2^+ implanted rapid-thermal-annealed silicon. *IEEE Electron Devices Letters*, EDL-7(3):190–192, 1986.

[77] H. J. Bohm, H. Kabza, T. F. Meiser, and H. Wendt. *ULSI Science and Technology.* S. Broydo and C. M. Osburn, 1987.

[78] C. Hill. 0.1 % ultra-uniformity in electrostatically scanned ion implantation systems. *Nuclear Instruments and Methods in Physics Research*, B19/20:348–358, 1987.

[79] D. J. Godfrey. Annealing and diffusion of fine geometry CMOS technologies. *Semiconductor International*, (5):216–220, 1985.

[80] M. Y. Tsai, F. F. Morehead, J. E. E. Baglin, and A. E. Michel. *Journal of Applied Physics*, 51:3220, 1985.

[81] W. L. Smith, A. Rosencwaig, D. L. Willenborg, J.Opsal, and M. W. Taylor. Ion implant monitoring with thermal wave technology. *Nuclear Instruments and Methods in Physics Research*, B21:537–541, 1987.

[82] M. A. Wendman and W. L. Smith. Thermal wave implant dosimetry for process control on product wafers. *Nuclear Instruments and Methods in Physics Research*, B21:559–562, 1987.

[83] D. Widmann and U. Schwabe. Limitations of ion implantation in MOS technology. pages 392–406, 1985.

[84] P. J. Pearson and C. Hill. 2D boron distributions after ion implant and transient anneal. *Journal de Physique*, 49(9/supp.C4):515-518, 1988.

[85] C. J. Curling, R. Hokke, and A. H. Reader. Two-dimensional profile determination of shallow arsenic doped regions in silicon. In *Inst. Phys. Conf. Ser. No. 100: Section 7*, pages 531–536, Oxford, England, 1989. Microsc. Semicond. Mater. Conf., IOP Publishing Ltd.

[86] D. P. God, J. H. Wills, G. R. Booker, M. C. Wilson, and D. J. Godfrey. SEM/TEM studies of etched si specimens to determine 1-D and 2-D dopant profiles associated with p-n junctions. In *Inst. Phys. Conf. Ser. No. 100: Section 7*, pages 537–542, Oxford, England, 1989. Microsc. Semicond. Mater. Conf., IOP Publishing Ltd.

[87] M. C. Roberts, G. R. Booker, S. M. Davidson, and K. J. Yallup. TEM studies of small geometry silicon MOSFETs. In *Inst. Phys. Conf. Ser. No. 67: Section 10*, pages 467–472, Oxford, England, 1983. Microsc. Semicond. Mater. Conf., IOP Publishing Ltd.

[88] R. Oven, D. G. Ashworth, and C. Hill. Simulations and measurements of the lateral spreading of ions implanted into amorphous targets. In *Simulation*

of semiconductor devices and processes, pages 429–440, Bologna, Italy, 1988. Tecnoprint.

Chapter 4

Electrical characterisation techniques

4.1 The objective

The need to measure dopant concentration profiles in silicon and III-V materials has lead to the development of a variety of characterization techniques. The different nature of the physical quantities monitored by those techniques may lead to overlapping, contradictory, complementary and sometimes misleading results if the techniques are used on their own. Since electrical conductivity determines the electrical characteristics of the fabricated devices, it is widely used to assess implanted semiconductors. Prior to making electrical measurements an annealing stage is necessary to activate the dopant. The purpose of this chapter is to review the characteristics that the 'ideal' measurement technique should possess, compare briefly most of the existing techniques and illustrate their capabilities. As it will be shown, most of those techniques possess inherent limitations that make impractical their industrial implementation. The need for a new technique for on-line monitoring is therefore evident.

The assessment of the existing layer stripping techniques is also a major objective of this chapter. Their main advantages and disadvantages will be pointed out. A more detailed study of the incremental sheet resistance technique with its associated measurement errors, limitations and software implementation features

will also be given. An implementation of this technique by use of Reactive Ion Etching was extensively used in the experimental part of the project.

4.2 'Ideal' profile evaluation technique: an illusion

Most of the techniques used for implant profile measurements make use of the different properties (for example optical, electrical etc) of the semiconductors. In order to assess the suitability and the level of accuracy of a technique, a series of requirements should be defined. The characteristics that an 'ideal' measurement technique should possess, [1] can be used as the benchmark:

1. **Ranges of application.** Junction source/drain implants, channel threshold adjustment implants, n-wells, p-wells, rapid dopant transitions (MBE layers), thin and thick implanted layers should be capable of measurement.

2. **Dynamic range.** The whole range of carrier concentrations between 10^{11} and 10^{21} carriers/cm^3 used for the various semiconductor devices, should be covered.

3. **Dynamic sensitivity.** Better than an order of magnitude sensitivity in carrier concentration is required over the entire dynamic range of carrier densities used.

4. **Depth resolution.** Depth resolution determined by the user is needed in order to conduct measurements on both thin (order of 0.1 μm or less) and thick (from 1 to 10 μm) implanted layers.

5. **Measurement interpretation.** The data processing should be as simple as possible. The measured quantity should not need frequent calibration against standards and should relate directly to the dopant concentrations. Excessive curve fitting should be avoided.

6. **Repeatability.** Measurement repeatability and minimum variation with time are very important for reliable characterization results.

7. **Interference and noise.** The technique should be free of any type of noise and correction factors.

8. **Measurement practicality.** Sample preparation should be minimal. Measurements should be able to be carried on a production wafer in a production environment with rapid turnaround time.

9. **Production line monitoring.** All the above features should co-exist in order to use such a technique on a fabrication line to monitor doping profiles and to ensure profile macro-uniformity.

4.3 Assessment of the carrier profiling techniques

The strong and weak points of the available profiling techniques have continuously been under investigation [2–4]. In this section the techniques will be assessed for their suitability for production line monitoring.

4.3.1 Spreading resistance

More than 25 years have passed since the first published work [5] on the spreading resistance phenomenon and its use for evaluating resistivity depth profiles. Hundreds of papers have been written on various aspects of the measurement so only a brief critical evaluation on the technique can be made here.

4.3.1.1 The nature of the measurement

The spreading resistance for a two-probe configuration is defined as the voltage difference between the probes divided by the current, $\Delta V/\Delta I$. In order to obtain an expression for the spreading resistance, the potential should be averaged over the contact area of the probe. The superposition theorem is also assumed to apply (the second pr obe does not perturb the potential due to the first probe). If two

probes of equal radii, α, are placed on the surface of a homogeneous, semi-infinite silicon sample of resistivity ρ, the spreading resistance can be obtained from [5]:

$$R_S = \frac{\rho}{2a} \tag{4.1}$$

Even for homogeneous samples the actual measured resistance, R_M, is given by :

$$R_M = R_S + R_B \tag{4.2}$$

where R_B is a resistivity-dependent barrier resistance term.

The measured spreading resistance for two probes, R_M, is a function of numerous variables; most of which are difficult to describe analytically:

R_M = f (resistivity, probe area, material, crystal orientation, surface smoothness, surface age, conductivity type, ...)

Therefore, it is evident that even for bulk samples $R_M \neq \rho/2a$, and a correction factor should be used. Two contact resistance models have been used, [6].

1. The barrier resistance model, where

$$R_M = R_B + C.F. \times \frac{\rho}{2a} \tag{4.3}$$

2. The effective radius model, where

$$R_M = C.F. \times \frac{\rho}{2a_{eff}(\rho)} \tag{4.4}$$

Those two models are general enough to describe the cases of thin, inhomogeneous semiconductor layers (where current flow is not radial and depends on the resistivities of the layers). The sampling volume correction factor, C. F., contains all the information concerning probe current density, probe current distribution, probe configuration, separation distance and other relevant measurement variables. The different models that are being used for the calculation of the C.F. are briefly presented in section 4.3.1.4.

4.3.1.2 Sample preparation

The comparative nature of the spreading resistance technique, implies that the sample preparation method must yield :

1. A highly reproducible surface.
2. A user-independent surface reproducibility.

Such a method has been developed, [6], but there are severe limitations on its implementation on an industrial line for process monitoring. This is not a matter of the equipment for sample bevelling or adjusting the bevel angle. It is mostly due to the huge skill and experience that the operators must possess in order to obtain the desired reproducibility. The situation gets much more complicated if thin layers are to be probed. Large bevel angles limit the resolution of the technique while small bevel angles make it difficult to distinguish the exact location where the initial wafer surface ends and the beveled surface starts as depicted in fig. 4–1.

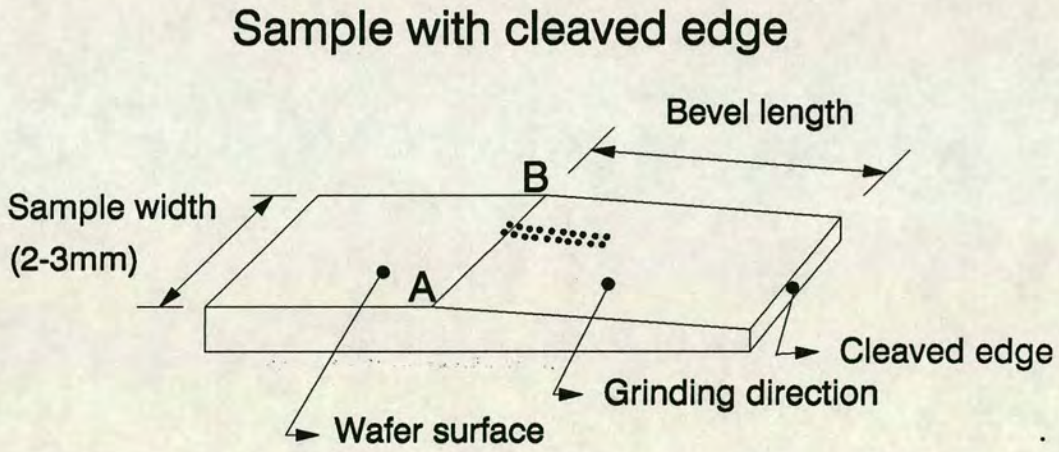

Figure 4–1: Spreading resistance measurements. For small bevel angles it is difficult to distinguish between the initial wafer surface and the beveled surface.

4.3.1.3 Calibration, probe preparation and stabilization

Since the spreading resistance technique is a comparison technique, a set of calibration samples are used in order to eliminate the effects of most of the variables

mentioned above. Calibration curves can apply to a particular measurement system, a particular pair of probes and a particular set of calibration and test samples at a particular time. However by isolating the above factors we cannot come up with a singly defined resistivity value, obtained directly under the two measuring probes. The probe material, the probe pressure and the probe deformation with time lead to a continuous change to the area of the contact between the probes and the material. Although appropriate probe conditioning methods might lead to the desired degree of probe tip texturing, [7], (so that the right number, type and distribution of microcontacts is achieved to make them act electrically as a single contact), probe deformation with time and measurements limit the technique reproducibility. Furthermore, the special set of calibration samples and the special probe conditioning procedures that have to be employed for thin layer measurements, resembles more an 'art' [6]. This in effect, severely limits the possibility of implementing the technique for on-line monitoring submicron product wafers.

4.3.1.4 Data processing

The conversion of the raw spreading resistance data to a carrier concentration profile is a very difficult task to implement, due to modelling dependence of the correction factors. The calculation of the spreading resistance correction factor using the Schumann-Gardner [8] multilayer Laplace equation [1] has reached the point where the calculation of the spreading resistance from the resistivity and the inverse calculation can be efficiently performed on a computer system by use of the appropriate algorithms. The inhomogeneous profile is modelled as a multilayer structure consisting of constant resistivity slabs. An excellent presentation of the computational problems and the algorithms development for that method of images can be found in [10].

---

[1]The complete mathematical description of the solution of the Laplace equation on cylindrical coordinates can be found in [9].

The computational problems encountered in this model have led to the development of methods making use of faster algorithms like the effective boundary approach [11–13] and the Berkowitz-Lux algorithm [14,10]. According to [6,10] this last algorithm is the most efficient and accurate to calculate the correction factor.

The local slope technique model, is an heuristically derived algebraic relation between the correction factor and the local depth derivative of the spreading resistance. It utilises a multilayer approximation to an inhomogeneous structure, [15], and is empirical in nature (since it uses the limiting values of the correction factor for a thin layer over an insulating and over a conducting substrate to evaluate a C.F. value for the whole range of structures between the two limits).

4.3.1.5 Applicability for submicron device profile monitoring

Profile distortions due to carrier spilling. The most significant failure of the modeling of the spreading resistance measurements has been fully recognized as devices shrink and thin implanted layers have to be measured. The inherent limitation of the Laplace model (and all of the models based on that equation), is on the use of the multilayer equations for the case of shallow layers where the net local charge is non-zero. Although, from the technology viewpoint there are no severe problems in measuring spreading resistance in submicron regions, the data interpretation model has to be scrutinised carefully. The Laplace equation cannot be used in a region where local charge neutrality is violated and the carrier and dopant vertical profiles are not identical [16]. The phenomenon is known as 'carrier spilling' since the free carriers originating from the dopant atoms spread out to the extent limited by the macroscopic electric field of the space charge region as presented in fig. 4–2.

The consequence of this spilling is the shift of the electrical junction (depth at which holes density equals electron density) from the metallurgical junction (donor atom density equals acceptor atom density). This shift in the vertical profile gets even more complicated if the sample bevel boundary conditions are

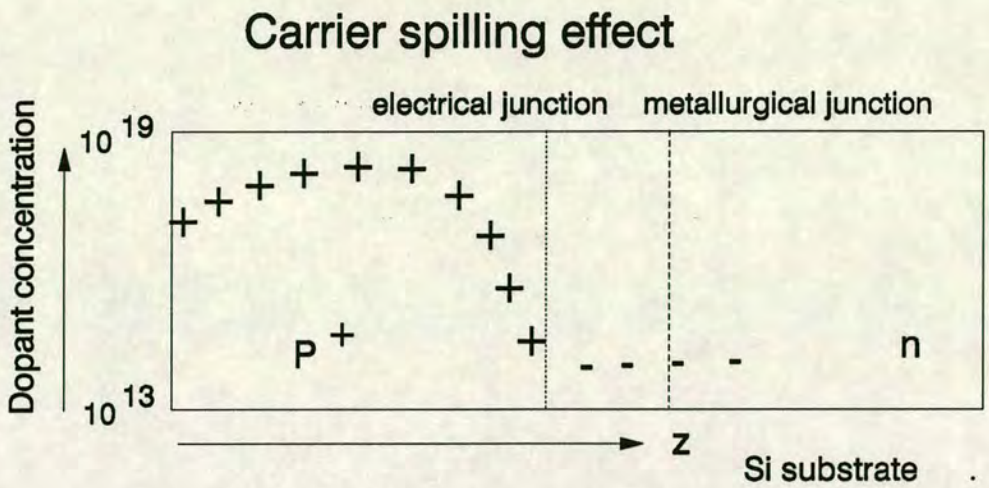

Figure 4–2: Free carriers move under the effect of ellectric fields and dopant concentration gradients. This effect is defined as carrier spilling and results in a separation distance between the electrical and metallurgical junctions.

taken into account. The Gauss law implication for the potential lines to bend up perpendicular to the bevelled surface induces a convergence or divergence of carrier spilling in two dimensions near the bevel. The existence of surface charges, the actual vertical profile shape, the bevel angle, the substrate concentration and the depth of the vertical structure affect the magnitude of the spilling effect, which in the case of Gaussian type implant profile leads always to shallower electrical junctions. Although techniques have been developed to account for such an effect for MBE grown layers, [17], the method is not suitable for industrial environment implementation.

Profile distortions due to bevelling. Another effect that complicates the situation is the effect of electrical field line distortion and additional redistribution of carriers due to bevelling, [18], which is enhanced for submicron structures. Since shallow angle bevels are used for shallow junctions, large displacements of the carrier distribution can occur due to the presence of the bevel. Depending on the exact nature of the dopant distribution, this can either push junctions deeper or shallower, [16]. The magnitude of this effect is a function of the boundary

condition. The surface charge present on a bevelled surface, which is not known and hard to estimate, is the main cause of this effect and it can severely distort measured profiles in lightly doped samples [16].

Resolution. Two different aspects of resolution have to be discussed [19].

1. Geometric resolution is the smallest increment in structure depth that can be measured. As such, it is controlled by the bevelling angle and the stage translation increments. Although a 10 Å geometric resolution has been obtained for a 4 minutes of arc bevel angle combined with a 2.5 μm stage increment [19], questions about the measured spreading resistance may arise. Spreading resistance value changes from point to point might be smaller than the error associated with each particular measurement (due to noise, bad contact, probe condition and other parameters). Therefore, increased need for data smoothing may perplex the data interpretation aspect of the technique. The exact determination of the bevel edge for very small bevel angles poses another limitation to the resolution.

2. Electrical resolution can be defined as the smallest change in resistivity, which can be resolved as a change in measured resistance. As mentionned above it is strongly dependent on the probe material, probe radii, seperation distance, probe texturing and sample surface condition. It is dominant over the geometric resolution for determining the overall resolution of the technique.

Dynamic range and sensitivity. There is virtually no limit to the dynamic range measured by the spreading resistance technique. Provided that the system hardware is capable of measuring resistance values from 1 to 10^9 Ohms, then the 10^{11} to 10^{21} cm^3 carrier concentration range can be covered. The dynamic sensitivity depends on the quality of the electrical contact and the calibration and preparation procedures of both probes and sample.

The measurement noise poses another limit on the technique sensitivity. As mentioned in [1] the increase in noise is a consequence of sampling very small volumes (this also happens to physical profiling techniques such as SIMS and AES). If a significant number of defects (stacking faults, dislocations) are included in the sampling region, barrier resistance and piezoresistive components of the measured resistance are affected by the strain fields of the defects. For thin layers or rapid dopant transitions containing crystalline defects the evaluated profiles are meaningless.

Noise level. If the profiled material contains a large number of crystalline imperfections and the sampling volume is small (see [1]), the probes will be sampling regions lying within the strain fields of those defects(stacking faults, dislocation loops). Therefore the measured resistance will change (due to changes in its barrier resistance and piezoresistive components) and the level of noise will be severely increased. For rapid dopant transitions and shallow junctions this effect will provide meaningless data.

4.3.2 Differential Hall effect technique

4.3.2.1 The nature of the technique

The theory of the Hall effect can be found in most solid state physics books [20]. The carrier concentration and carrier mobility profiles may be calculated from Hall voltage measurements and sheet resistance measurements. For the different combinations of the electric and magnetic field directions (which are perpendicular to each other) [2] [22,23] sheet resistance and Hall voltage are measured.

---

[2]The Ettingshaussen phenomenon, the Nernst phenomenonon, the Righi-Leduc phenomenon and the potential drop along the current direction are the side phenomena effects that their effect can be excluded by measuring voltage differences for the 4 possible electric and magnetic field-direction combinations [21].

A stripping method (for example anodic oxidation) can be used in order to remove successive thin layers from the sample and conduct measurements on each layer. The carrier concentration and mobility concentration versus depth can be evaluated from such a series of measurements [23].

4.3.2.2 Assessment of the technique

The carrier mobilities are evaluated from the Hall mobilities by use of the Hall scattering factor. This scattering factor depends on the scattering mechanism and its theoretical values are 1.18 for ionized impurity scattering and 1.93 for neutral impurity scattering. However, in most reported analyses a value of 1 is assumed [24] and this assumption is fulfilled for heavily doped Si (uncertainty in the scattering factor becomes important for concentrations below $10^{18}cm^{-3}$).

Uncertainty of the depth scale can be a potential problem of the method if the solution used for the anodic oxidation is not the most appropriate [3].

Sample preparation is the issue that makes the technique innapropriate for on-line monitoring. A rectangular area of several cm^2 has to be cut out from the wafer. Four small metal contacts close to the sample periphery have to be prepared with the aid of a wire bonder and an alloying furnace. The technique is therefore destructive.

4.3.3 Capacitance-voltage measurements

4.3.3.1 The nature of the technique

The concept of depth profiling by the measurement of capacitance was proposed in 1942 by Schottky. It has been thoroughly examined and developed for the last 30 years. The variation of the capacitance of a p-n junction, of a Schottky barrier or a MOS capacitor with the applied voltage bias can reveal the in-depth carrier profile [25–28].

4.3.3.2 Suitability assessment

An excellent review of the CV measurement techniques and measurement-device configurations which have been applied to derive shallow-dopant profiles in the near-surface region of semiconductors, with the operating principles and comparative advantages and disadvantages can be found in [29].

Resolution limit. Although Schottky barrier structures possess most advantages of the different CV measurement structures(due to their fabrication simplicity, their ability to measure profiles to a depth limited by avalanche breakdown and lack of distortion of the profile in fabrication) they suffer, as all CV techniques, from a resolution limit set by the Debye length, [30]. This limit is even more pronounced for submicron structures, where the shallow dopant profiles present steep tail regions. Changes in the doping profile that occur in a distance smaller than 2 Debye lengths cannot be traced. The Debye length is given by [31] :

$$\lambda_{\text{Debye}} = \sqrt{\frac{kT\epsilon_s\epsilon_0}{q^2N}} \tag{4.5}$$

where N is the local carrier concentration. Depletion is expected from both sides, but the Debye length is bigger in the low concentration profile region. For a substrate concentration of 10^{15}cm^{-3} a Debye length of $0.1\mu\text{m}$ is expected. This is about half the depth of the implanted layer for ULSI devices. The profile as-determined by the CV technique can be significantly different from the true implanted profile and may exhibit an 'artificial' exponential tail, which might be absent from the actual impurity atom distribution. Determination of the semiconductor doping profile right up to its surface is also limited although correction algorithms [32,33] improve the situation. Therefore, the resolution limit of the CV technique is prohibitive for ULSI junction profile monitoring purposes. However, the technique is excellent for production monitoring of lightly doped materials and most of all for the crucial step of the channel threshold implant [34,35].

4.3.4 Electrochemical capacitance-voltage measurements

4.3.4.1 The nature of the method

The principle behind the ECV profiling technique is a sequence of differential capacitance measurements combined with in-situ anodic dissolution. Its inherent advantage over conventional CV is that there is no limit to the depth to be characterized (due to junction breakdown under high bias). The space charge region within a semiconductor adjacent to an electrolyte, under certain biasing potentials, approximates to a Schottky barrier [36]. The Schottky barrier at that interface has a capacitance that is given by:

$$C = A\sqrt{\frac{\epsilon_r \epsilon_O n q}{2V}} \tag{4.6}$$

where V denotes the applied bias, A the cross section of the interface and n the carrier concentration at the edge of the depletion layer.

The depletion width, W_d can be obtained from the relation:

$$W_d = \epsilon_r \epsilon_O \frac{A}{C} \tag{4.7}$$

The measured carrier concentration, n, is made at a depth equal to the depth removed by the dissolution process, W_R, plus the depletion depth, W_d. The depth removed by the dissolution process can be calculated from the relation [37]:

$$W_R = \frac{M}{DANF} \int_0^t I dt \tag{4.8}$$

where

M , is the molecular weight of the semiconductor,

D , is the density of the semiconductor,

A , is the cross-section of the interface,

F , is the Faraday constant,

N , is the effective valence number that represents the number of electronic charges required to remove one molecule of the semiconductor,

I , is the dissolution current and

t , is the time.

The actual measurement of the capacitance is made using a modulation technique where a small modulation of the bias potential is added to produce a corresponding modulation of the depletion width, and hence the capacitance.

4.3.4.2 Method evaluation

Depth Resolution. The depth etch rate is one of the critical problems of the technique. Since, the method was initially developed for GaAs carrier concentration evaluation [38] and it was extended for Si characterization [39], problems with the most suitable electrolyte have occured [40]. Hydrogen bubbles evolving during the anodic dissolution process near the surface, can severely limit the etch rate, the etch uniformity and, eventually, the depth scale of the concentration profile. This problem can be reduced by the use of a pulsed jet of electrolyte in the cell. Depending on the electrolyte conecentration, various dissolution rates can be achieved varying from 1 to 3 μm/hour. It must be noted that diluted electrolytes, giving lower dissolution rates produce a better uniformity.

The depth scale and the etch uniformity can also be affected by the variability of the effective valence number, N, with anodic stripping conditions and electrolyte strength. The assumption that N remains constant during the profiling sequence cannot be always justified [39], since it depends on carrier concentration, carrier type, illumination, electrode potential and current level [41][and references therein]. This is one of the main reasons of possible technique inaccuracy.

Dynamic range and sensitivity. Profiles may be readily determined with the carrier concentration spanning over 4 orders of magnitude [3][page 204]. The problems that arise in ECV are mostly related to sample types and their corresponding doping levels. In order to achieve high sensitivity over the whole dynamic range, optimum bias potentials for the respective concentration levels have to be selected and should be adjusted if large swings in carrier concentration occur during the

measurement [1]. This decision has to be made from the CV, GV, IV characteristics of each sample both in the start and during the profiling. This operator input renders the technique inconvenient for a manufacturing environment.

4.4 Layer removal methods: a comparison

The standard methods used for the electrical assessment of ion implanted layers and the carrier concentration profile extraction are sheet resistance monitoring and sheet Hall mobility measurements. For both methods a surface stripping technique has to be used in order to conduct the measurements at increasing depths into the implanted layer [3]. Surface stripping by chemical etching, anodic oxidation stripping or ion-beam milling have been adopted so far. Those techniques will be briefly discussed and their inherent limitations for on-line monitoring will be highlighted.

4.4.1 Anodization technique.

As indicated in section 4.3 the anodization and stripping technique is one of the most commonly used methods for layer removal [42,43]. The wafer is connected to the anode and a Pt cathode is being used. The chemical solution used for the anodization inside the container (where the anode and cathode are situated) may vary [44]. During the process the solution should be irradiated with a tungsten-halogen lamp to accelerate the anodizing process. Typical currents used are about 10 to 15 mA/cm^2. The thickness of the oxide formed on the wafer is proportional to the final forming voltage and the conditions described (a typical value might be 5 Å per forming Volt). The oxide growth rate is not constant and a combination of constant current and constant voltage power supply conditions has to be used

[3]This holds true for measurements carried out on specially prepared test structures (ie van der Pauw structures) or on the as-implanted and annealed wafer.

[23]. Ellipsometry might be used if calibration of the system, rather than use of the approximate growth rate, is desired. Removal of the oxide takes place in HF solution. The oxide growth, oxide removal and sheet resistance measurement procedure is repeated until the junction is reached.

4.4.2 Ion beam etching technique.

A technique for the determination of the depth distribution of electrically active dopants implanted into silicon has been developed involving a Van der Pauw structure and ion beam etching as a method for layer removal [45]. An ion gun (described in [45]) is used to generate a beam. The ion gun has been found to operate quite satisfactorily using air(rather than the more usual Ar) and thus the ions used for bombardment are predominantly N^+ and O^+. Air is leaked until the pressure rises to around 5mTorr. At this pressure an anode voltage of 4kV produces a current around 1.5mA which is scanned along the specimen area. The sheet resistivity of the etched region of the Van der Pauw pattern is measured. The above procedure is sequentially repeated until the junction region is approached (erratic readings or decreasing sheet resistance). Some of the drawbacks of the technique are critically highlighted: Crystal damage caused by implantation was not found to influence the thickness of the removed layer. However, the dopant concentration has some influence on the etch rate of the sample. A 10 % variation of etch rate between a 10^{14} atoms/cm^3 and 10^{20} atoms/cm^3 concentration range has been found [46, page 90].

1. **Etch non-uniformity.** The uniformity of the removed material is less than 10 % over an area of mm^2. Although this might be adequate for a Van der Pauw structure, it might turn out to be a severe limitation if a whole wafer has to be scanned. The sources of non-uniformity arise mainly from variations in gas pressure, problems during scanning and beam stability.

2. **Increased processing time.** Although the technique for the layer removal is fast (compared for example to anodic oxidation) the processing time u-

tilised to create the Van der Pauw pattern, poses a limitation on the applicability of such a technique in a manufacturing environment. Photolithographic steps for pattern definition and the use of masking layers render the technique cumbersome to fit in an industrial line for process monitoring.

3. **Profile assessment.** The only realistic way to determine whether the profiles obtained by using a particular technique are valid is to compare them with the distributions obtained using another method of removal, not known to have the same sources of errors. In [45] the profile measured by the ion beam etching technique is compared to an anodic oxidation method of removal profile [47,48]. A shift on the ion beam etched profile about 400 Å towards the surface can be observed [45]. The shape of the curve does not seem to be changed due to the ion bombardment process step. The profile shift can be explained by the presence of an ion bombardment-induced amorphous layer. On the ion beam etched sample an amorphous, high resistance surface layer is created after the etching step (ellipsometry or channelling measurements verify this statement). The material sputtering and the damage penetration depth reach an equilibrium after a few seconds of etching. Thereafter the increase in depth penetration of each layer with dose and the etch rate of the layer do not vary with time, and the damage layer thickness should remain constant over the whole profile. The series high resistance that this amorphous layer presents on the sheet resistance measurements, is solely responsible for the observed profile shift. A more detailed discussion can be found in section 4.5.3.4 where the equivalent phenomenon for RIE etching is discussed.

Preferential impurity sputtering and 'knock-on' effects are small since the ion energy used is very small. A possible distortion of the profile might occur due to the proportion of the N^+ and O^+ ions that become electrically active. Comparison with the anodic oxidation profile shows that such an effect is negligible in the high concentration region and can only affect the properties of the profile tail region which lies 4 orders of magnitude lower than the peak region.

Therefore, it is evident that the method cannot be used to monitor a profile closer than 400 Å to the sample surface due to the ion bombardment-induced damaged surface layer.

4.4.3 Microetch ion gun technique.

In this method the layer is stripped by a low-energy ion beam. A standard commercially available ion gun was placed on top of a conventional vacuum bell jar [49]. A neutralized argon ion beam (1mA/cm^2, 1keV) was used for the etch. A 2 % uniformity over a 5cm diameter was achieved. The sputtering rate was 300 Å/min for silicon. The sheet resistance was measured by the Hall method. As discussed in the previous method, the damage from the physical ion bombardment caused a profile offset.

4.4.4 Chemical etching.

Si specimens can be etched in a solution of boiling NH_4OH, H_2O_2 and H_2O in a ratio of 1:1:6, [50]. The Si surface layer is etched by the NH_4OH while being oxidized simultaneously by the H_2O_2. By dipping the wafer in an aqueous HF solution the thin oxide layer is removed. Since for the oxide layer formation Si from the substrate is consumed, very thin layers of Si can be effectively removed. The depth removal versus etching time has been monitored. For etching times up to 40 minutes the etch rate is nearly linear and close to 12 Å per minute. No surface contamination has been observed on the etched surface(by use of ellipsometry and comparison to single crystal values). Due to its repeatability and consistency the method can be used for the evaluation of very shallow damage (for example from RIE etching or RF sputtering) down to depths of 500 Å. However, despite its resolution the method is very slow for on-line monitoring applications.

4.5 Four-point probe and sectioning technique

In attempting to apply the four-point probe to carrier concentration measurements on thin ion-implanted layers, a number of noteworthy effects might occur. Their relative contribution to erroneous measurements is discussed in some detail in the following sections.

4.5.1 Principles of the technique

4.5.1.1 Concept

Measurements of incremental sheet resistivity constitute a straightforward technique for determining carrier distribution with depth. The method consists of measuring sheet resistivity, removing a thin uniform increment, remeasuring the sheet resistivity and repeating the above procedure until the profile is complete, [51–53]. Sectioning can be implemented by any of the layer removal techniques described above.

4.5.1.2 The basic theory

The relationship between the bulk conductivity, σ(x), at any depth and the sheet conductivity, σ_s(x), is given by

$$\sigma_s(x) \stackrel{\text{def}}{=} \int_x^{x_j} \sigma(x)dx \tag{4.9}$$

where x denotes the depth measured perpendicularly to the surface and x_j is the bottom boundary of the conducting layer.

A first expression for obtaining the impurity concentration is obtained by differentiating eq.(4.9) :

$$\sigma(x) = -\frac{d\sigma_s(x)}{dx} \tag{4.10}$$

If we have a number of stripped layers, the derivative eq.(4.10) can be approximated to the measured data by use of the equation:

$$\frac{d\sigma_s(x)}{dx} \sim \frac{\Delta(\sigma_s)_i}{\Delta x_i} \equiv \frac{(\sigma_s)_{i-1} - (\sigma_s)_i}{x_{i-1} - x_i} = -qn_i\mu_i \tag{4.11}$$

where

n_i , is the average carrier concentration in the i-th removed layer

μ_i , is the average carrier mobility inside the i-th removed layer

Δx_i , is the thickness of the i-th layer removed (x_i is the depth after the i-th layer removal)

$\Delta(\sigma_s)_i$, is the sheet conductivity difference before and after the i-th layer removal

By solving the above equation for the carrier concentration we get:

$$n_i = -\frac{\Delta(\sigma_s)_i}{q\mu_i\Delta x_i} \tag{4.12}$$

A second expression for determining the impurity concentration with depth can be derived from eq.(4.10) :

$$\sigma(x) = -\frac{d[\rho_s(x)]^{-1}}{\rho_s dx} = -\frac{d\ln[\rho_s(x)]^{-1}}{\rho_s dx} = \frac{d\ln\rho_s(x)}{\rho_s dx} = \frac{1}{0.4343\rho_s}\frac{d\log\rho_s(x)}{dx} \tag{4.13}$$

4.5.1.3 Obtaining the mobility values

For both eq.(4.12) and eq.(4.13) the mobility values at different depths (actually at different concentration levels) are needed. Since the method used does not provide experimental mobility values, those have to be calculated from an analytical relationship. There is a significant variation in experimental curves throughout the literature regarding carrier mobility variation with doping concentration [44]. Those mobilities are drift or conductivity mobilities which coincide with Hall mobilities only in certain regions [44]. Those drift mobility values may differ from the effective mobility values, [54]. The above statement is true when the impurity concentration differs from the true carrier concentration. Degenerate regions (near

Constants from the empirical mobility expressions						
	μ^+ ($cm^2/V \times s$)	μ^- ($cm^2/V \times s$)	a	b	N_{ref1} ($atoms/cm^3$)	N_{ref2} ($atoms/cm^3$)
Holes	495	47.7	0.76		1.9×10^{17}	
Electrons	1330	65	0.72	1.5	8.5×10^{16}	5×10^{20}

Table 4–1: The constants values obtained from the empirical mobility equations.

the profile peak) and regions where carrier compensation exists (in the vicinity of the junction) fall in this category. Empirical curve fitted relationships for the measured conductivity mobility of holes and electrons versus the logarithm of doping concentration will be used, [55,44,56]. The equations used are:

For holes:

$$\mu_{eff}(x) = \frac{\mu^+ - \mu^-}{1 + \left(\frac{N}{N_{ref1}}\right)^a} + \mu^- \tag{4.14}$$

For electrons:

$$\mu_{eff}(x) = \frac{\mu^+ - \mu^-}{1 + \left(\frac{N}{N_{ref1}}\right)^a} + \frac{\mu^-}{1 + \left(\frac{N}{N_{ref2}}\right)^b} \tag{4.15}$$

The values for the previous two equations are given in Table 4–1. It will be shown in some of the following experimental chapters, that the deviation of the Hall measured mobilities from the effective mobilities calculated through this method is very small for the ion implanted profiles under test.

4.5.1.4 The algorithm choice

Both algorithms mentioned in the previous sections have been used for the evaluation of the carrier concentration profile. The mathematical formulation of the solution is close to the one described in [44].

At a set of points x_i (the increasing depths in Si), measurements are performed to obtain a set of points $(\rho_s)_i$ (the sheet resistances which are depth dependent). The objective is to calculate numerical values for the function N = f(x) (where

N denotes the carrier concentration) which is implicitly defined by the following equation which is actually eq.(4.11):

$$\frac{d}{dx}\left(\frac{1}{\rho_s(x)}\right) = -qN\mu_{eff}(N) \tag{4.16}$$

and the equations for the carrier mobility are eq.(4.14) and eq.(4.15).

The algorithm used to solve this problem must:

1. Evaluate numerically values for the inverse derivative of the measured sheet resistance at the various layer depths.

2. Use the derivative values to solve the implicit eq.(4.16).

Derivative evaluation. From eq.(4.12) it is evident that the impurity concentration depends on the slope of the sheet conductance with depth. Since the slope has to be evaluated from the data points, the difference of sheet resistivity and the incremental layer thicknesses removed are crucial in that slope evaluation. The main problem arises from the method used for slope extraction from the data points. If the differences between neighbouring points are used, severe problems arise if very thin layers are removed and the sheet resistivity does not change significantly for those successive removals. As a result the unrealistic scatter in slope points can lead to erroneous concentrations. From the other side, if a best curve fit is used through the entire set of points, the smoothed slope variation results in a carrier concentration profile that depends on the curve fit method. Several methods, such as an average technique utilizing several nearest neighbour points, Tchebyscheff polynomials and the weighted average technique can be used. High order polynomials combined with least square fit tend to oscillate badly and give a very poor approximation to the function.

Cubic splines with user specified knots [4] were found to be the most appropriate technique, since user knots-adjustment permits any type of data points to be successfully fitted. This type of fit can minimize the occurence of sporadic values for the derivatives, the major disadvantage for derivatives of unsmoothed discrete data.

In the second method, [57], the major variable in eq.(4.13) is the measured resistivity itself. The slope of the logarithm of the resistivity with depth can change by two orders of magnitude , while the resistivity itself changes by several orders of magnitude. This in effect reduces the effect of the smoothing and best curve fit procedure on the data points, and the resulting carrier concentration profile is closer to the real profile. By using cubic splines with user-adjusted knots both methods give similar results.

Solving the equation. The equation that must be solved numerically is the following:

$$\frac{1}{q}\frac{d}{dx}\left(\frac{1}{\rho_s(x)}\right) + N\mu_{eff}(N) = 0 \tag{4.17}$$

and is derived from eq.(4.16). It can be solved by use of a combination of the Newton-Raphson method and bisection (in order to assure fast and safe convergence). Therefore, the function F,

$$F = \frac{1}{q}\frac{d}{dx}\left(\frac{1}{\rho_s(x)}\right) + N\mu_{eff}(N) \tag{4.18}$$

and its first derivative, F′

$$F' = N\frac{d}{dN}\left(\mu_{eff}(N)\right) + \mu_{eff}(N) \tag{4.19}$$

---

[4]The NAG library subroutines E02 have been found to be fast and error free. For full information on the subroutines: The NAG Fortran Workstation Library Handbook, 1st edition, vol.1 from NAG Ltd, Wilkinson House, Jordan Hill Road, Oxford, OX2 8DR, UK.

are being used for the Newton-Raphson iteration relation:

$$N_{n+1} = N_n - \frac{F(N)}{F'(N)} \tag{4.20}$$

A program has been written in FORTRAN for evaluating the carrier concentration profile from incremental sheet resistance measurements by use of the above algorithm. Output files are created containing the sheet resistance, sheet conductance, carrier concentration and carrier mobility values at both the measured and assigned depths. Plotting routines for viewing the plots on screen and sending them on a plotter have also been implemented. They support several driver configurations for PCs.

4.5.2 Magnitude of the measuring current

4.5.2.1 The phenomenon

Four point probe is a direct experimental technique, since no calibration of the measured quantity (sheet resistance) to any standards is needed. However, it is necessary to obtain good electrical isolation between the epitaxially deposited or ion-implanted layer on a substrate of the opposite conductivity type. A qualitative explanation of how the measuring current level affects the measurements will be presented, since a wrong current choice might lead to an erroneous concentration profile.

The typical structure measured by a four point probe is schematically depicted in fig. 4–3. We assume that current flows through the outer probes and voltage is measured between the two inner. Due to leakage currents across the junction, a biasing arrangement is allowed to form [58]. The junction under the negative contact (-) is forward biased while the junction under the positive contact (+) is reversed biased. The following cases can be considered:

Case 1. For small measurement currents. The voltages that appear directly across the junction are correspondingly small. From the I-V characteristic

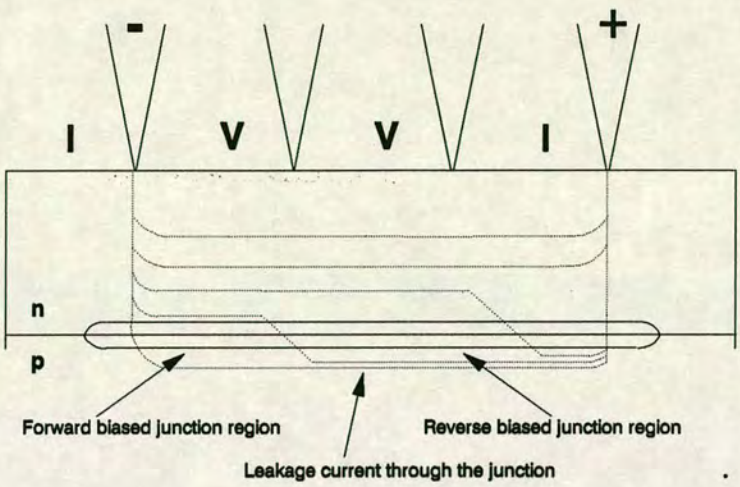

Figure 4–3: A typical stucture (diode) measured by four point probe technique.

curves of fig. 4–4(the I-V slope at the origin), the junction appears as a fairly high resistance.

The current is split into 2 components [59]; most of the current passes through the implanted layer, while a much smaller portion passes through the substrate. The magnitude of the ratio of those currents is a function of the sheet resistance of the implanted area and of the sheet resistance of the substrate. The presence of any localized imperfections in the junction will give rise to abnormally large leakage current, which will strongly affect the current distribution. The situation is depicted in fig. 4–4, where the two current components and the junction characteristics at 3 points on the leakage path are displayed.

Case 2. For medium measurement currents. As the measurement current increases the junction area which is being biased, increases as well. As the current increases, the reverse biased junction area reaches the area under the voltage probes. The decreased area through which the implanted region current flows(due to increased depletion width and increased reverse biased junction area) constitutes the main reason for a rise in the V/I measured value.

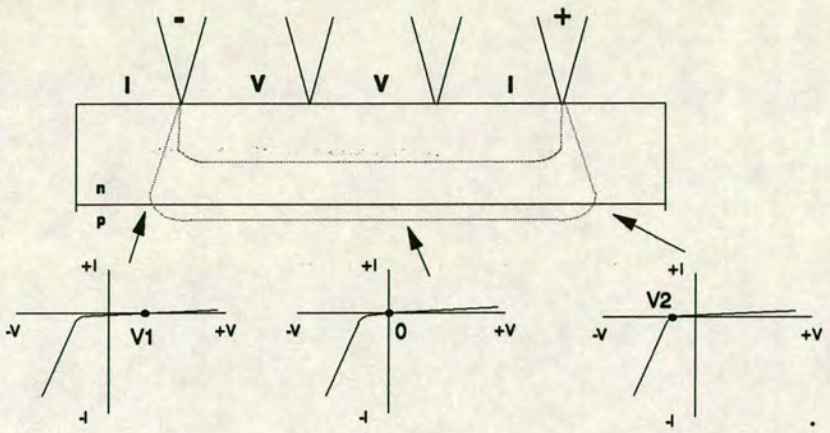

Figure 4–4: A schematic of the two current components during a four-point probe measurements. The junction characteristics at 3 points on the leakage path are also displayed.

Case 3. For high measurement currents. As the measurement current increases, a point is reached where the junction breaks down in a region near the positive contact. A corresponding sharp drop in the V/I measured value is expected.

4.5.2.2 Conclusions

It is evident that in the study of annealing behaviour of ion implanted layers, the influence of a leaky junction is noticeable. For low-temperature annealing (600°C), where the sheet resistance is high and the junction properties are poor due to ion damage, the above effect is even more pronounced. It is necessary to keep the current setting as low as possible, so that the isolating junction would operate near its zero bias point of fig. 4–4. In order to achieve this requirement whenever sheet resistance measurements were employed in the experimental procedures, initial measurements were performed over the available range of currents (5μA to5mA). The current setting chosen was the one that gave the lower sigma variation over the wafer and the lower sheet resistance values.

4.5.3 Surface preparation and measurement precautions

Surface preparation and a number of cautionary measures have been found necessary in applying the four-point probe method in conjunction with a layer stripping technique, to extract carrier concentration profiles from ion-implanted layers.

4.5.3.1 Carrier injection

If the current density at the probe tips becomes too high, and exceeds the value of J_{crit}, [60]

$$J_{crit} = n_0 q v_{sat} \tag{4.21}$$

where q denotes the electrical charge, v_{sat} the saturated drift velocity in the material under investigation and (n_0) the local free carrier density, carrier injection can occur. By forcing a high current level through the probe, J might exceed its critical value and the excess current can only be carried by the local excess carrier concentration, $n - n_0$, injected from the probe tips into the semiconductor. This results in erroneous sheet resistance measurements.

4.5.3.2 Recombination rate of injected carriers

A high recombination rate for the injected carriers at the current probes is desired. If carriers recombine as soon as they are injected, the conductivity is not modulated by their presence. Measurements are performed in the dark to prevent carrier generation by the incident light, since optically generated carriers (by photons) can lead to errors in the measured sheet resistivity. Those effects are more pronounced in the high resistivity layers (where carrier lifetimes are usually long).

4.5.3.3 Surface treatment

In order to obtain better contacts, special treatments have been used [61] to alleviate measurement errors. Techniques like lapping or sandblasting are not appropriate for implanted layers in highly polished wafers. For implanted n-type layers,

a mild oxidising treatment (expose to atmosphere for 2h) and for p-type layers a hot dip in hydrogen peroxide, are recommended. In all cases measurements immediately after an HF dip should be avoided. The way that surface treatment can affect the apparent resistivity is discussed in [63]. The presence of an inversion layer close to the surface may result in the measurement of the sheet resistance of just that layer(if the probes do not punch through it) or of the series sheet resistance of the layer and the bulk(if they pass through it and contact the bulk).

4.5.3.4 RIE damaged surface layers

The damaged surface formed by the RIE process influences the measurements of resistivity profiles, since it may create serious damage to the crystal lattice sometimes extending well below the surface. A model equivalent to the one employed for the damage induced by a grinding process [64] may be used to explain how RIE induced damage affects the resistivity measurements. The model structure is depicted in fig. 4–5.

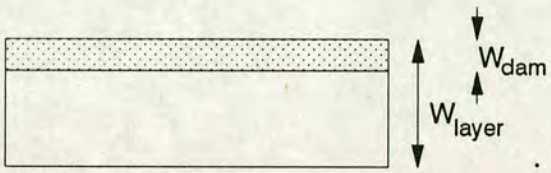

Figure 4–5: Schematic representation of the RIE-damaged crystal model. The damage and implant layer depths are not drawn to scale.

The RIE damaged layer(whose nature is discussed in section 6.2.3) can diminish the electrical conductivity because of the current path interruption at the damage sites. In order to express the influence of those crystal faults on the overall measured resistivity of the implanted layer, a layer of thickness w_{dam} can be introduced whose conductivity is close to zero and its thickness denotes the depth by which the implanted layer thickness, w_{layer} is diminished. The overall measured conductance is thus the sum of the conductances of the damaged and undamaged layer conductances. This can affect the dopant profile evaluation (by use of the

differential sheet resistance method). In order to minimize this effect the RIE-enduced damage has to be eliminated from the sheet resistance measurements. This optimization will be developed in chapter 6.

4.5.4 Surface depletion effect

4.5.4.1 The phenomenon

The presence of surface depletion effects is due to the existence of surface states on the air-exposed semiconductor surface [64,65]. The abrupt termination of the lattice or the defects at the semiconductor surface pin the Fermi-energy level (in the forbidden energy gap) at the surface, creating a depletion region just below the surface. The carriers within that region become trapped in the immobile surface states and do not contribute to the electrical conductivity.

4.5.4.2 Mathematical formulation

Measurement of a profile consists of four point probe measurements and etching of a thin layer; this cycle is repeated until the junction is reached. During the measurement procedure the raw sheet resistivity is first inverted to sheet conductivity at each measured depth. Subsequently the adjacent incremental sheet conductivity values associated with each removed layer are subtracted. If the depleted charge is kept the same from strip to strip, the effect of the depletion region on the conductivity values is identical for each layer and does not intervene in the profile evaluation. The only implication is that the incremental sheet conductivity should be assigned at the edge of the depletion region, at a distance equal to the depletion width, w, for all layers below the surface. Therefore, the apparent profile has to be translated by w towards the semiconductor bulk. This is the case for a uniform profile doping [64](since the depletion width value w depends strongly upon the carrier concentration value).

For a non-uniform ion implanted profile, the situation is much more complicated. An algorithm for correcting the apparent profile can be found in [66].

4.5.5 Carrier spilling effect

An interference of major concern is the carrier spilling effect which was explained in section 4.3.1.5. As it was explained earlier, it is due to Debye length smearing and it thus poses a limitation to all the carrier concentration techniques. The Debye length is the minimum distance over which the electric field in a semiconductor may change by a factor of e. If a sharp dopant transition is present (a junction for example) this implies that carriers have to spill and lead to a smeared distribution in response to the local field conditions. Corrective algorithms have been used in CV analysis to convert carrier profilesto dopant distributions, [30–32]. However, the phenomenon is relevant only when dopant profiles are inferred from carrier concentration profiles (due to the model being used).

4.5.6 Error and limitations of the technique

As with any measurement technique, it is of vital importance to identify the sources of errors, quantify their contribution and interprete the results appropriately.

4.5.6.1 Electrical measurement error

The depth resolution and measurement accuracy are primarily determined by the accuracy with which values of sheet resistance and depth are measured. To evaluate the carrier concentration n(x) from the sheet resistance results using a discrete etching technique, small differences over 4 decades have to be measured. If substantial errors in n(x) and μ(x) are to be avoided, the etch step has to be kept sufficiently large so that sheet resistance increments (ie the difference in sheet resistance between successive measurements) are an order of magnitude greater than the associated sheet resistance measurement error. The depth resolution is therefore directly limited by the accuracy to which the sheet resistance values can be measured. An estimate of the relative standard deviation error (uncertainty) for the carrier concentration is obtained in Appendix A from equations A.11 and A.12. The use of the α_{σ_s}, α_x andα_μ factors (defined as the average value over the

difference between successive measurements of the same quantity) in equations A.8 to A.10 demonstrates how rapidly the profile scatter will increase by a change in either the value of the measurement itself or of the difference between the successive measurements. Therefore, in order to keep the scatter in carrier concentration below 10 % (3 σ value), the minimum depth resolution of the technique can be evaluated for the various implant applications [5].

4.5.6.2 Etch rate variation with depth

The thickness of the removed layer can be measured after each RIE step by using a surface profilometer. Therefore, etch rate variations due to doping concentration variation with depth inside the material, can be accurately monitored. This may be considered as an advantage over the anodic oxidation technique, where the etch rate is measured at the end of the profiling method and a linear dependence with time is assumed, [67,68]. This is of particular importance if rapid transitions of the doping profiles occur.

4.5.6.3 Spatial etching variation across the sample

The etching uniformity across the sample is examined thoroughly in section 6.3.3.1

4.5.6.4 Etch non-uniformity within a small region

If an area is defined for etch and subsequent measurement by four-point probe, thermal-wave or any other method, the uniformity of the etch rate within the area is crucial for determining the depth resolution. Therefore, the area must be very uniformly etched in order to have the desired quantity measured and assigned at an accurate depth in silicon. This etch micro-uniformity is also treated in section 6.3.3.1.

---

[5]The uncertainties of all the measured and evaluated quantities are defined as the three standard deviation values of those quantities.

4.5.6.5 Implications on the measurement technique.

Deviations between apparent and true carrier profile. The equations used to calculate n(x) and μ(x) do not take into account the surface depletion effect [64]. The importance of the effect has to be assessed. Since the depletion layer thickness under the free surface of the sample, w_s, is related to the surface carrier concentration n_s by the equation

$$w_s = \sqrt{\frac{2\phi_B \epsilon_0 \epsilon_r}{q n_s}} \tag{4.22}$$

where ϕ_B denotes the surface potential and all other symbols have their usual meanings. Since n_s is a function of depth we expect to have a depletion depth variation. If the carrier concentration profile is increasing with depth, the depletion depth will decrease for consequent layer stripping steps (as it can be seen from the above equation). During the RIE step carriers are removed from an actual material thickness smaller than the etching step increment (since no carriers are assumed to reside in the depletion layer). Accordingly the calculated carrier concentrations would be less than the true carrier concentrations. In regions of decreasing carrier concentration the apparent carrier concentration values will be greater than the respective true carrier concentration values. It is therefore evident that the depletion effect leads to stretch-out of the profile leading edge (close to the surface) and compression of the profile trailing edge.

Depth scale error. As it was explained in section 4.5.4.2, an error arises from the assignment of the calculated carrier concentration at an apparent depth x_i rather than the true depth $x_i + w_i$. A simple correction is not possible due to the complex relationship between carrier concentration and depth scale [66].

4.6 Conclusions

From section 4.3 it is apparent that the traditional profiling methods cannot be implemented in an industrial environment for on-line monitoring. The sources of error of the existing layer stripping techniques have been carefully investigated and assessed. In section 4.4 it has been shown that all the existing layer removal techniques can be used in a sequential mode (layer stripping and measuring steps) until the junction is revealed. This imposes a time retardation which is incompatible with the requirements for on-line measurements. The lack of a fast profiling technique can therefore be interpreted as the need for a fast sectioning technique, able to reveal several depths into Si with the minimum amount of processing steps and time. Such a technique should be used as an interface on the existing surface monitoring techniques of implanted layers, in order to accomplish implant profile extraction. The new method must be thoroughly checked against the sources of errors identified above, if the desired high depth resolution imposed by ULSI design rules is to be achieved.

Bibliography

[1] A comparative study of carrier concentration profiling techniques in silicon: spreading resistance and electrochemical CV. In D. C. Gupta and P. H. Langer, editors, *Emerging Semiconductor Technology, ASTM Special Technical Publication 960 (ASTM STP 960)*, pages 558–572, Philadelphia, PA, 1986. Fourth International Symposium on Semiconductor Processing, 1986, San Jose, California, ASTM.

[2] Dopant Profiling Techniques and In-Process Measurements. In D. C. Gupta and P. H. Langer, editors, *Emerging Semiconductor Technology, ASTM Special Technical Publication 960 (ASTM STP 960)*, Philadelphia, PA, 1986. Fourth International Symposium on Semiconductor Processing, 1986, San Jose, California, ASTM.

[3] P. L. F. Hemment. Measurement of ion implantation. In J. F. Ziegler, editor, *Ion Implantation Science and Technology, Second Edition.* 1988.

[4] D. H. Dickey. Diffusion profile studies using a spreading resistance probe. *Extended Abstracts of the Electronics Division, Electrochemical Society*, 12(1):Abstract No 57, 1963.

[5] R. G. Mazur and D. H. Dickey. A spreading resistance technique for resistivity measurements on silicon. *Journal of the Electrochemical Society*, 113(3):255–259, 1966.

[6] R. G. Mazur and M. Pawlik. Spreading resistance seminar. Technical report, November 1989.

[7] R. G. Mazur and G. A. Gruber. Dopant profiles on thin layer silicon structures with the spreading resistance technique. *Solid State Technology*, 24(11):64–70, 1981.

[8] P. A. Schumann and E. E. Gardner. Application of multilayer potential distribution to spreading resistance correction factors. *Journal of the Electrochemical Society*, 116:87–91, 1969.

[9] O. Koefoed. *The application of the Kernel Function in Interpretation of Geoelectrical Resistivity Measurements.* Gebruder Borntraeger, Berlin-Stuttgart, 1968.

[10] M. Pawlik. A comparison of sampling volume correction factors in high resolution quantitative spreading resistance. In D. C. Gupta and P. H. Langer, editors, *Emerging Semiconductor Technology, ASTM Special Technical Publication 960 (ASTM STP 960)*, Philadelphia, PA, 1986. Fourth International Symposium on Semiconductor Processing, 1986, San Jose, California, ASTM.

[11] S. C. Choo, M. S. Leong, and K. L. Kuan.)n the calculation of spreading resistance correction factors. *Solid State Electronics*, 19:561, 1976.

[12] S. C. Choo, M. S. Leong, H. L. Hong, L. Li, and L. S. Tan. A multilayer correction scheme for spreading resistance measurements. *Solid State Electronics*, 20:839, 1977.

[13] D. C. D'Avanzo, R. D. Gat, and R. W. Dutton. High speed implementation and experimental evaluation of multilayer spreading resistance analysis. *Journal of the Electrochemical Society*, 125:1170, 1978.

[14] H. L. Berkowitz and R. A. Lux. An efficient integration technique for use in the multilayer analysis of spreading resistance profiles. *Journal of the Electrochemical Society*, 128:1137, 1981.

[15] D. H. Dickey and J. R. Ehrstein. Semiconductor measurement technology: spreading resistance correction factors for silicon layers with non-uniform resistivity. *NBS Special Publication*, 400-48:400–448, 1979.

[16] S. M. Hu. Between carrier distributions and dopant atomic distributions in beveled silicon substrates. *Journal of Applied Physics*, 53:1499–1510, 1982.

[17] H. Jorke and H. J. Herzog. Carrier spilling in spreading resistance analysis of Si layers grown by molecular-beam epitaxy. *Journal of Applied Physics*, 60(5):1735–1739, 1986.

[18] P. J. Severin. Formal comparison of correction formulase for spreading resistance measurements on layered structures. *Spreading Resistance Symposium:NBS Special Publication*, 400-10:27–44, 1974.

[19] J. R. Ehrstein. Spreading resistance measurements:an overview. In D. C. Gupta and P. H. Langer, editors, *Emerging Semiconductor Technology, ASTM Special Technical Publication 960 (ASTM STP 960)*, Philadelphia, PA, 1986. Fourth International Symposium on Semiconductor Processing, 1986, San Jose, California, ASTM.

[20] E. H. Putley. *The Hall effect and semiconductor physics.* Dover, New York, 1968.

[21] Univers. of Athens Solid State Physics Lab. Hall phenomenon - Magnetoresistance measurements. Laboratory documentation for the 4th year Solid State Physics Laboratory experiments(in Greek), 1986.

[22] J. W. Mayer, O. J. Marsh, G. A. Shifrin, and R. Baron. Ion implantation in silicon: Electrical evaluation usimg Hall-effect measurements. *Canadian Journal of Physics*, 45:4073–4089, 1967.

[23] L. Bouro and D. Tsoukalas. Determination of doping and mobility profiles by automatic electrical measurements and anodic stripping. *Journal of Physics E: Sci. Instrum.*, 20:541–544, 1987.

[24] A. C. Bear. Galvanometric effects in semiconductors. In *Solid State Physics*. Academic Press, New York, 1963.

[25] J. Hilibrand and R. D. Gold. *RCA Review*, 21:245, 1960.

[26] N. I. Meyer and T. Guldbrandsen. method for measuring impurity distributions in semiconductor crystals. *Proceedings of the IEEE*, 51:1631, 1963.

[27] B. J. Gordon. A microprocessor based semiconductor measurement system. *Solid State Technology*, 21:43, 1978.

[28] E. H. Nicollian, M. H. Hanes, and J. R. Brews. Using the MIS capacitor for doping profile measurements with minimal interface state error. *IEEE Transactions on Electron Devices*, ED-20:380, 1973.

[29] D. J. Bartelink. C-V Profiling. *Proc. of the Microelectronics Measurement Technology Seminar*, 1979.

[30] W. C. Johnson and P. T. Panousis. The influence of Debye length on the CV measurement of doping profiles. *IEEE Transactions on Electron Devices*, ED-18(10):965–973, 1971.

[31] C. P. Wu, E. C. Douglas, and C. W. Mueller. Limitations of the CV technique for ion-implanted profiles. *IEEE Transactions on Electron Devices*, ED-21(6):319–329, 1975.

[32] K. Ziegler, E. Klausmann, and S. Kar. Determination of the semiconductor doping profile right up to its surface using the MIS capacitor. *Solid State Electronics*, 18:189–198, 1975.

[33] J. R. Brews. Correcting interface-state errors in MOS doping profile determinations. *Journal of Applied Physics*, 44(7):3228–3231, 1973.

[34] B. J. Gordon. On-line Capaitance-Voltage doping profile measurement of low dose ion implants. *IEEE Transactions on Electron Devices*, ED-27(12):2268–2272, 1980.

[35] R. O. Deming and W. A. Keenan. Low dose ion implant monitoring. *Solid State Technology*, 28(12):2268–2272, 1985.

[36] P. J. Holmes. *Electrochemistry of Semiconductors.* Academic Press, London, 1972.

[37] T. Ambridge, J. L. Stevenson, and R. M. Redstall. Applications of electrochemical methods for semiconductor characterization. *Journal of the Electrochemical Society*, 127(1):222–228, 1980.

[38] T. Ambridge and M. M. Factor. An automatic carrier concentration profile plotter using an electrochemical technique. *Journal of Applied Electrochemistry*, 5:319–328, 1975.

[39] C. D. Sharpe and P. Lilley. The electrolyte-silicon interface:anodic dissolution and carrier concentration profiling. *Journal of the Electrochemical Society*, 127(9):1918–1922, 1980.

[40] C. D. Sharpe, P. Lilley, C. R. Elliott, and T. Ambridge. Automatic electrochemical profiling of carrier concentrations in indium phosphide. *Electronic Letters*, 15(20):622–624, 1979.

[41] Y. Arita. Formation and oxidation of porous silicon by anodic reaction. *Journal of Crystal Growth*, 45:383–392, 1978.

[42] P. F. Schmidt and W. Michel. *Journal of the Electrochemical Society*, 104:230, 1957.

[43] J. C. C. Tsai. Shallow phosphorus diffusion profiles in silicon. *Proceedings of the IEEE*, 57:1499, 1969.

[44] J. C. Plunkett, J. L. Stone, and A. Leu. A computer algorithm for accurate and repeatable profile analysis using anodization and stripping of silicon. *Solid State Electronics*, 20:447–553, 1977.

[45] S. M. Davidson. Rapid profile measurements in ion implanted silicon. *Journal of Physics E: Scientific Instruments*, 5:23–26, 1972.

[46] W. K. Hofker. Implantation of boron in silicon. *Phillips Research Reports, Supplements*, (8), 1975.

[47] G. Dearnaley, J. A. Freeman, G. A. Gard, and M. A. Wilkins. Implantation of B into Si. *Canadian Journal of Physics*, 46:587–595, 1968.

[48] N. G. Blamires, M. D. Mathews, and R. S. Nelson. Improved profiles of electrical activity in boron implanted silicon. *Physics Letters*, 28A:178–179, 1968.

[49] O. Cahen and B. Netange. A new method for fast measurement of ion implantation profiles. *Proceedings of the European Conference on Ion Implantation*, page 192, 1970.

[50] W. Kern and D. A. Puotinen. Radiochemical study of semiconductor surface contamination. *RCA Review*, 32:64–87, 1971.

[51] R. P. Donovan and R. A. Evans. Incremental sheet resistivity technique for determining diffusion profiles. *National Bureau of Standards, Special Publication*, SP-337:123–131, 1970.

[52] C. S. Fuller and J. A. Ditzenberger. Diffusion of donor and acceptor elements in silicon. *Journal of Applied Physics*, 27(5):544–553, 1956.

[53] E. Tannenbaum. Detailed analysis of thin-phosphorus diffused in p-type silicon. *Solid State Electronics*, 2:123–132, 1961.

[54] S. M. Sze and J. C. Irvin. Resistivity , mobility and impurity levels in gaAs, Ge and Si at 300°k. *Solid State Electronics*, 11:599, 1968.

[55] D. M. Caughey and R. E. Thomas. Carrier mobilities in silicon empirically related to doping and field. *Proceedings of the IEEE*, 55:2192–2193, 1967.

[56] S. Wagner. Diffusion of boron from shallow ion implants in silicon. *Journal of the Electrochemical Society*, 119:1570, 1972.

[57] R. A. Evans and R. P. Donovan. Alternative relationship for converting incremental sheet resistivity measurements into profiles of impurity concentration. *Solid State Electronics*, 10(1):155–157, 1967.

[58] W. J. Patrick. Mobility in Si epitaxial layers. *Solid State Electronics*, 9:203, 1965.

[59] G. Dearnaley, J. H. Freeman, R. S. Nelson, and J. Stephen. *Ion Implantation.* North Holland, Amsterdam, 1973.

[60] P.H. Ladbrooke. Current spreading at contacts to planar gunn devices. *IEEE Transactions on Electron Devices*, ED-20:56, 1973.

[61] R. Bader and S. Kalbitzer. Carrier concentration profiles of ion-implanted silicon. *Applied Physics Letters*, 16(1):13, 1970.

[62] W. R. Runyan. *Semiconductor Measurements and Instrumentation.* McGraw-Hill, 1975.

[63] H. Frank. Influence of damaged surface layer on resistivity and mobility of thin semiconductor sheets. *Solid State Electronics*, 9:609–614, 1966.

[64] A. Chandra, C. E. Wood, D. W. Woodard, and L. F. Eastman. Surface and interface depletion corrections to free carrier-density determinations by Hall measurements. *Solid State Electronics*, 22:645–650, 1979.

[65] A. Many, Y. Goldstein, and N. B. Grover. *Semiconductor Surfaces.* North Holland, Amsterdam, 1965.

[66] Y. K. Yeo, R. L¿ Hengehold, and D. W. Elsaesser. Surface-depletion effect correction to nonuniform carrier distributions by Hall measurements. *Journal of Applied Physics*, 61(11):5070–5075, 1987.

[67] N. D. Young and M. J. Height. Automated Hall effect profiler for electrical characterization of semiconductors. *Electronic Letters*, 21:1044, 1985.

[68] S. R. Blight, R. E. Nicholls, S. P. S. Sangha, P. B. Kirby, L. Teale, and al. Automated Hall profiling system for the characterization of semiconductors at room and liquid nitrogen temperatures. *Journal of Physics E: Scientific Instrumentation*, 21:470–479, 1988.

Chapter 5

Physical Dopant Profiling Methods

5.1 The objective.

Materials characterisation performed by use of electrical measurements can at best provide information regarding electrical activity of the various layers and interfaces. In contrast, analytical techniques can directly measure fundamental semiconductor properties such as doping level, point defect density, chemical composition and interface density.

The final circuit and device characteristics are indisputably electrical-activity-dependent. Therefore, the determination of the carrier profile with depth is essential. However, the as-implanted dopant distribution with depth can be of particular importance. The absolute value of the retained dose(not the activated dose), the level of activation of the implanted ions, the compensation effects between donor and acceptor impurities and the effect of the presence of ions at concentrations above the solid solubility limit on the diffusion constants of the implanted ions are some of the areas where surface analysis techniques can prove invaluable.

In this chapter the main impurity depth profiling techniques will be compared. However, only Secondary Ion Mass Spectroscopy will be covered in detail since the technique has been used in the experimental work of this project. The emphasis is on the role of the physical profiling methods for VLSI and ULSI applications.

Their specific characteristics and their sensitivity, accuracy and resolution will be compared. The question to be answered will be if they can be used for on-line monitoring after any ion implant step.

5.2 Introduction.

Depth distribution analysis of chemical composition is a special case of microlocal analysis and requires the compositional analysis of thin layers (ultimately mono atomic layers) defined on a depth scale. While a variety of these surface sensitive techniques use photons or electrons to produce the analytical signal, they rely on an energetic ion beam to probe the sample surface. Both destructive and non-destructive techniques can give that information.

1. **Destructive techniques.** In those techniques, material removal has to take place. Such techniques comprise mechanical sectioning(either ball cratering or tapered sectioning) or chemical sectioning (ie electrochemical polishing [1]) with subsequent chemical analysis of the removed material. However, the lack of control of surface reactions between consequent steps limits the depth resolution to about 10nm. *In situ* use of ion sputtering for surface erosion in combination with any surface analysis technique, has enhanced the depth resolution [2, 3]. In sputtering, the sample is bombarded by ions which are accelerated to a typical energy of 0.5-5keV. The transfer of a small fraction of that energy to surface atoms, causes them to leave the sample. The different categories of sputtering are summarized in Table 5–1. Consequent analysis of the abraded sample or of the residual surface reveals the concentration profile. Secondary ion mass spectroscopy (SIMS), Auger electron spectroscopy (AES), X-ray fluorescence spectroscopy (XPS) and electron spectroscopy for chemical analysis (ESCA) are the most common techniques.

2. **Non-destuctive techniques.** The impinging beam of ions generates the analytical signal. A well-defined dependence exists between the analytical

Sputtering categories			
Categories	**Definitions**	**Modes**	**Definitions**
Physical	Incident ion energy transfer to the target atom resulting in its ejection.	**knock-on**	Ion energy transfer after after one or a just a few collisions.
		linear cascade	Higher amount of energy is transferred causing recoil cascades.
		spike	larger density of recoiled atoms.
Chemical	Formation of metastable compound at the target surface.		

Table 5–1: The general categories of sputtering from primary ion beams. Subsequent classification of physical sputtering takes in account the number of target atoms involved.

signal measured and its depth of origin. The concentration profile is thus obtained without any erosion of the target. Such methods include ion scattering spectroscopy (ISS) and Rutherford backscattering spectroscopy (RBS).

5.3 Secondary Ion Mass Spectroscopy (SIMS)

5.3.1 Principles, instrumentation and operation.

In secondary ion mass spectrometry (SIMS) the sample is maintained in a vacuum chamber and bombarded by a monoenergetic beam of primary ions. As a result, particles are sputtered from the sample surface, some of which are in the form of secondary ions. The principle of the method is graphically depicted in fig.5–1 and is summarized in the following subsections. Of interest to SIMS is not just the ejection of target atoms but the subsequent ionization, either positively or negatively, of these species. This ionization process can be divided into two

general categories: (1) ionization internal to the target and (2) external processes. Internal ionization involves breaking of the bonds by the primary ion followed by emission of charged species. Most other mechanisms are considered external ionization resulting from processes such as Auger or resonant interaction between the sputtered atom and the sample surface. In order to optimize the sensitivity of SIMS, one wishes to maximize the sputtered ion yield. This is achieved by using either an electronegative (ie oxygen) or electropositive (ie cesium) species as the bombardment ion. The information collected is a curve of ion current against time where the ion current is related to the m/e ratio of the impurity diffused in the sample. In order to obtain the desired depth concentration profile two steps have to be taken:

1. **Depth standardization.** The 'erosion rate' of the surface of the sample has to be accurately measured.

2. **Concentration standardization.** By having a standard sample in which the impurity has the same chemical environment as the analyzed sample and an accurately measured concentration (using another method) the ion current scale can be converted into a concentration scale.

5.3.2 Elemental depth concentration profiling

Depth profiling represents the most important application of SIMS for semiconductor materials.

5.3.2.1 The technique.

For a depth profile, a fast sputter rate is needed. This is achieved by employing a focused ion beam of high primary ion current density. In order to prevent the collection of ions from the sloping crater walls, the primary ion beam is scanned over a large area (about 5 times the beam diameter). A sputtered crater is thus formed. By limiting the acceptance area of the mass spectrometer to the central portion of the crater, contributions from the crater walls are minimized. Other

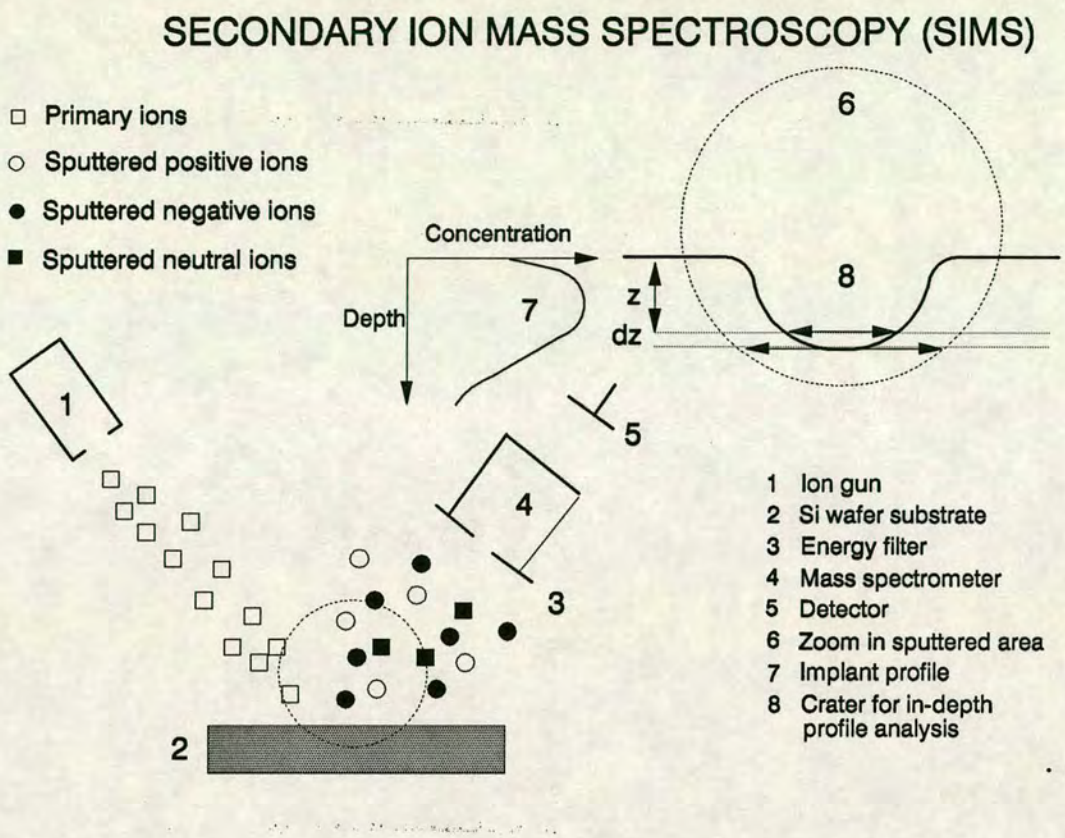

Figure 5–1: A schematic of the depth profiling SIMS configuration.

approaches to produce a well-defined area of uniform current density without distortions from the crater walls [4, 5] place too much demand on the focusing quality and stability of the primary beam and never completely remove the edge contribution. The crater formation technique of the sputtering and depth profiling process is schematically depicted in fig. 5–1. The spectral overlaps acceptance area of the mass spectrometer is limited to the central portion of the crater by the use of an electronic aperture, [6].

The scale measurement circuitry is coupled to the scan voltage so that it is activated only when the beam strikes a small central part of the crater. Reducing the aperture of the mass spectrometer limits the number of accepted ions and therefore reduces the measured signal. As the sputtering process proceeds, the buried interface is exposed and detected as a rectangular peak. The abscissa can be converted into a depth scale by calibrating the sputtered crater with a profilometer.

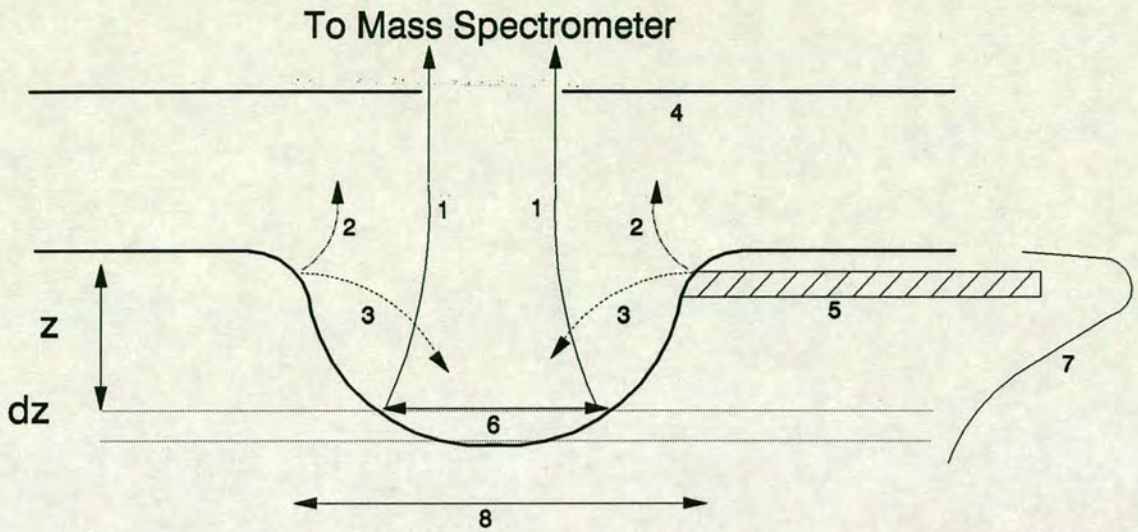

Figure 5–2: A schematic representation of the main effects that limit the dynamic range of the depth profiling SIMS configuration.

5.3.2.2 Dynamic range.

The dynamic range obtained by SIMS can vary from three to six decades. Some of the effects are shown in fig. 5–2.

1. **Memory effect.** Sputtered material is deposited onto nearby surfaces, especially from the upper part of the crater's wall. The extraction lens, which is placed as close as possible to the target for higher extraction efficiency, is mostly susceptible to that effect. As it approaches the sample the amount of deposited material on the lens increases. Therefore a tradeoff between dynamic range and detection sensitivity always has to be made.

2. **Redeposition.** Material from the crater edge can be sputter-deposited over the analyzed area, A_e, in the center of the crater and resputtered again, thus contributing to the detected signal. If this material comes from a high

concentration region (ie from near the peak depth of the implant) it increases the background signal and therefore narrows the dynamic range. A larger crater area, A_b, might help to reduce this effect.

3. **Neutral component of the primary beam.** Charge exchange collisions within the beam produce a neutral component in the primary ion beam which cannot be focused and therefore bombards an area bigger than A_e. If this area is within the spectrometer field of view -which is usually the case- it will contribute to the signal when the electronic gate is open. The only way to avoid it is by having the electrostatic deflection of the primary beam as close as possible to the substrate, in order to eliminate the possibilities of neutralization of the primary beam and to ensure that only ions strike the sample.

4. **The ion implant dose.** The lower detection limit is around 10^{15}atoms/cm^3 so for low doses where the peak value does not exceed 10^{17}ions/cm^3, the dynamic range is restricted [7].

5.3.2.3 Detection limits and sensitivity

SIMS's elemental detection sensitivity has been discussed in terms of theoretical expectations and experimental measurements by various researchers [8, 9].

The minimum detectable level of an element in a given sample depends on:

- the element characteristics
- the primary ion species
- the total primary current deliverd to the target
- the solid acceptance angle
- the analyzer's efficiency for secondary ions
- the general background produced by the analyzer
- the secondary ion detector background
- the secondary ion detector efficiency

- the chemical composition of the matrix in which the element is present

In theory, optimization for high sensitivity can take place through control of all but the first two parameters through instrument design. There are various factors that can reduce the detection limit:

1. **Chemical composition of the sample matrix.** It has a direct and uncontrollable effect in detection sensitivity through two mechanisms. It can be the source of unwanted molecular and multiply-charged ion species that appear at mass positions of interest (see next paragraph) and it influences the secondary yield through differences in the electronic properties of the materials.

2. **Spectral overlaps.** Molecular ion interferences can be controlled by two methods: analyze secondary ions with high initial energy and/or employ a m/e analyzer with a resolution over 3000. By using the first method, the ion yield is reduced by the same amount as the reduction in molecular ion yield relative to atomic ion yield. This, however, leads to large reduction in detection sensitivity. Therefore, the second method is more desirable from the analytical standpoint. The most common spectral overlap occurs while analyzing As in Si when molecular ions like $^{30}Si^{29}Si^{16}O^{+}$ with m/e=75 interfere with the As signal. Their discrimination can be achieved by using a bias potential for the sample. P of m/e=31 is overlapped by $^{30}Si^{1}H$. Only a high resolution mass spectrum at m/e=31 (ie $M/\Delta M = 5000$) would clearly show the separation of the two peaks [10].

5.3.2.4 Profile depth resolution.

One of the main problems of ion erosion is the depth resolution. The loss of resolution with depth can be expressed, [11,12] as:

$$\Delta z = \alpha + \beta z^{\gamma} \tag{5.1}$$

where z denotes the depth, Δz the depth dispersion and α, βamdγ are constants.

(a) Instrumental factors.

Primary ion beam inhomogeneity. In order to extract meaningful depth profile information from SIMS data we should maintain a constant primary ion current and uniform primary ion current density over the central part of the crater(where secondary ions are extracted) during the raster sweep [13,14]. Instrumental factors connected with the beam sweep system(x and y sweep voltage time-linearity, individual trace overlapping depending on beam dimensions, etc) have to be well designed. Depth resolution, Δz, increases with sputtered depth z but the relative depth resolution, $\Delta z/z$, is constant and equal to a few % [15].

Sputtering conditions. The important factors that determine the relative ranges of particles in a given film are the projectile particle energy, the angle of incidence of the primary ion beam on the surface and the atomic number and mass of both projectile particle and target atom. Higher energy values lead to increased recoil or knock-on mixing in subsurface layers and would therefore show a more pronounced profile tail [16]. Contraction of the zone of mixing occurs for angles of incidence further away from the normal to the sample surface(increase of the ion penetration depth). Increased primary ion mass also leads to profile broadening [14].

(b) Ion-matrix effects. The characteristics of the collision cascade that is induced in the target by the incident ion has direct impact on the profile distortion [13,14].

Atomic mixing in subsurface layers. Collision cascade mixing broadens both leading and trailing edges of the profile [17]. Recoil implantation (where incoming ions knock-on dopant atoms in the forward direction),[18], collapse of defects in dislocation loops (thus producing local variation of the sputtering yield),[19] and radiation-enhanced diffusion(where vacancy and/or interstitial assisted diffusion takes place in the ion-damaged region) are the principal underlying mechanisms [20].

Crystal orientation. The sputtering yield and the erosion velocity [21] depend on the target crystal orientation.

(c) **Initial surface roughness.** Initial surface roughness can induce the formation of cones and can cause non-uniform erosion [22,23]. The substantial influence of the initial surface roughness on depth resolution has been verified experimentally [24,25].

(d) **Reactive element presence.** The presence of reactive elements such as H, C, N and O enhance the secondary ion yield and thus affect the technique's accuracy for the first 10-30 Å.

(e) **Native oxide presence.** An effect that complicates the depth profile analysis is connected to the presence of adsorbed and reacted surface oxygen [26]. The resulting chemical enhancement of secondary ion yield at the surface prevents an accurate ion intensity measurement within the first few Å from the surface.

(f) **Dynamic implantation range effect.** At the initiation of the sputtering process the projected range of the primary oxygen [1] occurs at a depth of a few hundred Å below the surface. Therefore, significant enhancement of the secondary ion yield does not occur until the sputtering front reaches the depth where the oxygen concentration is high enough for the chemical emission ion production mechanism to predominate over kinetic emission [27]. After the peak concentration value of primary oxygen is reached, the secondary ion count reaches a steady-state oxygen-enhanced value and the concentration profile is accurate. This problem can be overrided if a thin surface oxide is produced by controlled oxygen flooding [28], oxygen ion bombardment or high oxygen pressure [27,26].

---

[1] Oxygen (electronegative) is used as the bombarding element to enhance the formation of positive ions. Therefore, high sensitivity for the detection of electropositive elements (p-type implants) can be achieved.

(g) Bombardment-induced roughness. A non-amorphized surface region can lead to primary beam channeling [29,30]. This in effect results in uneven sputtering and therefore promotes the development of surface roughness (ie cone and ridge formation). Formation of an oxide surface layer by using one of the above mentioned methods eases the situation.

(h) Primary ion induced profile distortion.

Redeposition effect. Profile depth resolution is directly effected by the redeposition effect (see section above) which mostly distorts the low concentration tail of the profile [31,28].

Memory effects. Memory effects and adsorption of gas phase impurities also significantly distort profiles at low concentration levels.

In order to avoid serious error during depth profile measurements especially errors resulting from secondary ion yield enhancement, it has become common practice to obtain a normalization signal [32]. This is achieved by monitoring an ion species of the matrix. In order to have reliable results, the species chosen for the monitoring is ^{28}Si which gives a fairly strong signal.

5.3.3 Retrospective depth profiling.

Three dimensional SIMS analysis of materials [33] will inevitably find increasing applications particularly in ULSI applications. SIMS analysis can detect trace elements at concentrations below 1ppb, with an ultimate depth distribution of a single monolayer and a lateral resolution of 50nm. These three limits of detection, depth resolution and lateral resolution cannot be achieved simultaneously since they are inter-dependent. However, a 3-D SIMS imaging system [34] can give the optimum compromise. A central feature of such a system is the capability for retrospective depth profiling [35]. This technique makes it possible to extract a depth profile of a chosen area from a previously acquired three-dimensional stack of images [36,34]. A sequence of two dimensional images is taken at increasing

depths from the original surface. The retrospective choice of gated area from which the depth profile is detected, allows the detection limit to be optimised.

5.4 Auger Electron Spectroscopy (AES)

5.4.1 The nature of the technique

The analytical signal, the Auger electron, is emitted in a three electron process as the material is bombarded with a beam of E_P electrons, typically in the 5-10keV energy range. This causes a core level ionization process resulting in the emission of a core electron of E_K energy. The excess energy is utilized by the decay of a higher energy E_{L1} electron to fill the vacancy. At this point two processes may occur. The energy of the transition, $E_K - E_{L1}$, may be released as a photon whose energy is characteristic of the element from which it originates. This process is called fluorescence and forms the basis of X-ray fluorescence spectroscopy(XFS). The energy might also be transferred to another electron (ie of the L_2 level) which is then ejected from the atom as an Auger electron if the energy is bigger than its binding energy. Several such Auger transitions ($KL_1L_1, KL_1L_2, KM_2M_4$ etc) can occur with various transition probabilities. The kinetic energy of the Auger electron from an XYZ transition may be estimated from the empirical relation:

$$E_{XYW} = E_X(Z) - E_Y(Z) - E_W(Z + \Delta) - \phi_A \tag{5.2}$$

where Z is the atomic number of the atom involved, E denotes the binding energy values, ϕ_A represents the work function of the analyzer material and the term Δ accounts for the higher energy level of the doubly ionized state as compared to the sum of energies for individual ionization of the same levels.

5.4.2 Depth profiling using AES.

The basic instrumentation requirements for AES include an electron gun for target excitation, an ion gun for in-depth profiling measurements, a manipulator for

positioning the sample and an electron spectrometer for energy analysis of the emitted electrons. A review of the AES for studying interfaces can be found in [37–43]. Since contamination of the surface during the analysis has to be avoided,[44, 45], ultra high vacuum conditions are needed. For typical measurement times of 100s the partial pressure of reactive gases (ie CO, H_2O, C_xH_y) should be below 10^{-10} torr while inert gases pressure can be several orders of magnitude higher. The vacuum requirements are not as stringent (10^{-7}torr) for profile measurements due to ion sputtering of the surface by the Ar ion beam.

Some of the factors that affect the depth resolution during AES profiling are ion beam uniformity across the sample area, the Auger electron escape depth and sample inhomogeinity. The small depth from which the Auger electrons originate (less than 20 Å) gives AES an excellent depth resolution. However, the ion beam sputtering for profile extraction reduces the final depth resolution.

The spatial resolution can be as low as 50nm if a higher degree of focus can be attained in the bombarding electron beam.

As it is also the case for SIMS, the sensitivity decre ases as the lateral resolution or the depth resolution are increased. The AES sensitivity also depends on the excitation current level.

5.5 Rutherford Backscattering Spectroscopy

5.5.1 Nature of the technique

RBS is a semi-nondestructive technique for measuring elemental profiles [46] and crystal perfection [47]). The sample is bombarded with light ions, usually He, at energies of a few MeV. Any ions that are backscattered undergo energy analysis in order to determine the atom responsible for the scattering and the depth below the surface at which the atom is located. The incident beam loses energy on the way into the sample, during scattering and on the way out of the sample. The atoms close to the surface contribute to the high energy profile since scatter is minimal.

Lower energy particles come from various depths below the surface. Since the energy loss provides the depth scale, no sputtering is required. Therefore, side effects like preferential sputtering, knock-on and atomic mixing are eliminated. However, profile information is more difficult to extract than for SIMS since the information concerning both elemental identification and depth must be extracted from a single energy. Therefore, signal overlaps from deeper depths and mass information are areas where problems may occur. Better results can be obtained from the combination of sputtering with RBS [48].

5.5.2 Assessment of the technique

The measured signal from a particular element depends on the ion flux, the analysis area, the cross-section, the volume concentration, the depth resolution, the acquisition time and various geometrical factors. Sensitivity, spatial resolution, depth resolution and signal acquisition time are inter-related.

The depth resolution is limited by the energy resolution of the detector and the geometry in the experimental set-up. Resolutions as low as 50 Å range can be achieved by using small exit angles. However, the analysis depth for such a configuration is limited.

The spatial resolution is mainly limited by the beam size which is several millimeters [2]

The sensitivity in a Si substrate depends on the atomic number of the element being detected; the heavier the mass of the impurity, the higher the achieved sensitivity. Volume sensitivity for heavy mass elements is around 10^{18} to 10^{19}cm^{-3}. For low mass impurities (B, F) the technique has very low sensitivity.

The main advantages of the technique are its non-destructive testing capability and the possibility of obtaining both atomic and damage profiles from channeling

---

[2]Focused systems with beam sizes in the micron range exist but are not routinely produced.

experiments. The increased cost of high energy particle accelerator, the expertise needed to obtain an optimum system configuration for each element type and implant profile, the poor sensitivity to low mass impurities and the induced crystal damage from He beams a few microns in diameter are drawbacks that prevent RBS from becoming an on-line monitoring tool.

5.6 Comparison

5.6.1 Sputtering rate standardization.

For the destructive measurements the calibration of the depth from the sputtering rates is difficult as it involves typically a range of $10^2 - 10^3$Å (for ULSI). Crater depths are usually determined after the end of the analysis by light optical interferometry or mechanical stylus techniques eg Dektak. For very shallow implants, deeper craters are produced for the depth calibration purpose and furthermore a **linear** relation between sputter rate and depth is assumed. The accuracy of the calibration of the depth scale is therefore under question and other parameters such as uniformity of the sputtering rate and crater flatness do not play a protagonistic role in the measurement error -as opposed to the theory predictions and consults-. This problem is aggravated if rapid concentration transitions occur. Those increase the nonlinearity between sputtering rate and depth. The only desirable method for depth calibration would be a continuous monitoring of the sputtering rate. This would mean an on-line monitoring of the re-deposition rate of the sputtered material.

5.6.2 General comments

For the first 20 Årange both SIMS and AES can be in error for the measured concentration values. SIMS is very sensitive to the presence of a native oxide layer and gives a higher concentration value than the true one. AES is affected by

interference from hydrocarbons and the resulting signal attenuation gives a lower concentration value.

Up to a depth of a few nanometers, AES is very accurate due to the one-to-one relation between signal level and concentration value. SIMS underestimates concentration values due to a decrease in oxygen concentration. This inaccuracy can be reduced by the techniques described in section 5.3.2.4.

The main advantages of AES are its good spatial and depth resolution and its sensitivity to both light and heavy elements. However severe limitations due to the sputtering implications (ion beam damage, matrix effect, preferential sputtering etc), UHV vacuum operation requirements, high cost and system operator experience keep the technique away from a manufacturing environment for routine profile analysis.

For SIMS analysis the standardization sample may not be very homogeneous. Heterogeneity errors may therefore arise, but their order of magnitude is less than the depth standardization errors [28].

Higher sensitivities obtained by SIMS are achievable only on a small number of expensive, dedicated, high-performance and guru-driven instruments and not by the low cost, massively marketed ones. Bearing in mind operation skills, data quantification complexity and capital equipment cost it is unlikely that they will be adopted for on-line profile monitoring in production environments.

The chemical sensitivity of all the electron probe techniques is below the sub-ppm region. This level corresponds to impurity doping levels which are crucial for the electrical behaviour of ICs. SIMS has an inherent high sensitivity reaching 1 part in 10^9 for the Si important impurities. The limit of its sensitivity is imposed mostly by the vacuum environment, the spectrometer efficiency and the ion yield.

The non-destructive nature of the AES analysis offers several possibilities to the user. Bystoppingthe ion gun action, no sputtering takes place and a complete spectral analysis correlating as many elements as desired at a specific depth can be performed. From another point of view the inclusion of a sputtering gun as an accessory The inherent depth profiling of the SIMS analysis does not normally

permit such analysis even at very low sputter rates. They are limited to measure one mass at a specific level using magnetic mass analyzers. For another mass the magnetic field has to change and during the changeover time the depth can change. Reducing the sputter rate is not feasible since recontamination of the surface and increase of the background signal would reduce the sensitivity. Multiple ion detection mass spectrometers introduce other instrumentation problems and on balance do not offer a better solution.

5.6.3 Conclusions

Requirement for surface analysis techniques is clear and they can offer good depth resolution and sensitivity. The main characteristics of the major surface analysis techniques are presented in Table 5.6.3. However, mainly due to cost, set-up and operating requirements, such techniques are very difficult to implement for on-line monitoring. Furthermore, in order to accommodate the increased spatial and depth resolutions of ULSI applications, the user of surface analysis techniques faces:

1. Further reduction of the small area probed by the beam.

2. Severe signal reduction from those small probed areas.

3. Modification of the sample by the probing beam especially for characterization of small areas.

Table 5.2: Comparison of Physical Profile Techniques

#	**Techniques** / *Characteristics*	**SIMS**	**AES**	**SAM**	**ESCA(XPS)**	**RBS**	**ISS**	**NAA**
1	*Incident Beam*	ions	electrons (0.1-5keV)	electrons (0.1-5keV)	X-ray or U-V photon	HE^+ 2-6MeV	ions (0.2-2keV)	neutrons
2	*Emitted Particles*	secondary ions	Auger e	Auger e	photo-electrons	backscattered He^+, He^{++}	scattered ions	neutrons
3	*Destructive*	yes	yes	yes	yes	no	no	no
4	*Lateral Spatial Resolution*	$2\mu m$	$50nm - 1\mu m$	$50nm - 1\mu m$	$150\mu m$ – 1mm	1mm	$1 - 100\mu m$	1cm
5	*In-depth Resolution*	50 Å	20 Å	20 Å	20 Å	20 Å	50 Å	$1\mu m$
6	*Depth Information*	3nm	1-20nm	1-20nm	0.5-2nm	$1\mu m$ top exposed layer	50 Å	1 μm
7	*Detectable Elements*	H-U	Li-U	Li-U	Li-U	He-U	Li-U	Li-U
8	*Detection Limit* (in atoms/cm^3)	$5 \times 10^{15} - 5 \times 10^{18}$	5×10^{19}	1×10^{21}	5×10^{19}	5×10^{18}	1×10^{19}	$5 \times 10^{11} - 5 \times 10^{18}$
9	*Detection sensitivity* (in ppm)	0.1 -100	1000	20,000	1000	1000	1000	0.00001-100
10	*Probe diameter (in μm)*	10^3	25 - 100	4 - 15	10^4	10^3	10^3	10^4

Bibliography

[1] L. P. Erickson, A. Waseem, and G. Y. Robinson. Characterization of ohmic contacts to InP. *Thin Solid Films*, 64:421–426, 1979.

[2] P. H. Holloway. Characterization of electron devices and materials by surface-sensitive analytical techniques. *Applied Surface Science*, 4:410–444, 1980.

[3] S. A. Schwartz, C. R. Helms, W. E. Spicer, and N. J. Taylor. High resolution Auger sputter profiling study of the effect of phosphorus pileup on the $Si - SiO_2$ interface morphology. *Journal of Vacuum Science and Technology*, 15:227–230, 1978.

[4] J. W. Guthrie and R. S.Blewer. Improved tuning of ion microprobes. *Rev. Sci. Instrum.*, 43:654, 1972.

[5] R. S. Blewer and J. W. Guthrie. Means of obtaining uniform sputtering in an ion microprobe. *Surface Science*, 32:743, 1972.

[6] H. Liebl. Secondary ion mass spectrometry and its use in depth profiling. *Journal of Vacuum Science and Technology*, 12:385–391, 1985.

[7] R. L. Cochran. Fast atom bombardment/mass spectrometry (FAB/MS) and its industrial applications. *Applied Spectroscopy Review*, 2:137–187, 1986.

[8] H. W. Werner, editor. *Diagnostic techniques for microelectronic materials, processes and devices.* NATO Advanced Study Institute Series. 1986.

[9] A. Benninghoven. Observations of surface reactions by statical method of secondary ion mass spectroscopy. *Surface Science*, 28:541, 1971.

[10] W. Katz and G. A. Smith. Materials characterization using Secondary Ion Mass Spectrometry (SIMS). *Scanning Electron Microscopy*, IV:1557–1566, 1984.

[11] S. Hofmann. Quantitative depth profiling in surface analysis: a review. *Surface and Interface Analysis*, 2(4):148–160, 2.

[12] P. Laty, D. Seethanen, and F. Degreve. Microroughness induced on solids by ion bombardment. *Surface Science*, 85(2):353–364, 1979.

[13] W. K. Hofker, H. W. Werner, D. P. Oosthoek, and H. A. M. deGrefte. Influence of annealing on the concentration profiles of boron implantations in silicon. *Radiation Effects*, 17:83, 1973.

[14] F. Schulz, K. Wittmaack, and J. Maul. Implications in the use of secondary ion mass spectroscopy to investigate impurity concentration profiles in solids. *Radiation Effects*, 18:211, 1973.

[15] G. Blaise. Concerning the problem of high depth resolution using ion sputtering. *Scanning Electron Microscopy*, I:129–137, 1986.

[16] J. A. McHugh. Ion beam sputtering- The effect of incident ion energy on atomic mixing in subsurface layers. *Radiation Effects*, 21:209, 1974.

[17] K. Wittmaack and R. Wach. Profile distortion and atomic mixing in SIMS analysis using O primary ion beam. *Nuclear Instruments and Methods*, 191:327–334.

[18] U. Littmark and W. O. Hofer. Recoil mixing in high fluence ion implantation. *Nuclear Instruments and Methods in Physics Research*, 170(1-3):177–181, 1980.

[19] N. Hermanne. A necessary condition for the appearance of damage-induced surface topography during particle bombardment. *Radiation Effects*, 19(3):161–169, 1973.

[20] Z. L. Liau, B. Y. Tsaur, and J. W. Mayer. Influence of atomic mixing and preferential sputtering on depth profiles and interfaces. *Journal of Vacuum Science and Technology*, 16(2):121–127, 1979.

[21] G. Blaise. *Fundamental aspects of ion microanalysis. Material characterization using ion beam.*, volume Series B Physics 28 of *NATO Advanced Study Institute Series*, pages 143–238. 1978.

[22] U. Littmark and W. O. Hofer. The influence of surface structures on sputtering:anular distribution and yield from faceted surfaces. *Journal of Material Science*, 13:2577–2586, 1978.

[23] G. Carter amd B. Navinsek and J. L. Whitton. Heavy ion sputtering induced surface topography development. In R. Behrisch, editor, *Sputtering by ion bombardment II*, pages 231–269. Springer-Verlag, Berlin, 1983.

[24] S. Hofmann, J. Erlewein, and A. Zalar. A depth resolution and surface roughness effects in sputter profiles using AES. *Thin Solid Films*, 43:275, 1977.

[25] H. J. Mathieu, D. E. McClure, and D. Landolt. Influence of ion bombardment on depth resolution in Auger electron spectroscopy analysis of thin gold film on nickel. *Thin Solid Films*, 38:281, 1976.

[26] R. K. Lewis, J. M. Morabito, and J. C. C. Tsai. Primary oxygen ion implantation effects on depth profiles by secondary ion emission mass spectrometry. *Applied Physics Letters*, 23:260–262, 1973.

[27] G. Slodzian and J. F. Hennequin. *C. R. Acad. Sci.*, B 263:1246, 1966.

[28] B. Blanchard, N. Hilleret, and J. B. Quoirin. Application of ionic microanalysis to the determination of boron depth profiles in silicon and silica. *Journal of Radioanalytical Chemistry*, 12:85–94, 1972.

[29] L. Francken and D. Onderdelinden. Influence of planar channelling on single crystal sputtering. pages 266–277, Amsterdam, London, New York, 1970. Proc. Int. Conf. Atomic Coll.Phen. in Solids, Brighton 1969, North Holland.

[30] D. Onderdelinden. Single-crystals sputtering including the channelling phenomenon. *Canadian Journal of Physics*, 46:739–745.

[31] M. Croset. Quantitative analysis of boron profiles in silicon using ion microprobe mass spectrometry. *Journal of Radioanalytical Chemistry*, 12:69–74, 1972.

[32] J. M. Morabito. Materials characterization by SIMS. *Analytical Chemistry*, 46:189, 1974.

[33] F. G. Rudenauer. Spatially multidimensional SIMS analysis. *Surface and Interface Analysis*, 6:132–139, 1984.

[34] S. R. Bryan, W. S. Woodward, D. P. Griffis, and R. W. Linton. Secondary ion mass spectroscopy/digital imaging for three dimensional characterization of solid state devices. *Journal of Vacuum Science and Technology*, A3:2102–2107, 1985.

[35] D. R. Kingham, A. R. Bayly, D. J. Fathers, P. Vohralik, J. M. Walls, and A. R. Waugh. Three dimensional secondary ion mass spectrometry imaging and retrospective depth profiling. *Scanning Microscopy*, 1(2):463–469, 1987.

[36] A. J. Patkin and G. H. Morrison. Secondary ion mass spectrometric image depth profiling for three dimensional elemental analysis. *Analytical Chemistry*, 54:2–5, 1982.

[37] R. Rye, T. E. Madey, J. E. Houston, and P. H. Holloway. Chemical state effects in aes. *Journal of Chemical Physics*, 69(4):1504–1512, 1978.

[38] T. E. Gallon and J. A. D. Matthew. *AES and its applications to surface studies.*, volume Vol.3 #1 of *Review of Physics in Technology*, pages 31–64. 1972.

[39] M. Thompson. *Applications of Auger Electron Spectrometry.*, volume 24. Pergamon Press, 1977.

[40] J. T. Grant. *Surface analysis with Auger Electron Spectroscopy.*, volume 13 of *Applications of Surface Science.* 1982.

[41] P. H. Holloway. Application of Surface Analysis for electronic devices in applied surface analysis. *ASTM STP.*, 699:5–23, 1978.

[42] P. H. Holloway and G. E. McGuire. *Characterization of electronic devices and materials.*, volume 4 of *Applications of Surface Science*, pages 410–444. 1980.

[43] Observation of impurity profile in ion implanted silicon by Auger Electron Spectroscopy. In *Japanese Journal of Applied Physics*, volume Suppl.2 Pt.2, pages 819–822. Proc. of the 2nd Int. Conf. on Surfaces, 1974, 1974.

[44] S. Hofmann. In A. Benninghoven, J. Giber, J. Lazlo, M. Riedel, and H. W. Werner, editors, *Proc. of the Third Intern. Conference on SIMS (Budapest1981)*, page 186, Berlin, 1982. Springer Verlag.

[45] J. W. Coburn. Sputtering in the surface analysis of solids: A discussion of some problems. *Journal of Vacuum Science and Technology*, 13:1037, 1976.

[46] W. K. Chu, J. M. Mayer, and M. A. Nicolet. *Backscattering Spectrometry.* Academic Press, New York, 1978.

[47] L. C. Feldman, J. M. Mayer, and S. T. Picraux. *Materials analysis by ion channeling.* Pergamon Press, New York, 1982.

[48] K.Wittmaack and N. Menzel. Significantly extended analytical potential of Rutherford backscattering spectrometry by in situ combination with low energy sputtering. *Applied Physics Letters*, 53:1708, 1988.

Chapter 6

Pattern etch transfer technique

The objective of the Pattern Etch Transfer (PET) technique is to create a number of rectangular trenches of increasing depth into silicon, by use of a single photolithography step. The trenches are first patterned into photoresist by variation of the exposure time for each trench. Reactive Ion Etching (RIE) is then used to transfer those trenches into silicon, by a simultaneous etch of the photoresist and the Si substrate [1]. Implant damage or dopant profiles can then be obtained from mesurements performed on the flat silicon surface at the bottom of each trench.

A schematic representation of the PET technique is depicted in fig. 6–1. A low-gamma photoresist is spun on the Si wafer. An optical stepper [1] is used to expose the photoresist. For quick throughput the area of the trench is defined by the framing blades of the stepper.

The number of trenches and their position on the wafer can be defined in the stepper run file. Increasing exposure time for each trench is used to give an exposure matrix. The initial exposure time and the time increment between neighbouring trenches are also defined in this run file. Process parameters for a specific resist and developer are optimized for uniformity of depth inside the trench and the lowest possible contrast for the photoresist/developer combination.

---

[1] An 8010 Optimetrix optical stepper with a 10X reduction was used for this work but almost any stepper can be programmed to perform the PET exposure sequence.

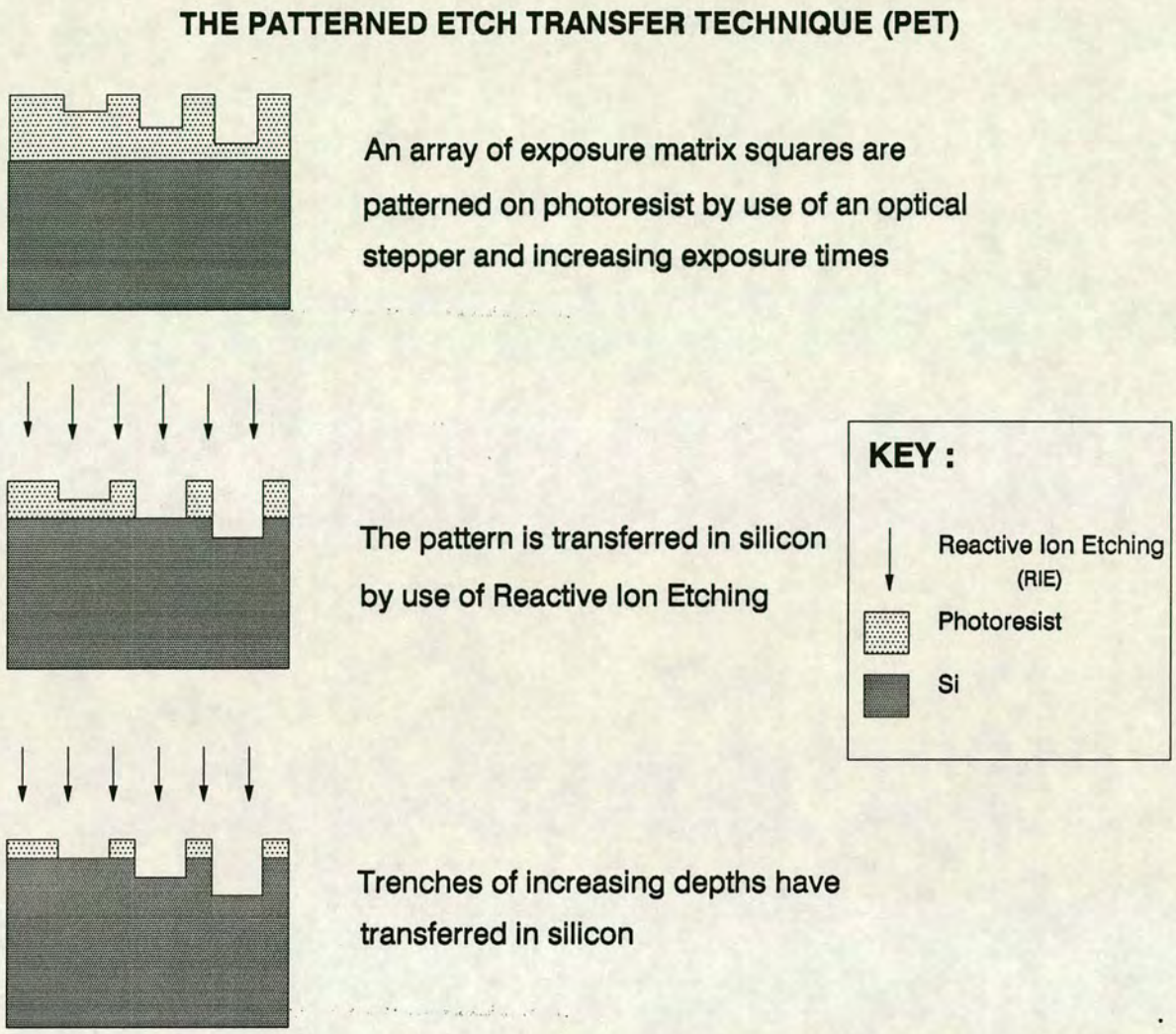

Figure 6–1: A schematic representation of the PET technique implementation.

To implement the above idea, a low γ photoresist should be used to obtain better control over the trench depths by variation of the exposure time, as it will be explained later in this chapter.

Reactive Ion Etching (RIE) is used to transfer the pattern from the photoresist to the Si wafer. CF_4 and O_2 in the plasma simultaneously etch the photoresist and the Si substrate. The RIE process parameters (power, pressure, total flow rate, temperature and gas mixing ratio) have to be optimized to minimize RIE-induced damage and give low selectivity etching. The exposure matrix pattern is thus transferred to the Si wafer, and wells of various depths are formed.

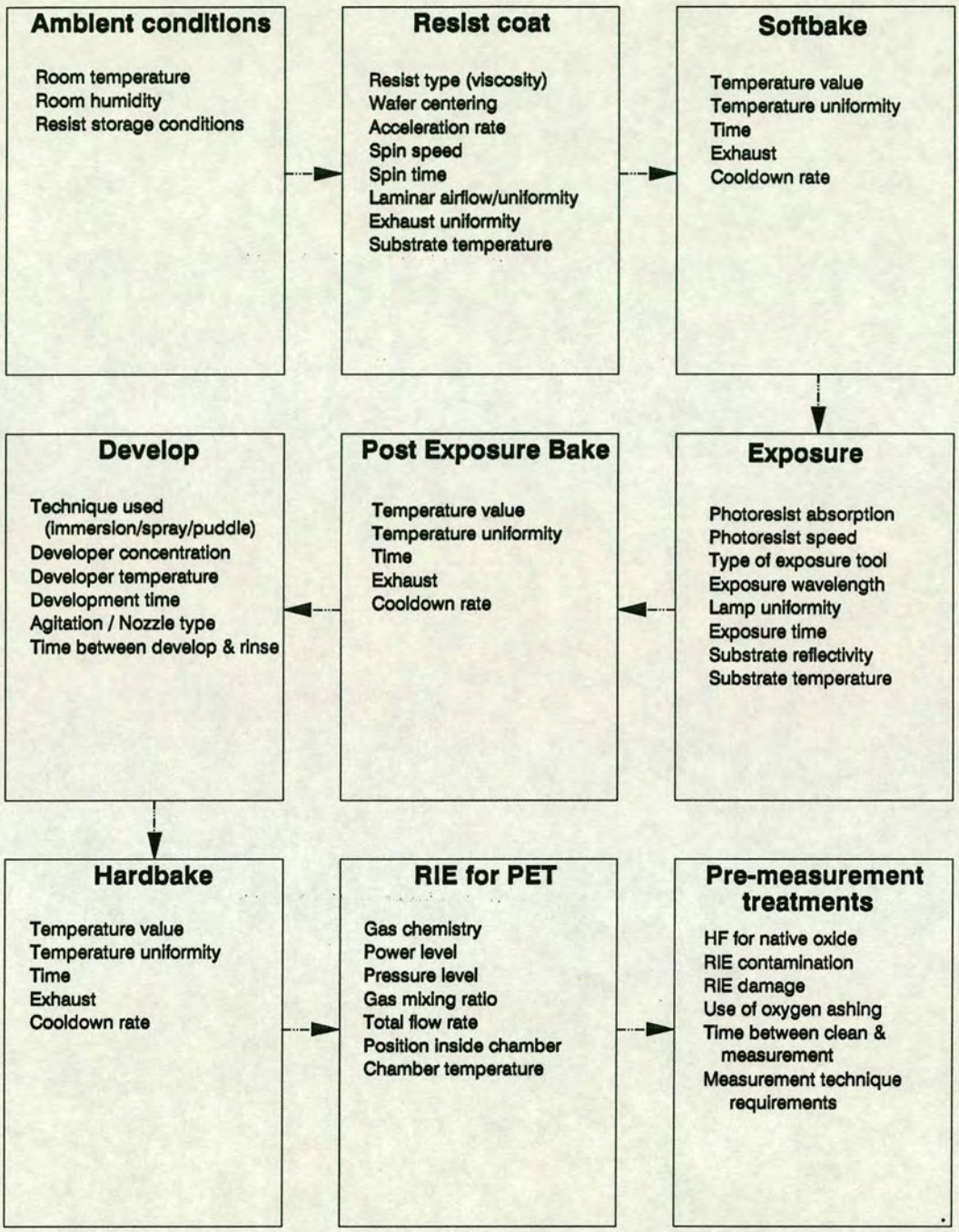

Figure 6–2: The process parameters that are accessible to the user of the PET technique. They have to be optimized to fit the PET requirements.

6.1 Photoresist Patterning optimization

6.1.1 Definitions of contrast and energy to clear

During the lithographic process a pattern is produced on a resist layer by exposure of predetermined regions of the resist to a UV light source. For positive photoresists, as the amount of incident energy increases, the amount of resist that dissolves in the developer solution increases.

The usual goal of a photoresist/developer evaluation is to develop a process with the largest process latitude (stable linewidth control) while having the best possible resist profile (sidewall angle). A large number of variables can affect the photolithographic process. Those variables are depicted in fig. 6–2.

Image contrast, or differential solubility, is a simple method for better predicting process performance. In order to characterize a photoresist and developer combination by use of an optical stepper, the characteristic curve of the system is obtained by varying the exposure dose and measuring the percentage of remaining photoresist. An example of such a curve can be seen in fig. 6–3. Two crucial values that can be determined from the above curve are the resist/developer contrast (γ value), and the energy to clear (E_0). The contrast value can be obtained from:

$$\gamma = \left[\log_{10}\left(\frac{E_1}{E_0}\right)\right] \tag{6.1}$$

where E_1 is the energy value where 80 % of the photoresist has been developed and E_0 is the energy value where 10 % of the photoresist is cleared.

Gamma or contrast is an indicator of edge profile of the photoresist at the interface between the exposed and unexposed areas. Generally, high γ values correspond to an increasingly vertical edge profile and a better resolution capability for the photoresist system.

Energy to clear, E_0, is the minimum exposure required for positive photoresist to completely clear to the underlying substrate during development.

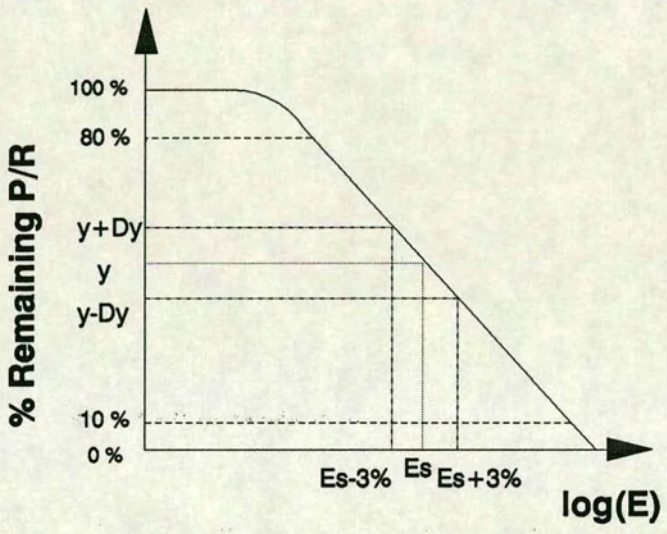

Figure 6–3: The contrast or γ curve for a combination of a photoresist and a developer solution.

By using those two image contrast values, the performance of the combination of the photoresist and developer solution used together can be controlled and optimized.

6.1.2 Methodology for using the image contrast technique

In order to use contrast as a parameter for optimization, an accurate and repeatable method of determining its value must be used. Positive resist is spin coated on bare silicon substrate. After undergoing the specified softbake process, the wafer is exposed on an optical stepper using the available incremental exposure program, which is a standard feature of the stepper software. The wafer is then processed with the necessary post-exposure bake (PEB) and development. The resist film thickness is then measured in relation to its corresponding exposure dose. This step is crucial for the accuracy of the calculated contrast value. It is also necessary to measure the unexposed resist thickness before and after development in order to evaluate the resist loss during development.

The exposure dose and the film thickness values are then fed into a spreadsheet program. The contrast is determined by performing a linear regression of the remaining film thickness normalized to the unexposed film thickness after development and the logarithm of the exposure time [2]. Only data points where the remaining thickness is between 10 percent and 80 percent of the original film thickness are used in the regression. For best results more than 10 points should lie in this region. It is also necessary to perform at least 5 measurements on a cross-like structure within each exposure field. Each of the values of the remaining resist thickness entered in the contrast curve is the average of those 5 measurements at each exposure dose field. The square of the correlation coefficient for the contrast

---

[2]Exposure dose is a linear function of exposure time. Therefore, exposure time is the process parameter used in the stepper exposure file to control the exposure dose of the resist.

curve can be calculated to indicate the quality of the linear fit. If everything was done optimally this value should exceed 0.98, otherwise the experiment would need to be repeated.

We can therefore conclude that the measured contrast is a relative number and can prove useful when comparing a resist/developer system for different photolithography process parameters.

6.1.3 Selection of the appropriate photoresist/developer

Different exposure doses result in different percentages of remaining photoresist. By intentionally increasing the exposure dose, trenches of increasing depth can be observed on the photoresist after the development step. However, trench depths are also sensitive to unintentional exposure dose variation across the exposure field. In the PET technique a low γ value is desired. The reason for such a choice is that it implies low contrast values so any variation in exposure dose has a minimum impact on the remaining photoresist thickness. As a result both smaller step height increments and low sensitivity to intensity variations can be achieved.

The intensity variation across the field of exposure [3] is around 3 %. From the curve of fig. 6–3, γ can be evaluated from the linear part of the curve slope:

$$\gamma = \frac{2\Delta y}{\Delta x} \tag{6.2}$$

where

$$\Delta x = \log(E_s + 3\%E_s) - \log(E_s - 3\%E_s) = \log(1 + 3\%) - \log(1 - 3\%) \approx 0.026$$

For an array of N squares that are exposed for different times, the step difference should not be smaller than the 3σ variation along each step. We must have, therefore:

$$\frac{2\Delta y}{100\%} \leq \frac{1}{N} \tag{6.3}$$

---

[3] A Mimir optical meter was used to measure the intensity at 10 sites along the field of exposure.

Therefore, there is a limit of the maximum number of exposed squares imposed from the Δy value. For a specified number of steps there is a maximum γ value which can be derived from eq.(6.2) and eq.(6.3). For depths from 0.1 to 0.2 μm, a maximum allowable γ value of 2 would give a very good resolution.

A number of different resist and developers combinations were assessed and the BPR-300 (OCG) photoresist with a 3:1 LSI developer showed a low contrast value (1.86). The above combination also had a good uniformity of remaining photoresist thickness across each exposure field (variation below 3 %).

The maximum number of trenches depends also on their area. If sheet resistance measurements are to be made at the bottom of the trenches in Si, the trench area has to be maximized in order to avoid current line distortion at the trench edges. For a 3-inch wafer a maximum of 16 trenches for sheet resistance monitoring was found to give non-distorted results.

6.1.4 The PET requirements

The main requirement of the photolithography step of the PET technique is to achieve a low γ value for a photoresist/developer combination. The depth uniformity inside each trench, the step height difference between neighbouring trenches and the process repeatability are the main criteria for selecting the appropriate process parameter values.

6.1.5 Obtaining the appropriate unexposed photoresist thickness

Starting with the spin coating process, the first parameter that needs to be determined is the photoresist film thickness. The main parameters that affect the unexposed photoresist thickness are the volume of the photoresist spread over the wafer, the speed of rotation of the wafer, the softbake temperature and the softbake time. Since no underlying topography is existant there is no need to optimize the resist coating thickness for incoupling of E_0 and γ with respect to thin film

interference. However, large thickness non-uniformities lead to variable E_0 and γ values across the exposure field. Therefore, it is necessary to achieve a good thickness uniformity. In order to find the optimum values for the best possible thickness uniformity across the wafer, a series of preliminary experiments was undertaken in order to select the values for parameters other than the spin speed. Therefore, some of the experimental results of the following subsections had to be taken in account. In this experiment the volume of photoresist in the syringe was 0.75ml, the softbake temperature was 78°C and the softbake time was 45s. The photoresist thickness was measured at 11 points on each wafer using the AFT-Nanospec. The results are displayed in fig 6–4. The wafer to wafer resist thickness variation is lower than the intra-wafer variation.

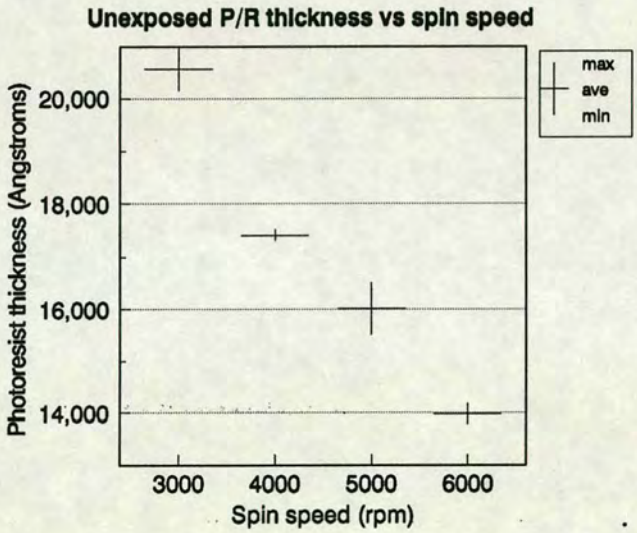

Figure 6–4: Unexposed photoresist thickness versus spin speed. Max, min and ave refer to the 3-σ upper and lower limits and the average resist thickness values measured at 11 sites across the wafer.

The repeatability of the resist thickness for a random spin speed was tested. The 5000rpm value, which gave the worst sigma value in fig. 6–4, was chosen. Measurements were performed at 10 sites for three wafers and the results are presented in fig. 6–5.

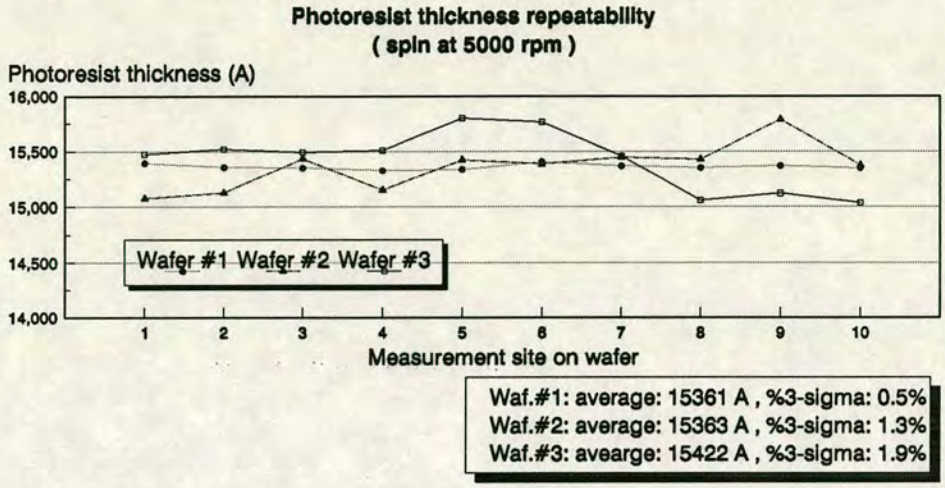

Figure 6–5: Repeatability of the photoresist thickness measurements at a 5000 rpm spin speed for 3 wafers (10 measurement sites).

6.1.6 Softbake and PEB parameters optimization

Once an appropriate film thickness has been found, the next step is to optimize the appropriate softbake and PEB. The manufactured photoresist solutions contain less than 0.5 % water. This amount of water is lowered during softbake, light exposure and post-exposure bake (PEB). The effect of the softbake process is to lower the solvent content as well as the water content of the film. The softbake is necessary in order to stabilize the solvent content and obtain reproducible resist thickness [2]. Loss of solvent occurs even at room temperature ('room-temperature softbake') [2], but is not uniform. Since the PET technique requires good thickness uniformity, the softbake time and temperature have to be optimized. In [2, page 214] experimental evidence on the advantages of the combination of low softbake temperatures with PEB is produced. Reproducibility of resist thickness during development are among them.

A preliminary set of experiments showed that the temperature variation during softbake is more crucial than the time variation in determining photoresist thickness. In order to determine the minimum temperature for softbaking the temperature varied from 50 to 95°C for various time intervals. The resist thickness, value and uniformity were monitored after the softbake process. The results

are shown in fig. 6–6. The optimum T_{soft} is chosen to be 78°C. This is the lowest temperature for which the curve's slope is minimum and constant. The low curve slope is desired since it reduces resist thickness variations. Lower T_{soft} values (eg 70°C) increase resist thickness variations. Higher softbake temperatures increase the γ value and are not desirable. Similar curves were obtained for various softbake times and the best uniformity was produced by a 45s softbake at 78°C.

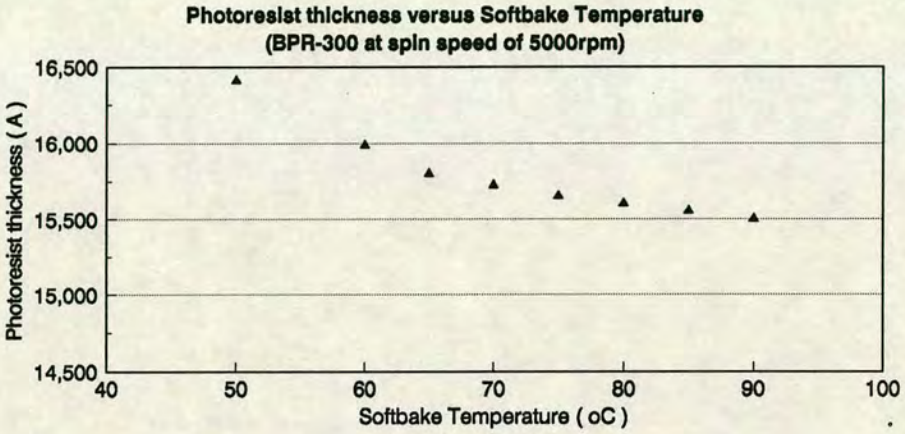

Figure 6–6: The photoresist thickness variation as a function of softbake temperature.

The combined effect of softbake temperature and post-exposure bake temperature on the γ value of the photoresist/developer (BPR-300, LSI 3:1) is displayed in fig. 6–7.

PEB is the resist process stage that takes place prior to development. Its effect is to stabilize the resist film thickness. Experimental evidence from resist thickness change versus T_{PEB} in [3], shows that increased temperature reduces the thickness. The reduced water content is known to cause increased crosslinking [4] of the photoactive compound (PAC) [4]. Therefore, increased T_{PEB} increases crosslinking and thus reduces solubility. How can increased T_{PEB} optimize the PET technique? It is this shift in the exposure dose to clear, that lowers the γ

[4]When the PAC thermolytically or photolytically degrades to form a ketene, in the absence of water, the ketene forms an ester linkage with other PAC molecules.

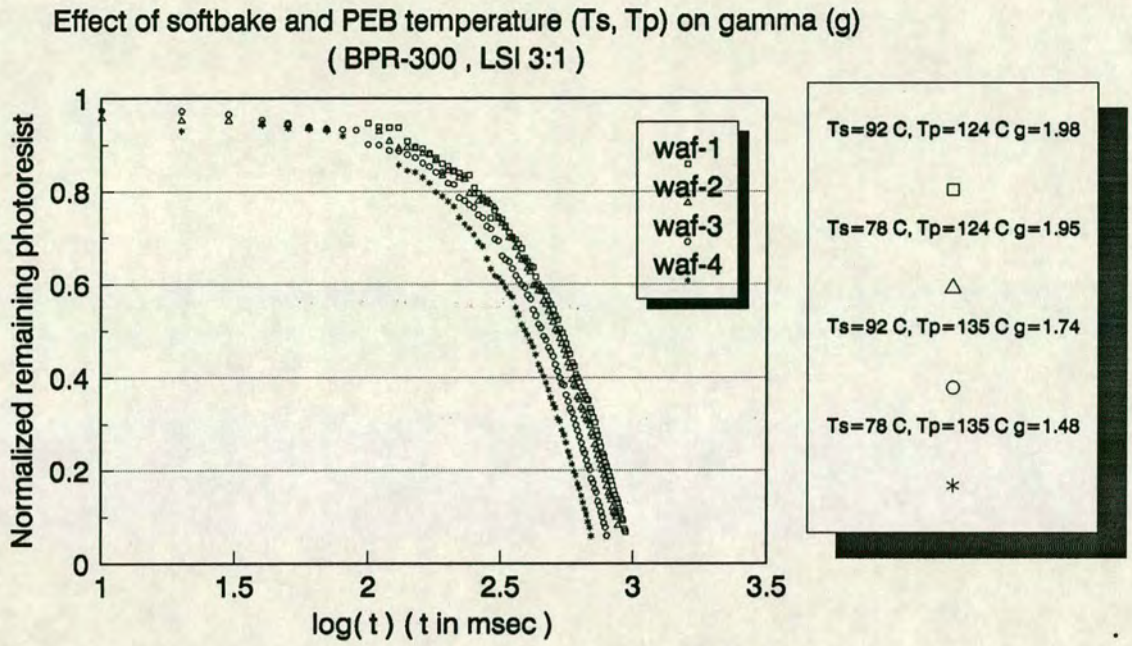

Figure 6–7: The gamma values (g) for the BPR-300 photoresist and LSI 3:1 developer for various combinations of softbake and post-exposure bake (PEB) temperatures.

value of the photoresist/developer in use. This effect is presented in fig. 6–8. The photoresist used is the BPR-300 (of OCG) and the developer is LSI analyzed in a 3:1 ratio into water. The softbake takes place for 45s at 78°C and the PEB time is 45s.

6.1.7 Step measurement

In order to measure the trench depths produced in resist films, two methods were used. Dektak surface profilometry was used in order to compare the step height difference between the unexposed area (outside the trenches) and the exposed trenches. Those were performed both along the length and along the width of each trench. In the second method, photoresist thickness measurements were performed inside and outside the trenches. The difference between the averages of those measurements was considered as the trench depth. The resist thickness was

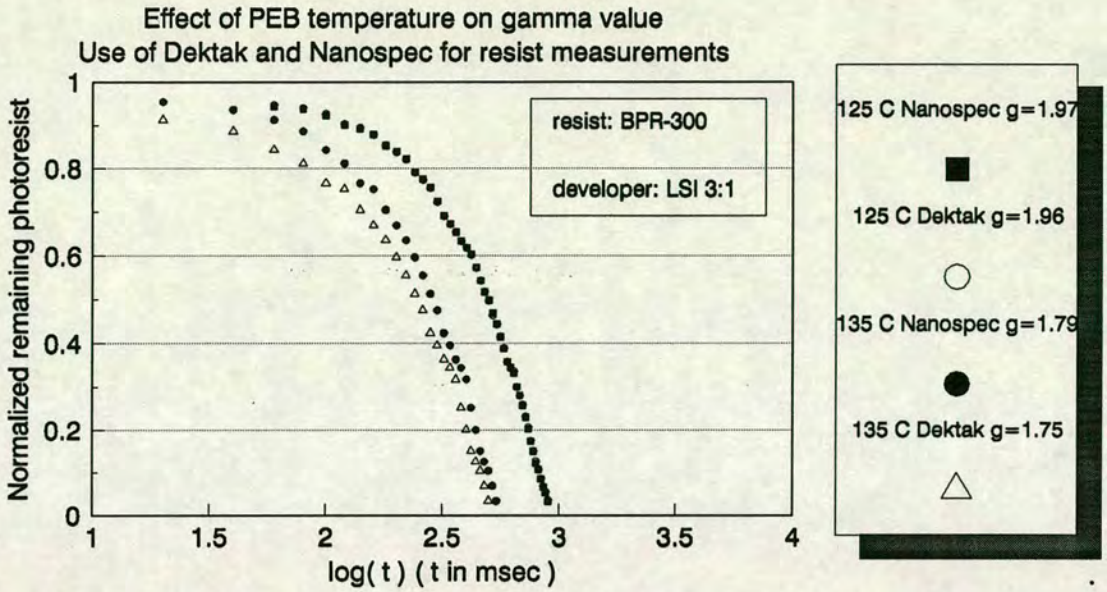

Figure 6–8: Comparison of gamma (g) values measured at 2 post-exposure temperature levels. Effect on gamma from the method used to measure remaining resist thickness (Dektak and AFT-Nanospec measurements).

measured by a Nanospec [5]. The required refractive index value of the photoresist (for the Nanospec film thickness evaluation) was obtained from ellipsometric measurements. It was found to be 1.73. A comparison of the differences in γ values obtained from the above methods is displayed in fig. 6–8.

Depth uniformity is obtained by the 3σ value of the depth measurements performed at 10sites across the trench. Large non-uniformities of remaining resist thickness across the flat bottom of each trench imply that the minimum step height between trenches in resist must increase. The underlying reason is to avoid depth overlap between neighbouring trenches. The uniformity of remaining resist

[5]Nanospec/AFT Model 010-0180 is a computerized film thickness measurement system which measures light intensity in the 390-800 μm range. Consists of a microspectrophotometer head,a processor-controlled grating monochromator, a photomultiplier tube detector and an amplifier.

thickness across the flat bottom of each trench varied with the softbake and PEB temperatures. exposure between the neighbouring trenches

6.1.8 The photolithography optimized recipe

The photolithography steps and the associated process parameter values described in this section, have been experimentally found as the most appropriate for trenches extending to depths to 2000 Å and depth resolutions between 100 and 300 Å.

The step height between neighbouring trenches is controlled by the exposure time pitch value. This is the value (in milliseconds) used in the stepper file to define the increase in exposure dose between neighbouring trenches. The example that follows indicates the use of the exposure time pitch to alter the step height between neighbouring trenches. Increased thickness non-uniformity across the flat bottom of the 2x2 mm square trenches at high softbake and low PEB temperatures was observed. By use of an exposure time pitch of 10ms a 3σ value of 120 Å and a step height of 100 Å was obtained. The undesired overlap of neighbouring trenches can be avoided by using a 20ms pitch in the stepper file. The step height increased to 180 Å while the non-uniformity remained unaltered, as expected.

The optimized recipe described in this section gave the best results for 2mm by 2mm exposure field areas. A step height of 90 Å with a 3σ of 75 Å was achieved. If larger exposure fields are used, the resist non-uniformity within each trench may increase to 140 Å or more due to the lamp induced non-uniformity. Therefore, each optimized recipe is valid for a specific trench area which is defined by the exposure field of the stepper.

6.1.8.1 Pre-coating treatment

A dehydration bake at 103 °C for 15s is necessary to eliminate water vapor from the wafer surface. HMDS coating is necessary for a better adhesion of the resist on the wafer.

6.1.8.2 Coating

Semi-automatic resist coating equipment was used.

1. Dispense 0.75ml of BPR-300 onto the centre of the wafer. The dispense takes place while the wafer is spinning at 500rpm and should be completed in 5s. Special care must be taken in order to avoid air bubbles inside the syringe head. The rate of dispense should be constant for acceptable thickness uniformity.
2. Accelerate to final spin speed for a preset time of 2s and spin at 5000rpm for 30s.

6.1.8.3 Coating inspection

Before proceeding to the softbake step, a visual inspection of the coating should take place. The resist coating should be uniform and clean from any dust particles. 5 Nanospec measurements in a cross pattern should be sufficient to confirm thickness uniformity. The cleanliness of the coating is mostly affected by the airflow over the track equipment and the cleanliness of the dispense line. The coating uniformity is mostly affected by chuck levelling, the speed of dispense, any suck-back at the end and the effectiveness of the initial resist spreading.

6.1.8.4 Softbake

Softbake should be performed on a hotplate for 45s. The hotplate temperature should be 78 °C.

6.1.8.5 Exposure

The exposure matrix (defined in the run-file of the stepper) should be used to adjust the position of the framing blades, the initial exposure time and the exposure time increment. It must be noted that the large exposure fields suffer from higher intensity non-uniformity of illumination intensity due to the light source

being coherent. For 10x10 mm square exposure fields (used to pattern trenches to be used for four point probe measurements on Si), the etch selectivity of resist over Si during the RIE step should be maximized in order to minimize the depth non-uniformity of the trenches in Si. An exposure time pitch of 10 or 20 ms is appropriate for achieving steps of 100 Å to 200 Å in resist. In order to operate on the linear part of the contrast curve, exposure should start above 500ms. In order to achieve smaller steps in the resist, operation in the non-linear part of the contrast curve should take place. However, the 3σ non-uniformity across the trenches might exceed the neighbouring trench depth differences when we operate at the non-linear part of the curve. It is the trench depth non-uniformity that sets the lowest possible resolution limit of the PET technique.

6.1.8.6 Post exposure bake

PEB should take place on a hot plate for 45 s at 135 °C.

6.1.8.7 Development

The development step is very crucial for the uniformity of the resist. Since the LSI developer is not metal-ion-free, the automated track with the spray development could not be used. The wafers were manually immersed in a tank developer (LSI diluted 3:1) and the wafer was moved with a uniform, slow speed from one tank edge to the other. Spray development is recommended for achieving better uniformities. The development time was 35 s and the wafer was rinsed in D.I. water for 1 min. The tank environment temperature was kept to 20 °C.

6.1.8.8 Hardbake

A 10 min oven hardbake at 100 °C results to a more uniform RIE etch.

6.2 Reactive Ion Etching Mechanism

The key advantage of all dry etching techniques is their potential to etch with high precision in a vertical direction, with minimal loss of critical dimensions in the photoresist or other masking materials. The second advantage of dry etching is the ability to control the etch rate, the anisotropy of etching and the selectivity by varying certain process parameters.

A broad understanding of the rates and mechanisms by which free radicals react with Si substrates is important for the selection of the appropriate RIE conditions for the Patterned Etch Transfer technique. Section 6.2.1 and 6.2.2 are devoted to a summary of the fundamental theory explaining the etching mechanism of Si and photoresist in a CF_4/O_2 plasma. The damage and contamination mechanisms present in such an environment are discussed in section 6.2.3.

6.2.1 Silicon reactive ion etching in a CF_4/O_2 plasma

6.2.1.1 Gas-surface chemistry steps

Reactive ion etching involves the reaction of an active gaseous species with a surface to form a volatile reaction product. If we consider an active gas etching a solid surface the following steps occur in sequence:

a. The active gas adsorbs on the surface by forming a chemical bond with the surface atoms (i.e. chemisorption).

b. The atoms on the surface form the product molecule by reaction (i.e. product formation).

c. The product molecule desorbs from the surface (i.e. desorption).

By blocking any of the above steps, etching of the surface does not occur. The reaction rates for those steps govern the overall etch rate. The gases used in reactive ion etching show insignificant chemisorption characteristics at room

temperature without the presence of a glow discharge. Therefore, they do not react spontaneously with Si.

6.2.1.2 The CF_4 glow discharge mechanism

The halocarbons are particularly useful etchants since they are relatively easy to handle, have low toxicity, are non-corrosive and are good for etching Si substrates. Tetrafluoromethane, CF_4, is one of the most frequently used freon gases for plasma etching in Si fabrication. It is normally extremely stable, but inside a plasma it dissociates into F atoms and fluorinated fragments, CF_x. When CF_4 is used as the sole feed gas for an rf plasma etch, no appreciable etch of either Si or SiO_2 on the wafer occurs. The etch rate of Si increases dramatically with the addition of several percent oxygen. By correlating the intensity of optical emission from excited fluorine atoms with the etch rate of Si in a $CF_4 + O_2$ plasma it was concluded [5] that F atoms are the principal etchant. However, it has been shown [6] that the maximum etch rate occurs at a lower oxygen concentration than that which produces a maximum concentration of F atoms. A brief outline of the set of elementary reactions involving species found in the plasma has been formulated in this section.

In the absence of oxygen, CF_4 is decomposed by the electrons that are within the proper energy range through the reactions:

$$e^- + CF_4 \longrightarrow CF_4^+ + 2e^- \longrightarrow CF_3^+ + F + 2e^-$$

$$e^- + CF_4 \longrightarrow CF_3 + F + e^-$$

$$e^- + CF_4 \longrightarrow CF_3 + F^-$$

The role of the first ionization process is to sustain the plasma by creating sufficient positive ions and electrons. Many other processes are possible which produce other ions such as $F^+, F^-, CF_2^+, CF^+, C^+$. These ions can be found in a CF_4 discharge, but they exist in very low concentrations not only because of their low probability of formation but because they are consumed in reactions with CF_4 to form more CF_3^+. On the other hand CF_3^+ does not react with CF_4.

The fluorine atoms, the principal etchants, are created through:

$$e^- + F^- \longrightarrow F + 2e^- \qquad \text{(detachment reaction)}$$

$$CF_3^+ + F \xrightarrow{+e^-} CF_2 + 2F \qquad \text{(dissociative recombination)}$$

The first reaction is the main source of fluorine atoms but the second is a significant contributor. Assuming now that no etching takes place, the loss of fluorine atoms is achieved through heterogeneous recombination that takes place on the wall of the chamber:

$$CF_3 + F \longrightarrow CF_4$$

$$F + F \longrightarrow F_2$$

and through homogeneous recombination:

$$CF_3 + F + M \longrightarrow CF_4$$

$$F + F + M \longrightarrow F_2$$

where M is a third body (for example atoms from the chamber walls) for the impact reactions. Through homogeneous and heterogeneous recombinations of CF_3 there is also production of C_2F_6:

$$CF_3 + CF_3 \longrightarrow C_2F_6$$

$$CF_3 + CF_3 + M \longrightarrow C_2F_6$$

If Si is put into the CF_4discharge, then F-atoms are removed by the etching process:

$$Si + 4F \longrightarrow SiF_4$$

Stainless steel inside the chamber also removes F-atoms. Due to the removal of F atoms, F concentration decreases, there is less F_2 and C_2F_6 concentration increases. Although F_2 is completely suppressed by the presence of Si, F atoms are still present due to the reactions of CF_3 radicals and SiF_x species (x=1,2,3):

$$CF_3 + F_2 \longrightarrow CF_4 + F$$

$$SiF_x + F_2 \longrightarrow SiF_{x+1} + F$$

6.2.1.3 Effect of oxygen addition to CF_4 plasmas

The addition of small ammount of oxygen (less than 20%) in the plasma, leads to a large increase in the F atoms concentration. Oxygen, as an oxidant, alters the balance between fluorine atoms and unsaturates (ie CF_3). The oxygen atoms are formed by the reaction:

$$O_2 + e^- \longrightarrow O + O + e^-$$

However, they do not directly react with CF_4 in order to form F . The four possible mechanisms for the increase in fluorine concentration due to added oxygen are [7]:

1. Oxygen reacts with species containing F to liberate fluorine atoms. This reaction may occur either on surfaces or in the gas phase.
2. Oxygen retards the loss rate of fluorine precursors (ie F^-) by removing species which would otherwise consume the precursors.
3. Oxygen retards the rate of homogeneous reactions of F atoms with other species by depleting the reactants via oxidation.
4. Oxygen retards the heterogeneous recombination of F atoms with other species either by reacting with them or by blocking access to the surface where recombination will take place.

The last mechanism is the least favorable, since only a small amount of oxygen would be required in the feed gas to reach the maximum concentration of F atoms, and additional oxygen would not have a marked influence. For the same reason it is unlikely that oxygen acts to poison surfaces against recombination of radicals. Since oxygen atoms will not directly react with CF_4 and since volatile products such as CO, CO_2, COF_2 are present, it was proposed [6] that either

$$CF_3 + O_2 \longrightarrow COF_2 + OF$$

or

$$CF_3 + O_2 + M \longrightarrow CF_3O_2 + M$$

is the most probable initial step. The above reactions compete with the two types of recombination reactions of F atoms because they reduce the available concentration of CF_3 and thus they enhance the F concentration. However, the OF radical is highly reactive and can be converted to F atoms through different reactions:

$$CF_3 + OF \longrightarrow COF_2 + 2F$$

$$OF + OF \longrightarrow O_2 + F_2^* \longrightarrow O_2 + 2F$$

while CF_3O_2 may produce F atoms directly by a series of free radical reactions involving fluoroxide compounds (for example $CF_3OOCF_3, CF_3OF, \ldots$) and radicals (for example $CF_3OOCF_3, CF_3O, \ldots$).

All the above reactions give an insight in mechanisms 2 and 3. The last two are initial steps for the type 1 mechanism as well. Oxygen atoms are produced in the discharge via

$$e^- + O_2 \longrightarrow O + O + e^-$$

$$e^- + O_2 \longrightarrow O^- + O$$

They can increase the F atoms concentration indirectly through reactions such as

$$CF_3OO + O \longrightarrow COF_2 + O_2 + F$$

The decrease in F concentration and CF_4 conversion with increased oxygen feed can be explained qualitatively through the variation of rates of the above reactions. This rate variation is intimately linked to the field-strength-to-pressure-ratio of the experiment. [6]

6.2.2 Photoresist etching

In resist stripping applications, the primary objective is the rapid removal of photoresist, without etching or damaging the substrate. This process is generally carried out in RIE mode, by using oxygen plasma [8].

6.2.2.1 The basic mechanism

A useful summary of the reactions occuring in an oxygen plasma can be found in [9]. Atomic oxygen ions rapidly undergo charge exchange with oxygen molecules to produce molecular ions and neutral atomic radicals. The first step in resist stripping is oxidation of the polymer surface, and oxygen atoms are the most reactive species. A carbon-hydrogen bond is first dissociated to produce a radical polymer species. An oxygen molecule can react at this site to form a peroxide radical; this radical can then abstract hydrogen from another polymer unit and thus form a hydroperoxide.

Both the formation of the initial radical and the hydroperoxides decomposition to form volatile fragments are slow processes. The supply of active oxygen species in the plasma enhances those steps that are etch rate limiting. It must be noted that the synergistic effect between neutral chemical etchant species and ion bombardment results in an even greater etch rate. Ion bombardment is the critical mechanism since the mere presence of oxygen atoms is not sufficient to ensure etching.

6.2.2.2 Fluorine addition in the plasma

Even a small addition of halogen atoms in an oxygen plasma, increases the etch rate dramatically [10]. Fluorine addition is accompanied by two primary effects, [8]:

1. Dissociation of the flourine-containing gas occurs inside the plasma. This is the source of fluorine atoms which are efficient at abstracting hydrogen from the polymer unit.

2. The presence of fluorine atoms, enhances oxygen dissociation which further enhances the etch rate. The maximum etch rate usually occurs when the proportion of the CF_4 feed proportion of the feed gas is 20-30 %. For higher CF_4 feed proportions there is a decrease in the etch rate.

6.2.2.3 Temperature effect

An increase in etch rate is observed at elevated temperatures due to its Arrhenius-type dependence on temperature [11]. The maximum temperature achieved increases with an increase in rf power or a decrease in pressure.

6.2.3 RIE-Induced Damage and Contamination in Silicon

6.2.3.1 Dry etching damage

In silicon bulk damage, as for example in the ion implantation process, the host lattice is considered to be stationary during implantation. The degree of damage is mainly determined by the incident energy, the dose of the bombarding ions and the target temperature. On the other hand RIE damage is a surface radiation effect in which we have **simultaneous** damage and etch processes. The degree of RIE damage is determined from the rate-limiting process. If the etch rate is fast enough, the damaged layer depth can be minimized. For very slow etch rates the host lattice can be considered stationary and the physical damage is maximized.

RIE causes this dynamic radiation effect in crystalline Si because of energetic particle bombardment. The particles involved are predominately positive ions accelerated by the electrical potential between the rf- coupled substrate electrode (the cathode) and the plasma. Since those ions travel through a low pressure halogen gas, they can be thermalised through collisions and also neutralised through charge exchange. Therefore, the energetic particles can be both ions and neutrals with kinetic energies varying over a wide range. The maximum possible energy they can acquire is set by the d.c. potential between the cathode and the plasma. Assuming that the Child-Langmuir law for ion transport phenomena through the plasma sheath is valid, the ion current is proportional to the 3/2 power of the d.c. potential difference; therefore RF power can change both ion energy and current.

The degree of damage is also linked to the type of dry etching technique being used. Since there are two broad classes of directional plasma-based dry etching techniques, physical etching and chemical-physical etching, the type of gas used

and its pressure are crucial in damage creation. The three different kinds of damage layers produced in Si are presented in the following subsections and are schematically presented in fig. 6–9.

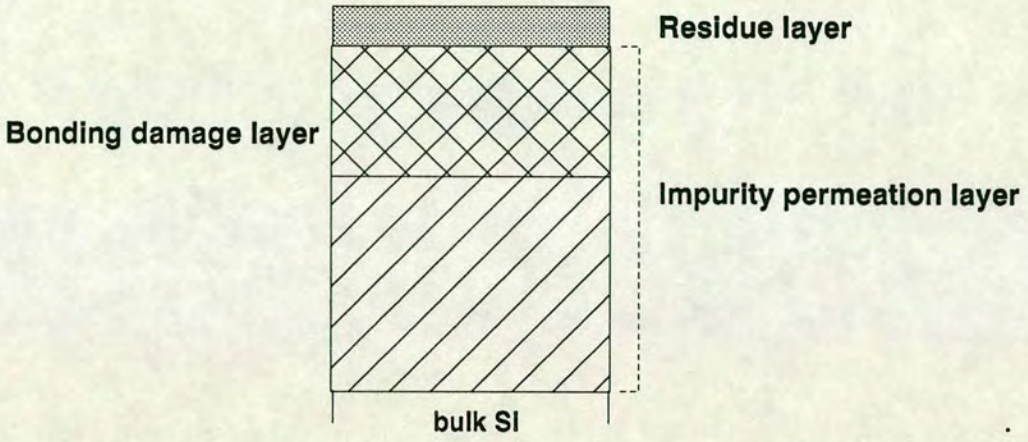

Figure 6–9: Schematic diagram of RIE induced damage and contamination in silicon.

6.2.3.2 Residue layer

The residue layer (R-layer) is a surface film whose presence depends on the etching chemistry. In the fluorocarbon-based RIE chemistries, a formation of reaction-blocking, polymer-like residue layers occurs on Si. Therefore, it is evident that this type of contamination is inherent to the process. In [12] it is shown that a SiF_xO_y layer is produced on the Si surface and its thickness and composition control the etch rate of Si. The existence of a residue layer can have a major effect on any type of surface monitoring measurements:

1. The electrical conductivity of the residue layer severely alters the sheet resistance measurements. This is due to the series resistance created near the surface.

2. The residue layer greatly affects the optical constants measured by surface sensitive techniques [6].

3. Surface roughening can occur due to micromasking effects from impurities contained within those layers. Sheet resistance repeatability severely deteriorates due to the surface roughness.

The R-layer can be avoided by using different etching chemistries. Since the PET technique is close ly linked with an etching chemistry that creates R-layers, alternative methods have to be used for reducing that type of damage. Oxygen ashing and an HF dip after the RIE step seem to minimize the effect of this layer on the doping and damage profile measurements. This will be futher investigated and presented in the following chapters, since surface monitoring techniques have to be used inside the PET trenches.

6.2.3.3 Impurity contamination and permeation layers

Contamination is an impurity incorporation in the lattice as well as modification of the surface material by incoming foreign atoms and molecules, including foreign material deposition such as polymer formation on the surface. A permeation layer (P-layer) may arise from unwanted radicals in the plasma and the reactor walls, the electrode material and the etched masked on patterned wafers. Metallic impurities such as Fe, Al, Na, Cr may also be involved. The presence of impurities in the P-layer can be reduced by better design of the etching system and by covering the etch chamber. Since the etching species permeate this layer due to implantation, channelling-enhanced implantation, recoil implantation and enhanced diffusion, this type of damage is always present if directional, physical etching is performed. However, the use of CF_4 and O_2 as the feeding gases for the PET technique makes

---

[6]Ellipsometry is an example of a surface sensitive technique which will be experimentally verified in the following chapters and used to monitor optical constants of a material.

the plasma etching more chemical-assisted and isotropic (ion bombardment-free) in nature. Therefore, the formation of such a P-layer is not a major problem and the cleaning procedures mentioned in the previous subsection can be used to remove it. Hydrogen permeation is discussed seperately in section 6.3.4.4.

6.2.3.4 Bonding damage

Ion bombardment is an inherent feature of the RIE process. The associated UV radiation and damage to weak hydrogen bonds are the main causes of weakened bonds and damage-enhanced chemical reactivity [13]. This layer is present in both physical and chemical-physical dry etching. Since it is impossible to eliminate this type of damage, sufficiently high etch rates are required in order to minimize it.

6.2.4 A physical approach to RIE damage

Radiation damage in crystalline silicon has been extensively studied for almost 30 years and many excellent review articles and books are available in the literature [14–16]. This overview takes a physical approach to that type of damage in order to quantify its effects. A simple model will be built up in order to find the minimum etch rate required to minimize the damage depth.

6.2.4.1 Its nature and definition

When an energetic particle, X-ray, electron, neutron proton or a heavy ion impinges on crystalline silicon and collides with the host atoms in the lattice, a part of the kinetic energy of an incoming particle is transformed into the recoil energy of the host atom.

1. If the recoil energy is higher than 10-15eV, ie the displacement threshold energy which is required to break four valence bonds with the four nearest neighbour atoms in the lattice, then the Si atom moves from the lattice site to an interstitial site, leaving behind a vacancy. Thus the displacement damage always results in vacancies and interstitials.

2. If the recoil energy is sufficiently bigger than the 15eV threshold, the displaced Si atoms can collide with other host atoms and produce a cascade of collisions. If damaged regions overlap one another, the crystalline Si undergoes a phase transition to the amorphous state.

The displacement threshold energy of 10-15eV corresponds to MeV photons set by the range of Compton scattering, about 100keV electrons, 50-75eV protons and 15-20eV carbon ions. It is obvious that only heavy ions in reactive plasmas can produce displacement damage in the bulk Si; electrons and photons in the plasmas are not a serious problem, as far as the bulk damage of Si is concerned. We expect that ion bombardment damage does exist even in the plasma etch operation mode due to the high plasma potential, although the extent of damage should be less than during the RIE mode.

As the ion energy decreases through collisions either in the plasma sheath or in the bulk silicon, ions can easily capture an extra electron and become energetic neutral atoms. The atom-atom interaction of those neutrals with the Si atoms, is a weak long-range attraction plus a strong short range repulsion(Fermi-Thomas type of interatomic potential). It can cause:

1. Heavy damage such as a displacement spike at the end of the ion range.
2. Deeper penetration of the incoming neutral atom in the Si bulk because of a lack of ionization energy loss which dominates in ion penetration.

Damage at the silicon near-surface may not be entirely caused by displacement damage through elastic collisions, especially if the silicon surface is covered with an insulator such as silicon nitride or silicon dioxide. Although insulators have not been used as masks in the following experiments native silicon dioxide is always present.

The primary defects directly generated by a high energy particle bombardment are vacancies and interstitials in the bulk silicon. Vacancies are mobile near 77°K and self-interstitials at 4°K . The other point defects such as divacancy, impurity interstitials and impurity-vacancy pairs, are stable at room temperature [14, 17].

More complex defect aggregates are formed, when either the electron fluence is very high [18] or a heavier particle, ie ion neutron or proton, is irradiated at room temperature [19]. Impurities in silicon such as carbon, iron and chromium are also mobile at room temperature when they occupy interstitial sites. It is therefore evident that both primary defects and plasma contaminants can diffuse into Si during the RIE process.

As opposed to the situation where defects are generated inside the bulk (where we have a gradual decrease in defect density towards the surface [20]), defects are super-saturated near the surface during RIE. Therefore, the surface is acting as a source of point defects which, in the case of vacancies and self-interstitials, are highly mobile at room temperature and can easily migrate deep into the bulk before being stabilized by combining with themselves or with impurities such as oxygen and carbon present in silicon.

RIE of silicon in a low pressure (10-200mTorr) glow discharge with CF_4 is a typical case of chemical-physical etching. A large negative sheath voltage is formed between the rf-coupled substrate electrode and the plasma as this potential accelerates positive ions like CF_3^+ resulting in Si sputtering. On the other hand, the chemical reactions explained above produce radicals which etch the Si at the surface by producing volatile SiF_4 species which are in turn pumped out of the chamber. That synergism between the sputtering caused by ions and the chemical attack of reactive neutrals produces a damaged portion at the near surface which is continuously removed at a speed defined as the etch rate. Ideally, we wish to etch away defects before they migrate into the bulk. However, this is very unlikely to happen as the etching rate is much slower than the migration speed of primary defects and because damage production is very high near the end of ion trajectories.

6.2.4.2 RIE parameter dependence on lattice damage

RIE is characterized by a large number of process control parameters such as etching gas, power, pressure, gas flow, temperature, and chamber geometry. The

character of the near-surface modifications depends critically on those parameters and shows great variations for different conditions. In order to adjust the above parameters an understanding of the characteristic depths determining the near-surface modifications and their link to the parameters is essential.

depth of origin of sputtered particles: They originate primarily from the two topmost atomic layers and their depth of origin does not exceed 5 Å [21].

depth of chemical attack of reactive neutrals: The thickness of the layer that is modified depends on the reactive etchant species and the substrate. For a Si substrate and fluorine atoms, the reacted layer is relatively thick and can extend up to 20 Å [22].

projected range of ions: The R_p value depends strongly on the maximum energy of the bombarding ions, therefore it can be adjusted by the power and pressure process parameters of the RIE.

diffusion length of a particle in Si: It gives a measure of the distance that an impinging particle will diffuse into the substrate during etching in a certain amount of time. Substrate etching tends to remove implanted impurities. Therefore, it is evident that this depth will depend on the etch rate and the respective process parameters. Qualitatively, the diffusion length is proportional to the root of time, t, whereas the amount of removed Si is proportional to t.

depth of the ion-induced collision cascade: For a low energy ion bombardment a cascade is a low probability effect and its depth does not exceed the projected range plus 20 Å.

6.2.4.3 Etch rate model

As the amount of residual damage in a substrate after RIE is mainly determined by the substrate etch rate, careful investigation of the correlation between etch

rate and damage is needed. For any value of etch rate the degree of disorder in the near-surface region of silicon is expected to initially increase with time of exposure in the plasma. This increase saturates and finally should reach a steady state situation where defect introduction and defects removal by the etching process are in a dynamic equilibrium. The time to reach that steady state and the level of the constant damage depend mainly on the etch rate.

In [23] there is an attempt to model the time variation of the damage for a CF_4/H_2 gas combination. The same type of model can be used for the CF_4/O_2 gas mixture. The approach is simplified by the following assumptions:

1. The effects of different ions on the Si substrate are independent and simply additive to one another.
2. The etching of the target and the creation of damage and trapping of ions in the Si substrate are treated as occuring simultaneously but independently.
3. According to [24] and [25] we can assume that the damage profile and the impurity profile coincide at the ion energies involved.
4. We assume that the damage profile can be closely approximated by a Gaussian distribution.

It is shown in detail in Appendix B that at a location x measured from the actual Si surface, the damage concentration reaches 99 % of its maximum possible value after a time t, given by :

$$t \geq \frac{2.69\Delta R_p + R_p - x}{s} \tag{6.4}$$

where

R_p, is the projected range of the impinging ions

ΔR_p, is the straggle of the ion range distribution and

s, is the etch rate.

For the rather low energies involved in the RIE chamber, ΔR_p might be considered numerically equal to R_p. According to the list of depths given above, a value of 25 Å for the projected range is a reasonable estimate for the energy values involved. The location of point x inside the substrate for which the residual

damage variation with time is examined, is set equal to the projected ion range, R_p.

Since depth is measured from the actual surface it is also set equal to 25 Å. Therefore, eq.(6.4) reduces to:

$$t \approx \frac{6.73}{s} \tag{6.5}$$

where the etch rate is expressed in nm/s and the time to reach the steady state is obtained in seconds. This relation and the experimental measurements will be used as an indication of the most suitable Si etch rate for the PET technique. For an etch rate of 22 nm/s, the time to reach steady state is around 0.6s. It is therefore evident that the PET structure will have a steady-state amount of resident residual damage for all depths, since the etching times involved will be more than 10s. Therefore, the evaluated differences of the monitored electrical, optical and thermal parameters between subsequent Si layers, will be free from RIE-induced damage.

According to the above model, it is expected that RIE damage will increase with rf power and decrease with pressure increase. The presence of a 'polymer' layer or oxide layer will reduce the amount of damage, since it will not permit high penetration depths of ions (like C and F) into the Si substrate. It is thus useful not to use an HF clean before the RIE step and to keep the native oxide layer as thick as possible.

6.3 RIE optimization experiments

6.3.1 The requirements

The objective in the following series of experiments is twofold.

1. We seek to obtain the lowest possible RIE-induced damage with the best possible wafer uniformity and a rather high etch rate for the different process parameters. Since our primary concern is to minimize the damage on Si, this can be achieved, according to the previous section, by:

- Using a high enough etch rate, so that the depth of the damage is minimized.
- Having more chemical and less physical etching(this results in a more isotropic etch, as well).

2. Measure the etch rate variation across the wafer.

6.3.2 Optimizing the process parameters

6.3.2.1 The gas choice

From the various gas combinations that can simultaneously etch Si and photoresist, the use of CF_4 and O_2 satisfies all the requirements set and discussed previously. It was therefore used as the etching gas in the plasma batch reactor operating in a conventional low pressure mode (less than 100mTorr), in the reactive-ion etching regime.

6.3.2.2 The effect of the oxygen percentage in the CF_4/O_2 gas

As it was explained in section 6.2.1.3 the addition of oxygen enhances the etch rate of Si [26–29], and favors the chemical etching mechanism. In order to maximize the etch rate inside the RIE etcher, the percentage of oxygen was varied and the etch rate was measured in the center of the wafer. The results of fig. 6–10 show that the maximum etch rate is achieved for a mixture with 9 % oxygen (the values of other process parameters are indicated on the graph).

6.3.2.3 The effect of RF power

It was shown in section 6.2.3 that the RF power level determines the ion energy. Therefore, RIE-induced damage increases with increasing RF power. In the RIE etcher used in the experiment [7] the minimum possible power of operation (500

---

[7]Plasmatherm PK2440 Reactive Ion Etcher.

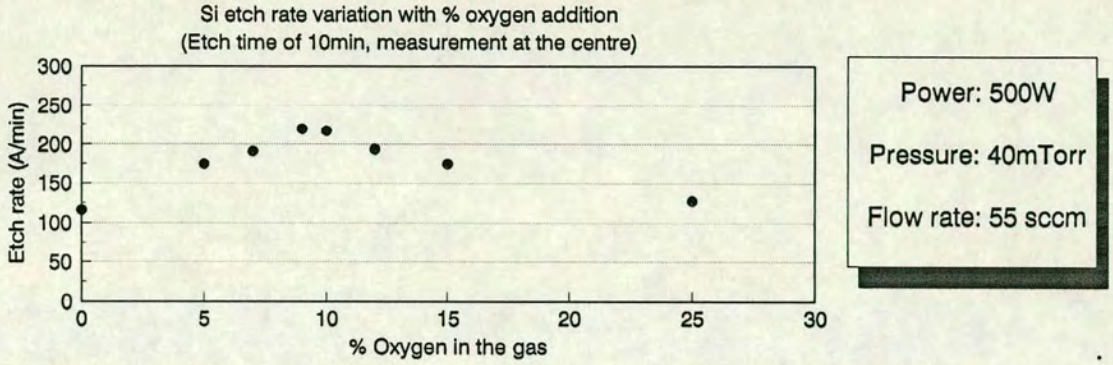

Figure 6–10: The effect of the addition of oxygen on the etch rate of crystalline silicon.

Watt) was selected in order to minimize the degree of induced damage. This choice results in a lower etch rate value but is essential. If a higher etch rate is required [8], a higher gas pressure can be used instead [30,31] so that the induced damage level will not deteriorate significantly. The RF power level does not have any significant effect on the average residence time of the active species. The residence time depends on PV/Q, where P is the reactor pressure, V is the reactor volume and Q is the total gas flow rate.

[8]This is the case if a deep implant has to be profiled and an etch rate of 220 Å per minute might be very slow for the on-line application of the technique.

6.3.2.4 The effect of the gas pressure

For the PET technique application, RIE is confined to pressures in the 20 to 100 mTorr range, since pressure affects the range of ion energies available. An increase in pressure, under a constant flow rate, is expected to lead in an increase of the residence time and particle collision rate and a decrease of the average electron energy [32, page 497]. In the CF_4 etching of Si, etching is accomplished by the radical species (fluorine atoms) formed by the dissociation of the CF_4 molecule. Increased particle collisions lead to increased fluorine atom concentration and thus to an increased etch rate. The variation of etch rate with pressure is shown in fig. 6–11. The values of the other RIE process parameters are indicated on the same chart. The x-axis of the graph represents the position on the wafer (across the radial direction inside the RIE chamber) where the etch rate measurements were performed. The observed etch rate non-uniformity is fully discussed in the next section. Two important observations can be made. Firstly, the etch rate variation with pressure is non-linear in the 40 to 70 mTorr regime. Secondly, there is very small difference in the etch rates between the 40 and 50 mTorr pressures.

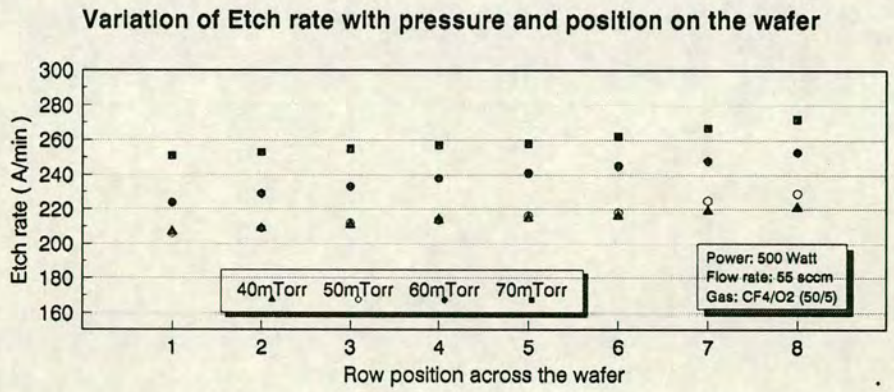

Figure 6–11: Etch rate variation with pressure. The effect of position across the wafer on the etch rate value.

6.3.2.5 The effect of total flow rate

The etch rate is dependent on the rate of generation of active species, the rate of consumption of those species and the rate of removal of reaction products (see section 6.2.1.1). The experimental results of fig. 6–12 can be theoretically supported. If the pressure value is kept constant, a low flow rate leads to species depletion. On the other hand an excessive flow rate results in active-species-residence-time decay. It therefore leads to a decrease of the active species generation rate. In both cases a decrease of the etch rate occurs. The optimum flow rate value (a maximum in the curve) can be chosen from the experimental results of fig. 6–12

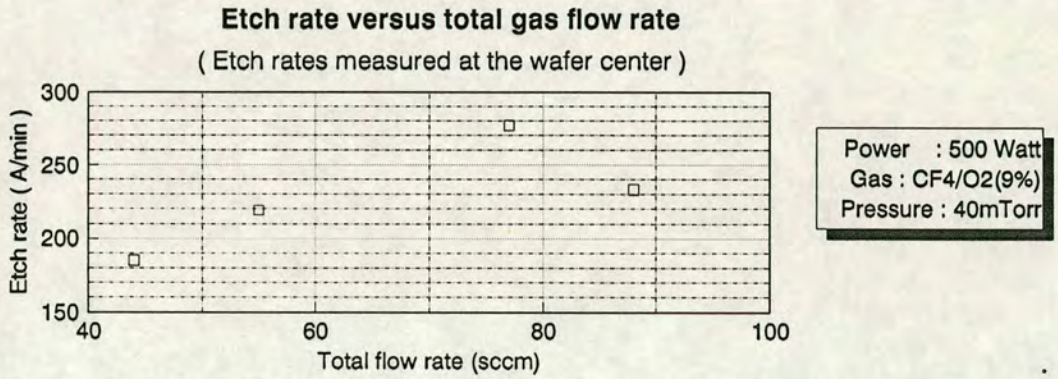

Figure 6–12: The variation of etch rate with gas flow rate, for a constant pressure.

6.3.3 The variation of etch rate across a wafer

The optimum operating RIE parameters for our PET technique, cannot be selected solely from the criteria of minimum induced-damage and etch rate requirements. A high degree of uniformity is needed across the bottom-flat of the trenches patterned into Si. The etch rate variation across the wafer and inside each trench has therefore to be investigated.

6.3.3.1 Intra-wafer etch rate non-uniformity.

Intra-wafer non-uniformity in RIE systems is a major problem. The phenomenon of edge-to-center decrease in etch rate, often referred to as the 'bullseye effect'[33],

is present in parallel plate radial flow systems. Since the etch rate is higher in the outer row of the etcher, in the whole experimental procedure the wafers are placed in the outmost row in the system, with the wafer flats tangent to the periphery of the chamber.

6.3.3.2 Etch rate variation along a wafer.

This type of etch rate variation can be regarded as the most crucial problem of the PET technique. The direction of variation coincides with the gas flow direction. Etch rate has been found to be higher near the periphery of the chamber where the gas inlet position is situated. A gradual decrease has been observed along the etcher radial direction. Different structures (trenches of different sizes across the wafer and masks) have been used to certify those observations.

The radial etch rate variation is depicted in fig. 6–13. The trench positions are presented in the wafer schematic (top right). Etch rate measurements were performed along columns which are parallel to the radial direction and along rows which are in the normal to the columns. In each column, 8 depth measurements were performed ie at each edge of the four trenches in each column. The duration of the RIE etch was 10 minutes. Dektak profilometry has been used at 5 different positions along each side of the trench. The etch rate was evaluated from the average of those 5 measurements. The average and the 3σ value of the evaluated etch rates at those 8 positions along column 1 are displayed on the top left chart of fig. 6–13. An increased uncertainty in the measured etch rate is evident as we approach the wafer flat (which is closer to the gas inlet of the chamber). Similar uncertainties in the measured etch rate that have been observed for the other 3 columns are not indicated on this chart.

For column 1 in the top left diagram, the etch rate increases as we approach the wafer flat, ie the highest etch rate is found at row 8 next to the wafer flat. The etch rate along the four different columns can be examined from the results that appear in the bottom left diagram of fig. 6–13. A similar etch rate variation trend along each column is evident.

The etch rate variation along each row is insignificant and within the measurement error as shown in the bottom right diagram. The duration of the RIE etch was 15 min for those measurements.

In order to examine the validity and repeatability of the above experimental results two different tests have been conducted:

1. The above experiment has been conducted for different RIE etching times(5, 10 and 15 minutes). The etch rate was, therefore, obtained from different etch durations. The negligible differences between the etch rates support the repeatability issue of the previous experiment. The inter-wafer etch rate non-uniformity follows the same trends.

2. In order to verify that the effect of etch rate variation along the radial direction of the chamber is not due to specific process conditions but is an intrinsic RIE chamber-induced effect, the experiment was repeated for a set of four different process parameters (total flow rate, pressure and gas ratio). The measured etch rates were different from those in the initial experiment. However, the etch rate inter-wafer non-uniformity trends were found to be identical to those of the initial experiment.

6.3.3.3 RIE process parameters and etch rate non-uniformity

The effect of RIE process parameter values on the etch rate variation across a wafer is of vital importance for the PET technique since it depends on repeatability of trench formation. Any lack of control over the etch rates across the wafer would make the PET technique useless. The key aspects of etch rate variation have been discussed in the section on optimization of the process conditions. A comparison of etch rate variations, by the addition of the position across a wafer as a functional parameter is the issue of this section. In fig. 6–14 the normalized etch rate variation is displayed for different gas flow rates. It is evident that the etch rate non-uniformity is a minimum for a 55 sccm total flow rate.

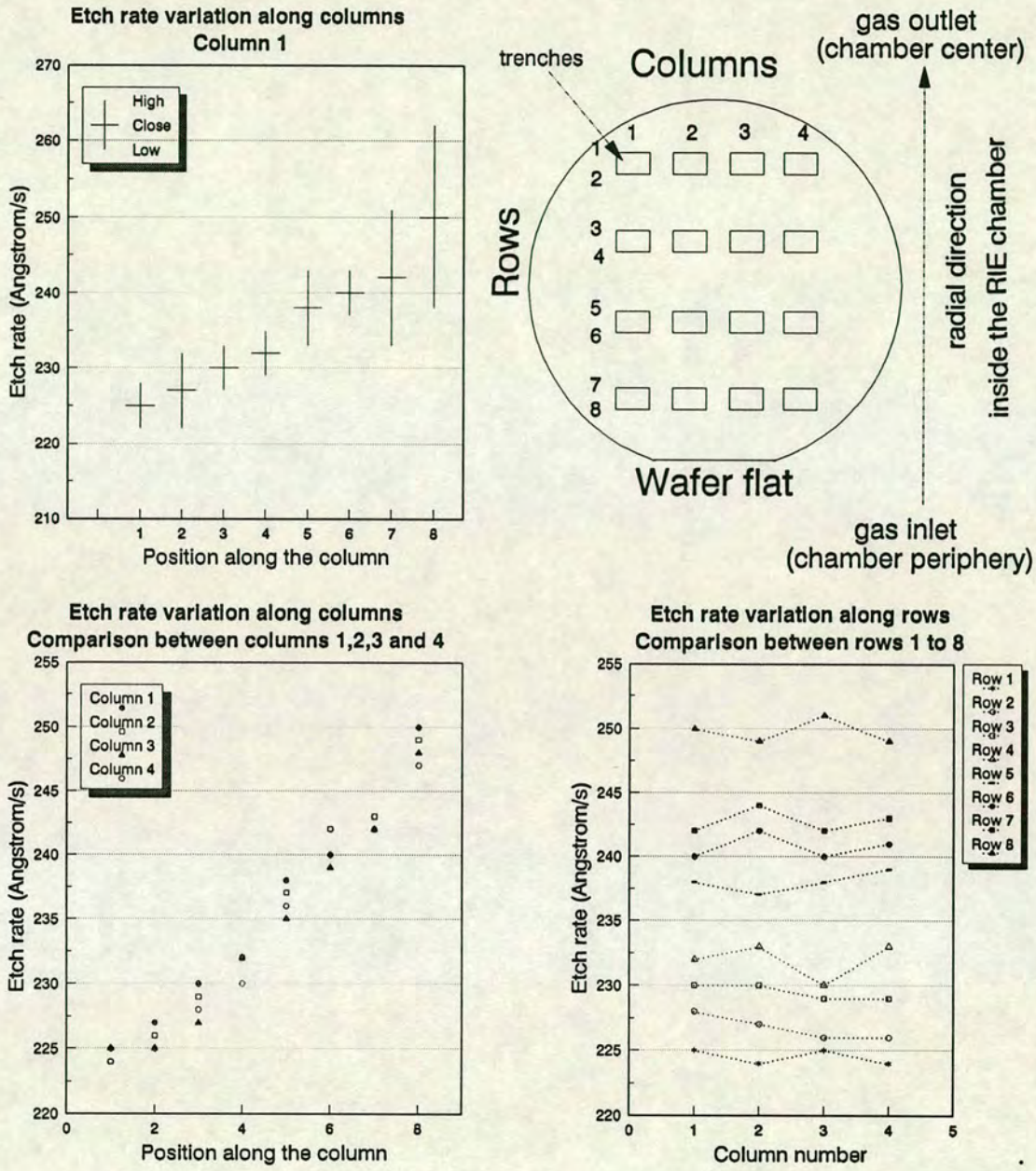

Figure 6–13: Etch rate variation on a wafer placed in the RIE etcher with the wafer flat tangent to the chamber periphery. An array of 16 trenches has been created by using photoresist as a mask. RIE etching took place for 10min. Dektak depth measurements along columns were obtained at each side of the 4 trenches. Therefore, a total of 8 measurements was performed along each column at the positions specified as rows 1, 2, 3, 4, 5, 6,7 and 8 on the upper-right schematic.

In fig. 6–15 the actual values of etch rate variation across the wafer can be observed.

The influence of pressure variation on the radial etch rate variation can be observed in fig. 6–11. For the 40 mTorr curve, the non-uniformity is low and therefore that pressure value seems the most suitable for creating deep trenches in Si where big variations from the expected depth might occur across the wafer due to the longer etch times.

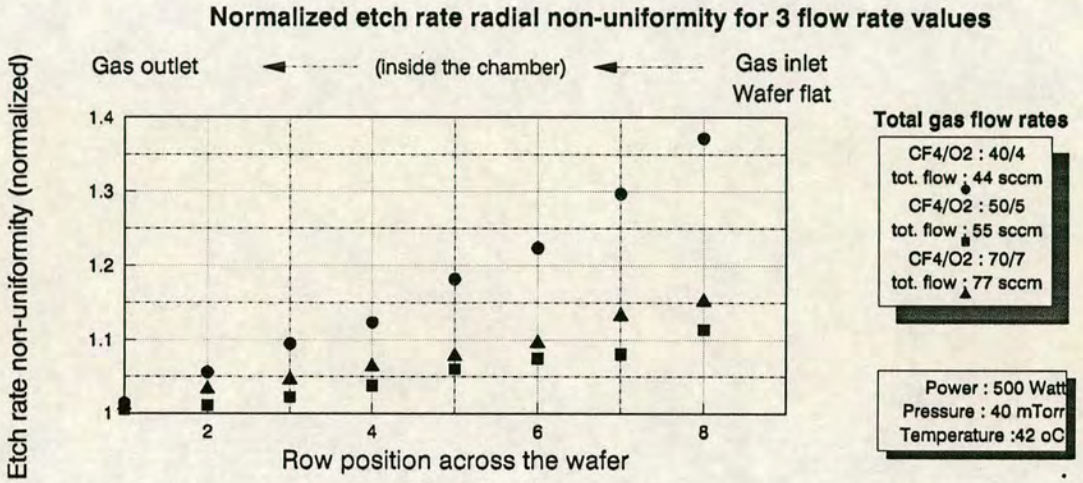

Figure 6–14: Normalized etch rate non-uniformities across a wafer, for different total flow rates values. The values of other process parameters are also listed.

6.3.3.4 Etch rate and selectivity aspects

Some more aspects of the etch rate have been investigated experimentally. Variation of photoresist and Si etch rate with RIE time is very important in converting the time scale into a depth scale. Measurements were performed across the central row of a 10 by 10 square trench array. Five measurements were performed in each trench and the average was evaluated.

The photoresist etch rate measured for 125°C and 135°C post-exposure bake (PEB) temperatures is displayed in fig. 6–16. The higher T_{PEB} results in an 8%

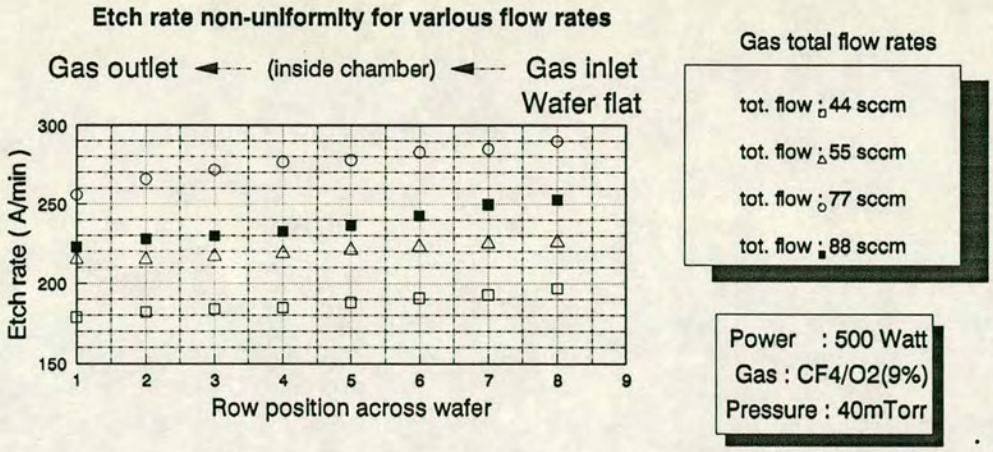

Figure 6–15: The etch rate variation across the wafer for different total flow rate values.

increase of the etch rate of the photoresist and leads to a higher etch selectivity of photoresist over Si.

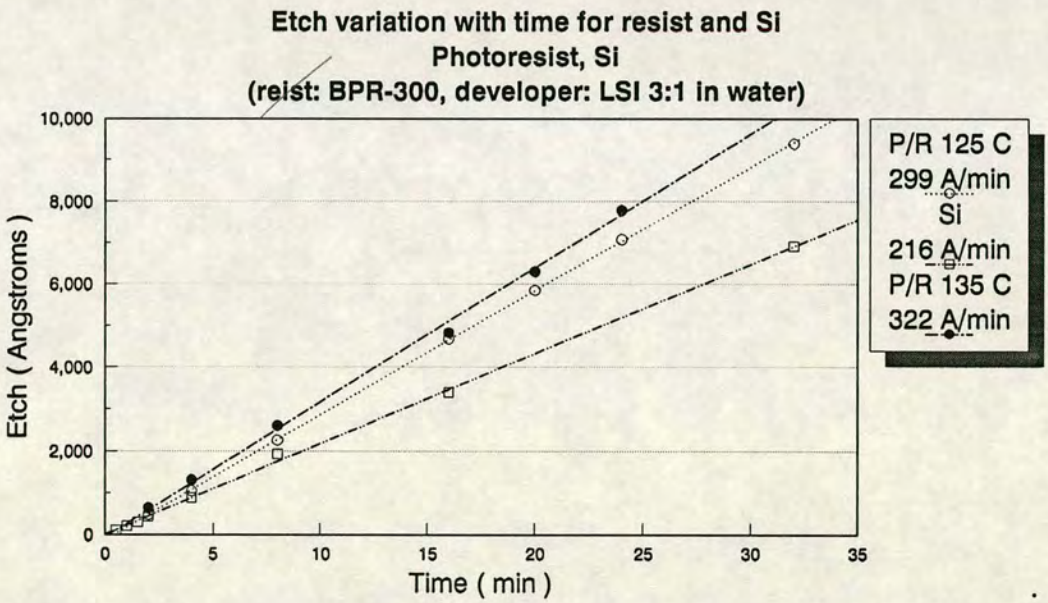

Figure 6–16: Etch variation with time for photoresist and Si. The photoresist (P/R) has been subjected to different post-exposure bake (PEB) temperatures.

The selectivity of the etch rate of resist over Si is crucial for effective pattern

transfer. A selectivity value of 1 leads to the exact replication of the trenches from photoresist into silicon. A high selectivity value leads to trenches of shallower depths to be transfered into Si. Such a selectivity is advantageous for profiling shallow implants. Higher selectivity values also improve the depth uniformity along the flat-bottom of each trench in Si. A selectivity of 1.41 was achieved in the stabilized PET process.

6.3.4 Observations and hints

6.3.4.1 Temperature

A constant temperature of 42 °C inside the RIE chamber has been used for all the experiments. Higher temperatures will result in an increase of the photoresist etch rate. They will thus affect the selectivity of photoresist over Si without affecting the degree of damage. An increase in the RIE electrode temperature seems to be the safest way to increase the selectivity without severely altering the Si etch rate.

6.3.4.2 Chamber condition

The dry etching technique suffers from a 'memory effect'. If other gases or materials have been previously used inside the chamber, they can change the etch rate and affect the contamination levels of the PET technique. A 15 minutes oxygen RIE pre-run is recommended to clean the chamber.

6.3.4.3 RIE set-up.

In order to RIE etch a wafer, a repetitive method is needed to minimize random errors. Oxygen ashing for 15 minutes has been recommended above. After placing the wafer(s) on the outer row of the etch electrode (where etch non-uniformities are minimum), the system is pumped down to a base pressure of 3mTorr. This base pressure value might vary from etcher to etcher due to the condition of the seals. When the base pressure is achieved, the gases are switched on at the desired

ratio. The pressure rises and stabilizes at a certain value (26.7mTorr for a 50 to 5 gas ratio and 3.0mTorr base pressure). This value depends(not linearly) on the base pressure value. About 2 minutes after the pressure has stabilized, we can set the desired pressure for the etch. As soon as this value is reached, we let the system stabilize (2 extra minutes) and initiate the etch at the desired power level. All the above pressure values should be consistent between different etch runs if high repeatability is desired.

6.3.4.4 Hydrogen permeation effect

Although hydrogen is not deliberately present in the gas that is used for the RIE, it exists as an impurity. The H_2O abundance is the source for atomic hydrogen and H^+ during any type of dry etching. It can permeate into Si at 400 Å beneath the silicon surface [34] or even deeper. Spreading resistance measurements have shown that it causes dopant deactivation and therefore lowers the carrier concentration [35]. This effect is more pronounced on p-type semiconductor layers [13]. The only way to avoid the problem is to try to get the chamber down to a very low base pressure before initiating the RIE.

6.3.4.5 Native oxide layer

Since native oxide formation cannot be avoided, great care should be taken to ensure that it is uniform and repeatable from wafer to wafer. A standard wafer treatment before the etch is necessary to ensure that no etch rate variation will take place due to the above effects. Native oxide growth is discussed in chapter 7. The time of the wafer exposure to air should be the same for all wafers before any RIE step. As mentio ned earlier, this oxide formation is desirable to reduce the RIE damage.

The wafers that have patterned photoresist on their surface exhibit a higher etch rate near the edges of the wells compared to the region in the centre of those wells. This effect is observed in all Dektak trench profiles across the wafer and should be taken into account in the depth measurements.

6.3.4.6 Impurity contamination clean

Impurities in the permeated and contaminated layers near the surface affect both electrical and optical measurements on Si. In order to remove the contamination without adding any more damage to the wafer a 3 minutes oxygen ashing followed 5 % HF dip is used. This treatment seems to stabilise the optical constants measurements.

6.4 The resulting PET structures

A PET structure with its trenches at the different depths (as measured by Dektak profilometry) can be seen in fig. 6–17 and fig. 6–18. A series of depths at 91, 222, 311, 438, 585, 817, 867, 934, 1329, 1782, 1967, 2093, 2310 and 2488 Å has been measured on a single wafer. The depth values of each Dektak printout are displayed in the bottom right corner of each scan (as AVG HT). They are the average between the position of the R and M vertical lines at each scan. The zero position is at the Si surface, therefore those heights appear with a negative sign. PET structures with their deepest trenches extending to a 5000 Å depths into Si, with a step difference of 300 Å between neighbouring trenches have also been fabricated for the characterization of deeper implants.

The PET technique has, therefore, been implemented and thoroughly studied. At the same time a two-dimension RIE etching technique has been developed. The intra-wafer non-uniformity for such a technique has been carefully investigated. A linear variation of the etch rate with the radial chamber position has been found. The slope of the linear variation depends on the specific process parameters. No appreciable etch rate variation has been found in any other direction across a wafer.

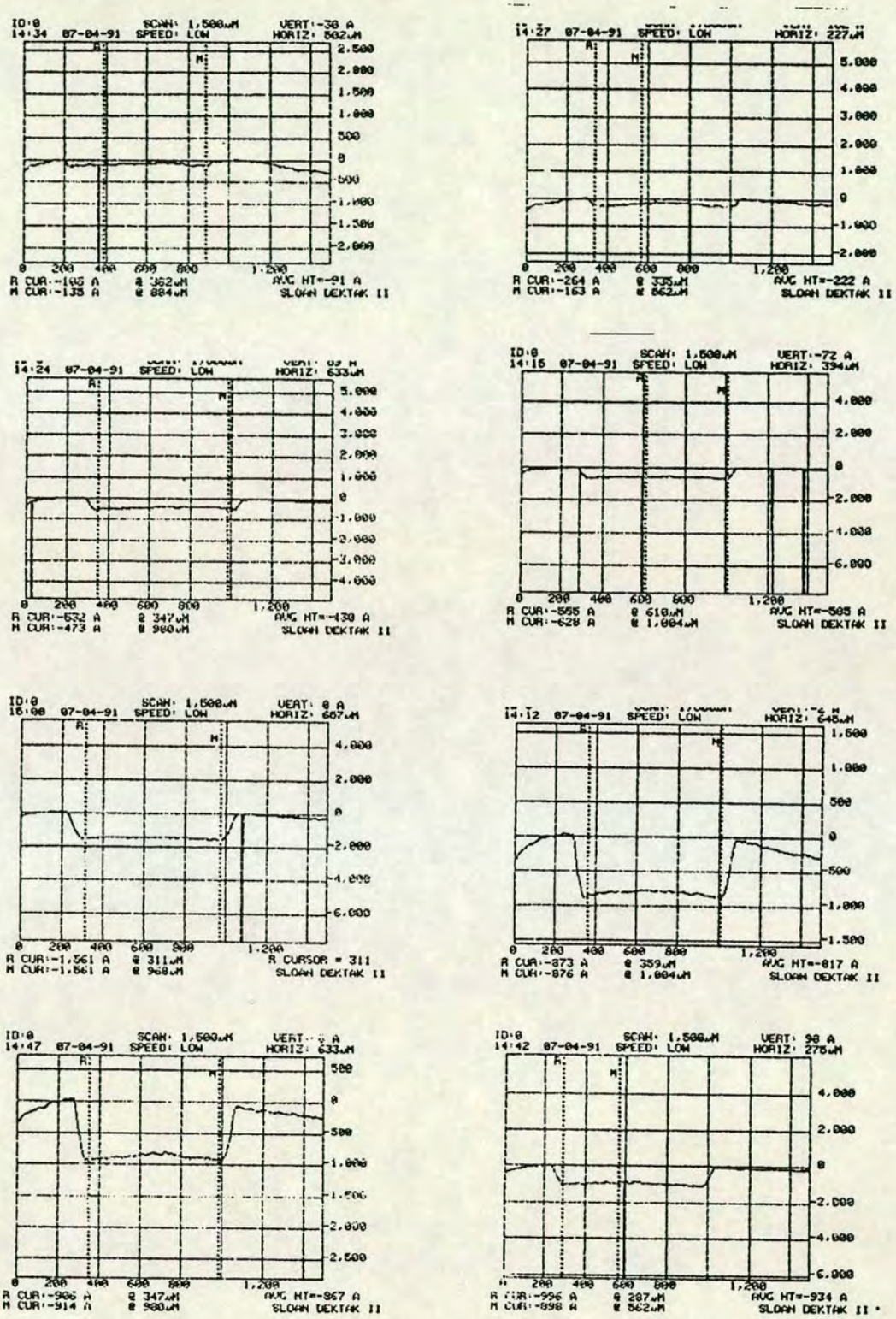

Figure 6–17: Dektak scans of neigbouring trenches in a PET structure. The depths are indicated at the bottom right corner of each scan and are the average value between the R and M vertical line positions. The measured depths are 91 Å, 222 Å, 438 Å, 585 Å, 311 Å 817 Å 867 Å 934 Å.

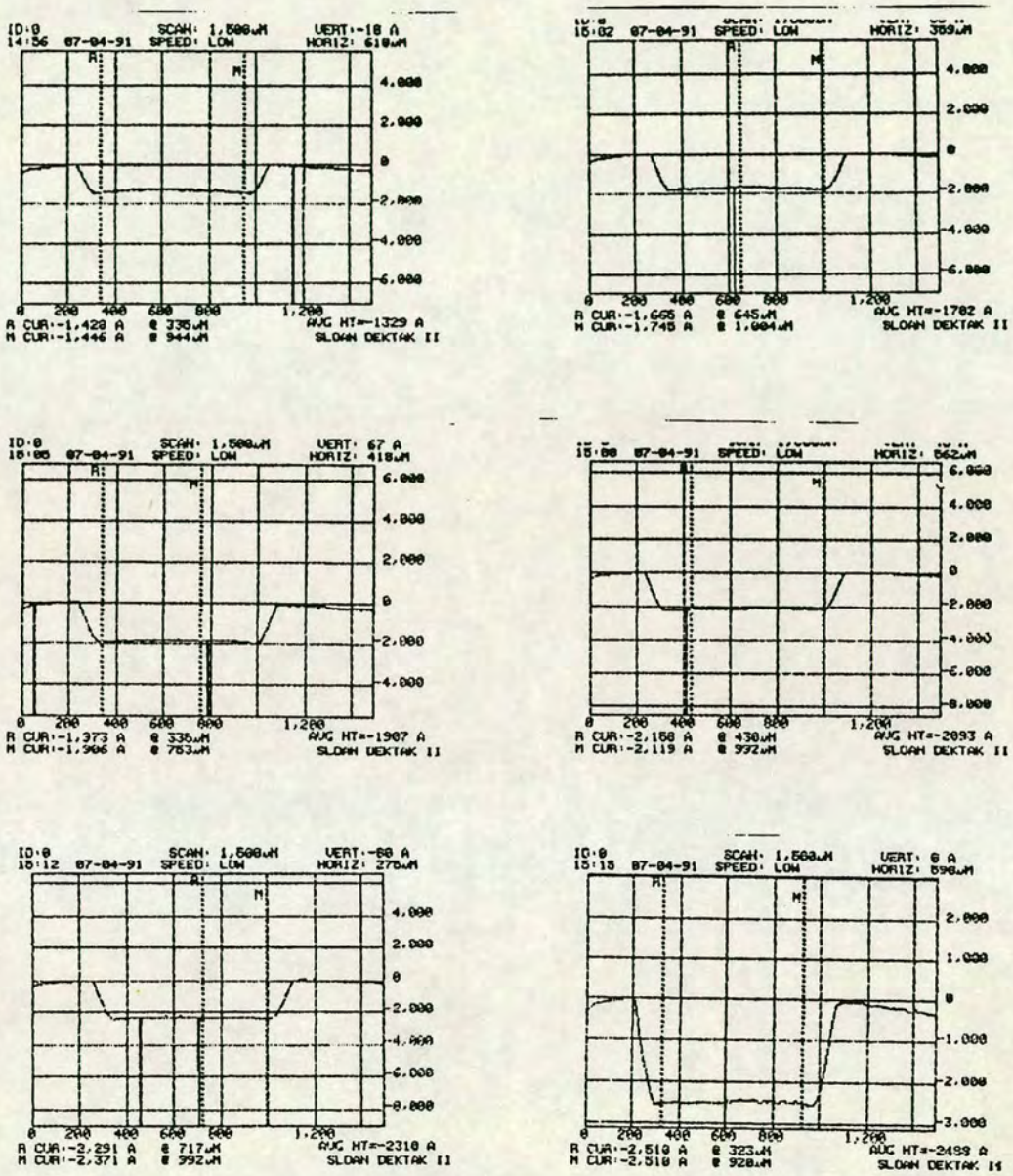

Figure 6–18: Dektak scans of neigbouring trenchess in a PET structure. The depths are indicated at the bottom right corner of each scan and are the average value between the R and M vertical line positions. The measured depths are 1329 Å, 1782 Å, 1967 Å, 2093 Å, 2310 Å, and 2488 Å.

Bibliography

[1] R. J. T. Bunyan. A novel technique for measuring concentration profiles of depths less than 1 μm. *B.Sc. Hons Project Report*, HSP 604.

[2] T. Batchelder and J. Piatt. Bake effects on positive photoresist. *Solid State Technology*, 8(8):211, 1983.

[3] M. Watts, T. Perera, B. Ozarski, D. Mayers, and R. Tan. Photoresist as its own process monitor. *Solid State Technology*, 13(7):59, 1988.

[4] J. Picansky and J. R. Lyeria. Photochemical decomposition mechanisms for AZ-type photoresist. *IBM Journal of Research and Development*, 23(1):43, 1979.

[5] W. R. Harshbarger, T. A. Miller, P. Norton, and R. A. Porter. *Applied Spectroscopy*, 31:201, 1977.

[6] C. J. Mogab, A. C. Adams, and D.L.Flamm. Plasma etching of silicon and silicon dioxide - the effect of oxygen additions to carbontetrafluoride plasmas. *Journal of Applied Physics*, 7:3796–3803, 1978.

[7] D. L. Flamm. Measurements and mechanisms of etchant production during the plasma oxidation. *Solid State Technology*, 4:109–116, 1979.

[8] M. A. Hartney, D. W. Hess, and D. S. Soane. Oxygen plasma etching for resist stripping and multilayer lithography. *Journal of Vacuum Science and Technology*, B7(1):1–13, 1989.

[9] A. T. Bell. *Techniques and Applications of Plasma Chemistry.* Wiley-Interscience, New York, 1974.

[10] L. Pederson. Structural composition of polymers relative to their plasma etch characteristics. *Journal of the Electrochemical Society*, 129:205, 1982.

[11] J. M. Cook and B. W. Benson. *Journal of the Electrochemical Society*, 130:2459, 1983.

[12] G. Oehrlein. Dry etching damage of silicon:A review. *Materials Science and Engineering*, B4:441–450, 1989.

[13] S. J. Fonash. An overview of dry etching damage and contamination effects. *Journal of the Electrochemical Society*, 137(12):3885–3892, 1990.

[14] J. W. Corbett. Electron radiation damage in semiconductor and metals. *Solid State Physics*, suppl.7, 1966.

[15] J. H. Crawford and L. M. Slifkin. *Point Defects in Solids*, volume 2. Plenum Press, 1975.

[16] N. B. Urli and J. W. Corbett. *Radiation Effects in Semiconductors*, volume Conf.Series No.31. Institute of Physics, 1977.

[17] G. D. Watkins. *Radiation Damage in Semiconductors*, volume 2. Academic Press, New York, 1965.

[18] Y. H. Lee and J. W. Corbett. EPR studies of defects in electron-irradiated silicon. *Physical Review*, B13:2653, 1976.

[19] K. Murakami, K. Masuda, K. Gamo, and S. Namba. *Ion Implantation in Semiconductors.* Plenum, 1975.

[20] K. L. Wang, Y. H. Lee, and J. W. Corbett. Defect distribution near the surface of electron-irradiated silicon. *Applied Physics Letters*, 33:547, 1978.

[21] D. E. Harrison, J. P. Johnson, and N. S. Levy. Spot patterns and Silsbee chain on a si crystal. *Applied Physics Letters*, 8:33, 1966.

[22] F. R. McFeely, J. F. Morar, N.D. Shinn, G. Landgren, and J. F. Himpsel. Sychnotron photoemission investigation of the initial stages of fluorine attack on si surface. *Physical Review B*, 30:764, 1984.

[23] G. S. Oehrlein, C. M. Ransom, S. N. Chakravarti, and Y. H. Lee. Silicon near-surface disorder and etch residues caused by $CClF_3/H_2$ reactive ion etching. *Applied Physics Letters*, 46:686, 1985.

[24] W. K. Chu, R. H. Kastl, R. F. Lever, S. Mader, and B. J. Masters. Distribution of irradiation damage in silicon bombarded with hydrogen. *Physical Review*, B 16:3851, 1977.

[25] J. E. Westmoreland, J. W. Mayer, F. H. Eisen, and B. Welch. Production and annealing of lattice disorder in silicon by 200kev boron ions. *Radiation Effects*, 6:161, 1970.

[26] H. Kinoshita and K. Jinno. *Japanese Journal of Applied Physics*, 16:381, 1977.

[27] A. Jacob. *Solid State Technology*, 20(6):31, 1977.

[28] S. Matsuo and Y. Takehara. *Japanese Journal of Applied Physics*, 16:175, 1977.

[29] J. W. Coburn and E. Kay. Some chemical aspects of the fluorocarbon plasma etching of silicon and its compounds. *Solid State Technology*, 22:117, 1979.

[30] N. M. Johnson, D. K. Biegelson, and M. D. Moyer. Mechanism for hydrogen compensation of shallow-acceptor impurities in single-crystal silicon. *Physical Review*, B31:5525, 1985.

[31] S. J. Fonash. Effect of ion beam sputter damage on Schottky barrier formation in silicon. *Applied Physics Letters*, 39:423, 1981.

[32] C. M. Melliar-Smith and C. J. Mogab. *Thin Film Processes.* Academic Press, New York, 1978.

[33] A. G. Nagy. Radial etch rate non-uniformity in reactive ion etching. *Journal of the Electrochemical Society*, 131:1871, 1984.

[34] G. S. Oehrlein, R. M. Tromp, Y. H. Lee, and E. J. Petrillo. Study of silicon contamination and near-surface damage caused by CF_4/H_2 reactive ion etching. *Applied Physics Letters*, 45:420, 1984.

[35] X. C. Mu, S. J. Fonash, A. Rohatgi, and J. Rieger. Comparison of the damage and contamination produced by CF_4 and CF_4/H_2 reactive ion etching: The role of hydrogen. *Applied Physics Letters*, 48:28, 1986.

Chapter 7

Ellipsometry

7.1 Objective

The PET structure technique can give a series of trenches of increasing depth into Si. In order to extract the ion implantation profile in Si, the values of a physical quantity measured at the flat-bottom of those trenches must take place. Ellipsometry, is a fast and non-destructive technique that might possess the requirements for such a measurement. The physical quantities to be measured are the refractive index and the extinction coefficient of the implanted layer. In order to assess the suitability of ellipsometry to be combined with the PET technique, the influence of ion implantation and RIE on ellipsometry results must be evaluated. The basic theory and the preliminary assessment experimentation are the subject of this chapter.

7.2 Theory

Ellipsometry is a technique that allows the determination of the optical properties of a surface or the optical properties and the thickness of a thin film, by measuring the effect of reflection on the degree of polarization of polarized light. It is based on the fact that a monochromatic electromagnetic wave changes its state of polarization if it strikes non-perpendicularly the interface between two dielectric media. A more detailed analysis of the physics involved in ellipsometry can by found in [1–4]. The two basic approaches which can determine the complex reflection coefficient of a sample are null ellipsometry and photometric ellipsometry [1]. Photometric ellipsometry determines the state of polarization of the probe beam by suitable measurements of its intensity. Null ellipsometry, which is used in the following experiments, comprises all techniques which are based on measuring the state of polarization indirectly by adjusting the azimuths of polarizing prisms and other instrument parameters for an extinction of light falling on a photodetector.

7.2.1 Basic principles

The purpose of this section is not to review the elementary basis for standard ellipsometry but to describe the ellipsometry principles used in a specific instrument, the E-Probe 200 [1] [5].

The most common standard ellipsometry optical configuration (PRSA) consists of a HeNe laser, a rotating polarizer, a quarter wave retarder, the sample, a rotating analyzer and a detector. In the E-Probe system a Photo-Elastic Modulator(PEM) takes the place of the quarter wave plate. Both configurations are depicted in fig. 7–1.

The wavelength of the laser is 6328 Å(red) and it acts as a highly intense, monochromatic source of collimated light with a linear polarization. The PEM

[1] E-Probe is the trademark of GRQ Instruments.

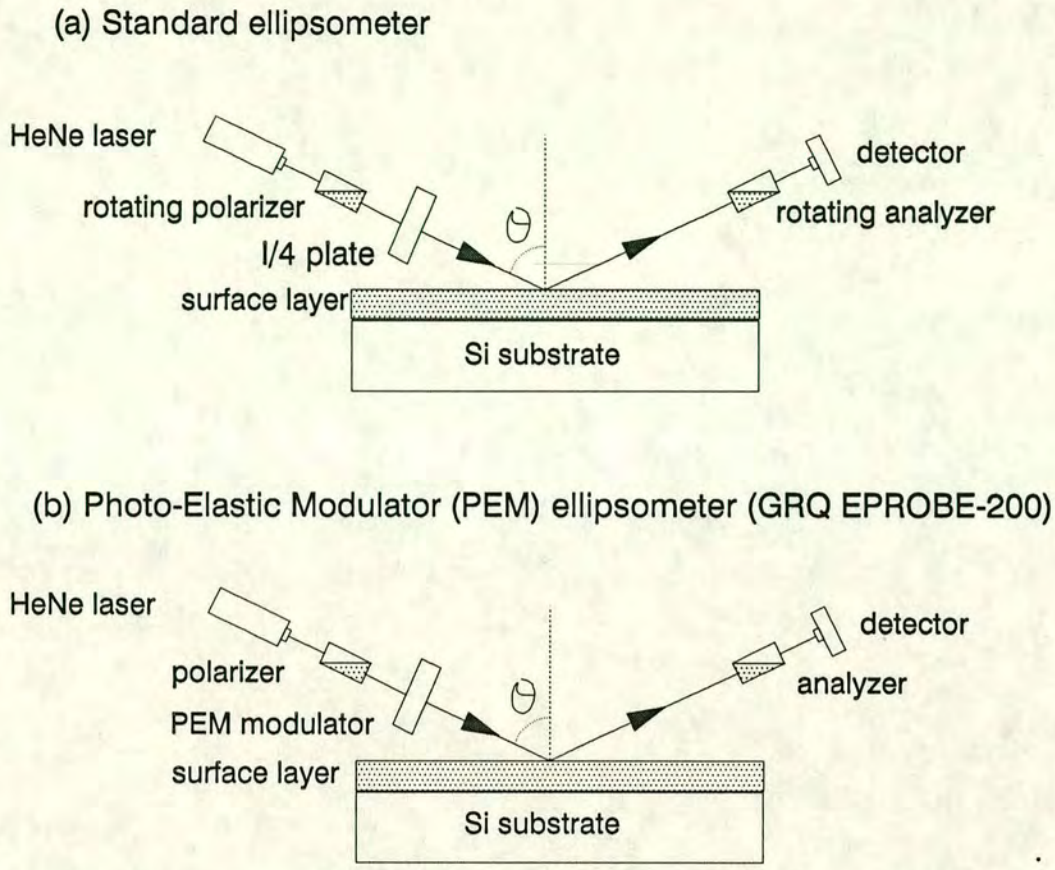

Figure 7–1: The standard and GRQ ellipsometer configurations.

provides a unique means of modulating the polarization of the incident light at a very high speed [6, 7]. This is done by resonantly driving a window of fused silica with a 100KHz pressure waveform, generated by applying a relatively low voltage oscillation to a piezo driving crystal mounted on one edge. It is this feature combined with the high intensity of the HeNe laser, which allows the system to sense surface extinction coefficient factors which are up to three orders of magnitude lower than in conventional instruments [5]. The light is next reflected from the wafer at an angle of 70° from the normal to the wafer surface. The reflected beam then passes through the polarizing analyzer prism and finally the fluctuating signal is received by the silicon detector. Data processing of this signal gives the two ellipsometric parameters Δ and Ψ. The analysis involves DC normalization of the AC component of the detected signal by its DC component and spectrum analysis to determine the amplitude of the most important (those with angular frequencies

ω and 2ω) Fourier components, I_ω and $I_{2\omega}$. Those values are then converted to a digital signal and are sent to a microprocessor to solve the resulting system of 2 equations for Δ and Ψ, [5] :

$$\Delta = \arctan\left[-0.832\left(\frac{I_\omega}{I_{2\omega}}\right)\right] \tag{7.1}$$

$$\Psi = \arctan\left[\frac{B}{2} \pm \sqrt{(B^2-4)}\right] \tag{7.2}$$

where

$$B = 1.727\left(\frac{\cos\Delta}{I_{2\omega}/I_{DC}}\right) \tag{7.3}$$

From the measured values of Δ and Ψ, the refractive index(n) and the extinction coefficient(k) can be obtained from, [8]:

$$n^2 - k^2 = \frac{\sin^2(\phi)\tan^2(\phi)\left(\cos^2(2\Psi) - \sin^2(2\Psi)\sin^2(\Delta)\right)}{(1+\sin(2\Psi)\cos(\Delta))^2} + \sin(\Psi) \tag{7.4}$$

$$k = \frac{\sin^2(\Psi)\tan^2(\Psi)\sin(4\Psi)\sin(\Delta)}{2n\,(1+\sin(2\Psi)\cos(\Delta))^2} \tag{7.5}$$

where ϕ is the angle of incidence.

7.2.1.1 Error effects in ellipsometric investigations

Like any experimental technique, ellipsometric measurements are subject to various errors.

a. **Random errors.** Imperfect determination of the intensity minimum and various noise sources in photometric components are the main sources of random errors. In general, the only way to reduce such errors to take a number of measurements and apply statistical procedures to the results.

b. **Equipment imperfections and systematic errors.** The accuracy of the measurements is determined by factors such as: mechanical precision and stability of the setup, imperfection of the optical components [9], deviation of the angle of incidence of the laser beam from 70^{circ}, bad mechanical alignment, the intrinsic accuracy of the data acquisition and processing system,

quantization noise generated by digital processing of the analogue photodetector output [10] and the optically or electrically generated noise [11, page 51]. The E-probe 200 that has been used for the experimental work in this project has software routines to control the setup and check the mechanical and electrical status of the ellipsometer. Furthermore, calibration routines and experiments have been used to optimize the instrument sensitivity and accuracy for measurements of oxide layers on top of Si substrates.

c. **Sample data errors.** Since the evaluation of an ellipsometric measurement requires the accurate knowledge of all optically relevant parameters of the sample -except for the two to be calculated-, any inaccuracy propagates through the numerical analysis. The same type of error can be observed if an inaccurate optical model is used and it is more thoroughly discussed in the following section.

7.2.2 Characterizing ion implantation by ellipsometry

Ellipsometry is a sensitive, rapid, nondestructive method which may be used to evaluate the complex refractive index of an absorbing layer or the real part of the refractive index and the thickness of a transparent layer on an absorbing substrate. Ion implantation-induced crystal damage causes variations in the optical parameters of the implanted region. Therefore, there is a change in the complex refractive index of the substrate surface. The largest change occurs when light at the band-gap energy or other interband transition energies is used [12]. By virtue of its experimental simplicity and non-destructive nature, there have been numerous efforts to use ellipsometry to investigate crystal damage resulting from ion implantation in Si. However, quantitative measurement of the refractive index and extinction coefficient changes are complicated by the fact that for Si the implanted wafer has a complex multilayer structure:

1. **A single-crystal substrate.**
2. **The ion implantion damaged layer.**
3. **A native oxide SiO_{2-x} $(0 < x < 1)$** over the damaged layer [13].

4. **The ambient medium.**

The ellipsometric amplitude ratio Ψ and the phase difference Δ can be related to physical parameters such as the complex refractive index and the layer thickness. Since this relation depends on the multilayer optical model adopted, interpretation of the method's results depends on the model being used. A formidable problem is selecting a film model that approximates to the physical configuration in such a way as to yield meaningful optical constants without being unduly complicated. Various ellipsometric model approximations have been made in the literature.

7.2.2.1 Simple models

The damage-only model. In this model the implanted wafer is regarded as a damaged layer only. Ellipsometric characterization of the damage has been reported for both high-dose ion implantation [14–16] and for doses as low as 3×10^{11}ions/cm^2 [8]. For both cases, the Δ and Ψ ellipsometric parameters are measured. Then by using eq.(7.4) and (7.5) the refractive index and extinction coefficient are evaluated. Since the above equations are valued only for a substrate with no layer on top of it, the so-called pseudo-optical constants $\overline{n}$ and $\overline{k}$ can be obtained. Although these parameters represent two-layer-average values and do not have a clear physical meaning, they can be effective for implant monitoring as they are dose-dependent.

Damaged layer under a 20 Å native oxide of assumed refractive index

In this two-phase material approximation based on [17], we assume that the upper phase is a 20 Å thick native oxide with a 1.46 refractive index value. The measured components of the complex refractive index are average values over some part of the implant distribution. Therefore, they can be only taken as effective values and assuming a damage layer of uniform depth. Since the absorption coefficient of amorphous Si is around $2 \times 10^5 \text{cm}^{-1}$ at 5461Å, for an implanted layer of 600 Å the incident light will be attenuated by more than a factor of e. It is therefore obvious that the contribution of the underlying substrate is less dominant and the model closely represents the implanted

layer. For very thin implanted layers (ie for less than 100 Å projected range) the model is not very accurate. Due to its simplicity this model has been used for many ion implant studies [18–21].

Damaged layer covering the substrate, neglecting native oxide The assumption here is that the thickness of the damaged layer is equal to the projected range R_p plus the straggle ΔR_p of the ion.

All the above models have proved to be useful for monitoring **relative changes** of both components of the complex refractive index, resulting from ion implantation. They are less adequate for considering actual values since the effective implant depth is neglected. In order to determine the degree of annealing or the surface condition of a wafer, a series of preliminary experiments was designed. Those preliminary experiments are discussed in section 7.3 while applications of the technique appear in chapters 8 and 9.

7.2.2.2 More complex optical models

Ellipsometry is extremely sensitive to the topmost layer, which in our case is a native oxide over the implanted layer. This means that four parameters have to be determined for each sample and wavelength, namely the native oxide thickness, the amorphous or damaged layer thickness and the complex refractive index of the amorphous layer. The complex refractive of the substrate (crystalline Si) and of the native oxide can be measured by other independent measurements or taken from the literature [22–24].

In refraction ellipsometry the experimental result is given by:

$$\rho \equiv \tan\psi \exp(i\Delta) \tag{7.6}$$

where ρ is the complex reflectance ratio. ρ, ψ and Δ are functions of the laser wavelength used in the measurements, the angle of incidence ϕ and the optical and physical properties of the reflecting system,

$$\rho = \rho(\lambda, \phi, \vec{B}) \tag{7.7}$$

$$\psi = \psi(\lambda,\, \phi,\, \vec{B}) \tag{7.8}$$

$$\Delta = \Delta(\lambda,\, \phi,\, \vec{B}) \tag{7.9}$$

where $\vec{B} = (b_1, b_2, \ldots, b_s)$ is the vector that contains the physical and optical parameters of the multilayer system, such as layer thicknesses (d_j), refractive indices (n_j) and extinction coefficients (k_j), s=3f+2 where f denotes the number of films of the system. From an ellipsometric measurement at fixed wavelength and angle we can determine only two unknown parameters, so several methods have been developed to increase the number of experimental data [1,25,26]:

a. measurements at different angles of incidence. In multiple angle of incidence (MAI) ellipsometry, for n distinct angles we will have 2n simultaneous nonlinear equations:

$$\psi_n^m = \psi_n^c(\lambda,\, \phi_n,\, \vec{B}) \tag{7.10}$$

$$\Delta_n^m = \Delta_n^c(\lambda,\, \phi_n,\, \vec{B}) \tag{7.11}$$

where the m and c superscripts denote measured and computed values respectively and the $\vec{B}$ vector contains the unknown parameters as before. The solution is the $\vec{B_0}$ vector that gives a minimum for the sum of squares of the residuals:

$$G\left(\vec{B}\right) = \sum_{i=1}^{n} \left\{ \left[\frac{1}{\epsilon_1}\right]^2 \left[\psi_i^m - \psi_i^c\left(\lambda,\, \phi_i,\, \vec{B}\right)\right]^2 + \left[\frac{1}{\epsilon_2}\right]^2 \left[\Delta_i^m - \Delta_i^c\left(\lambda,\, \phi_i,\, \vec{B}\right)\right]^2 \right\} \tag{7.12}$$

ϵ_1 and ϵ_2 denote the errors in the δ and ψ values measurements. It must be noted that the accuracy of the solution is reduced by cross-correlations between the fitted parameters [27].

b. multiple wavelengths. The situation is analogous to method a. The only difference here is that ϕ is constant and λ_n denotes the different wavelengths. Equations (7.10), (7.11) and (7.12) are therefore valid with the above changes for wavelength and angle values.

c. combination of MAI and multiple wavelengths. The equations are a combination of the two previous cases. For n different angles of incidence and l wavelengths we have a system of 2nl simultaneous nonlinear equations:

$$\psi^m_{n,l} = \psi^c_{n,l}(\lambda_l,\ \phi_n,\ \vec{B}) \tag{7.13}$$

$$\Delta^m_{n,l} = \Delta^c_{n,l}(\lambda_l,\ \phi_n,\ \vec{B}) \tag{7.14}$$

$$G\left(\vec{B}\right) = \sum_{i=1}^{n}\sum_{j=1}^{l}\left\{\left[\frac{1}{\epsilon_1}\right]^2\left[\psi^m_{i,j} - \psi^c_{i,j}\left(\lambda_j,\ \phi_i,\ \vec{B}\right)\right]^2 + \left[\frac{1}{\epsilon_2}\right]^2\left[\Delta^m_{i,j} - \Delta^c_{i,j}\left(\lambda_j,\ \phi_i,\ \vec{B}\right)\right]^2\right\} \tag{7.15}$$

d. different thicknesses of the same film. If we have m samples with different thicknesses of amorphous layers and if we make the assumption that the native oxide thickness is the same on all wafers, then 2m simultaneous nonlinear equations result:

$$\psi^m_j = \psi^c_j(n, k, d, d_j) \tag{7.16}$$

$$\Delta^m_j = \Delta^c_j(n, k, d, d_j) \tag{7.17}$$

where j = 1, . . . , m, n and k are the complex refractive index components for the amporphous Si, d is the average thickness for the native oxide and d_j is the thickness of the jth sample. For m $\geq$ 3 there is more data than unknown parameters. The experimental errors and model inaccuracies (ie for non-sharpness of interfaces) render the solution of the above system of equations inaccurate and therefore a least-squares solution must be sought. If, once more, we represent the variables as the components of $\vec{B_j} = (n, k, d, d_j)$ for each sample j, the solution is a vector $\vec{B_{j0}}$ that minimizes :

$$G\left(\vec{B}\right) = \sum_{j=1}^{m}\left\{\left[\frac{1}{\epsilon_1}\right]^2\left[\psi^m_j - \psi^c_j\left(\vec{B_j}\right)\right]^2 + \left[\frac{1}{\epsilon_2}\right]^2\left[\Delta^m_j - \Delta^c_j\left(\vec{B_j}\right)\right]^2\right\} \tag{7.18}$$

e. Sequential sectioning and measuring. In this approach an optical model is chosen and the optical constants are extracted according to it. Then, a

layer of material is removed using a chemical or physical method and the measurements are performed again. The optical constant values as a function of depth give the in-depth damage profile. The accuracy and details of this method are presented in detail in section 7.2.3.

7.2.3 Assessment of models for ion implantation monitoring

The effect of implantation-induced damage on the optical characteristics of Si is different from the case of compound semiconductors (eg GaP) [20]. The sensitivity of the optical constants of Si depends on the wavelength used. Changes in optical constants are attributed to a transformation of the energy band structure of Si associated with amorphous-phase formation. The disorder will cause broadening in k space and smear out the critical point regions -characteristic of the crystalline phase-. If the energy of light used is smaller than the interband transition energy, the integral density of states increases and the optical absorption coefficient ($= \frac{4\pi k}{\lambda}$) and reflectivity will increase.

7.2.3.1 Variation of n, k, R with implant parameters

1. **Variation of n, k and R with implant dose.** It has been reported that the degree of disorder increases with dose [28]. The effect of disorder production as a function of increasing dose for $^{11}B^+$ and $^{31}P^+$ implantation has been investigated using the different models mentioned earlier. The results are however, conflicting. In [29] the results from the four-layer optical model for ellipsometry were correlated with channeling experiments for different doses of the above mentioned-species. For a 40keV $^{11}B^+$ implant in the dose range of 3.0×10^{15} to 1.0×10^{16} ions/cm^2, the channeling spectrum shows a rather inhomogeneous disorder distribution. The energetic boron ions generate substantial disorder near the surface of Si and also a buried disorder peak at a depth of more than 1200 Å. This well-defined damage peak just below the surface has also been observed in [30, 31]. Ellipsometric coefficients are

extremely sensitive to surface layers. Therefore surface disorder dominates the apparent ellipsometric parameters while the buried disorder has only a secondary effect on these parameters because of the attenuation of the light while traversing the near-surface region. The rectangular, homogeneous shape of the damaged layer of the model is therefore inaccurate for doses below amorphization. The same type of behaviour is observed for 60keV P^+ implants in the 1.5×10^{14} to 3×10^{15}ions/cm^2 range [29]. Only after full amorphization of the target, can the ellipsometric results be accurate enough to follow the theoretical curve as derived from that model.

Dependence of the optical constants on ion-dose has also been studied and presented in [32]. The dose range over which there is a change (increase) in the optical constants is $10^{13} - 10^{16}$ ions/cm^2 for the P^+ monomer. The slope of the change is **not** constant through that dose range. There is a sharp slope increase in the $10^{14} - 10^{15}$ region which suggests that the sensitivity of the technique is high after the onset of the amorphous state (around 2×10^{14} for P). For doses higher than 10^{15}, slope decreases and suggests that ion-beam annealing is occuring. High-dose implants lead to a wafer temperature rise, which is insufficient to promote diffusion of the dopant-defect density but which may lead to some annealing of defects. The three-layer optical model [20, 21] seems incapable of detecting this self-annealing effect through extinction coefficient (k) monitoring. The rapid increasing of the extinction coefficient with increasing dose in the $10^{15} - 10^{16}$ range suggests an increase in the amorphous layer thickness with increasing dose or change of the degree of amorphousness [28, page 39]. However, refractive index saturation for that dose range reveals the self-annealing that takes place. The two-layer model of n and R parameters [14, 8] shows negligible sensitivity to dose variations. Extinction coefficient is the only dose-sensitive parameter in that model.

2. **Variation of n, k and R with implant energy.** For the four-layer model all three parameters, n, k and R, decrease as the implant energy is increased [32]. Any increase in implant energy moves the damage peak deeper into the target. As already mentio ned, ellipsometry is a surface sensitive technique

so n, k and R decrease as the damage peak moves away from the surface and towards the Si bulk. Those results show that ellipsometry is not suited to monitor implant depth variations due to implant energy variations.

3. **Variation of n, k and R with implant species** From the results of [33] lattice damage produced by light ions (ie B) cannot be monitored by ellipsometry with a high sensitivity. The calculated optical constants(especially in the four layer model) are the results of an integration with limits set by the wafer surface and the damage edge in the substrate as determined by the calculated amorphous layer thickness values. In order to compare the effects of the different implanted species by using induced lattice damage as a criterion, similar amorphous layer thickness values have to be investigated. From the results of [32] it can be seen that a B implant of 31 keV at 10^{14} ions/cm^2 gives the same optical constants as a 48 keV As implant at 10^{13}ions/cm^2. It is more likely that this result is due to the surface sensitivity 'disadvantage' of ellipsometry and not to its capability to distinguish between different species. A comparison of the optical constants for P monomer and dimer ion implants in [32] and of the As monomers and dimers in [33] shows that the distinction between optical constants for a mass ratio 2:1 is within the range of experimental error.

7.3 Preliminary experimental work

In order to use ellipsometry to monitor ion implantation damage a series of experiments was conducted in order to see the effect of the different models used to represent damage and of native oxide thickness. Furthermore, since the PET technique uses RIE, the sensitivity of the refractive index and the extinction coefficient to RIE induced damage has to be monitored.

7.3.1 Monitoring oxygen ashing

7.3.1.1 Defining the problem

While monitoring high dose ion implanted wafers using ellipsometry, it was found that sigma variations as big as 15% were produced in a 69 point wafer map of the n- and k-values. Such big variations make the dose correlation of n and k useless in that dose regime. The reason for such a high variance has to be scrutinized. During ion implantation, hydrocarbon contamination particles are deposited on the wafer's surface [34]. Their origin as discussed in chapter 2 is mainly the vacuum pumps. It was pointed out [35] the amorphization effects of the implanted layer are shielded by the contaminated layer. This became obvious from the effect of surface contamination on the values of the ellipsometric parameters Δ and Ψ [36]. Attempts were made to clean the surface by standard and more sophisticated chemical methods. As mentioned in [14] for low doses, implantation through a protective thin oxide film and subsequent oxide etching in an HF buffered solution is a satisfactory surface cleaning for optical purposes. However, higher doses, even through a protective oxide film, may lead to carbon contamination on the wafer's surface. This is due to recoil implanted carbon in the surface of the wafer. An oxygen plasma is widely used to remove carbon based materials (eg photoresist) in Si fabrication. It therefore constitutes a way of cleaning a carbon-contaminated wafer surface before conducting ellipsometric studies.

7.3.1.2 The experiment

In order to assess the effectiveness of oxygen ashing clean, the following experiment was carried out. Two wafers had their refractive index and extinction coefficient monitored after each of thirteen process events. Those events were:

1. Initial "clean" wafers.
2. Ion implant without any protective oxide.
3. Oxygen ashing 1 for 1min.
4. Native oxide removal in 10 % HF for 30 s.
5. Oxygen ashing 2 for 1min.

6. Native oxide removal in 10 % HF for 30 s.
7. Oxygen ashing 3 for 1min.
8. Native oxide removal in 10 % HF for 30 s.
9. Oxygen ashing 4 for 1min.
10. Native oxide removal in 10 % HF for 30 s.
11. 10 days exposure of the wafer to air
12. 10 % HF clean for 30s.
13. Oxygen ashing 5 for 3min.
14. Native oxide removal in 10 % HF for 30 s.

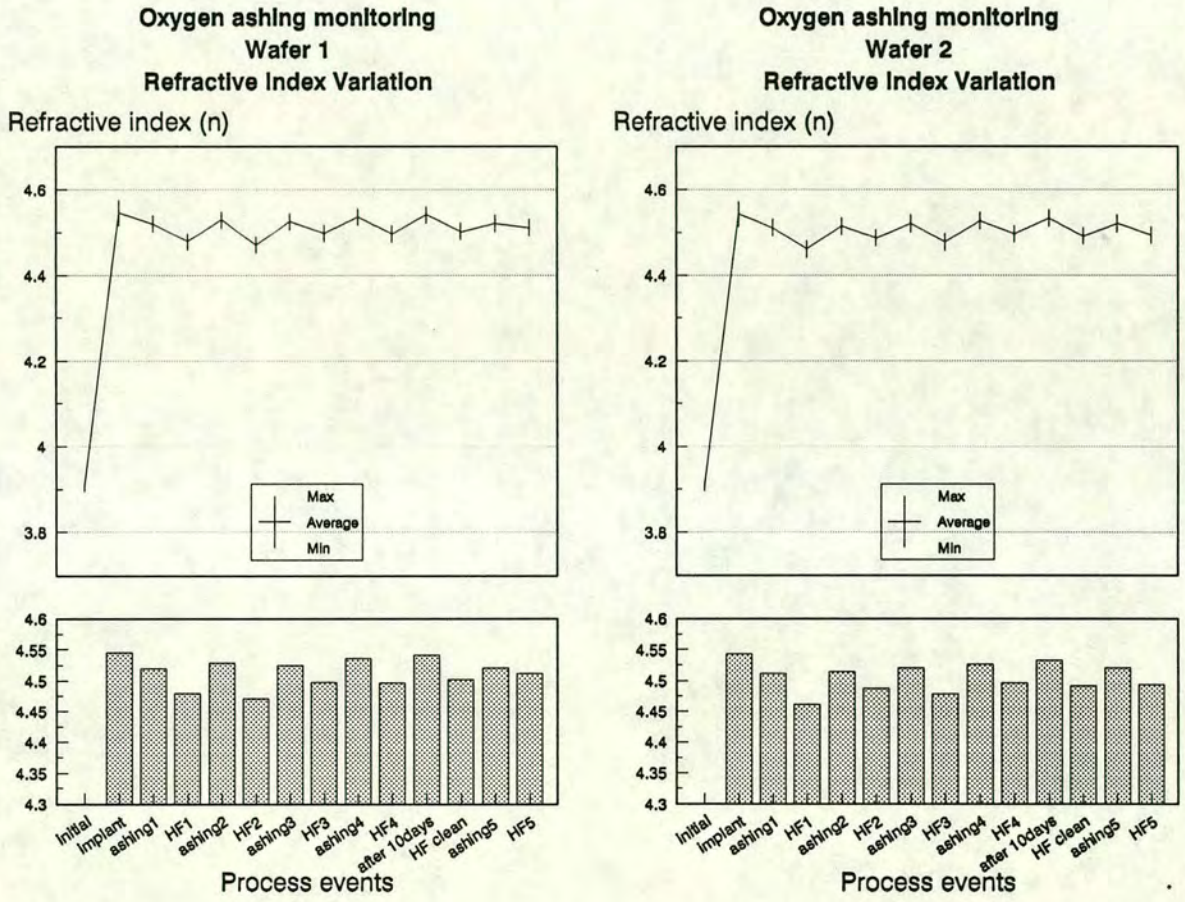

Figure 7–2: Refractive index variation after each of 14 process events. Maximum and minimum values represent 3-sigma values. The bar charts underneath each graph show the n variation in a larger scale.

For each step, an average value and a 3-sigma value was taken from the 16 measurement sites for each wafer.

7.3.1.3 Conclusions and discussion

The results are depicted in fig 7–2 and fig. 7–3. Two general comments can be made about the measurement accuracy. Both wafers present very close n- and k-values after most of the steps. Therefore, they reveal a good wafer-to-wafer reproducibility of the monitoring procedure. Thus the method proves to be accurate enough to be used in conjunction with the four-point-probe technique to assess the degree of annealing or the surface condition of a wafer. The 3-sigma values reveal that the n- and k- differences after each ashing and HF cleaning step are bigger than the experimental error.

In fig. 7–2 the refractive index monitoring results are presented. The big increase in the n value after the implant is due to the surface ion damage plus the carbon contamination effect. After the ashing step the n-value slightly drops. This decrease is due to the removal of the carbon contamination from the surface. The further n-value decrease after the HF clean shows the effect of removal of native oxide grown during the oxygen ashing step, which affects the measured refractive index. In order to ensure that this decrease is due to the oxide layer (and not to oxygen ashing damage removal or any other reason), after step 10 the wafer was left in the air for 3 days. The intention was to grow a native oxide of around 18 Å. The n-value after step 11 is close to the value after each ashing step while step 12 gives an n-value equal to those after each HF step. The result verifies the above assumption.

The same type of variations are shown by the extinction coefficent, k, in fig. 7–3. The 3 min ashing of step 13 does not decrease (within experimental accuracy) n or k values significantly more than the 1 min ashing in the previous steps. The variation in %-sigma after the oxygen ashing and HF cleaning steps is reduced to less than 4%.

The main conclusion from the above experiments is that, although oxygen ashing can be effective in cleaning hydrocarbon off the wafer surface molecules for ellipsometric monitoring, oxide removal is still necessary in order to have a more

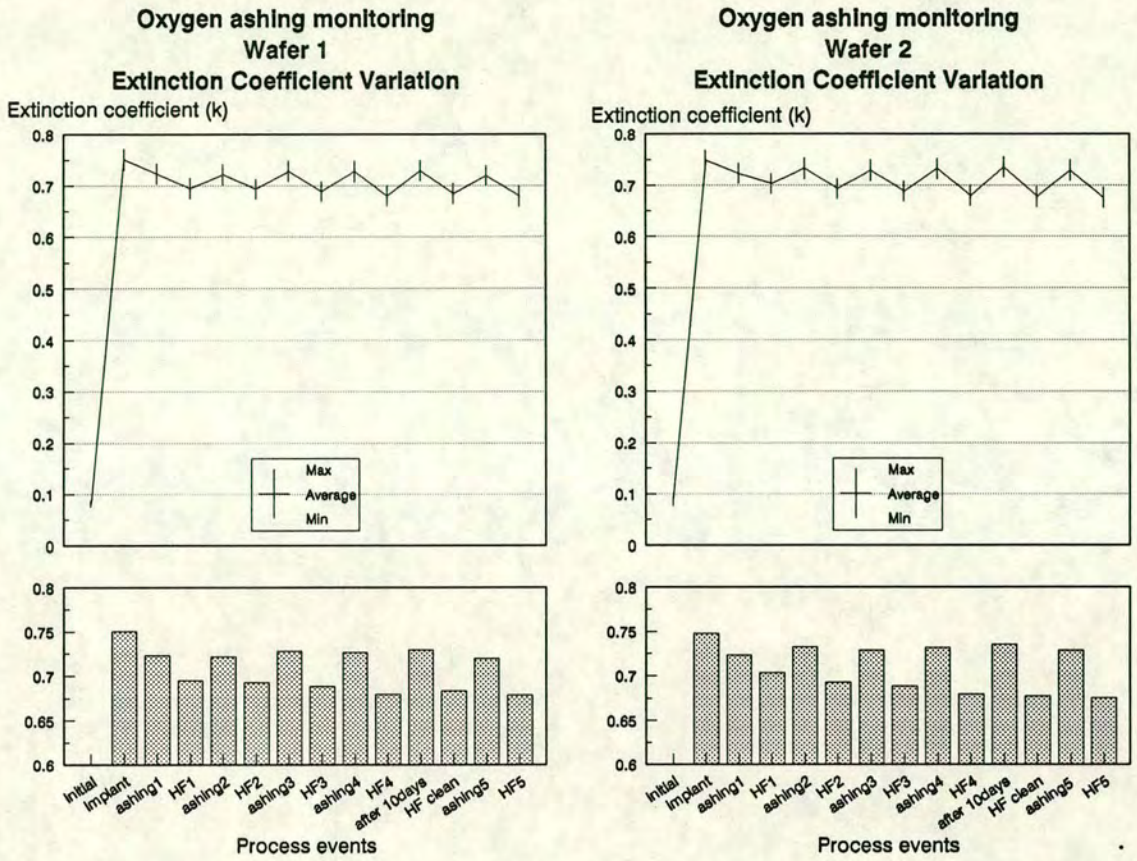

Figure 7–3: Extinction coefficient variation after each of 14 process events. Maximum and minimum values represent 3-sigma values. The bar charts underneath each graph, present the n variation in a larger scale.

accurate layer model. This principle of operation must be respected, especially if a simple model approximation is attempted.

7.3.1.4 Optimum time for oxygen ashing

In order to evaluate the optimum time of oxygen ashing for cleaning the implanted surface the n and k values were monitored after each HF cleaning step. The results are presented in fig. 7–4 and fig. 7–5. It was found that n increases with ashing time while k decreases. However the k decrease is within the experimental error so we cannot be sure if it is a real decrease or a measurement error. A rule of

thumb would be that a 2-3 min ashing is long enough to etch away the carbon contaminants and stabilise the k coefficient.

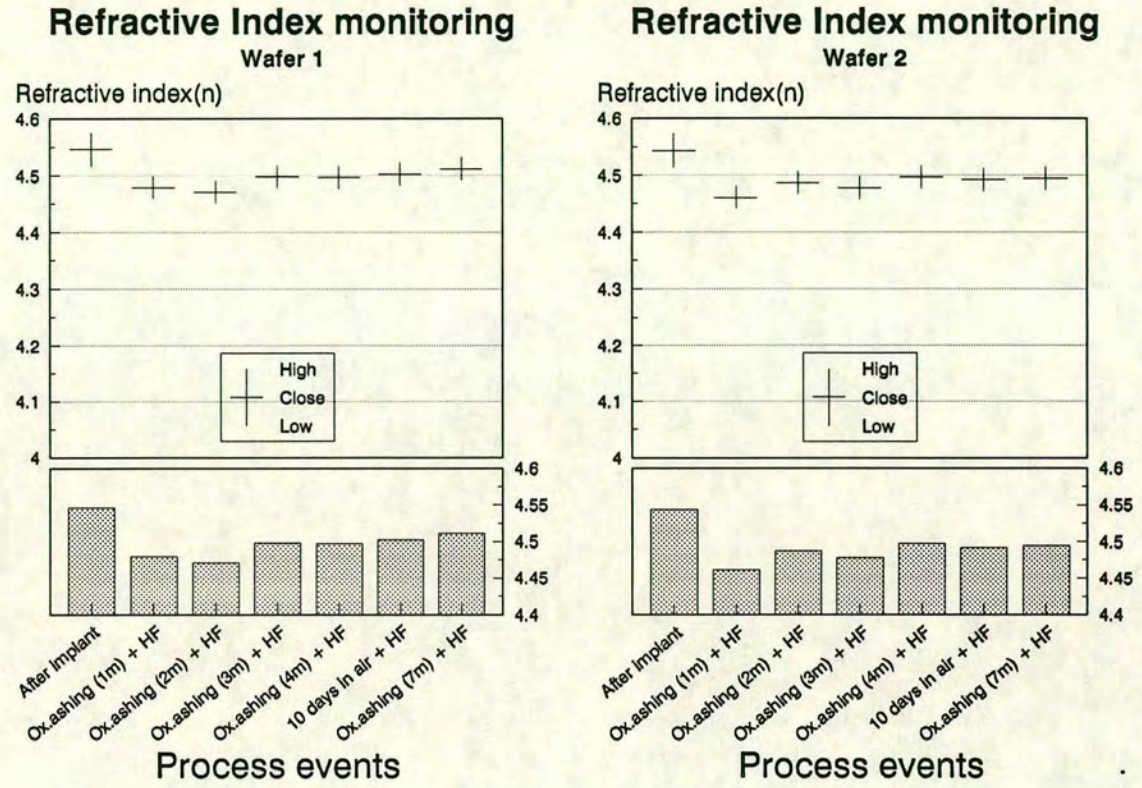

Figure 7–4: Refractive index variation with oxygen ashing time. Maximum and minimum values represent 3-sigma values. The bar charts underneath each graph present the average-n-values variation in a larger scale.

7.3.2 Measuring native oxide growth

7.3.2.1 Defining the problem

For the subsequent effective use of ellipsometry it is necessary to know how refractive index and thickness values for native SiO_2 change with time. Furthermore, the ellipsometry results need to be cross-correlated with the results obtained using other techniques.

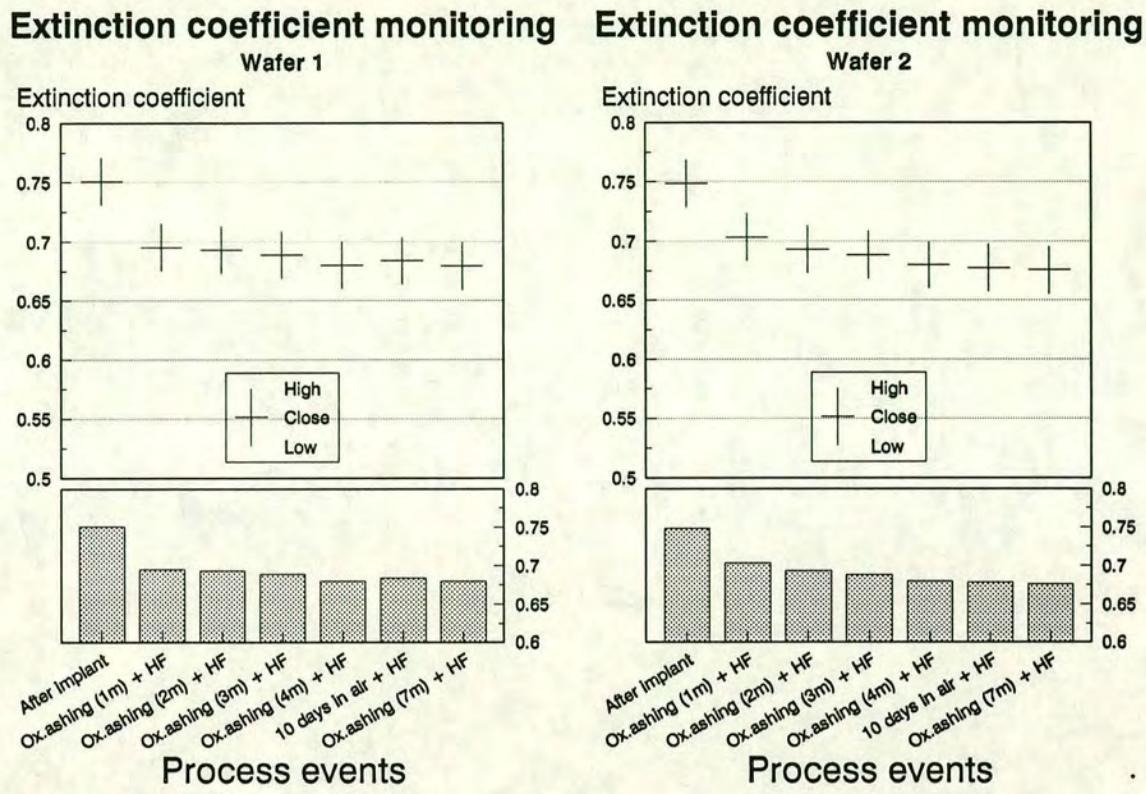

Figure 7–5: Extinction coefficient variation with oxygen ashing time. Maximum and minimum values represent 3-sigma values. The bar charts underneath each graph present the average-k-values variation in a larger scale.

7.3.2.2 Experimental work

a. **Checking the GRQ ellipsometry algorithms.** Before performing any measurements it is useful to see the effect of the assumed refractive index value on the native oxide thickness evaluated using the 1a model of GRQ [5]. In this mode of ellipsometry the oxide thickness is evaluated from an assumed refractive index. The refractive index value was varied from 1.35 to 1.46 and the results appear in table 7–1. It can be seen that a 2 Å variation is the result for the n variation in the above range. Therefore, the oxide thickness variation due to different n-values is smaller than the 3-sigma error (3 Å) de-

rived from measurements over 69 points. A value of n=1.46 Å can therefore be used for the native oxide.

GRQ ellipsometer algorithm testing					
Wafer #	n	Thickness(Å)	% Sigma	Sigma (Å)	# of points
D1S	1.35	16	6.4	1	69
D2S	1.42	15	6.5	1	69
D3S	1.43	14	5.9	1	69
D4S	1.44	14	6.3	1	69
D5S	1.45	14	6.2	1	69
D6S	1.46	14	6.9	1	69

Table 7–1: Variation of the evaluated native oxide thickness for different refractive index values of the GRQ ellipsometer algorithm

b. Native oxide growth. In order to achieve reproducible results in the ellipsometry experiments, the native oxide thickness as a function of time has to be monitored. At the same time, the n and k optical parameters were also monitored. The model used to derive n and k does not take into account the native oxide presence (for the simple optical model, see section 7.2.2.1). This experiment is of vital importance in order to understand the effect of the native oxide thickness variation on the n, k values. The reproducibility of the results from wafer to wafer was tested by performing the experiment on 3 p-type, < 100 > wafers. The results of those experiments (16 measurement points per wafer situated in a square array) are presented in fig. 7–6 in such a way that comparison between wafers and between the trends of the thickness, refractive index and extinction coefficient variations can be easily made.

The major conclusions that can be drawn from those results are:

1. All three physical parameters (d, n, k) show a remarkably high repeatability from wafer to wafer.

2. The oxide thickness which is around 3 to 4 Å immediately after the HF clean takes about 20h to triple in thickness but afterwards the rate of growth decreases. After 5 days of exposure in the air a value of 18 Å is achieved. Very little growth with time takes place after that thickness value.

3. The refractive index average values undergo a slight decrease with increasing oxide thickness. However, the measurement error does not permit any comments on its variation. We can only say that the refractive index shows negligible sensitivity to the native oxide thickness, therefore the optical model being used does not affect the Si n-value monitoring. This is advantageous for monitoring ion implantation damage since it shows that refractive index is not surface sensitive but averages values over a depth.

4. The extinction coefficient closely follows the oxide thickness increase. The measurement errors are low enough to allow us to state that it is extremely surface sensitive and that any k-value monitoring must be done with great care so that exactly the same type of structure (oxide-damage-crystalline Si) is being produced. This is the subject investigated by the experiment of section 7.3.3.

7.3.3 Monitoring RIE damage

7.3.3.1 Problem definition

In order to reveal a damage profile, ellipsometry combined with RIE will be used. As it was shown in the previous section, k-values are very surface-sensitive. Therefore, the native oxide thickness must be monitored as a function of RIE time. A wafer has been monitored after each RIE step and its n,k and d values have been carefully recorded.

7.3.3.2 Results and discussion

The experimental results appear in fig. 7–7. The following conclusions can be drawn:

1. The native oxide thickness after each RIE step is approximately the same(within experimental errors) irrespectively of the RIE time. Its value of around 10 Å is similar to the oxide grown after 2 days of exposure to air. The HF clean does not seem to be able to reduce this d value. A plausible explanation is that there is a micro-roughness of the Si surface, which permits a larger number of oxygen atoms to bond to Si (as opposed to a 'smooth' Si surface where fewer Si bonds are available for oxygen atoms).

2. Refractive index values show, once again, that the refractive index is not at all sensitive on the oxide layer thickness.

3. The sensitivity of extinction coefficient to oxide thickness is again remarkable. The k-values after each RIE step are very close to each other, assuming that they are RIE-time independent.

7.3.4 Conclusions

As it was verified experimentally, relative damage evaluation through the extinction coefficient value, k, is meaningful. Errors can be caused by ignoring the oxide layer thickness. Therefore, an HF dip process step must be included prior to any ellipsometry measurements for damage monitoring on bare silicon substrate.

The above experiment also provides good evidence that a highly-reproducible 3-layer structure (oxide, ion damaged Si, crystalline Si substrate) can be achieved by RIE. RIE time does not seem to affect the physical model of the structure and, most of all, does not have side-effects on the n and k values of Si. This conclusion can justify the use of the simple ellipsometry optical model for damage monitoring at different depths in the subsequent experiments. This approach can give relative but repeatable results and is a first order approximation to problems arising from:

1. Optical constants that are not homogeneous over the entire penetration depth range of incident light.

2. A damage layer thickness that varies for different implantation parameters.

3. An implanted layer that may have many types of disorder such as amorphous regions, lattice strain, vacancies and interstitials distributed randomly and non-uniformly throughout the layer.

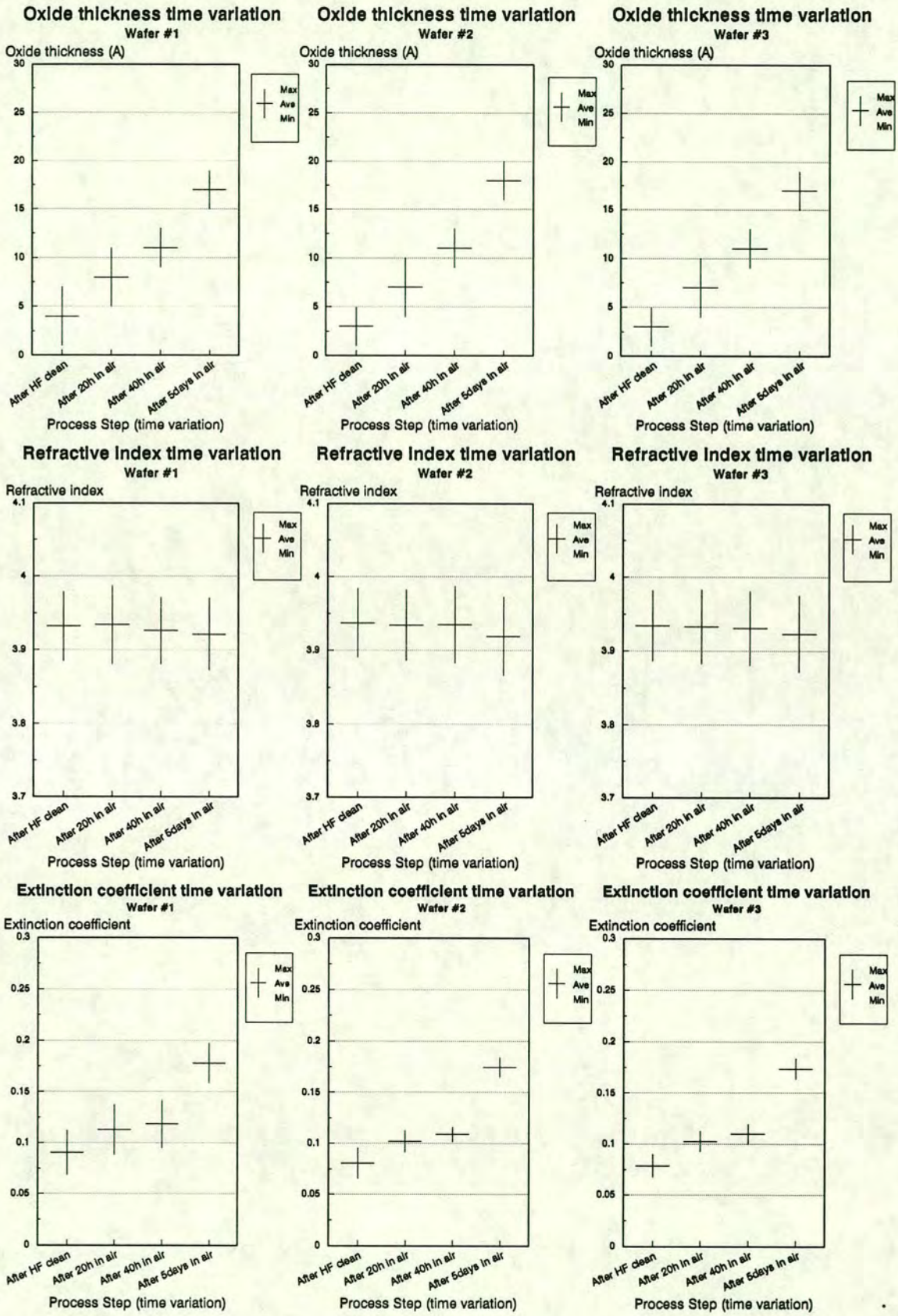

Figure 7–6: Comparison of native oxide thickness, refractive index and extinction coefficient as a function of time for three wafers. Max and min values are the 3-sigma error levels of 16 sites measurements.

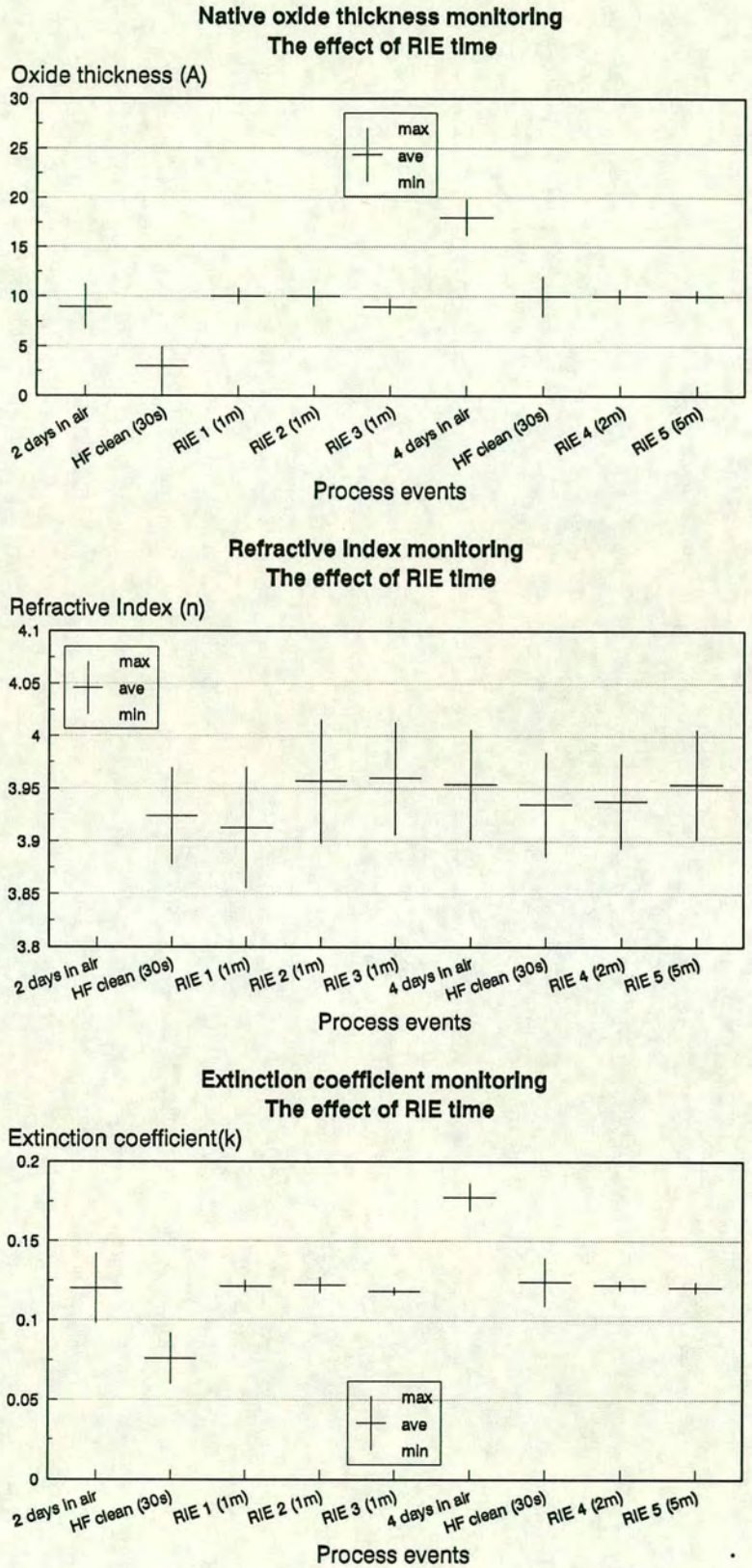

Figure 7–7: Monitoring native oxide thickness, refractive index and extinction coefficient as a function of Reactive Ion Etching time. Max and min values are the 3-sigma error levels of 16 sites measurements. The number in parentheses after each RIE step indicates the etch duration

Bibliography

[1] R. M. A. Azzam and N. M. Bashara. *Ellipsometry and polarized light.* North Holland, Amsterdam, 1977.

[2] K. H. Zaininger and A. G. Revesz. Ellipsometry:A valuable tool for surface research. *RCA Review*, 25:85, 1964.

[3] D. E. Aspnes. Studies of surface, thin film and interface properties by automatic spectroscopic ellipsometry. *Journal of Vacuum Science and Technology*, 18:289, 1981.

[4] R. M. A. Azzam. Ellipsometric configurations and techniques. *Proceedings of the Society of Photo-Optical Instruments Engineers*, 276:180, 1981.

[5] J. C. Cheng. GRQ Instruments Co., 1920 Holmes St.,Bldg F,Livermore, CA 94550, USA, document no. 200-1.2-1187 edition, November 1987.

[6] J. C. Cheng, L. A. Nafie, and P. J. Stephens. *Journal of the Optical Society of America*, 65(9):1031, 1975.

[7] G. A. Osborne, J. C. Cheng, and P. J. Stephens. *Review of Sci. Instr.*, 44(2-1):10, 1973.

[8] K. Watanabe, M. Miyao, I. Takemoto, and N. Hashimoto. Ellipsometric study of silicon implanted with boron ions in low doses. *Applied Physics Letters*, 34(8):518–519, 1979.

[9] D. E. Aspnes. Effects of component optical activity in data reduction and calibration of rotating-analyzer ellipsometers. *Journal Opt. Soc. Amer.*, 64:812, 1974.

[10] K. Riedling. Accuracy of digital Fourier transformation detection systems for high speed rotating analyzer ellipsometers. *Thin Solid Films*, 155:151, 1987.

[11] K. Riedling. *Ellipsometry for Industrial Applications.* Springer Verlag, 1987.

[12] T. C. McGill, S. L. Kurtin, and G. A. Shifrin. Optical reflection studies of damage in ion implanted silicon. *Journal of Applied Physics*, 41(1):246–251, 1970.

[13] S. I. Raider and R. Flitsch. Abstract:Stoichiometry of SiO_2/Si interfacial regions. Ultrathin oxide films. *Journal of Vacuum Science & Technology*, 13:58, 1976.

[14] K. Watanabe, T. Motooka, N. Hashimoto, and T. Tokuyama. Ellipsometric study of annealing processes of phosphorus-ion-implanted layers of si. *Applied Physics Letters*, 36(6):451–453, 1980.

[15] K. Vedam and S. S. So. Characterization of real surfaces by ellipsometry. *Surface Science*, 29:379, 1972.

[16] A. Kuchirkova. Effect of annealing on the reflectance spectra of implanted silicon. *Radiation Effects*, 28:129, 1976.

[17] B. C. Dobbs, W. J. .Anderson, and Y. S. Park. Investigation of ion implanted GaP layers by ellipsometry. *Journal of Applied Physics*, 48:5052, 1977.

[18] M. M. Ibrahim and N. M. Bashara. Ellipsometric study of 400 kev ion damage in silicon. *Surface Science*, 30:662, 1972.

[19] J. R. Adams and N. M. Bashara. Profiles in P_{31}^{+} ion implanted silicon by ellipsometry. *Surface Science*, 49:441, 1975.

[20] K. Nakamura, T. Gotoh, and M. Kamoshida. Implanted As redistribution during annealing in oxidizing ambient. *Journal of Applied Physics*, 50:3985, 1979.

[21] K. Nakamura and M. Kamoshida. Characterization of $^{31}P^{+}$ implanted Si layers by ellipsometry. *Radiation Effects*, 42:29, 1979.

[22] M. Fried, T. Lohner, G. Vizkelethy, E. Jaroli, G. Mezey, and J. Gyulai. volume B15, page 422, West-Berlin, 1985, 1986. Proc. 7th Int. Conf. on Ion Beam Analysis.

[23] D. E. Aspnes and A. A. Studna. Dielectric functions and optical parameters of Si, Ge, GaP, GaAs, GaSb, InP, InAs, InSb from 1.5 to 6.0 eV. *Physics Review*, B27(2):985, 1983.

[24] I. H. Malitson. Refractive indices of SiO_2RR. *J. Opt. Soc. Am*, 55:1205, 1965.

[25] G. H. Bu-Abbud and N. M. Bashara. *Applied Optics*, 20:3020, 1981.

[26] S. A. Alterovitz, G. H. Bu-Abbud, J. A. Woollam, and D. C. Liu. An enhanced sensitivity null ellipsometry technique for studying films on substrates. *Journal of Applied Physics*, 54:1559, 1984.

[27] M. Fried, T. Lohner, G. Vizkelethy, E. Kotai, G. Mezey, and J. Gyulai et al. Optical properties of thermally stabilized ion implantation amorphized silicon. volume B19/20, pages 577–581. Proc. 7th Int. Conf. on Ion Beam Analysis, 1987.

[28] I. Ohdomari, M. Ikeda, H. Yoshimoto, N. Onoda, Y. Tanabe, and T. Ito. *Ion Implantation in Semiconductors.* Plenum, New York, 1977.

[29] T. Lohner, G. Mezey, E. Kotai, F. Paszti, A. Manuaba, and J. Gyulai. Characterization of ion implanted silicon by ellipsometry and channeling. *Nuclear Instruments and Methods*, 209/210:615–620, 1983.

[30] J. J. Grob, P. Siffert, R. Prisslinger, and S. Kalbitzer. page 24, Warwick, 1975. Proc. Int. Conf. on Application of Ion Beams to Materials.

[31] R. Grotzschel78, R. Klabes, U. Kreissig, J. Rudiger, and A. Schmidt. page 65, Budapest, 1978. Proc. Int. Conf. on Application of Ion Beam Modification of Materials.

[32] M. Delfino and R. R. Razouk. A four-phase complex refractive index model of ion-implantation damage. optical constants of phosphorus implants in si. *Journal of Applied Physics*, 52(1):386–392, 1981.

[33] M. Delfino and R. R. Razouk. Optical constants of Arsenic and Boron implants in Si determined by a four-phase complex refractive index model. *Journal of the Electrochemical Society*, 129(3):606–609, 1982.

[34] M. Yamaguchi and T. Hirayama. Surface contamination of silicon produced by ion implantation. *Japanese Journal of Applied Physics*, 15:365, 1976.

[35] T. Lohner, G. Mezey, E. Kotai, F. Paszti, L. Kiralyhidi, G.Valyi, and J. Gyulai. Albany, New York, 1980. Proc. of the Conf. on Ion Beam Modification of Materials.

[36] T. Lohner, G. Valyi, G. Mezey, E. Kotai, and J. Gyulai. The role of surface cleaning in the ellipsometric studied of ion-implanted silicon. *Radiation Effects*, 54(3-4):251–252, 1981.

Chapter 8

Comparison of profiling methods and PET.

8.1 Introduction.

In chapter 6 the PET technique was introduced and optimized. In chapter 7 a series of experiments revealed the advantages and drawbacks of ellipsometry as a standard surface measurement technique that can be used to extract information correlated to the degree of damage generated through ion implantation.

The shrink towards submicron geometries and the increased complexity of implant processes imply a requirement for a fast, accurate on-line technique for implant profile monitoring. Since sequential etching and measuring is time-consuming for implant profiling, the combination of the PET technique with standard surface measurement techniques can offer a significant advantage. The PET technique provides a series of rectangular, flat-bottomed trenches in Si. Depth increments of less than 100 Å have been achieved. The trench dimensions can vary from several microns to several centimeters square. Most of the standard surface measurement techniques can be used inside those trenches.

In order to assess the technique, a sequence of experiments was designed. The primary objectives of the experimental work was:

- Implement PET for different types of implants and apply some of the standard surface measurement techniques to reveal damage and concentration profiles.
- Evaluate the profile variation across a wafer.
- Identify the causes of such a profile variation.
- Investigate how 2-D profile variations across the wafer affect the PET technique accuracy.
- Correlate the PET profile measurement results with profiles obtained by use of other techniques.

The implant species, energy and dose were those used for the 1.5 micron, n-well, CMOS process of the EMF. The two junction implants of BF_2^+ and As^+ are appropriate to monitor how the technique behaves for shallow implants. The BF_2^+ implant was performed at 40keV at a dose of $2x10^{15}cm^{-2}$ and the As^+ was performed at 90keV at a dose of $7x10^{15}cm^{-2}$. Both implants were performed through an oxide layer of around 300 Å and were annealed at 1000°C for 5s using Rapid Isothermal Annealing. Those two types of implants will be used for the experiments throughout this chapter.

8.2 Assessment of ellipsometry and four-point probe applicability to PET-type structures

8.2.1 Experiment objectives

The general experimental plan is schematically depicted in fig.8-1. The overall assessment of the implant and its anneal can only be realized if the previous assessments are proved to be satisfactory. The short-term targets of the experimental work described in this chapter are:

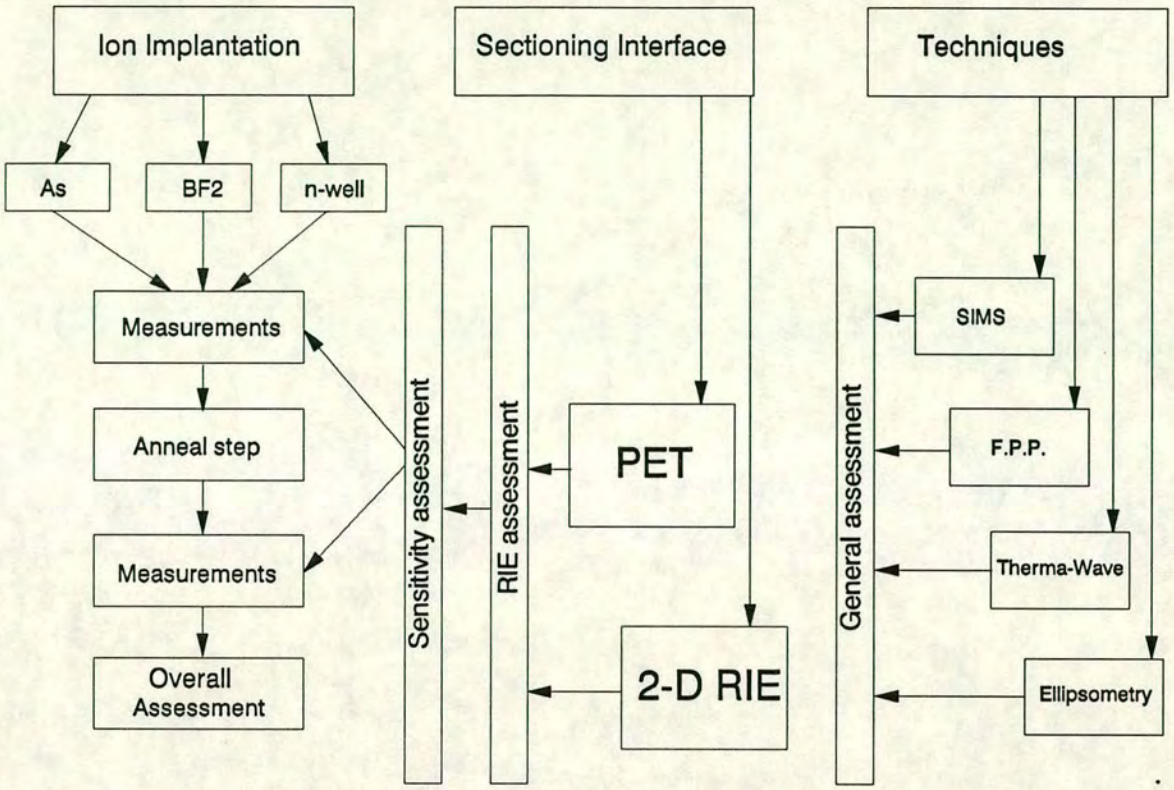

Figure 8–1: The general experimental plan for the development of an accurate method of fast assessment of implant profiles,

- To assess the sensitivity and the ability of ellipsometry and four-point probe measurements to monitor ion implantation damage and carrier concentrations.
- To assess the sensitivity of ellipsometry and four-point probe measurements on RIE etching time.
- To conduct a series of experiments in order to reveal relationships between those variables and how they correlate to theoretical predictions.
- To successfully use the two-dimensional RIE sectioning technique as a method to obtain non-uniformities of the implant profiles.
- To successfully use the PET technique as the sectioning method for rapid dopant profile measurements.

8.2.2 Initial experiments of implant damage monitoring using ellipsometry

The preliminary experiments of RIE damage measurement using the ellipsometry techniques of chapter 7 showed that:

1. There is always a 10 Å-thick native oxide on the RIE etched Si wafer, irrespective of the RIE time.

2. Both refractive index and extinction coefficient of Si do not vary with RIE time (k varies only due to native oxide thickness change).

Therefore, the simple optical model and the n- and k-values derived from it will be adequate to represent the effect of implant and RIE steps on those parameters. Their values will also be compared to the sheet resistance values.

8.2.2.1 The sample geometry and the method used

The optical constants of the three types of wafers (n-junction, p-junction, n-well) were measured before and after the implant and RTA steps.

The sample geometry is depicted in fig. 8–2. The wafers were covered with photoresist. By using a contact printer, row 4 of fig. 8–2 was exposed for a long-enough time to give complete development of the photoresist. At the end, the resist was therefore completely removed. Reactive ion etching took place for a 2min time interval. The remaining photoresist was then stripped off in fuming nitric acid. Sheet resistance and ellipsometric parameters across the whole wafer were then monitored. Both a 15 point line scan across a diameter (normal to the etched row) and a 16 square array scan were used in order to give a complete representation of the whole wafer. For the square array, four measurements took place for each row and the average and 3-sigma values were calculated. The step height between the initial Si surface and the RIE etched surface was measured using stylus surface profilometry (Dektak).

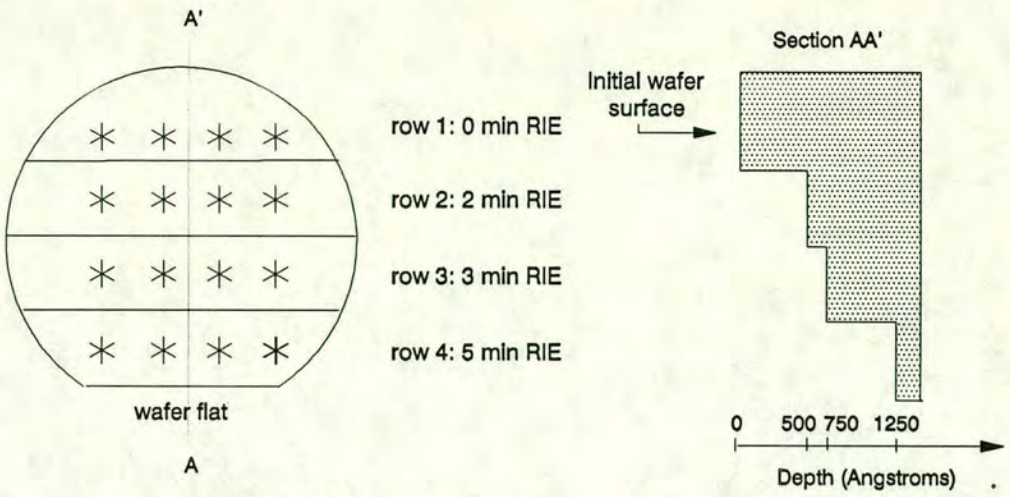

Figure 8–2: The sample geometry used for obtaining three different depths in Si. The wafer was masked with photoresist and an increasing number of rows were exposed for RIE etch each time. The asterisks designate the measurement sites.

The above procedure was repeated but on this occasion, photoresist was removed from rows 3 and 4 so that they could be etched for 1 minute. A final cycle exposed row 2 in addition to rows 3 and 4 and they were etched for 2 minutes. The last row (row 1) was not etched in order to provide a substrate reference surface. The total etch times and final wafer profile is shown in fig. 8–2.

8.2.2.2 Monitoring etch damage by use of ellipsometry

The n- and k-monitoring results for the three implants are presented in fig. 8–3, fig. 8–4 and fig. 8–5 and will be discussed seperately. The structure discussed above was used for assessing etch damage.

For the BF_2 implant the n- and k-values before implant are very close for all rows, fig. 8–3. The implant, as expected, leads to a substantial increase of both n and k. A possibility of implant non-uniformity is revealed in the direction normal to the rows. This is evident since both the n- and k-values decrease from row 1 to row 4 in process step 2 of fig. 8–3). This non-uniformity is **not** a measurement artifact or native oxide thickness variation since a 48h wafer exposure in air

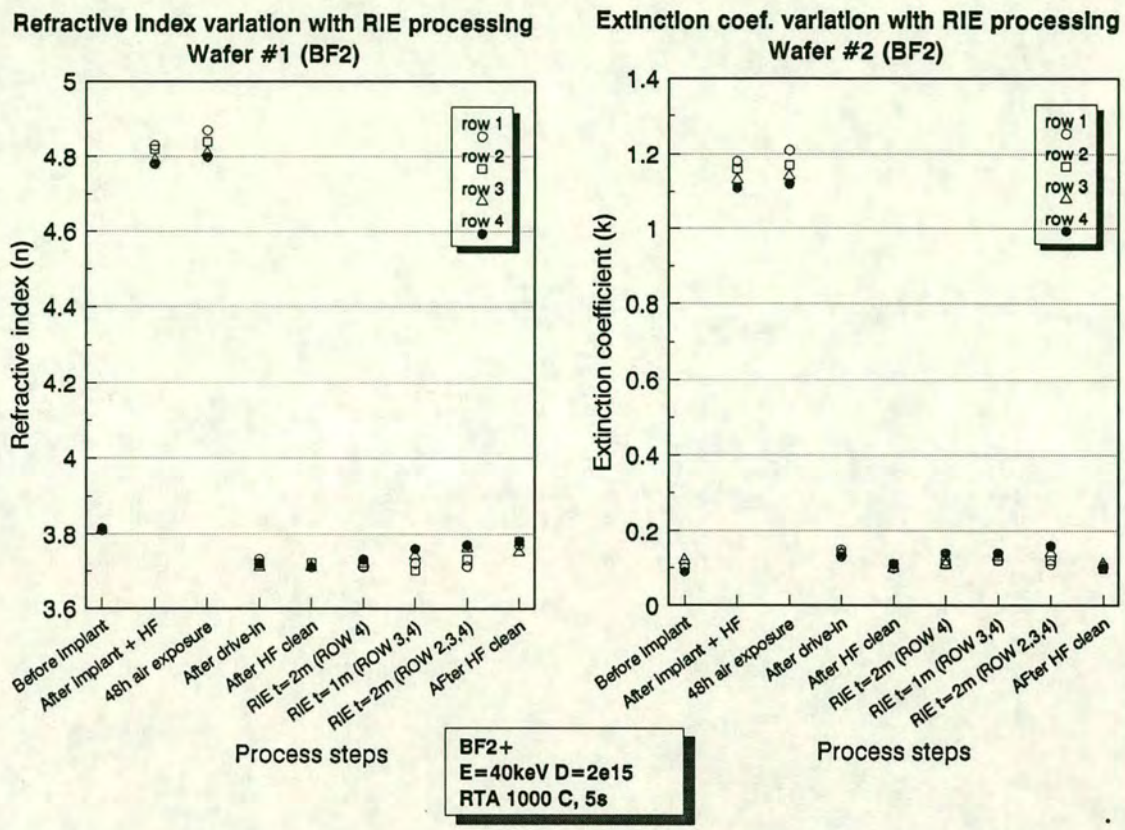

Figure 8–3: Monitoring n and k for the BF_2 junction implant before and after anneal for different depths into Si. Rows 1, 2, 3 and 4 were RIE etched for a total time of 0, 2, 3 and 5 min. The 3-σ variation is 0.050 for n and 0.075 for k.

(process step 3 of fig. 8–3) would be long enough for a native oxide to grow over the whole wafer. This uniform oxide growth could effectively hide any implant non-uniformity.

The effect of RTA (process step 4 of fig. 8–3) is to reduce the n and k values to the unimplanted Si levels. This observation proves that the annealing stage was successful in removing the implant damage. As it was mentioned in the previous chapter, this optical model just averages n and k values over a depth in Si and is very surface sensitive. Therefore, from the process step 4 n- and k-values we can only deduce that the **near surface region has restored its crystallinity.**

This conclusion can be theoretically supported by the fact that the implant dose used is high enough to cause complete amorphization of the target. Thus, surface recrystallization is eased(see chapter 2).

An etch rate of 250 Å/min was measured during the RIE process. All 3 etch cycles (process steps 6, 7 and 8) do not lead to any significant variations of n and k above the unimplanted Si levels. Therefore, the crystallinity of the implanted region after annealing extends at least to a depth of 1250 Å below the wafer surface. The HF clean removes the native oxide layer and slightly lowers the n and k values - within measurement error -.

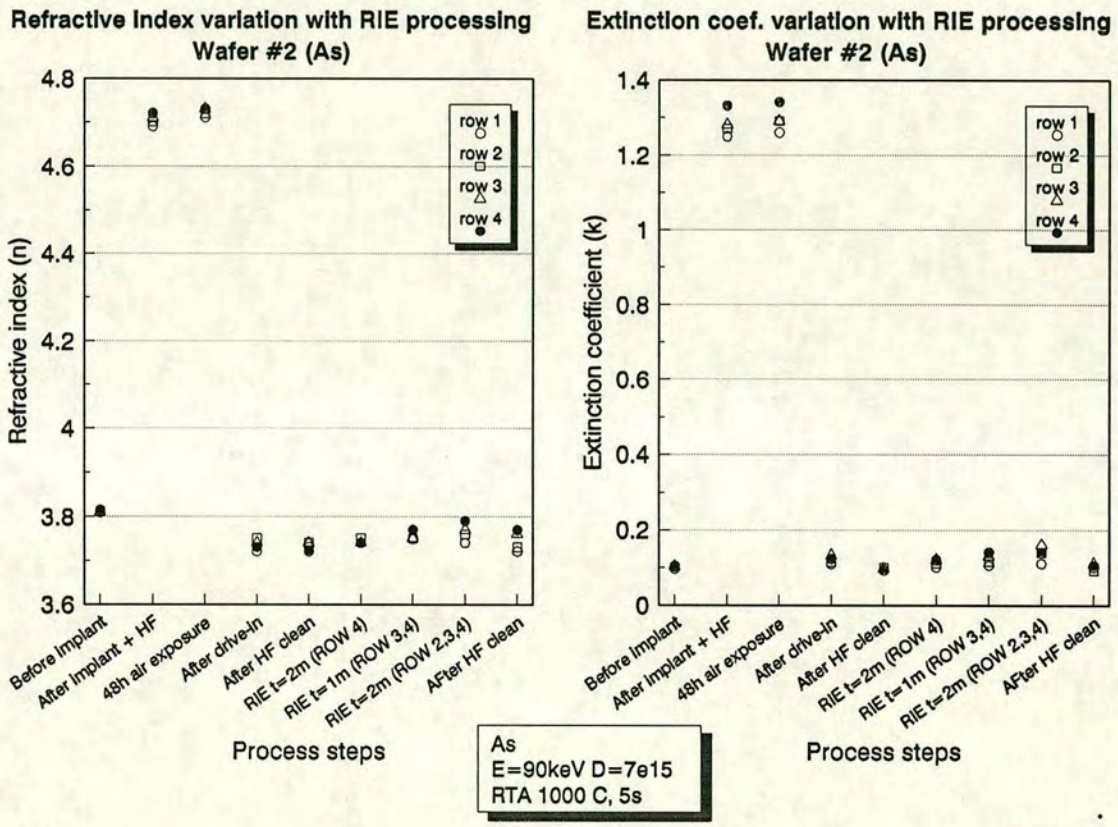

Figure 8–4: Monitoring n and k for the As junction implant before and after anneal for different depths into Si. Rows 1, 2, 3 and 4 were RIE etched for a total time of 0, 2, 3 and 5 min. The 3-σ variation is 0.050 for n and 0.075 for k.

The As implanted wafer exhibits similar behaviour to the previous wafer, fig. 8–

4. However, there are also some distinctinctions. The n and k values after the As implant are different from the corresponding BF_2 values due to the difference in mass, energy and dose (see chapter 7). However, the n and k values after the RTA step are similar to the BF_2 wafer. This effect can be attributed to complete amorphization after the implant followed by re-crystallization of the Si surface layer after an adequate annealing step.

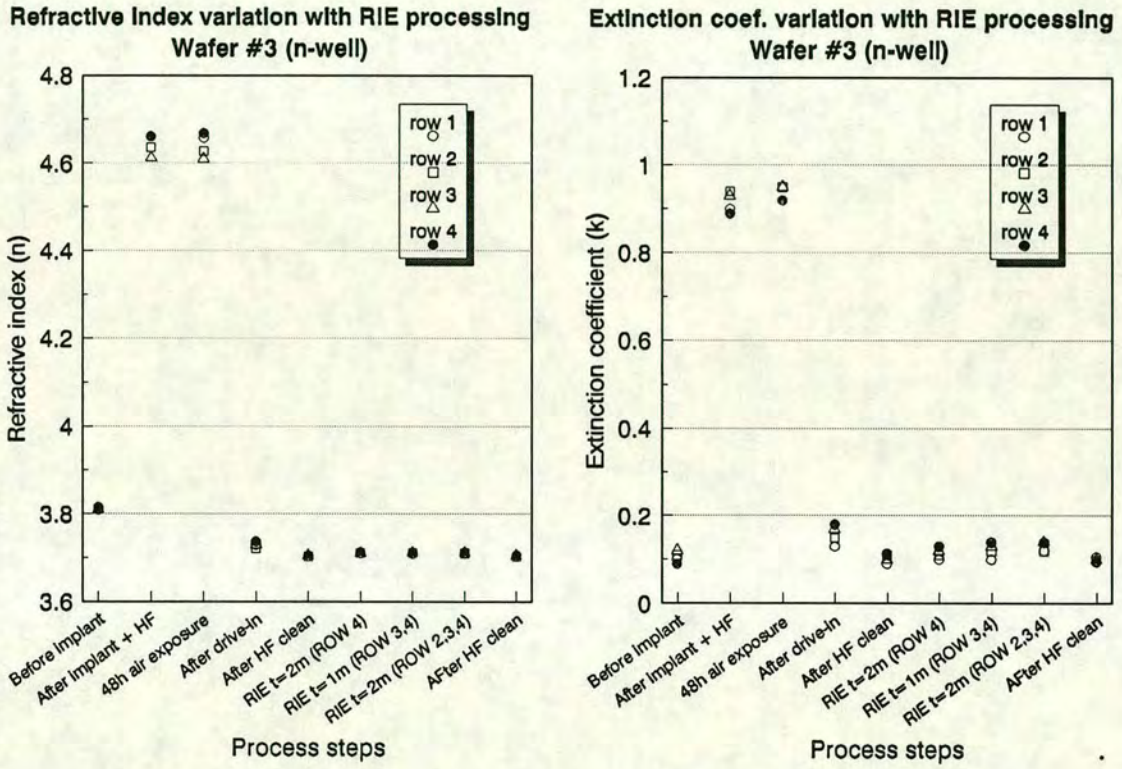

Figure 8–5: Monitoring n and k for the n-well implant before and after the drive-in for different depths into Si. Rows 1, 2, 3 and 4 were RIE etched for a total time of 0, 2, 3 and 5 min. The 3-σ variation is 0.050 for n and 0.075 for k.

The n and k values of the n-well wafer present similar trends to those of the previous wafers for the steps before RIE processing. The three RIE steps do not have a significant effect on n and k. This is expected since no damage will be present near the surface after the long, drive-in step.

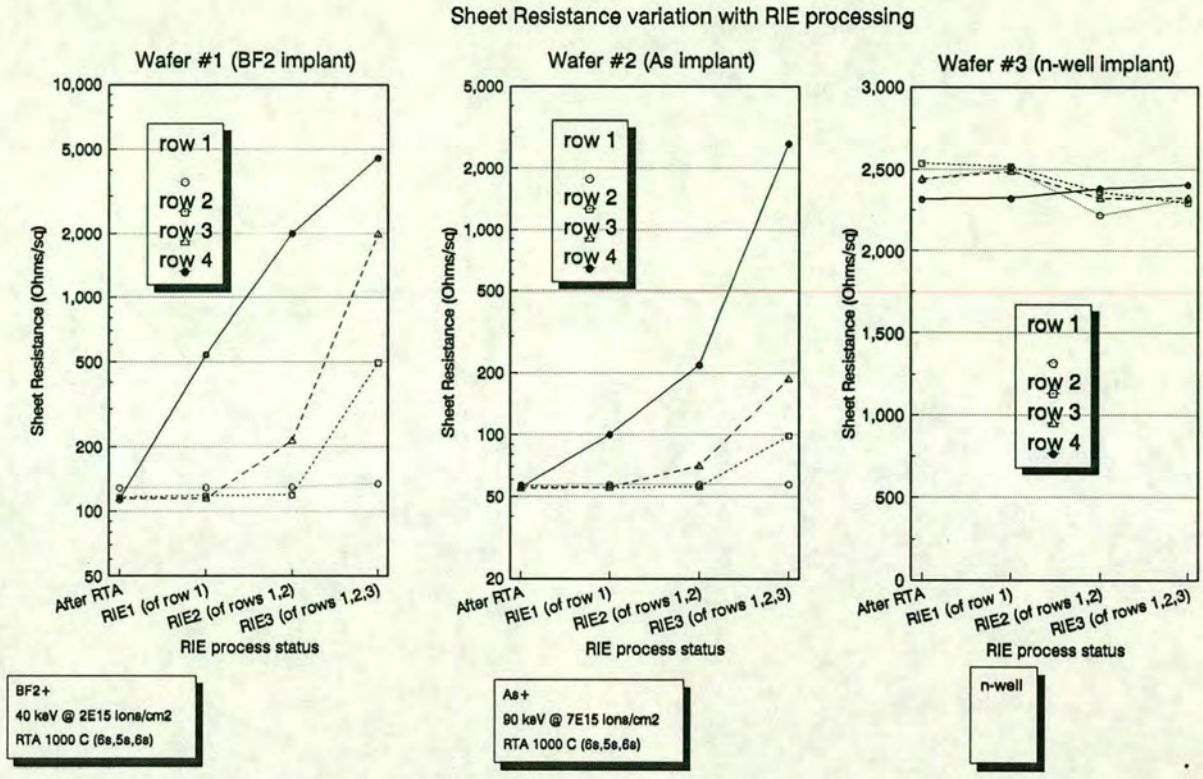

Figure 8–6: Monitoring sheet resistance after anneal and drive-in for different depths into Si. Rows 1, 2, 3 and 4 were RIE etched for a total time of 0, 2, 3 and 5 min.

8.2.2.3 Assessing sheet resistance sensitivity to RIE

The sheet resistance values for all three wafers after the annealing stage are presented in fig. 8–6. The minimization of damage during the RIE steps assures that the increase of sheet resistance with depth is due to the removal of implanted layers (and to the concommitant change in the total number of active carriers residing inside the implanted layer) and not to an increase of damage with RIE time. This conclusion is reinforced by the sheet resistance values of the n-well implant of fig. 8–6. For a 1 micron deep n-well, a 1000 Å layer removal should not have any appreciable effect on the sheet resistance value. Any observed increase of the sheet resistance can be attributed to RIE damage. However, the sheet resistance does

not increase after each RIE step but remains constant within the measurement error limits.

Seperate experiments have also been carried out to re-confirm the above conclusion. Boron was deposited on n-type wafers and driven-in for 18h. A wet oxidation with HCl was then carried out for 15 min to soften the boron glass. HF was used to etch the oxide. The concentration profile was expected to be uniform down to the junction (1.5 μm depth). The sheet resistance of 2.35 Ohms/sq. should be identical for step removals much shallower than the junction depth, irrespective of the RIE time. It was found that RIE etching between 0 and 40 minutes did not affect the sheet resistance value.

8.2.2.4 Conclusions

It was experimentally verified that RIE etching time does not have appreciable effects on both the optical constants and the sheet resistance measurements, for RIE conditions similar to those used for the PET technique. Therefore, the PET technique trenches can be used for ellipsometric and sheet resistance measurements. The combination of the PET technique with ellipsometry and other methods will be discussed and compared to other standard methods in the following section for two different species (BF_2 and As).

It has also been found **feasible** to assess the degree of crystallinity achieved after an annealing stage and the approximate depth at which damage still exists, by using ellipsometry and RIE sectioning. However, since after annealing the n and k values undergo small changes, the sensitivity of the technique is low. The need for a complementary technique in order to interprete those results is essential. Although Transmission Electron Microscopy (TEM) seems ideal as an alternative technique it is difficult to use it on-line, mainly due to its long measurement-time and high cost. A combination of ellipsometric and sheet resistance measurements would be ideal to comment on the state of activation inside the implanted and annealed layer.

8.3 Comparison of damage and carrier profiles using the PET technique and other methods

In order to make a comparison between different profiling techniques, an experiment using eighteen wafers was designed. Six wafers were used for the BF_2 implant, six for the As implant and the rest for an n-well implant.

The wafer-to-wafer variation of optical constants was described in the previous chapter. The wafer-to-wafer sheet resistance variation is depicted in fig. 8–7. The measurements were performed over 69 sites on each wafer, and the average values with the 3σ variation indicate an acceptable wafer-to-wafer repeatability for such a comparison experiment.

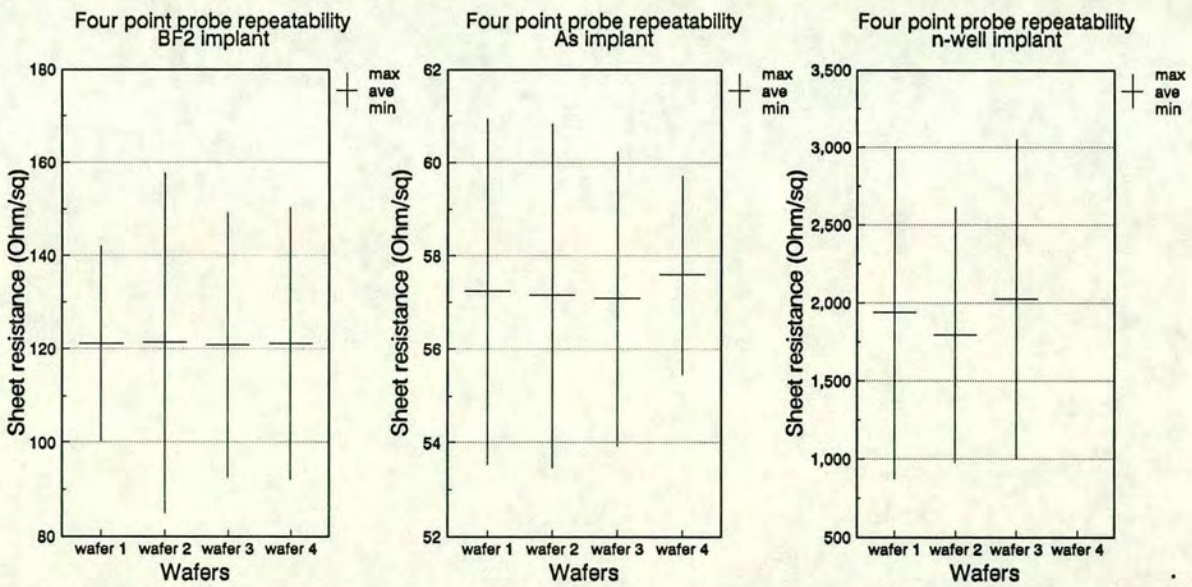

Figure 8–7: The average and 3σ values of sheet resistance over the wafers to be used for the experiment. They are evaluated over 69 sites for the 3 different types of implant.

8.3.1 As implantation

8.3.1.1 Carrier profile from Hall measurements

A stripping (differential) Hall measurement system [1] was used to measure sheet resistance, carrier concentration and carrier mobility. The measured values versus depth are presented in fig. 8–8. The simultaneous measurement of both sheet resistance and carrier mobility makes this method a very accurate benchmark for the assessment of the new technique.

In order to assess whether the RIE etch used for stripping Si distorts the measured carrier profile, a second profile measurement was performed on a 3 min RIE etched sample. The profile tracing was expected to begin at a depth of around 680 Å (the etch rate of Si was found to be 227 Å per minute for this particular wafer site). The experiment and the profile fit indicates a trench depth of 660 Å which is very close to the value of the Dektak measurements. The comparison between the two profiles in fig. 8–9 confirms the following assumptions:

1. The extracted profiles match, within experimental accuracy, for depths deeper than 680 Å.
2. No distortion of the carrier concentration due to the RIE strip process (for 3min) can be observed.

8.3.1.2 Two dimension carrier profile comparison

Sheet resistance measurements over 69 wafer sites combined with RIE layer stripping were used for the extraction of the 2 dimension (2-D) implant profile variation. The thickness of the stripped layers was controlled by the RIE time parameter (etch rate varied from 210 to 226 Å per min across the wafer surface). The sample geometry for the 2-D measurements is depicted in fig. 8–10.

---

[1]The measurements were carried out on an HL5900 Stripping Hall System, from Bio-Rad.

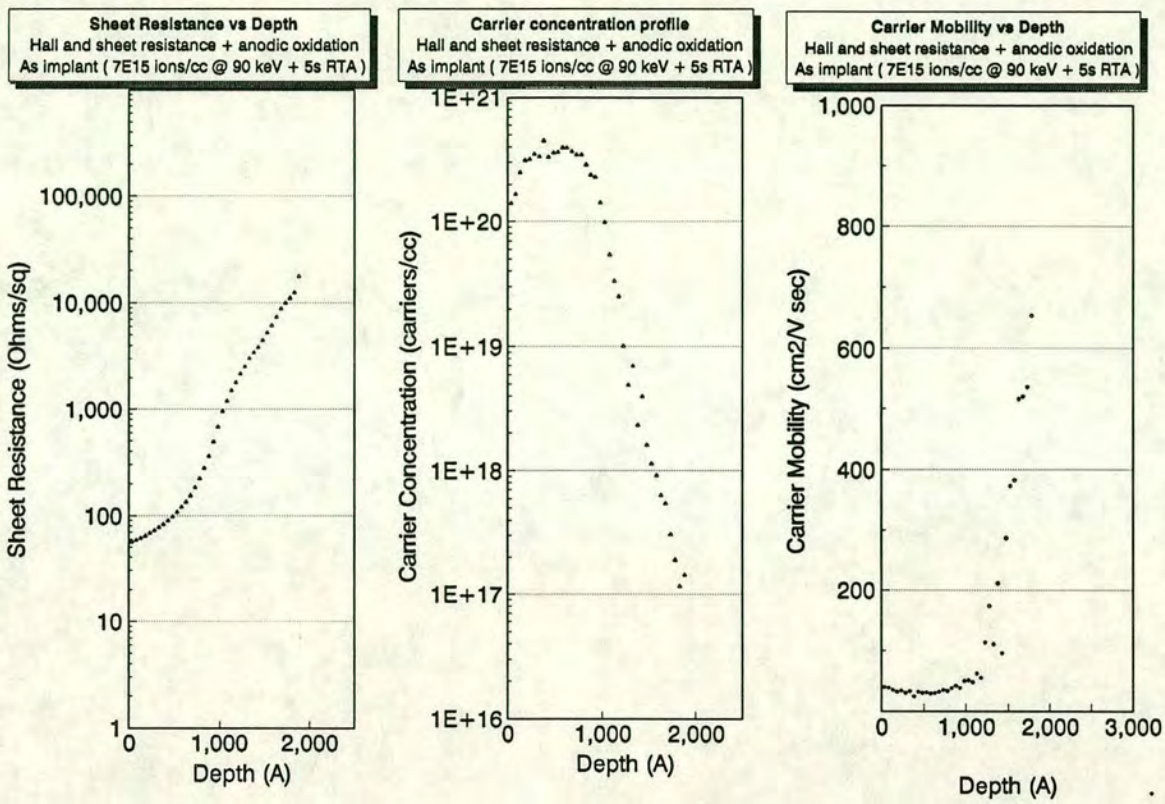

Figure 8–8: The sheet resistance, carrier concentration and electron mobility as measured and evaluated by Hall measurements and anodic oxidation stripping.

The measurements were averaged across each of the rows and the 9 rows contained 5-7-9-9-9-9-9-7-5 measurement sites respectively. The sigma values across each of the rows (parallel to the wafer flat) were found to be at least 3 times smaller than the respective values across the columns. This is suspected to be due to the position of the wafer inside the RIE etcher. The wafer flat is at a tangent to the periphery of the etcher chamber and normal to the gas flow direction. As gases flow from the periphery towards the gas outlet in the center of the etcher, this causes radial etch non-uniformities. In fig. 8–11, the average and 1-sigma values of the sheet resistance (over those 69 points) for each RIE Si strip step are presented. A comparison of the 1-sigma sheet resistance values over the rows and over the columns as depicted graphically in the last graph of fig. 8–11 provides

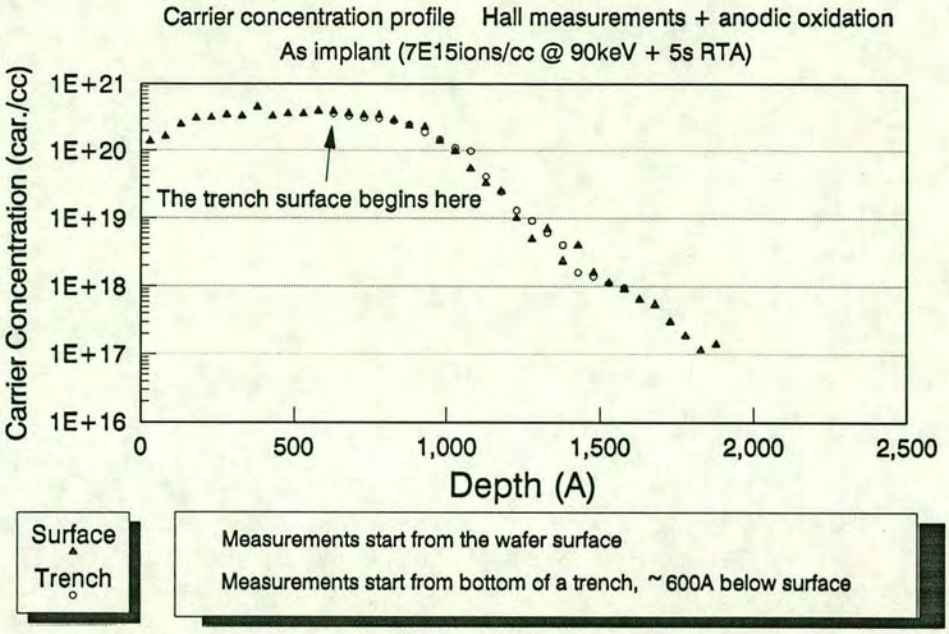

Figure 8–9: Carrier concentration profile of the As implant evaluated by Hall measurements and anodic oxidation. The profile is extracted from the surface and from a RIE etched region around 660 Å below the surface.

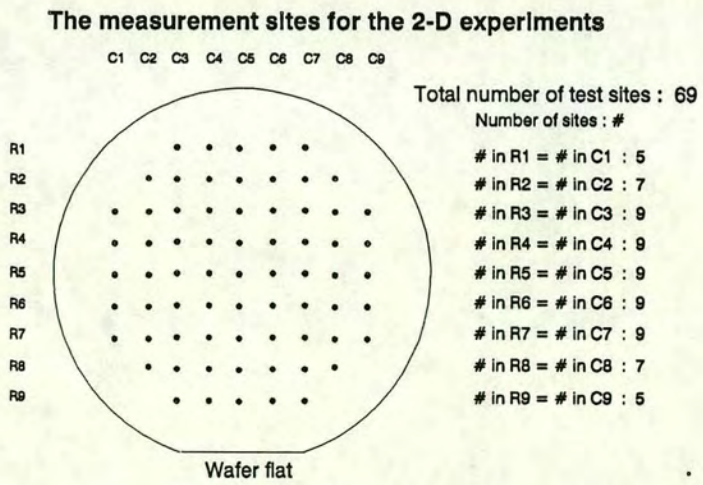

Figure 8–10: The measurement sites and the associated rows and columns for the 2-D profiling experiment.

experimental confirmation of the above suggestion. The conclusions drawn from the experimental data are:

1. The sheet resistance variation across each row is below 1 % of the sheet resis-

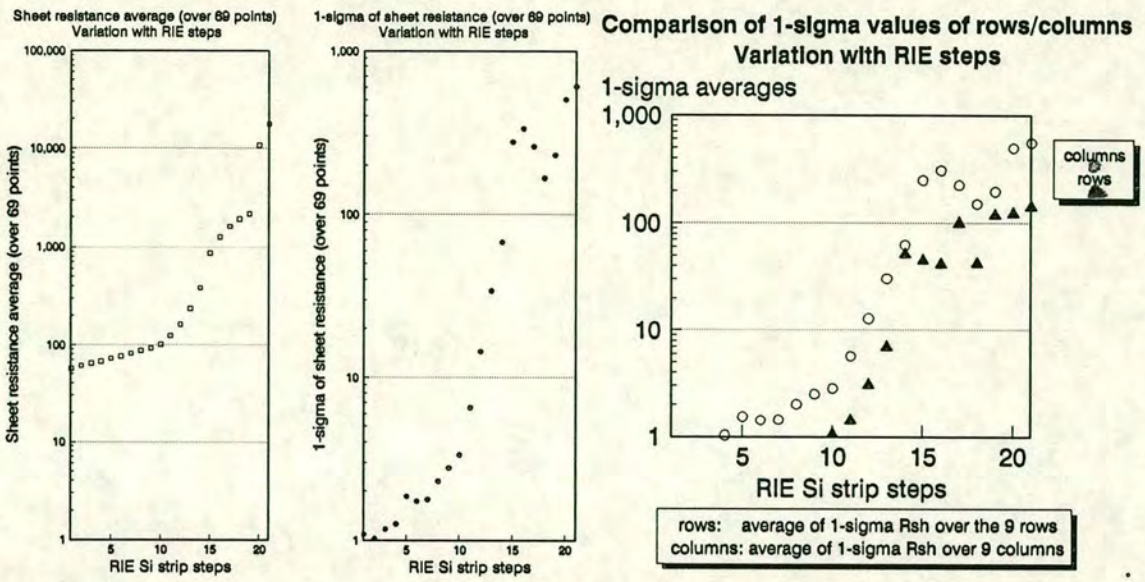

Figure 8–11: The first two graphs present the average and 3-sigma sheet resistance values over 69 sites for each RIE step. In the last graph the averages of the 3-sigma sheet resistance values for the 9 rows and the 9 columns are compared.

tance average row value, and therefore there is no indication of RIE-process-induced etch non-uniformity across the row. This observation assures us that there is no significant carrier concentration profile distortion along each row, and therefore the PET technique sheet resistance and carrier profile results will **not** suffer from distortion between trenches of different depths that are found along the same row.

2. The rapid increase of the 1-sigma value of sheet resistance variation along the columns for consecutive RIE steps is an indication of possible RIE non-uniformity in the radial direction inside the etcher. In order to verify that the variation is not due to an implanter malfunction or an RTA-induced radial non-uniformity, the following simple experiment was performed. Three wafers were implanted, RTA- annealed and RIE-etched. The only difference between them was their orientation. During the implant their flats were

parallel and pointing downwards. During RTA wafer 2 and 3 were rotated by 45 degrees (with respect to the wafer flat position of wafer 1). During the RIE etch wafer 1 and 2 had their flats tangentied to the periphery of the etcher's electrode, while wafer 3 had a 45 degree twist. The identical results of wafer 1 and 2 after a 5 min etch showed that the RTA was uniform. Their 2-D sheet resistance maps were twisted by about 45 degrees with respect to the sheet resistance map of the 3rd wafer. Therefore, the observed radial non-uniformity is induced by the RIE process. A correction for the variation in etch rate along each column, ie across a radial direction inside the etcher, must take place as explained earlier in the optimization of the PET technique.

In fig. 8–12 the average sheet resistance values of 8 rows are overlaid on the same diagram for comparison. The depth values are not the same for all rows since they have been corrected to account for the different etch rates. Rows 1, 2 and 3 have similar etch rate values (225 , 222, 220 Å/min), while the etch rate for row 8 is 215 Å/min.

For the first 10 etch steps (up to a 600Å depth), there is no significant difference in the average sheet resistance values between the rows. The difference becomes apparent near the middle of the curve, but it usually does not exceed 10 %. The situation does not change significantly for measurements deeper in Si. This is a further proof of the point, that **the sheet resistance monitoring of the initial wafer surface is not enough to prove implant and anneal uniformity.** As has been mentioned earlier, the contribution of deep, low carrier concentration layers of Si to the average sheet resistance is small.

By using a cubic spline curve fit for the sheet resistance versus depth measurements and the dedicated software package described in section 4.5.1.4, the carrier concentration and mobility values versus depth were extracted iteratively. The carrier concentration and the mobility profile variation along the direction normal to the rows are displayed in fig. 8–13 and fig. 8–14.

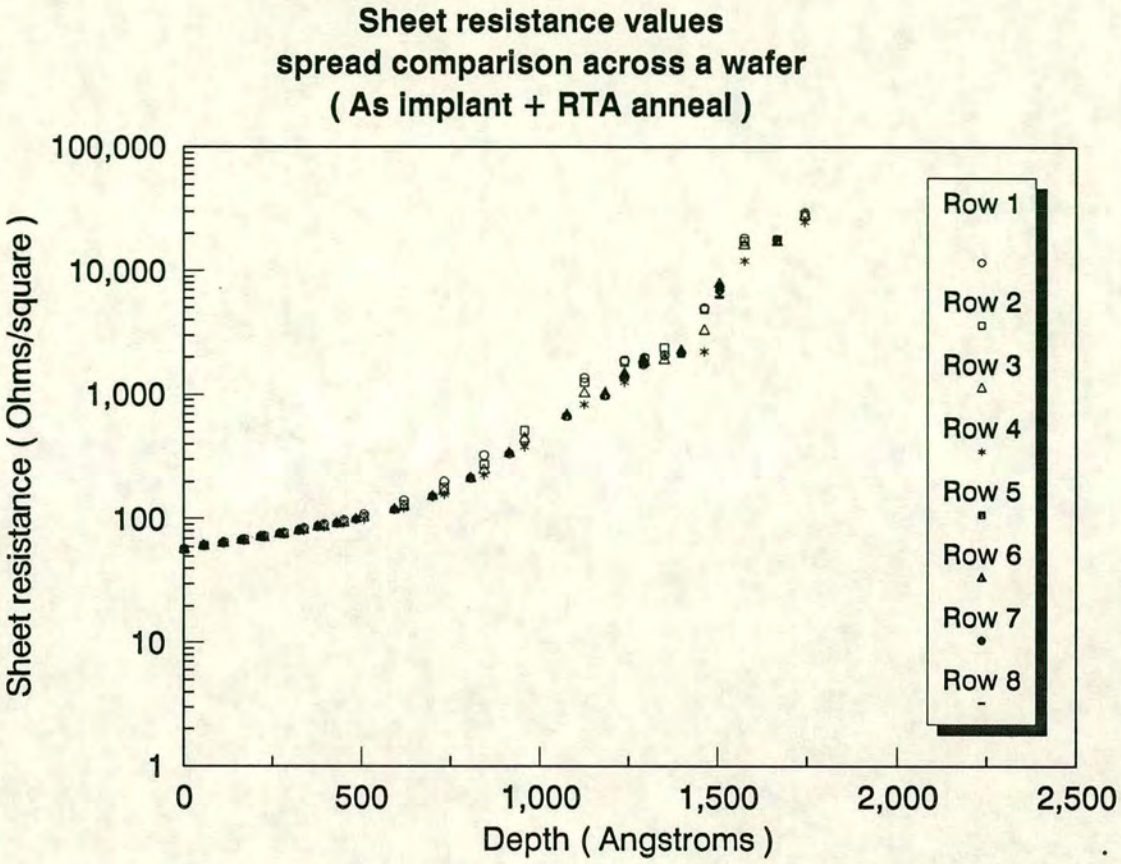

Figure 8–12: The sheet resistance values spread across a wafer. The average sheet resistance values along each row are compared. Rows are parallel to the wafer flat.

The remarkable carrier concentration profile resemblance down to 1000 Å is followed by variations in tail distributions among rows. An existing non-uniformity for depths deeper than the projected range of the implant can thus be monitored.

The electron mobility 2-D profile variation was extracted by using bulk mobility values (see section 4.5.1.4 and section 4.5.1.3). The spread of mobility values between the different rows is due to the carrier concentration spread. This is due to the iterative, corrective nature of the algorithm used for the carrier profile evaluation.

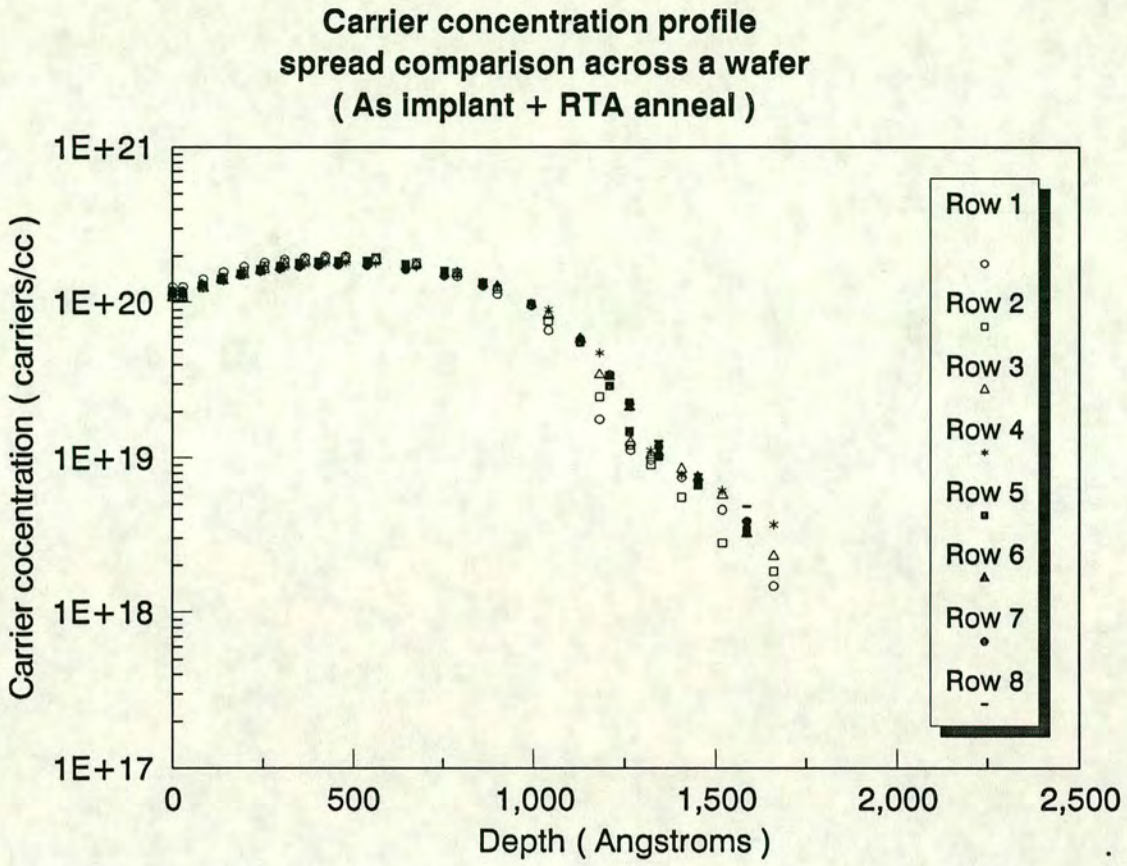

Figure 8–13: The carrier profile variation on the direction from the wafer flat (row 1) to the opposite end (row 8).

8.3.1.3 Measurements repeatability

One of the main objectives set in this experimental work, was to identify the contributions of different sources of error in the profile evaluation. Since the carrier profile is derived from sheet resistance values at various depths, it is crucial to separate the x-y position variation of sheet resistance from the repeatability error of measurements at the same site. Some of the results of this series of experiments are presented in fig. 8–15 and fig. 8–16.

The measurements were carried out on the 69 site array used previously. For each row, after each RIE Si layer strip, a 10 measurement repeatability test was performed. The results in fig. 8–15 and fig. 8–16 indicate the outcome of the

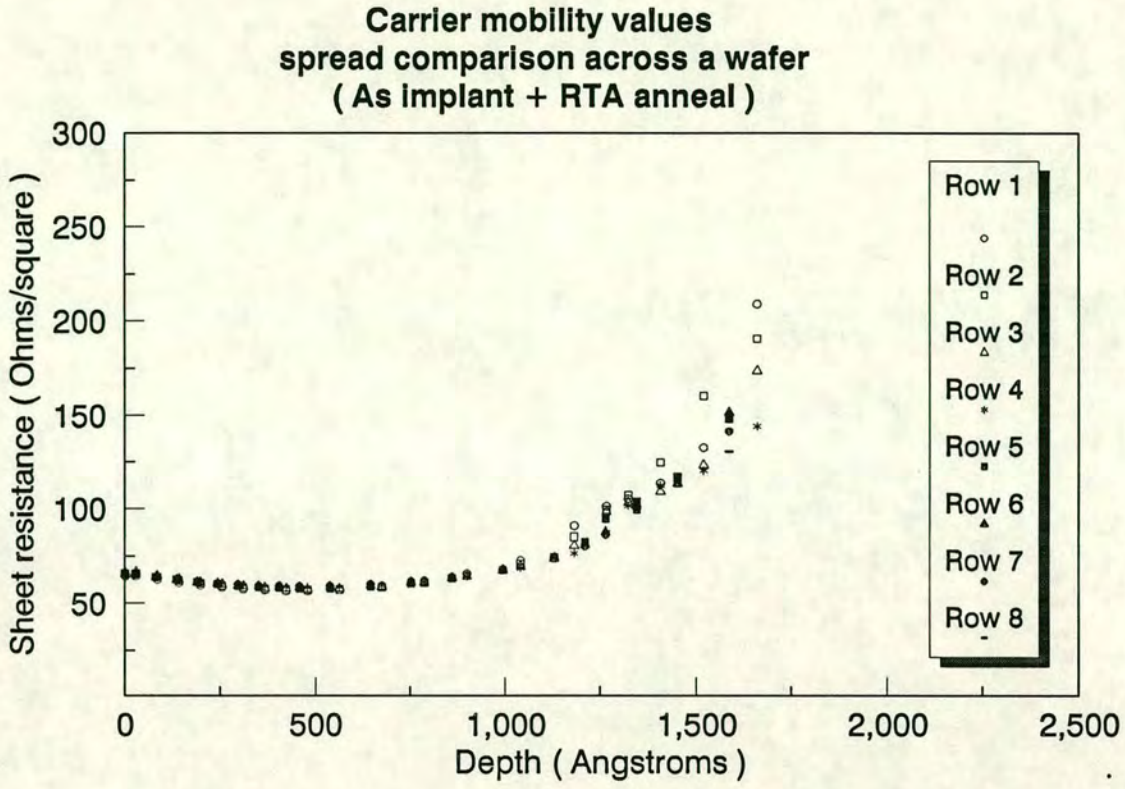

Figure 8–14: The mobility profile variation across the normal to the wafer flat direction.

experiment for the central points of rows 1,2,8 and 9. The choice of the central point of the rows does not affect the repeatability results. For all depths the 3σ repeatability is below 2 % of the average sheet resistance value. Therefore, the error does not exceed the measurement marker size which represents the average values (ave) on the curves. The minimum (min) and maximum (max) values on the curves are the minimum and maximum values measured across all 9 rows. Therefore, they represent the maximum spatial variation of sheet resistance among the various rows. For the first 600 Å the repeatability error is of the same order as the sheet resistance spatial variation. However, for deeper depths the spatial non-uniformity seems to increase and it therefore overrides the repeatability error.

The carrier concentration profiles derived from the ave, min and max sheet resistance curves are depicted in the second column graphs of fig. 8–15 and fig. 8–16.

The sheet resistance repeatability error does not distort the carrier concentration profile shape. On the other hand, the max and min curves seem to deviate from the ave curve for depths deeper than 800 Å.

The row to row variation of the carrier profile can therefore be attributed to non-uniformities induced by the implant and annealing steps. The 2-dimension RIE technique sensitivity can reveal those profile variations.

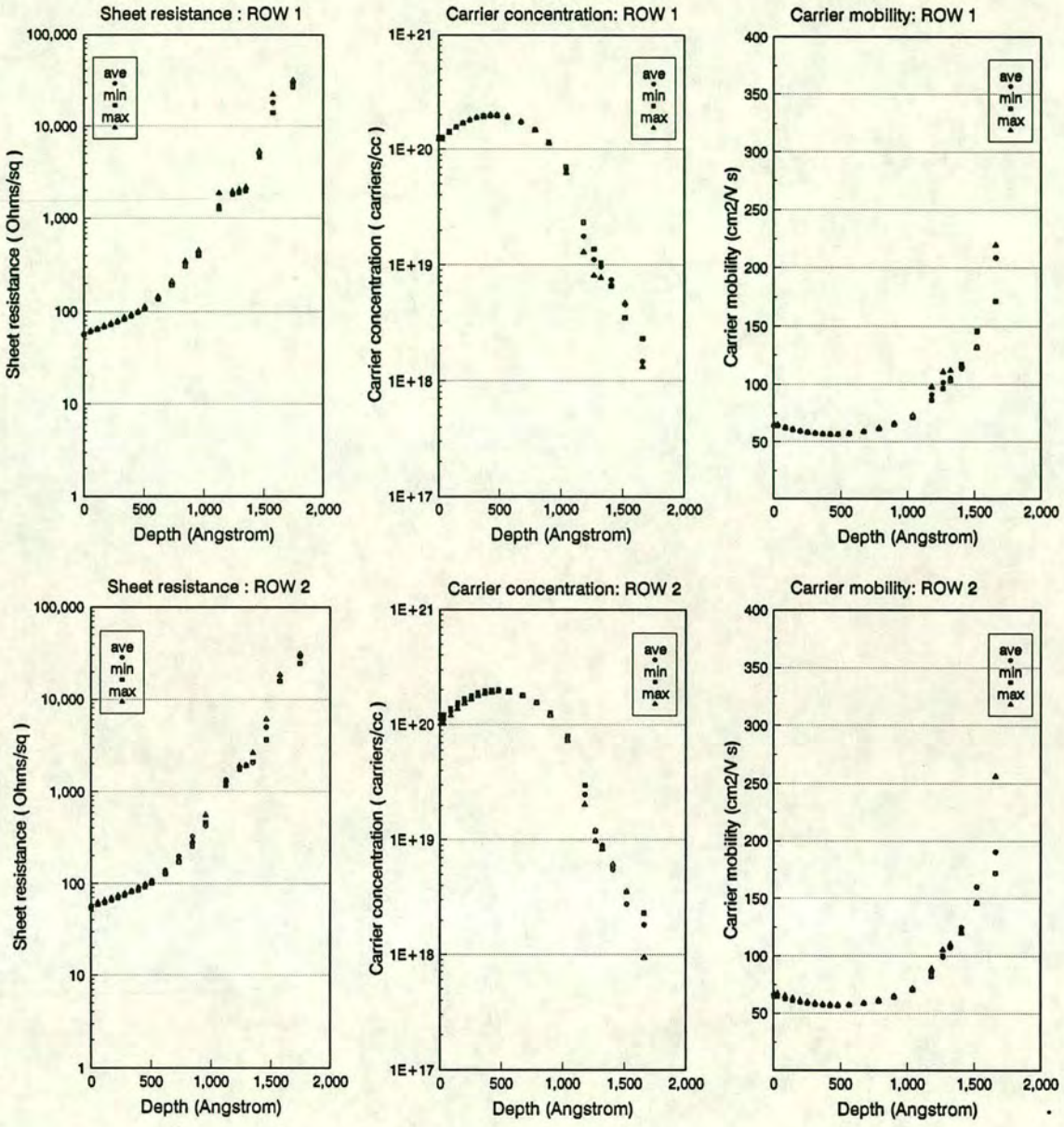

Figure 8–15: Sheet resistance measurements versus depth, carrier profiles and mobility profiles extraction for the As implant. Comparisons between rows 1 and 2. The ave curves for all graphs represent the average values. The repeatability error for each point of the sheet resistance measurements does not exceed the marker size. The max and min curves represent the max and min sheet resistance values obtained across all 9 rows. The carrier concentration and carrier mobility ave, max and min curves are derived from the ave, max and min sheet resistance curves respectively.

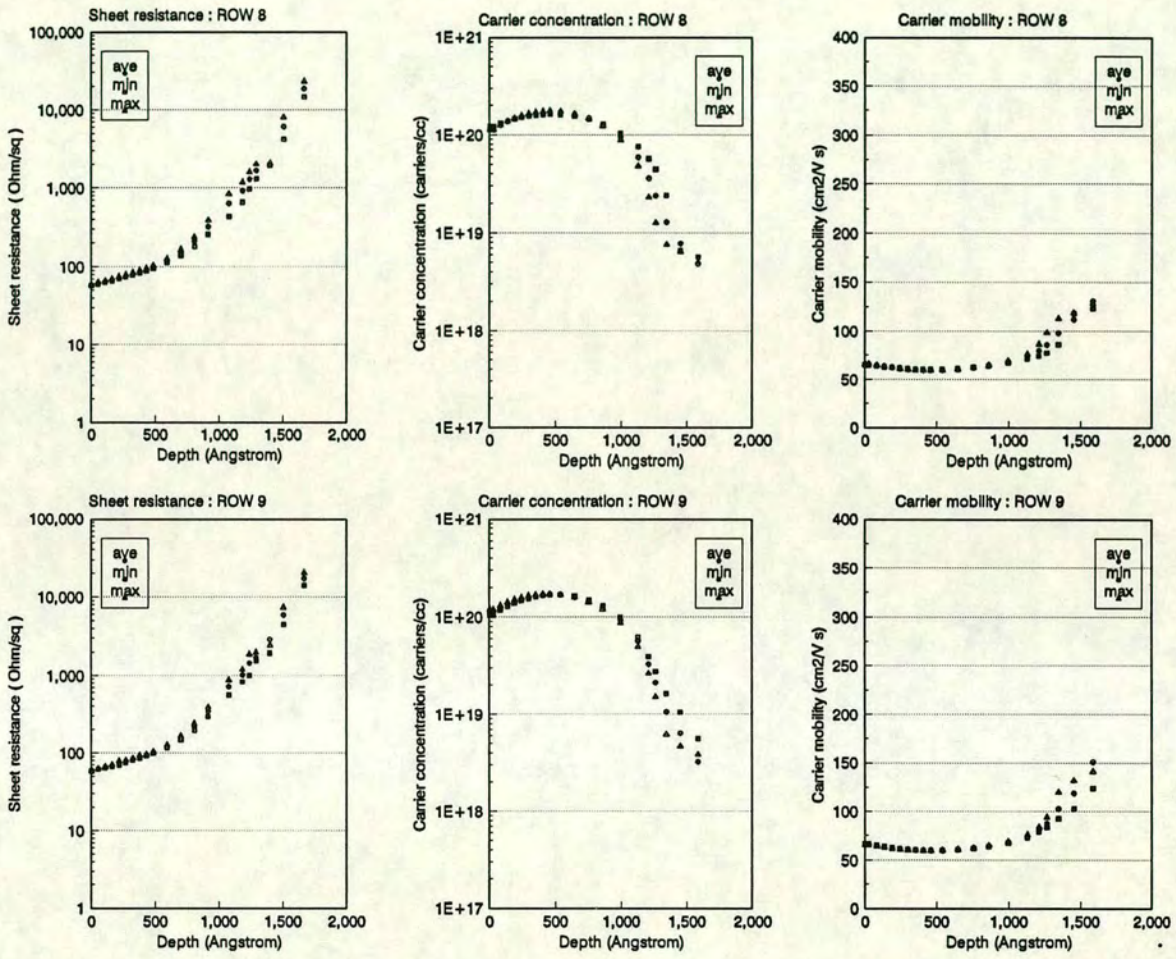

Figure 8–16: Sheet resistance measurements versus depth, carrier profiles and mobility profiles extraction for the As implant. Comparisons between rows 8 and 9.

8.3.1.4 The PET technique combined with ellipsometry

The PET structure geometry. The structure used for the PET technique was a 4x4 array of square trenches. Each square of the array was defined by use of the optical stepper framing blades(see PET technique chapter) to be a 5×5 mm. From the experimental work on the development of the PET technique it was found that smaller area trenches have better uniformity during the photoresist exposure, photoresist etching and Si etching procedures. The 1mm spot size of the laser beam used for the ellipsometric measurements, imposes the lower limit in the dimensions of the squares. The positions of the trenches across the wafer, were chosen to be on the x- and y- axis coordinates used by the built-in 16 site array of the GRQ ellipsometer.

The PET technique characteristics. The objective was to create a series of trenches of increasing depth with around 100 Å depth increments. This exposes layers from the surface to a depth close to the expected junction depth. In order to achieve the right trench depths into Si, the wafer was photoresist coated and exposed to light for increasing time intervals of 20ms. An AFT-Nanospec was used each time to determine the photoresist thickness at the 16 sites. This process was repeated until the desired uniformity along the bottom of the trenches was achieved. RIE etching took place for a time interval long enough to expose the Si substrate of the shallowest trench for 30s inside the etcher. The wafer was then placed in the oxygen asher for photoresist strip. HF clean took place immediately before the ellipsometric measurements. The measurements (and the HF clean) were repeated twice in order to assess the repeatability of the method. No significant variations existed, indicating a high degree of repeatability.

The depths of the trenches were measured using a Dektak profilometer. An average of three measurements for each trench was extracted and assigned as the depth in Si at that site. The 3σ variation was assigned as the measurement error. The depth measurement error appears in all the graphs for each trench depth and is around 75 Å.

The ellipsometric measurements were carried out at an incident angle of 70 degrees and a wavelength of 6328 Å using a He-Ne laser source.

Refractive index monitoring. The refractive index depth profile for the As ion implanted specimen is presented in fig. 8–17. The first point of the graph depicts the refractive index value of crystalline Si (measured before the implant). The use of the oxygen ashing has eliminated the carbon contamination from the surface (residue layer, see 6.2.3.2). The error in the n value measurement does not allow the accurate extraction of the depth where the profile peak should exist. The decrease in n for depths deeper than 1700 Å indicates that we are on the profile tail. The refractive index value at a depth of 2100 Å approaches the crystalline silicon value, indicating that we are in the vicinity of the junction.

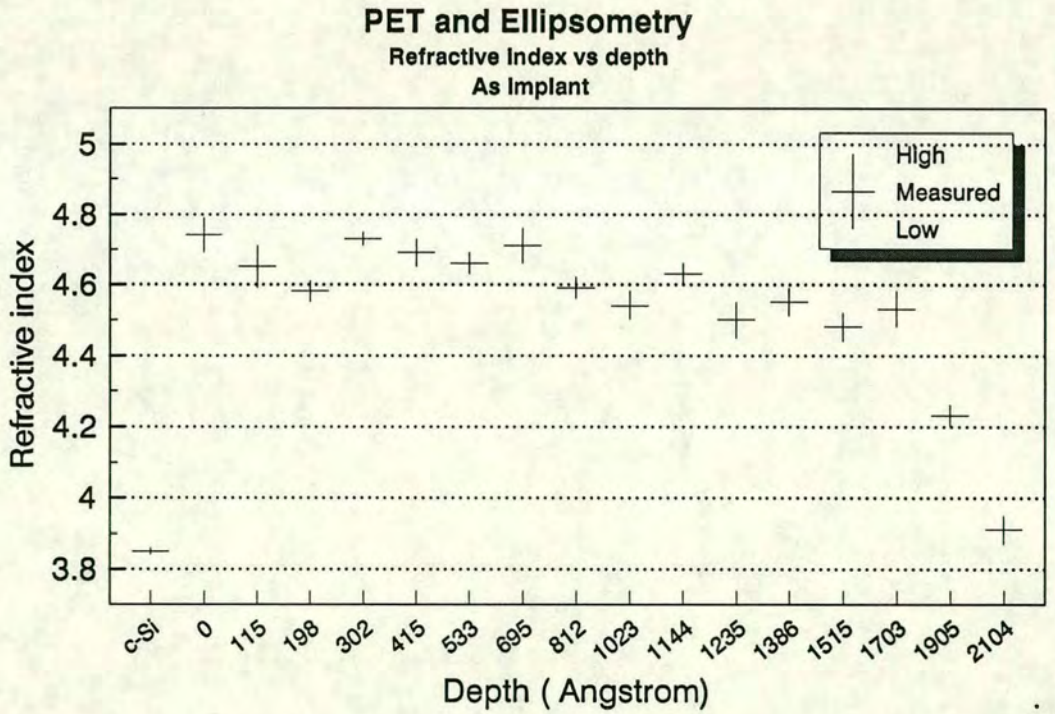

Figure 8–17: The refractive index variation with depth into Si. The PET structure has been used to create the various depths. The leftmost n-value on the x-axis indicates the crystalline Si value before the implant.

Extinction coefficient monitoring. The extinction coefficient depth profile for the As ion implanted specimen is presented in fig. 8–18. The first point of the graph depicts the extinction coefficient value of crystalline Si (c-Si) measured before the implant. The increased sensitivity of the extinction coefficient on dopant concentration and damage, makes it possible to extract a profile peak at about 530 Å. The k value decreases to a value close to that of c-Si at around 2100 Å. The junction must exist at a deeper depth since the k-value can be further lowered towards the extinction coefficient value for crystalline silicon. The number of trenches was not enough to reveal the junction layer.

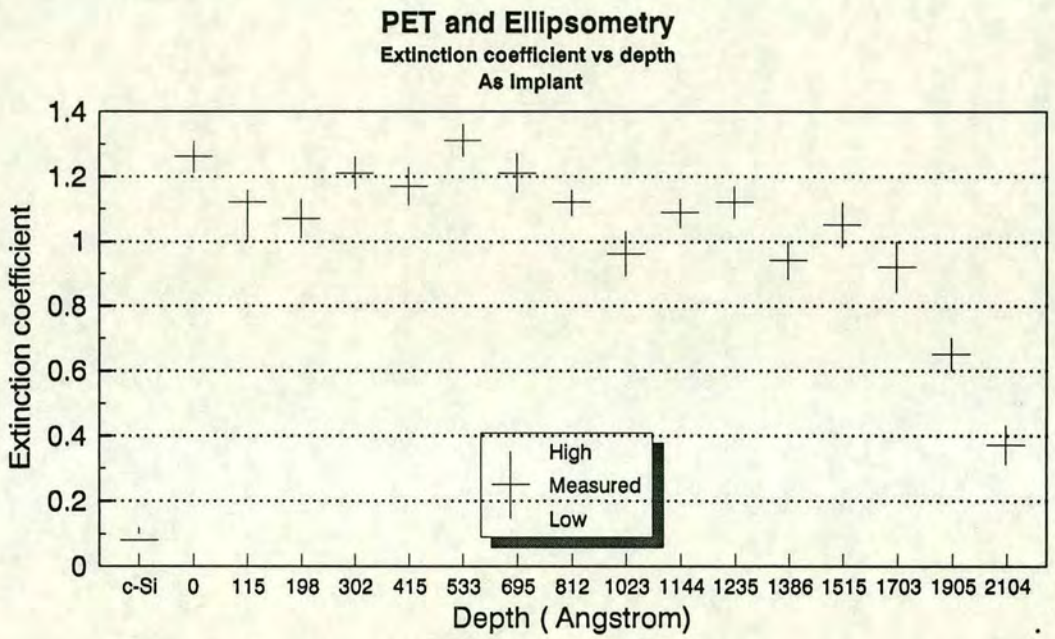

Figure 8–18: The extinction coefficient variation with depth into Si. The PET structure has been used to create the various depths. The left most k- value on the x-axis indicates the crystalline Si value before the implant.

Conclusions. The damage peak position (530 Å) seems to be slightly shallower than the carrier concentration peak position revealed by Hall measurements (570 Å). This is expected since the damage is increased in the region just before the ion rest position. The extinction coefficient is ideal to determine the junction depth of

the implant with a good accuracy since its value depends on changes in the damage state of the single crystal silicon. This evaluation can prove extremely useful to assess implants where channeling effects can shift the junction and severely affect the device electrical characteristics. Refractive index was shown to be less sensitive to damage. No measurements were performed after the anneal step, since as it was experimentally shown in chapter 7 both n and k values are very close to their c-Si values and the sensitivity of the technique is limited by the measurements error.

8.3.1.5 The PET technique combined with four-point probe

The PET structure geometry. The structure used for the PET technique was a 4x4 array of square trenches. Each square of the array was defined by use of the optical stepper framing blades to be 10 $\times$ 10mm. Photoresist exposure uniformity of such a large area is not so good, but the four-point probe size and its resolution impose the lower limit of area requirement. The etching procedure of the photoresist and the underlying Si substrate lead to a higher uniformity; the higher the value of the selectivity of photoresist over Si, the better the uniformity that results. Instead of exposing the trench area in one exposure, multiple neighboring exposures of the same time duration are used in order to scan the whole trench area. This is necessary due to the intrinsic stepper lamp induced non-uniformity if large areas are exposed. The positions of the squares across the wafer were chosen to be on the x- and y- axis coordinates used by the 16 site array of the GRQ four-point probe.

The PET technique characteristics. The optimum trench depths were transferred into Si by use of the PET technique. The wafers were then placed inside the oxygen asher for photoresist stripping. This type of treatment cleans the wafer surface from any organic contaminants and has a direct impact on the repeatability of the sheet resistance measurements. The sheet resistance was monitored three times inside each trench and the average value was used. The 3σ variation inside each measurement site is close to the 2-D sheet resistance variation value.

The depths of the trenches were measured using a Dektak profilometer. The five measurements average for each trench was used as the trench depth. The 3σ variation was defined as the depth measurement error.

Comparison between PET and 2-D results. The PET along with the 2-D four point probe results appear in fig. 8–19. A perfect match between the sheet resistance values of the two curves occurs down to a depth of 500 Å. The PET structure trenches give lower sheet resistance values for greater depths. The resulting difference in slopes between the two sheet resistance profile curves is the reason for the mismatch of the extracted carrier concentration profile curves. This is apparent in fig. 8–19 and affects the carrier profile match in the tail region. The difference in slopes between the two sheet resistance curves in the 600 Å region is responsible for the shift in position between the peaks of the two carrier concentration profile curves.

The possibility of a wrong geometric factor while measuring the sheet resistance does not seem to occur, since experiments conducted using different trench areas (defined by a contact mask) showed that no noticeable sheet resistance distortion due to proximity to trench edges existed.

The sheet resistance mismatch is more likely due to non-uniformities that occur during the implant or annealing steps. The large trench size which is needed for four point probe measurements limits the spatial resolution of the technique. Therefore, the technique is not able to measure profile variations along the wafer. However, it is fast and it can give a carrier concentration profile with minimal process requirements.

Conclusions. The PET structure seems to be appropriate to identify the carrier profile peak position and to give a relatively accurate carrier concentration peak. The profile match is satisfactory to depths about twice the implant peak position. The PET technique combined with sheet resistance monitoring could be used as an indication of whether the right shape of carrier concentration profile on the fabrication line has been achieved. However, the spatial profile variations are of

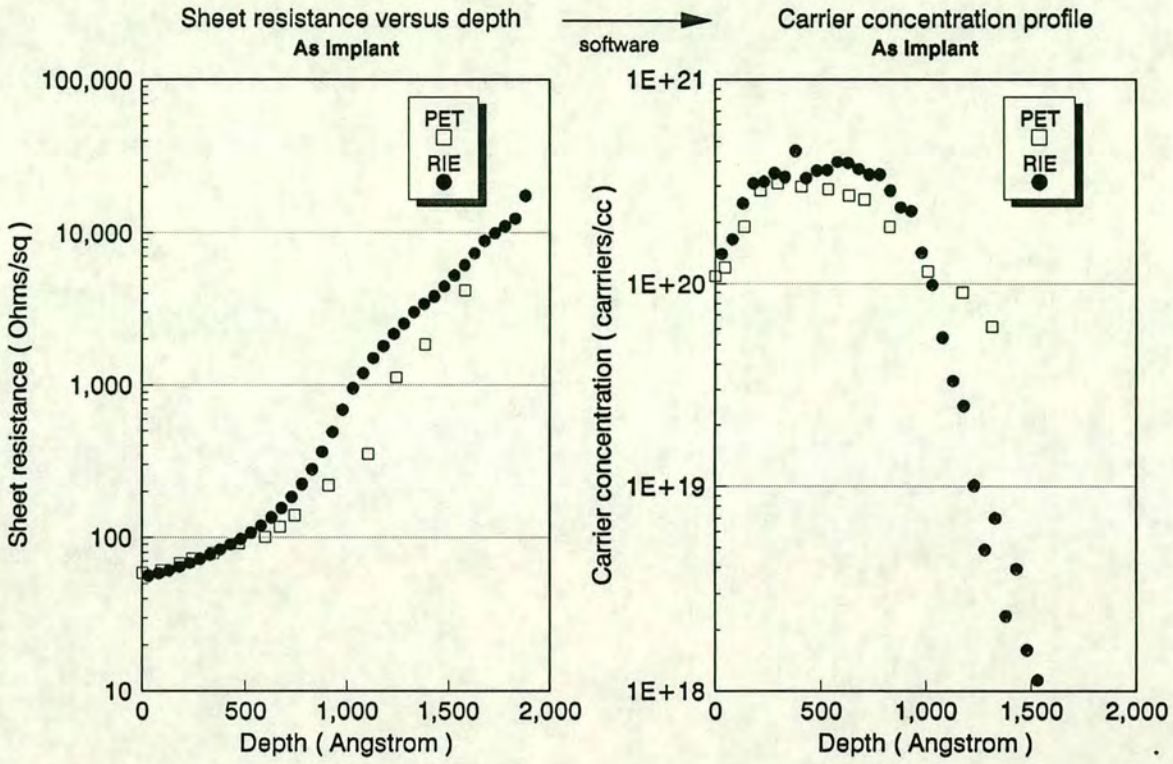

Figure 8–19: A comparison of the measured sheet resistance and the software evaluated carrier concentration by using the PET structure and a whole surface RIE etch. The implant species is As.

the same order as the 3-σ error of the PET curve. Therefore, the sensitivity of the technique is limited by the measurement repeatability and the spatial non-uniformity; whichever of the two gives the larger σ value.

8.3.1.6 Thermal wave measurements.

Thermal waves [2] can be used to monitor implant damage. However, measurements of the As implanted and annealed wafer will be discussed in this section

[2]The Therma-Wave technique is discussed in full detail in section 9.2.1.

[3]. The annealing conditions were identical to those used for the carrier profile measurements. The PET structure used was a 10 x 10 array of 2mm by 2mm square trenches. The small area of the trenches leads to an improved exposure uniformity along the bottom of each trench. The Therma-Wave signal was evaluated in 20 of those trenches as the average of 5 measurements. The trench depth was measured by a Dektak profilometer. The depth was taken to be the average of 3 Dektak scans. The Therma-wave signal variation was less than 3% and the depth accuracy has a 3σ of 75 Å. The results are presented in fig. 8–20.

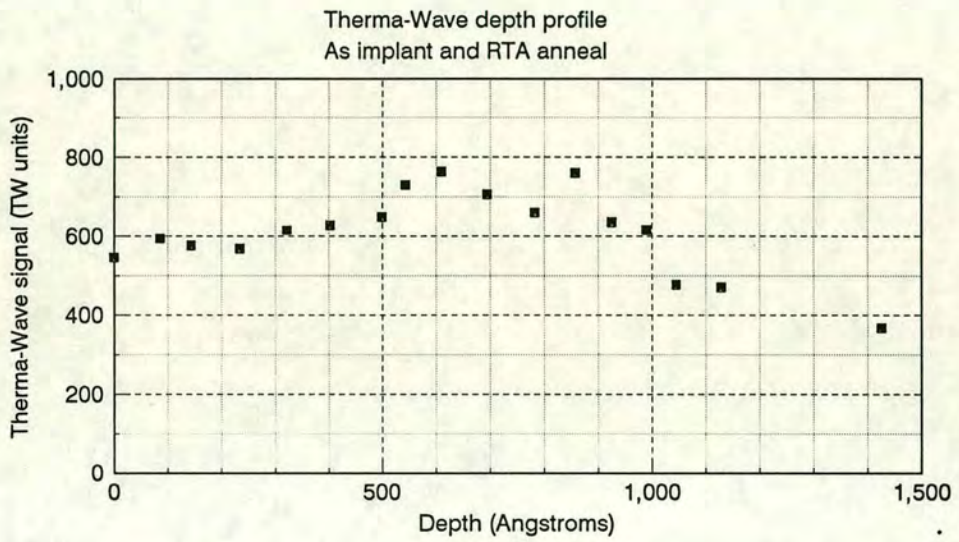

Figure 8–20: The variation of the Therma-Wave signal with depth monitored on trenches of a PET structure. The measurement took place after the wafer was annealed (RTA, 5s, 1000°C). The RIE damage-induced signal for increasing RIE times has been subtracted from the measurements.

The curve shows that the depth profile of the secondary defects after anneal, has two peaks at 600 Å and 900 Å. The first peak is located in the high carrier concentration regime. The second peak can be due to the diffusion of secondary de-

---

[3]Therma-Wave measurements were carried out at Digital Equipment Scotland Ltd, South Queensferry, West Lothian.

fects towards the bulk during the RTA cycle since a defect concentration gradient towards the bulk Si is present and the RTA time is short enough not to redistribute the implanted ions. The thermal wave signal monitors both implanted ion concentration and ion induced damage (see 9.2.1.1). Therefore, for post-anneal measurements, the peak region concentration should give the main contribution to the thermal wave signal. As a result, the above experimental observations are in agreement with theory.

8.3.2 BF_2 implant

8.3.2.1 Carrier profile from Hall measurements

Hall measurements and anodic oxidation were once more used as the benchmark carrier concentration profile evaluation technique[4]. The results of the sheet resistance measurements of a BF_2 implanted sample are presented in fig. 8–21. As in the case of the As implant, a second concentration profile has been extracted from the same wafer for a sample that has undergone RIE treatment for 2 min. The comparison of the two sheet resistance versus depth profiles is depicted in fig. 8–21. No sheet resistance distortion due to RIE damage can be monitored. However, the two carrier(hole) concentration profiles do not match as well. This is purely an artifact of the carrier profile extraction algorithm since the sheet resistance profiles match is excellent. The choice of the user-specified knots position for the cubic splines fit, is critical in the evaluation of the slope of the sheet resistance curves.

The hole mobilities extracted from the Hall measurements are presented in fig. 8–22.

---

[4]The measurements were carried out on an HL5900 Stripping Hall System from Bio-Rad.

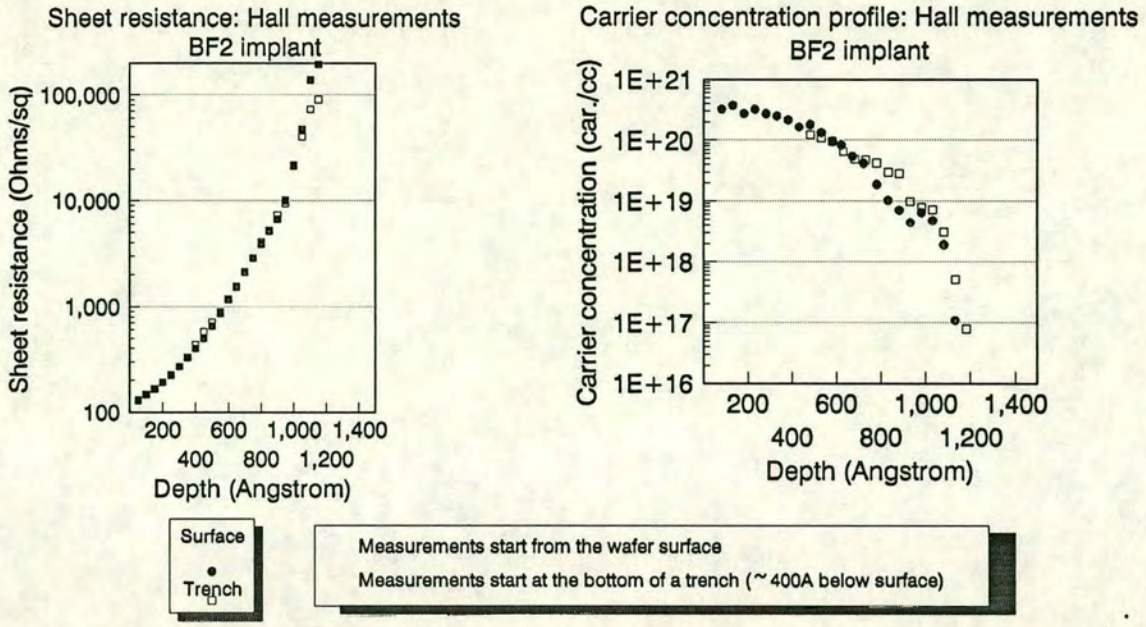

Figure 8–21: Carrier concentration profile of the BF_2 implant evaluated by Hall measurements and anodic oxidation. The profile is extracted from the surface and from measurements starting from a depth around 400 Å below the initial surface. A trench of the PET structure was used for that reason.

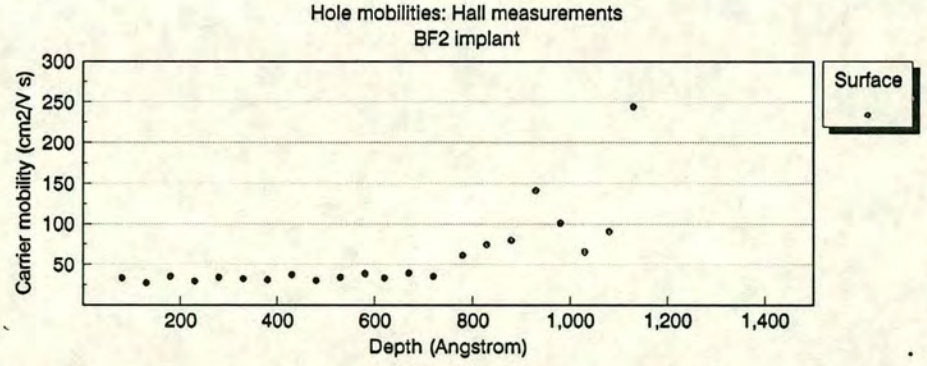

Figure 8–22: The hole mobilities versus depth evaluated from Hall measurements.

8.3.2.2 Two dimension carrier profile comparison

The sheet resistance measurements were performed over 69 sites. RIE was used each time to strip a layer of Si. The thickness of each layer varied from 53 Å for

the first 11 layers (equivalent to a 15s RIE time) to 106 Å (ie 30s RIE duration) for the rest. The depth resolution is higher than the 3 sigma depth error of 42 Å. The sheet resistance measurements across each row were averaged as described in section 8.3.1.2.

As depicted in fig. 8–23 the 3-sigma variation of the sheet resistance along a row is at least 2 to 3 times lower than the variation along a column. Since the depth scale error due to etch rate variation has been taken into account into those graphs, the observed difference implies an implanter-induced error.

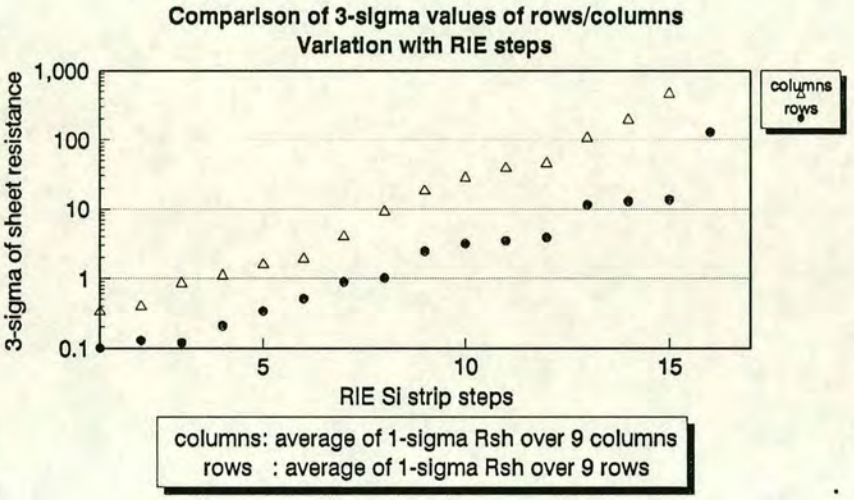

Figure 8–23: Comparison of the 3σ sheet resistance values between rows and columns for the various depths obtained by the RIE steps.

The sensitivity of the technique can be demonstrated by its ability to reveal implant profile variations among different rows. The variation from row 1 (near the wafer flat) to row 8 is presented in fig. 8–24. The sheet resistance increases for depths greater than 600 Å. The same type of sheet resistance behaviour is observed across all rows. This higher variation near the tail of the sheet resistance curves leads to a broadening of the carrier concentration profile tail, as it can be seen in fig. 8–25. This experimental observation strengthens the validity of the argument concerning the inability of surface- sheet-resistance-monitoring to reveal changes occuring in the lower-concentration parts of the carrier profile. The evaluted mobility variation between 8 different rows, presented in fig. 8–26 is

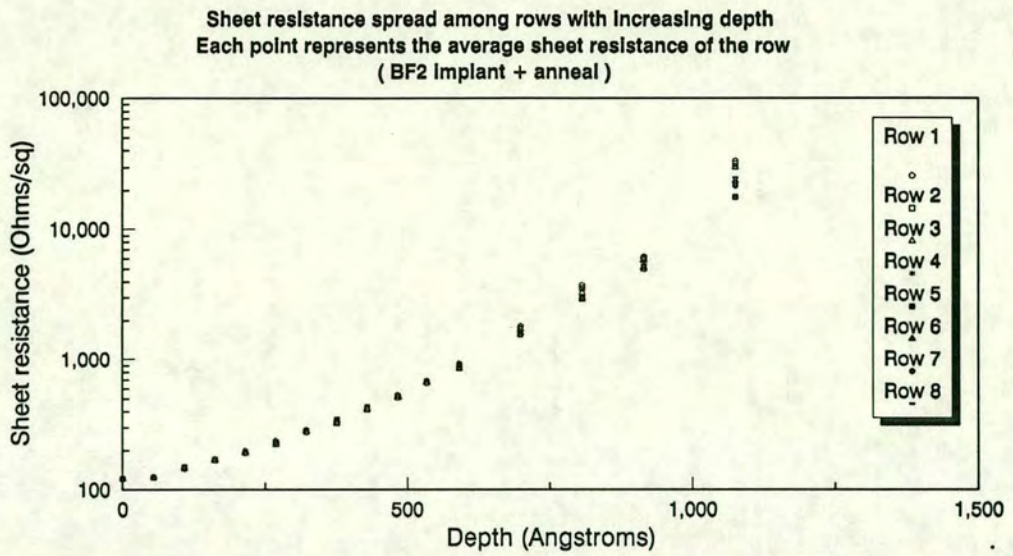

Figure 8–24: The sheet resistance versus depth measurements spread across a wafer. The profiles were evaluated at each of the 8 rows.

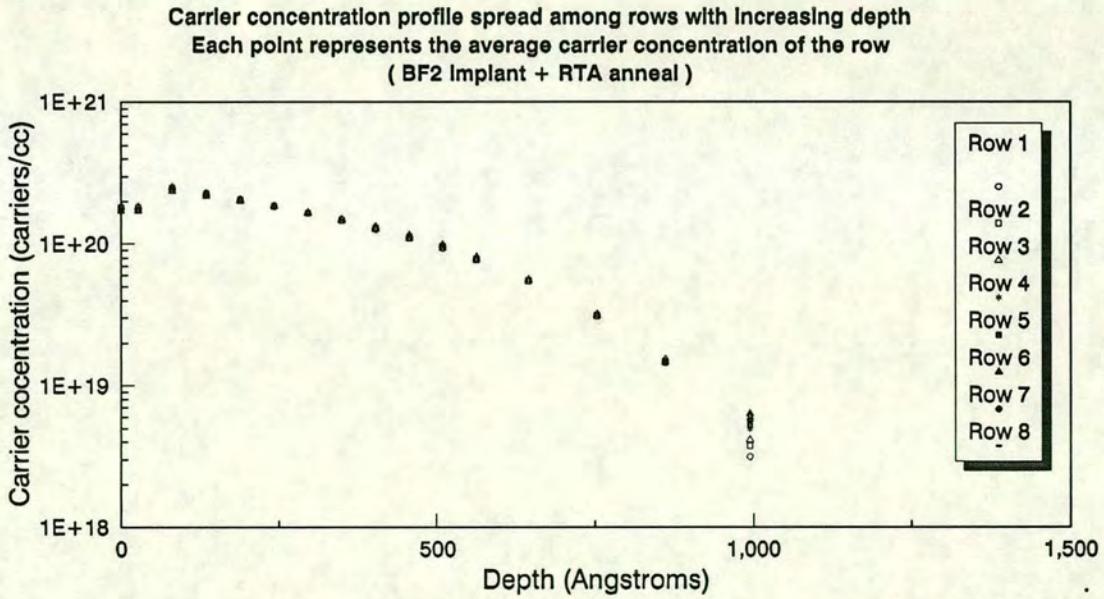

Figure 8–25: Carrier profiles spread across the wafer. Profiles were evaluated at each of the 8 rows.

minimal down to 1000 Å. An increased difference between the rows can be observed as the junction depth is approached. This is due to the similar type of behaviour of the concentration profile and the carrier mobility profile (since both carrier

and mobility profiles are extracted iteratively from the sheet resistance curve). The above experimental observations prove that the 2-dimension RIE method can

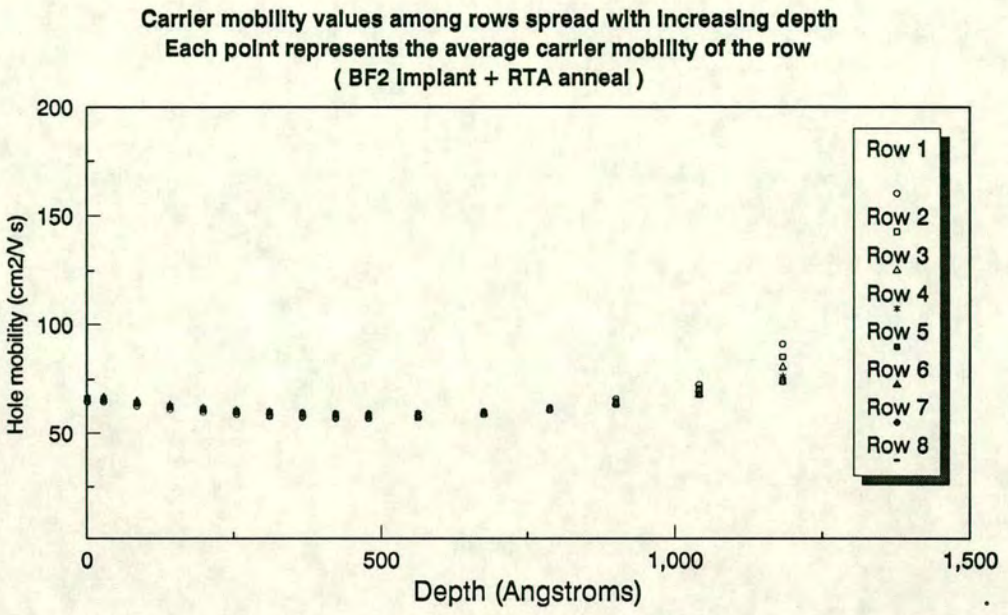

Figure 8–26: The electron mobility profile spread across a wafer. The profiles were evaluated at each of the 8 rows.

reveal the existence of non-uniformities induced by the implant and anneal steps. The sheet resistance and carrier concentration profiles of fig. 8–27 and fig. 8–28 compare the profile non-uniformity at rows 1, 2, 8 and 9 to the measurements repeatability error. Similar results to those of the As implant are obtained.

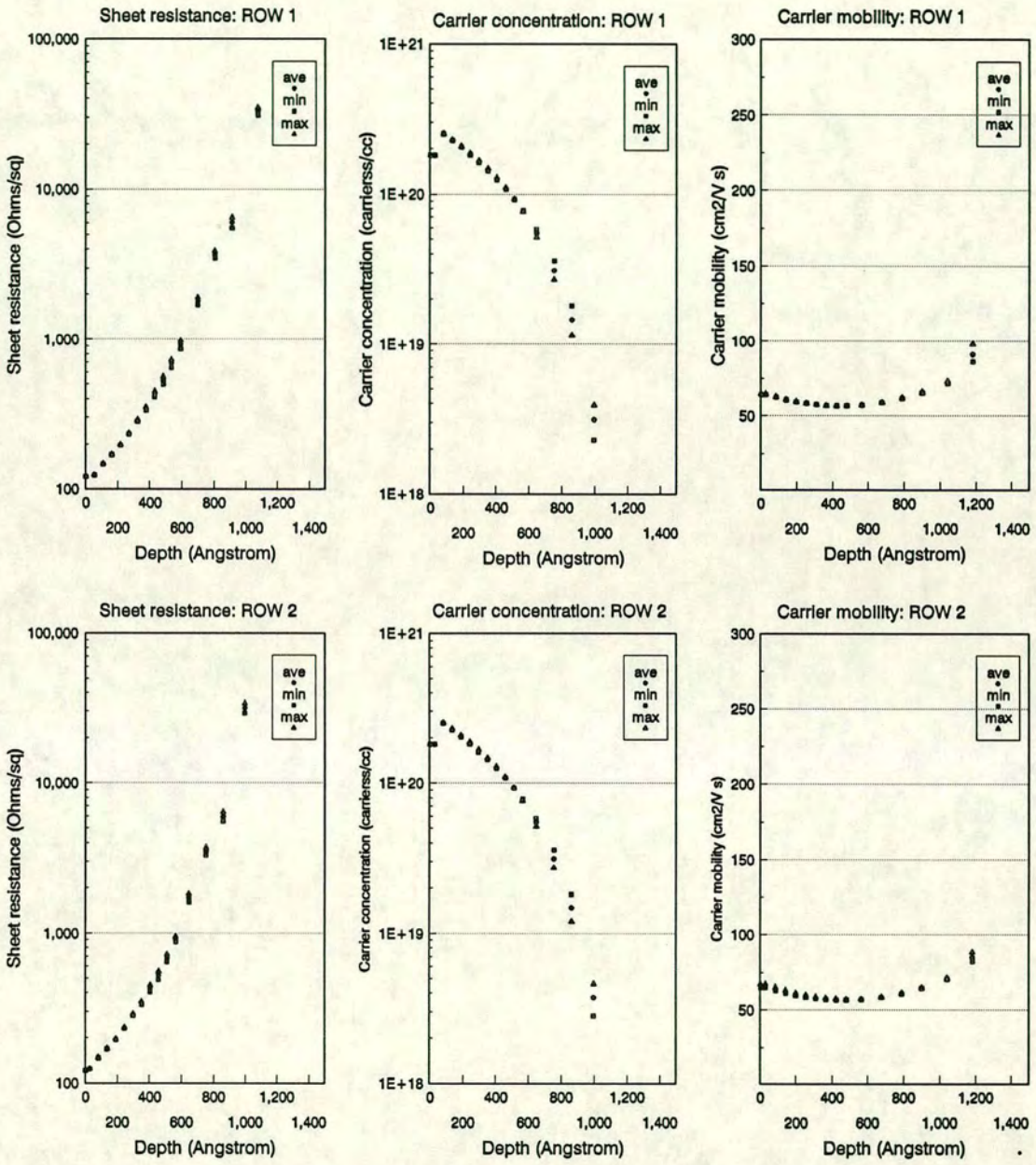

Figure 8–27: Comparisons between rows 1 and 2.

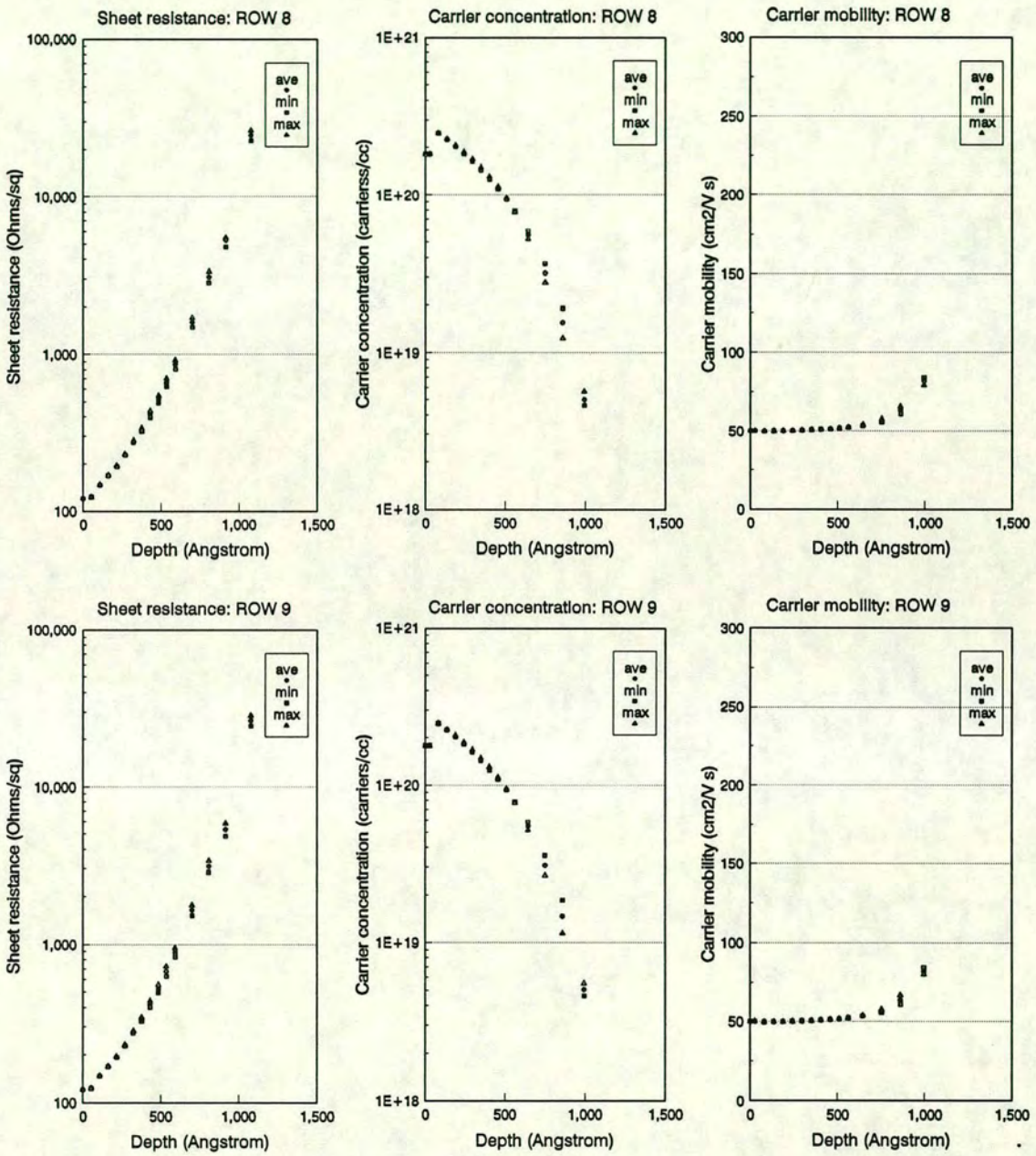

Figure 8–28: Comparison between rows 8 and 9.

8.3.2.3 The PET technique combined with ellipsometry

The PET structure geometry. The structure and the technique are identical to the one described in section 8.3.1.4.

The PET technique characteristics. The technique characteristics have been discussed in section 8.3.1.4.

Refractive index monitoring. The refractive index depth profile for the BF_2 ion implanted specimen is presented in fig. 8–29. Oxygen ashing and HF dip have been used immediately prior to the measurements. The low sensitivity of the refractive index does not permit us to locate the depth of the damage profile peak The decrease in n-values for depths greater than 830 Å indicates that we are on the damage profile tail. The refractive index value at a depth of 1480 Å is close to the crystalline silicon value, indicating that we are in the vicinity of the junction.

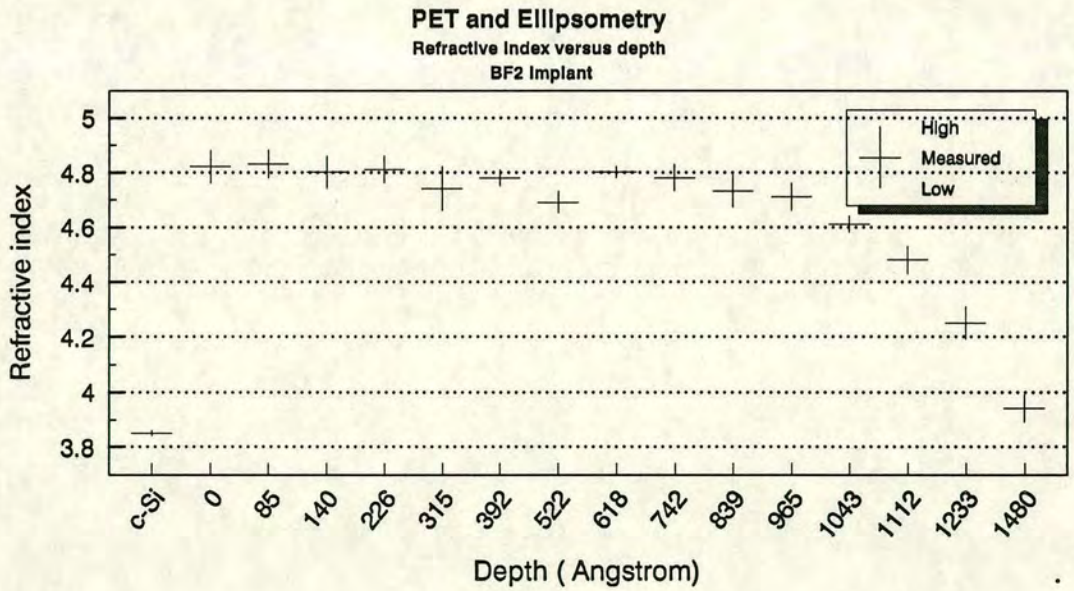

Figure 8–29: The refractive index variation with depth into Si. The PET structure has been used to create the various depths. The left most n- value on the x-axis indicates the crystalline Si value before the implant.

Extinction coefficient monitoring. The extinction coefficient depth profile for the BF_2 ion implanted specimen is presented in fig. 8–30. The first point of the graph depicts the extinction coefficient value of crystalline Si (measured before the implant). Due to the increased sensitivity of the extinction coefficient to dopant concentration and damage, we can locate the damage profile peak at depth of 85 Å. The damage in the 140 to 750 Å regime seems constant (within the measurement error). The extinction coefficient value at 1500 Å suggests that we are in the vicinity of the junction.

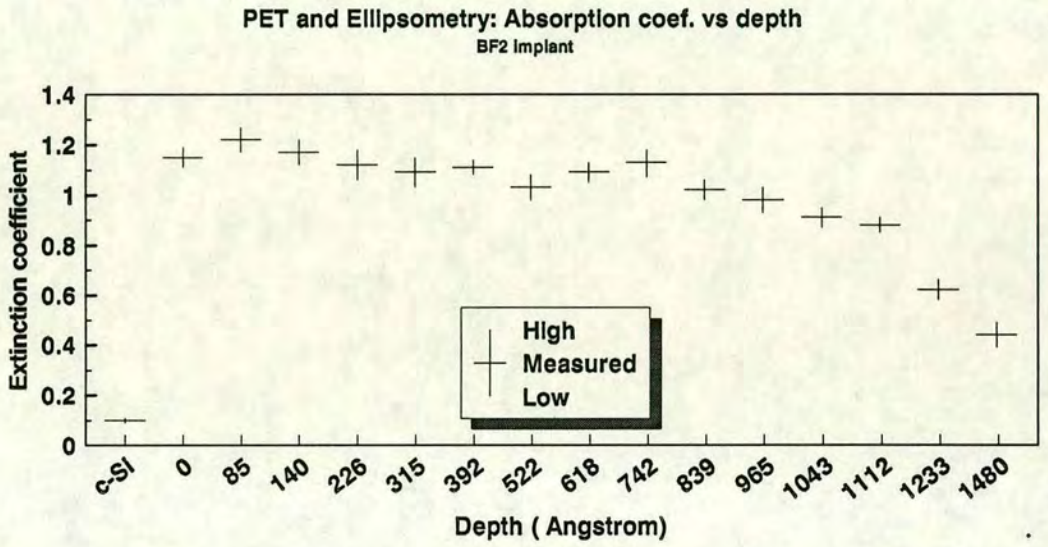

Figure 8–30: The extinction coefficient variation with depth into Si. The PET structure has been used to create the various depths. The left most k- value on the x-axis indicates the crystalline Si value before the implant.

Conclusions. The damage peak position (85 Å) seems to be slightly shallower than the carrier concentration peak position as revealed from Hall measurements (100 Å). This is expected since the damage is increased in the region just before the ion rest position. The extinction coefficent is ideal to determine the junction depth of the implant with a good accuracy since its value depends on the change of the damage state of single crystal. The refractive index is not so sensitive (as it

was also experimentally found and discussed for the As implant in the previous section) and can be misleading if used for junction depth evaluation.

8.3.2.4 The PET technique combined with four-point probe

The PET structure geometry. The structure geometry is identical to that described in section 8.3.1.5.

The PET technique characteristics. The characteristics are the same as those mentio ned in section 8.3.1.5. The only difference is that a depth of 1700 Å should be achieved. Therefore there is a need for the exposure time pitch which is defined in the optical stepper file to be increased in order to achieve the desired depth with the 4 x 4 array of trenches.

Sheet resistance monitoring The PET measurement results appear in fig. 8–31 with the RIE results. The match between the measured sheet resistance and extracted carrier profiles is excellent within the whole depth range. This shows that there is no need for a geometric correction factor in the four-point probe measured sheet resistance due to current distortion near the trench edges (proximity effect).

Conclusions. The PET technique is particular useful in revealing the carrier profile peak position and concentration value and is adequate as a fast method for obtaining the profile shape with a satisfactory accuracy.

8.3.3 Conclusions

Two different methods for extracting carrier and damage profiles from ion implanted wafers have been tested on shallow junction implants. Both methods employ RIE etching as the sectioning technique. No significant error due to the RIE process step has been found from a carefully designed assessment procedure.

The first method, a series of whole-wafer etching and measuring operations, is a 2-dimension monitoring method. It can provide the profiles at 69 (or 225) points

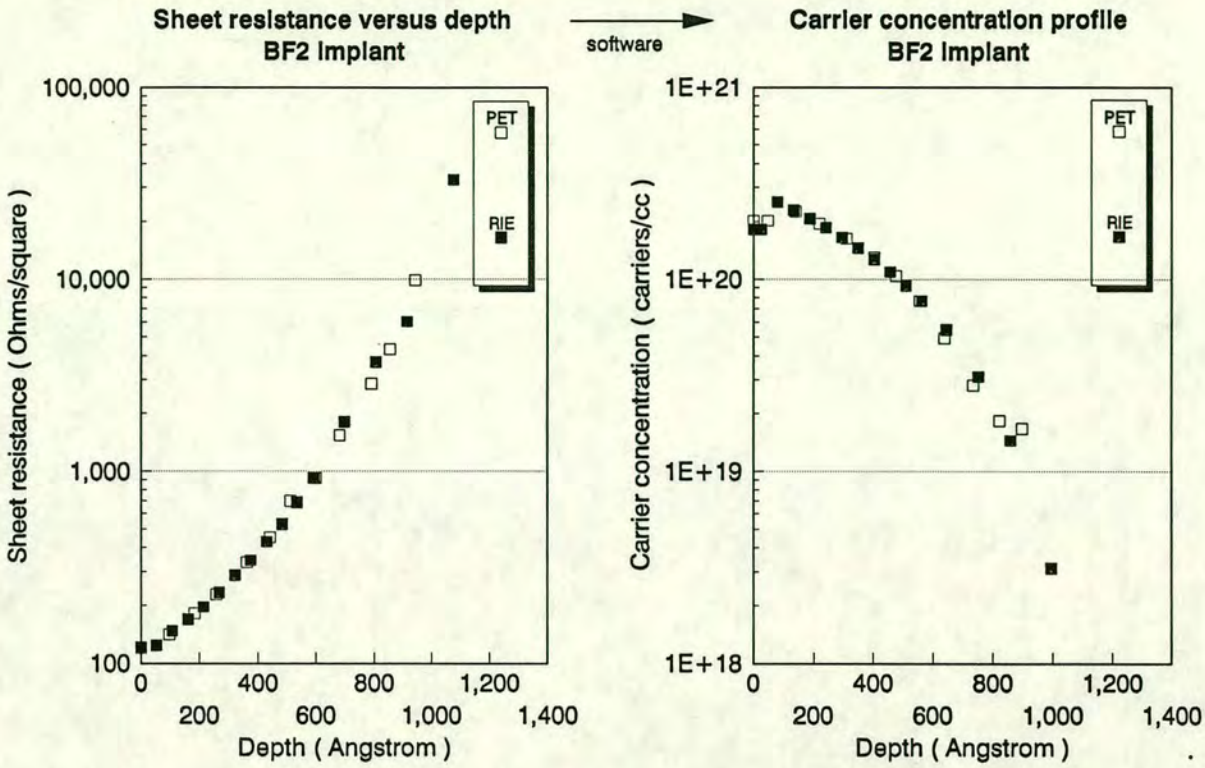

Figure 8–31: A comparison of the measured sheet resistance and the software evaluated carrier concentration by using the PET structure and a whole surface RIE etch. The implant is BF_2.

across a 3-inch wafer. The extracted data can prove extremely useful for assessing profile uniformity across the wafer. The depth accuracy of the method has a 3σ value of 75 Å. The monitoring depth into the implanted silicon crystal depends on the depth resolution of the measurement technique used (four-point probe, ellipsometry, Therma-Wave). The method is adequate for accurate assessments of the implant and anneal non-uniformities along a wafer. This technique has been used as the benchmark technique for assessing the second method.

The second method uses the PET technique as a fast method for providing a series of rectangular trenches in Si. Four-point probe, ellipsometry and therma-wave measurements have been used to extract carrier and damage profiles from those trenches. The depth resolution of the technique is in the 75 Å regime.

Its accuracy depends on the size of the trench used for the measurements (the smaller the trench area, the better the accuracy). The 2-dimensional profiling technique has been used as the means of assessing the degree of profile variation across the wafer and the way such a variation can affect accuracy. It was found that the method can give a profile which is accurate enough to be used for the fast assessment of the implant and anneal process steps.

Both methods were compared to coventional techniques (Hall measurements and anodic oxidation) and they both presented a high degree of consistency.

Chapter 9

Correlations between profiles.

9.1 Introduction

An implant step can be validated by the implementation of existing measurement techniques (four-point probe, thermal-waves etc) at the flat-bottom trenches of a PET structure. The feasibility and accuracy of such measurements has been investigated in the previous chapters. In order to monitor both dopant and damage implant profiles and examine their degree of correlation and how well the experimental results can be explained by theory, a series of experiments was designed. The experimental set-up, the results and the conclusions are discussed in this chapter. The objective is to assess the ability of the PET technique to give on-line information concerning the damage profile shape, the degree of activation after anneal and the carrier concentration profile. Any on-line monitoring technique should be applicable over the whole implant range. Therefore, high dose double implants at different dose and energy levels were monitored and the resulting dopant and damage profiles were analysed and compared.

9.2 The thermal wave technique

A critical review of the thermal-wave technique is given in this section since the method has been extensively used in combination with the PET structure for damage profile evaluation.

9.2.1 Principles of the technique

A schematic depiction of the thermal-wave laser beam deflection technique [1, 2] is presented in figure 9–1. Two low-power laser beams are used. The Ar^+ ion laser beam is acousto-optically modulated at frequencies up to 20MHz, directed through a beam expander and then focused to a 1μm diameter spot size on the wafer. This is the heating beam and it has an incident peak power of 12mW. Absorption of light from the intensity-modulated Ar-ion pump laser generates thermal waves[1] and plasma waves[2] within the surface region of the wafer [3].

The 633nm beam of a 5mW He-Ne laser, the probe beam, is directed through a beam expander, a polarizing beam splitter and a quarterwave plate, reflected off a dichroic mirror and then focused onto a 1μm diameter spot on the wafer about one beam radius from the center of the modulated heating beam [3]. The probe beam is deflected by the periodic change in local slope of the sample surface. The reflected probe beam passes through the quarterwave plate again, and since it is 90° out of phase from the beam leaving the He-Ne laser, it is directed by the polarizing beam splitter to the bicell photodector, which measures the periodic deflections of the probe beam.

---

[1]Thermal wave is a modulated temperature profile.

[2]Plasma wave is the modulated plasma density of photoexcited carriers prior to their recombination.

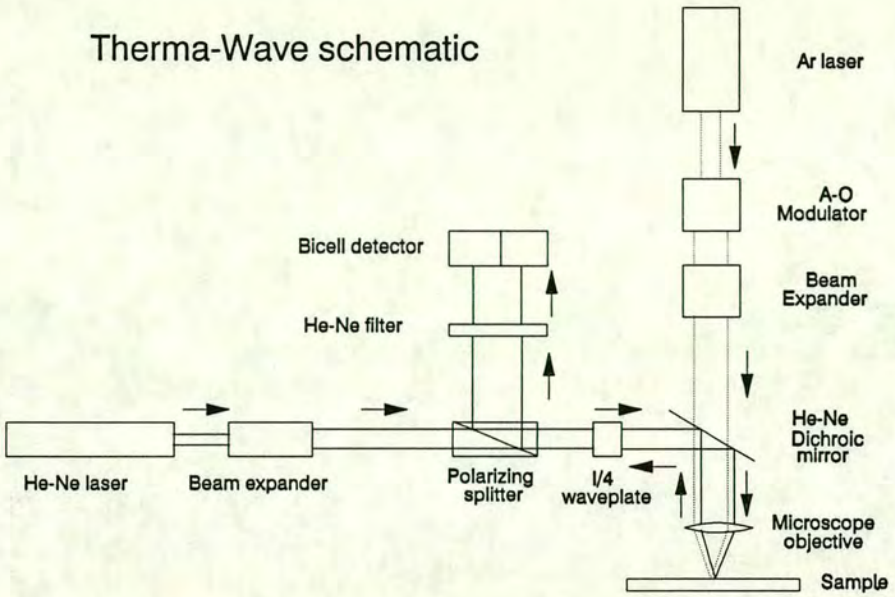

Figure 9–1: Block diagram the laser-based thermal wave generation and detection of the Therma-Probe 150 system.

In order to evaluate the spatial and depth resolution of the method, the quantity of interest is the propagation depth [4] of both waves. For the thermal waves this quantity, μ_t is defined as:

$$\mu_t = \left[\frac{2\kappa}{\rho C\omega}\right]^{1/2} \tag{9.1}$$

where κ represents the thermal conductivity of the material, ρC is the specific heat of that volume(ρ is the density and C is the specific heat) and ω is the angular frequency of modulation of the pump laser.

If high modulation frequencies (eg 1MHz) and low recombination times (eg silicon samples) are assumed, the propagation depth for plasma waves, μ_p can be approximated by the equation:

$$\mu_p \approx \left[\frac{2D}{\omega}\right]^{1/2} \tag{9.2}$$

where D represents the ambipolar diffusion coefficient of the material.

It therefore follows that the higher the modulation frequency, the shallower the propagation depth for both waves, for a specific material. For Si at 1MHz the propagation depth is about 2μm [5].

In response to the time-varying heat stimulus of the Ar^+ source, a periodic temperature variation occurs within a small volume of the wafer. The amplitude of the temperature fluctuation is typically 10 to 20 °C. Minor, nondamaging and reversible changes of the surface of Si are the result of the periodic, small amplitude temperature oscillations in the heated volume. In semiconductors those changes include both local thermoelastic expansion and photoexcited electron-hole plasma effects [3] confined in the above domain. Those changes are detected by the He-Ne laser 'probe' through the modulation of the sample reflectivity. For intrinsic Si the thermal and plasma wave effects on Si reflectivity are comparable in magnitude and opposite in sign. Therefore, we get a relatively small net reflectivity modulation. For highly disordered semiconductors, however, there is a sizable change in the modulated reflectance signal with increasing lattice damage. This is due to the more significant effect of lattice disorder on the photoexcited plasma than on thermal waves [2]. The modulation of the sample reflectivity, $\Delta R/R$, is defined as the thermal-wave measured signal, refered to as signal in the rest of this chapter.

9.2.1.1 Ion implant monitoring ability

The ion implantation process can be monitored by the thermal wave system due to both the partially disordered Si crystal layer (from the ion implant process) and the lattice perturbation due to the implanted ions themselves. In both cases, the thermal-wave-induced thermoelastic and optical effects are changed in proportion to the number of the implanted ions [5].

9.2.1.2 Ion implantation monitoring applications of the technique

1. Dependence on ion dose. Since the measured signal is sensitive to the level of damage present in the surface layers of the wafer it can be used to monitor the implanted dose in Si. The dose range over which the signal changes is in the range: $10^{11} - 10^{15}$ions/cm^2. However, appreciable ion dose sensitivity has been found to extend below 10^{10}ions/cm^2 and up to 10^{17}ions/cm^2 [6].

A means of measuring that dependence is through the sensitivity defined in [6] as:

$$S = \frac{dF/F}{dD/D} \tag{9.3}$$

the percent change in measured signal, F, caused by a unit percent change in dose (D). The observed sensitivity minimum for As, B and P in the $10^{12} - 10^{13}$ions/cm^2 region [6], does not represent a real damage phenomenon since no such minimum is observed if the double implant technique is used in this dose range (see measurements in section3.4.6.1). Since the signal measurement error does not exceed 2 % of the measured value, this sensitivity minimum is a technique artifact in that dose range.

The industry trend to use shallower junctions has given rise to the need for monitoring the implant dose for very small ion energies. According to [7], this has been achieved by creating a dose calibration curve against the signal for the specific low energy used. After each implant the wafer is monitored and the dose value is checked against this calibration curve.

2. Dependence on energy. Since the ion energy determines the degree of crystal damage a strong dependence on energy is expected. However, according to [6], the signal levels off for medium energies (80-120keV) and decreases for higher energies for B. For As and P, the signal increases with a slower rate for higher energies than for lower ones. A possible explanation is that the method is not sensitive to damage at depths reached by the higher energy boron ions. Additional measurements, [5], in the 10keV to 200keV have shown that the dependence of the signal on ion energy is relatively minor.

4. Dependence on oxide thickness. Growth of an oxide layer of 300 - 500 Å prior to implantation is commonly used in order to avoid channelling effects. Since the thermal wave technique can monitor oxide thickness it is possible to identify dose non-uniformity across a wafer which is due solely to oxide thickness fluctuations. This is achieved by subtracting the 2-D maps of implanted dose and oxide thickness signals as measured on the same sites. The resultant 2-dimensional

map represents the dose non-uniformity due to the implant process step [7]. The signal increases as the oxide layer thickness increases, [5]. Since the thin-film interference in the oxide layer is taken into account in the TW signal measurement, the increase of the signal level with increasing oxide thickness does not arise from optical effects. It can be attributed to the ion beam interaction within the oxide layer, causing the implant damage to be shifted towards the surface and thus confined to a shallower region.

5. Dependence on planar channeling. Since ions that undergo planar channeling are deflected along the channel while keeping most of their energy, they do not cause significant damage. Therefore the signal should be lower than usual if planar channeling takes place. According to [6] the signal is more sensitive than sheet resistance indetecting channeling. However, no experimental evidence is given by [6] to support the claim.

6. Dependence on dose rate. For doses below the threshold for amorphization, the signal is sensitive to the ion beam current. As the beam current increases the signal value saturates. The effect of dose rate on damage has been investigated [8], [9] and it was shown that the residual damage level is connected to the temperature history of the sample during the implant. A more simplistic approach to the dependence on damage (and dose rate) of the signal is the following, [6].

The primary assumption made, is that isolated defects created by the impinging ions are unstable at room temperature, while aggregates of such defects are stable. The crucial parameter is the number of defects created per impinging ion. For light ions, where the ratio is low, creation of stable aggregates requires defects from a number of ions. Only for medium dose rates(where we do not expect to have any effect on wafer temperature) would the residual damage increase with dose rate. For heavy ions, where the ratio is high and cooperative effects dominate the stable aggregates, residual damage is not affected by the dose rate variation.

7. Dependence on species. The difference in atomic mass for the different implanted ions results in a different level of residual damage, the more massive the ion the greater the lattice damage created. The signal lies in the 1100 to 600 units range for As^+, P^+, BF^+, B^+ in decreasing order of signal magnitude [7], [6]. As a result, it provides the ability to detect wrong species selection, although tight tolerance on implant doses results in narrow acceptable windows on the signal.

8. Threshold voltage inspection. The dose range for threshold implants is low (5E10 to 5E12 ions/cm^2) but the signal is sensitive enough in that regime to monitor it. The enhancement threshold voltage has been measured by electrical test on completed transistors and has been correlated to the TW signal just after the implant, showing a correlation coefficient of 98.1% [10].

9. Detection of ion implanter malfunctions. Scan lock-ups, loss of beam integrity and other similar failures can be detected due to the small spot size of the laser beam which gives a high spatial resolution. TW monitoring can thus increase the yield.

9.3 Experimental preparations

9.3.1 Objectives

Fast, on-line implant monitoring techniques require high spatial resolution and direct measurements of physical quantities without the need for calibration standards and procedures. Since those requirements are not fullfilled by any single technique a combination of techniques has to be used. Sheet resistance measurement is a direct method with a limited spatial resolution of 0.25mm. Thermal-waves on the other hand, provide an indirect method with a high spatial resolution of 1 μm. The former method monitors the carrier concentrations generated from activated dopants, while the latter monitors the combined effect of the degree of damage and the dopant (active and non-active) concentrations. The collection

of information with the aid of both methods can offer a complete picture of the implant and annealing step. Therefore, those were the methods chosen for the on-line monitoring of implant profiles. The results must be compared with SIMS measurements performed after the anneal step and SUPREM IV simulations. The degree of correlation among the above methods has to be investigated and theoretically explained.

9.3.2 Designing the experiment

9.3.2.1 The sample geometries

The x-y dimensions of PET-structure trench used for the thermal-wave measurements were chosen to be 3mm by 1mm with a gap of 0.5mm between neighbouring trenches in both directions. An array of 20 by 10 (200) trenches was transferred to Si using the PET technique. The depths of the trenches were measured by a surface profile measuring system (Dektak). The assigned depth values were the average of three Dektak scans across the 1mm side of the trench. They were performed at the center and the two edges of the trench. The depth difference between adjacent wells is typically around 100 Å and the 3-sigma variation across each does not exceed 80 Å. In order to avoid introducing damage that would affect the thermal-wave signal, the depth measurements were performed after the thermal-wave measurements. The trench surface area for the four-point probe measurements is 10x10 mm square[3]

9.3.2.2 The implantation parameters

3-inch, n-type, 14-20 Ωcm wafers with a < 100 > orientation were used for the experiment. The implants chosen w ere the following:

---

[3]As explained in chapter 6, those big trench areas can be achieved by exposing small neighbouring dies in the wafer stepper. Care must be taken so that overlap or unexposed regions between the neighbouring dies do not occur.

Wafer # 1. (BF_2 implants in n-type wafer)

1st implant: **6.0x10^{16}ions/cm^2@90keV(60scans@1.0x10^{15}ions/cm^2)**

2nd implant: **2.0x10^{16}ions/cm^2@25keV(20scans@1.0x10^{15}ions/cm^2)**

Wafer # 2. (BF_2 implants in n-type wafer)

1st implant: **2.0x10^{16}ions/cm^2@90keV(20scans@1.0x10^{15}ions/cm^2)**

2nd implant: **6.0x10^{15}ions/cm^2@25keV(6scans@1.0x10^{15}ions/cm^2)**

Wafer # 3. (BF_2 implants in n-type wafer)

1st implant: **6.0x10^{15}ions/cm^2@90keV(60scans@1.0x10^{14}ions/cm^2)**

2nd implant: **2.0x10^{15}ions/cm^2@25keV(20scans@1.0x10^{14}ions/cm^2)**

Those implants are intended to produce box-type dopant profiles. Due to the high doses being used, a significant part of the dopant concentration should remain inactive after the annealing step. A large number of scans is used for the high dose implants, to minimize the in-situ annealing effect that takes place during implantation (due to increased temperature on the target). The energies that are being used are selected in order to achieve the box-type dopant profile shape [4] and incorporate both low (25keV) and medium (90keV) values. Double implants are difficult to monitor accurately by simple sheet resistance measurements due to the interaction of the two implant profiles and the intrinsic averaging of the sheet resistance method (see also chapter 1 and chapter 3).

Thermal-wave and SIMS measurements were performed after the implant step. Four wafers similar to those described above were annealed using RTA. The sheet resistance measurements were performed:

1. In combination with RIE layer removal over a two-dimensional (69 points) matrix across the wafer, in order to reveal dopant profile non-uniformities across the wafer. Those results constituted the benchmark for the PET implementation.

---

[4] SUPREM IV calculations have been used to specify the energies.

2. Inside the PET structure trenches (implementation of the fast dopant profiling method).

SUPREM IV [5] has been used to simulate the two ion implantation steps for each wafer. The physical parameters chosen for the simulations, were the default values of the model in use (Pearson IV distribution was chosen as the implant model).

9.3.2.3 Preliminary experiments

Reactive ion etching (RIE) has been optimized to induce minimal damage in Si during the PET structure formation. RIE damage in Si can be nondestructively monitored by use of Thermal-waves [11]. The effect of RIE damage on thermal-wave measurements has therefore to be carefully investigated to insure that the RIE-induced damage signal does not distort the actual damage profile measurements. In order to evaluate the effect of RIE time on ion induced damage in crystalline silicon, the signal level was monitored for different RIE etch times. This is necessary since for the PET technique, different trenches are RIE-etched for different time intervals resulting in different levels of damage. A wafer was divided into 6 zones which were etched for 0, 1, 3, 8, 10 and 15 minutes respectively. A line TW scan, fig. 9–2, shows the increasing signal levels for increasing RIE times. For time intervals longer than 8 minutes the signal does not indicate any further increase beyond the 300 units. Two clean n-type and p-type wafers were also used to monitor the TW signal for undamaged wafers. The results are depicted in fig. 9–3 and fig. 9–4.

---

[5]SUPREM IV is the fourth version of the Stanford University integrated circuit process simulator program SUPREM and is distributed by Technology Modelling Associates Inc.

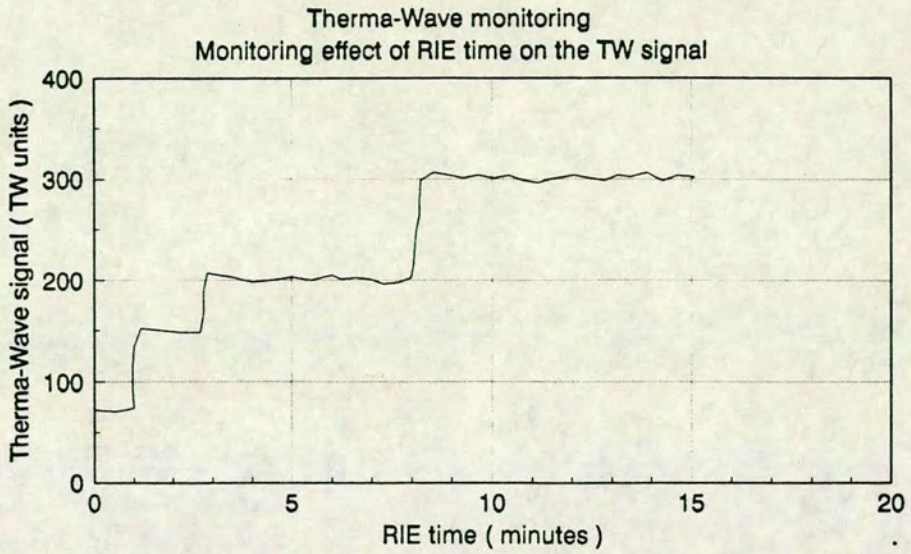

Figure 9–2: The Therma-Wave signal level as a function of the RIE time duration. The RIE time intervals on the graph are 0, 1, 3, 8, 10 and 15 minutes. For etching times longer than 8 minutes, no further increase of the signal is observed.

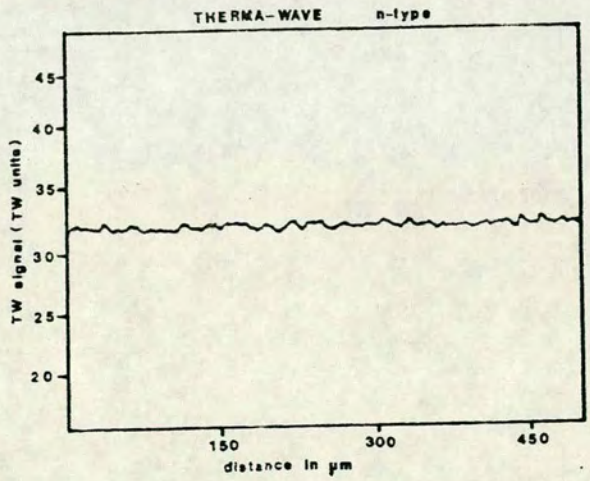

Figure 9–3: The Therma-Wave signal level for a n-type wafer.

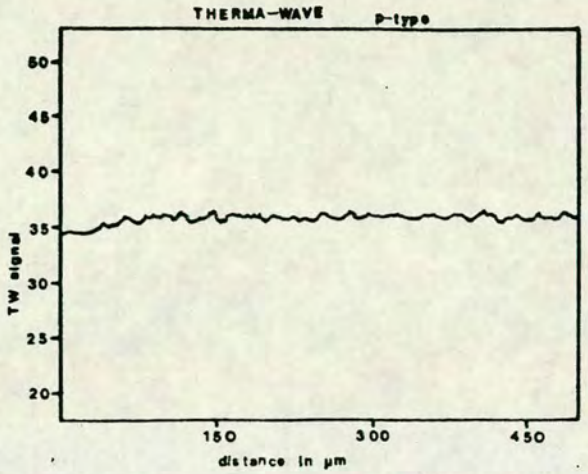

Figure 9–4: The Therma-Wave signal level for a p-type wafer.

9.4 Experimental results

9.4.1 PET and Therma-Wave

9.4.1.1 Wafer 1

In fig. 9–5 the signal of the damage profile of the first wafer is displayed. The signal does not decrease monotonically with depth, as suggested in [12]. Instead, it reveals a peak at 580 Å due to the damage induced by the two implants of different energies and doses. For greater depths it decreases down to a value of around 300 units. This value is equal to the signal value revealed in fig. 9–2 for a RIE etch longer than 8min. It is of no practical use to gather data for deeper depths, since the 300 units signal is going to dominate for etching time longer than 8 minutes.

The 'bump' that appears near the 1300 Å depth could, at first thought, be attributed to the end-of-range-loops damage created by the implants. However, the SIMS results of fig. 9–5 indicate a similar type of profile shoulder at 2000 Å. This is due to the phenomenon of dissociation of the BF_2 molecule (inside the ion beam) before impact with the target. Therefore, the boron and fluorine

atoms acquire the full acceleration energies of the molecule (90 keV and 25 keV for the two implants) and they penetrate deeper in the wafer than the respective boron and fluorine atoms that dissociate inside the Si wafer. Both boron and fluorine atoms contribute to a deeper ion induced damage, thus constituting the main reason of the depth disagreement between the SIMS profile shoulder and the damage profile 'bump'. Further discussion on the SIMS results will take place in section 9.4.1.3.

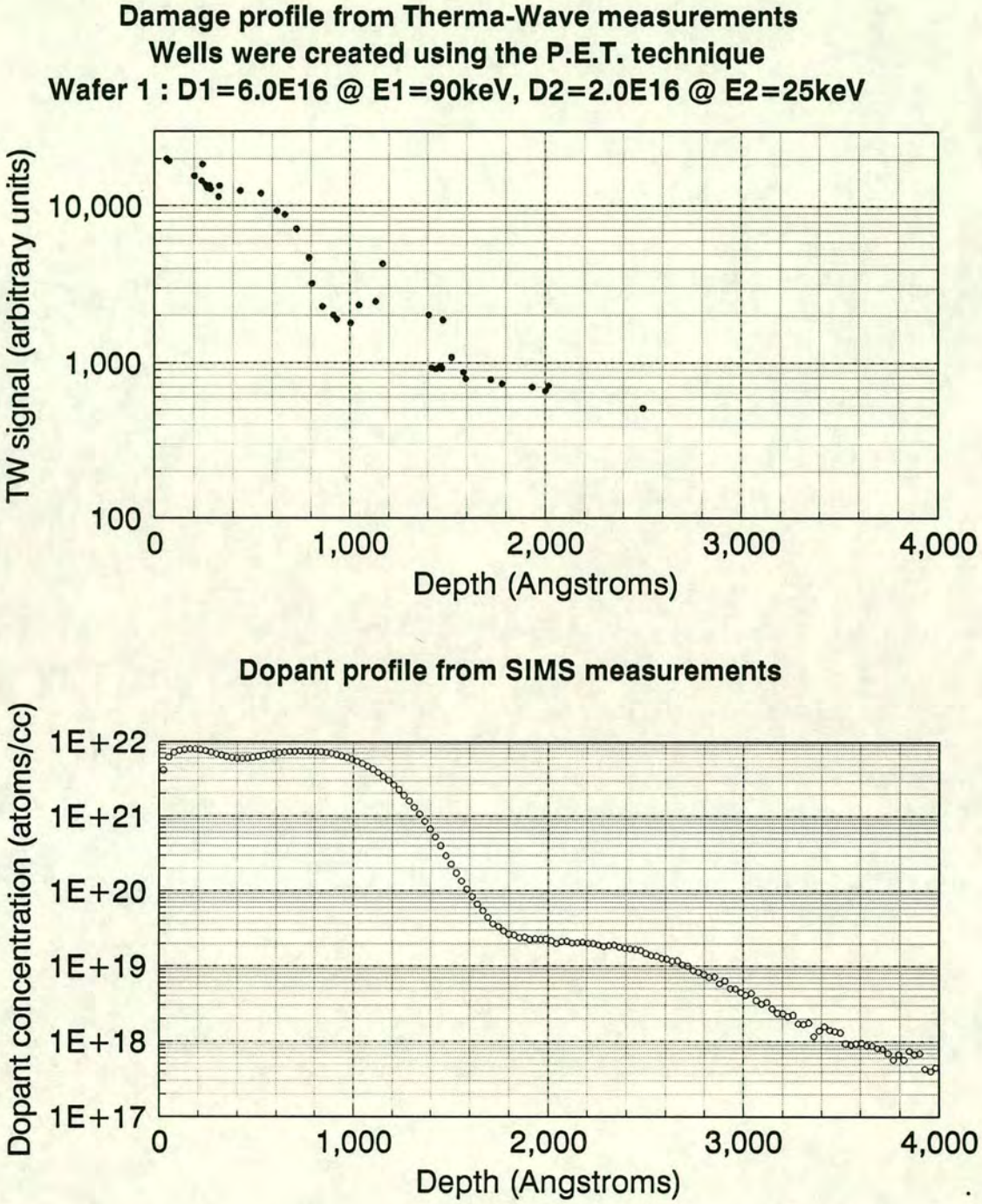

Figure 9–5: A comparison between the damage profile and the dopant profile for wafer # 1. Therma-Wave and SIMS measurements have been used.

Dopant profile peaks, according to the SIMS measurements, can be found at 230 Å and 800 Å. No clear damage peak can be observed after the two high dose

implants although complete amorphization of the substrate has occured. The maximum damage value is obtained at the Si surface. For increasing depth, damage level decreases. This decrease can be attributed to the decrease of the amorphization depth as measurements are performed inside the PET trenches of increasing depth into silicon.

There is a 200 Å disagreement on the depth of the second peak between the two experimental techniques. The two different quantities monitored by the two techniques can conceptually explain the depth disagreement between the two types of profiles. Dopant atoms are the implanted ions that, eventually, come to rest in the target. Near the end of their range, they are expected to move with very low kinetic energy since they lose energy from the elastic collisions they undergo with the host atoms. For low energy ions the nuclear interaction mechanism dominates over the electron stopping mechanism and the degree of induced damage increases. The thermal-wave measurements monitor those damage-traces of the dopant ions. Therefore, it is expected that a damage peak should appear at a shallower depth than a dopant peak. The depth difference between those peaks should be a function of energy, dose, temperature and masses of both the dopant and the host atom. The depths at which the SIMS dopant profile peaks are observed can be compared

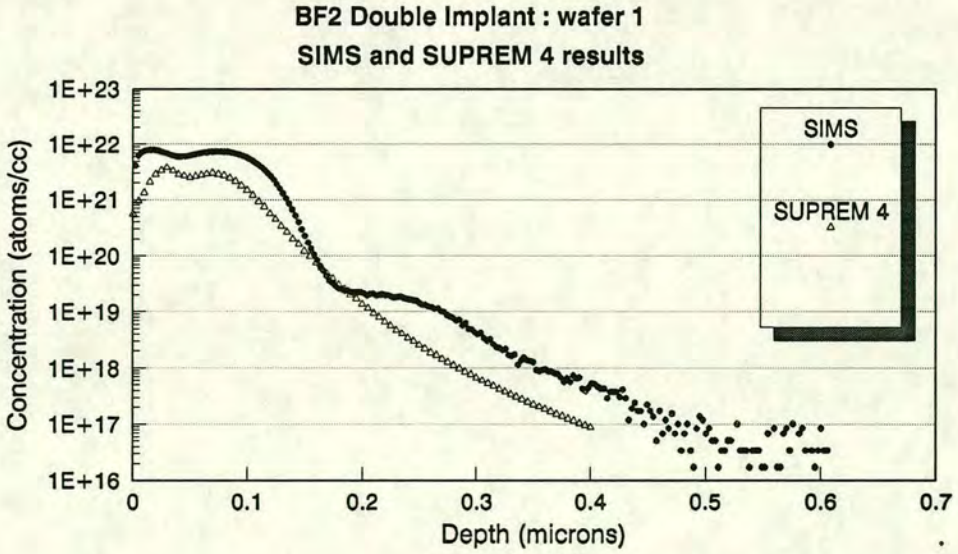

Figure 9–6: Suprem 4 doping profile simulation for wafer 1.

to the SUPREM-4 simulated profile of the double implant. The simulation appears in fig. 9–6 and the dopant concentration peaks are found around 380 Å and 780 Å. The simulated high-dose implant peak depth location is in agreement with the SIMS results. However, the simulation seems to give a much deeper low-energy-implant peak. This is due to the difficulty in modelling low energy implants. The models used are not satisfactory and the results are taken from linear interpolation between experimental values that are kept in tables [6].

9.4.1.2 Wafer 3

In fig. 9–7 the Therma-Wave and SIMS measurements of the third wafer are displayed. The two damage peaks appear at around 200 Å and 600 Å and the 'bump' due to molecule dissociation before impact with the target, in the 1900 Å to 2400 Å depth regime. The 'bump' is not as pronounced as in wafer 1 measurements. The dopant profile extracted from SIMS measurements gives the peak depths at 210 Å and 800 Å.

The first, high dose implant creates a completely amorphized region which extends to a depth equal to the projected range of the boron ion. The 600 Å peak can be attributed to the dominanation of the electron stopping mechanism for boron ions that come to rest at their projected range depth. Therefore, this damage peak should appear at a shallower depth than the dopant concentration peak.

The second implant, due to the lower implant energy, results in a shallower projected range for the boron ions. Therefore, it increases the dopant concentration in the near surface region. As a result, the concentration of interstitial boron atoms is increased. The 200 Å peak of the thermal-wave profile can be, therefore, attributed to the pronounced changes of the thermoelastic properties of the substrate, due to the high concentration of dopant atoms in that region.

---

[6]For more details consult the Technology Modelling Associates, Inc. SUPREM 4 manual.

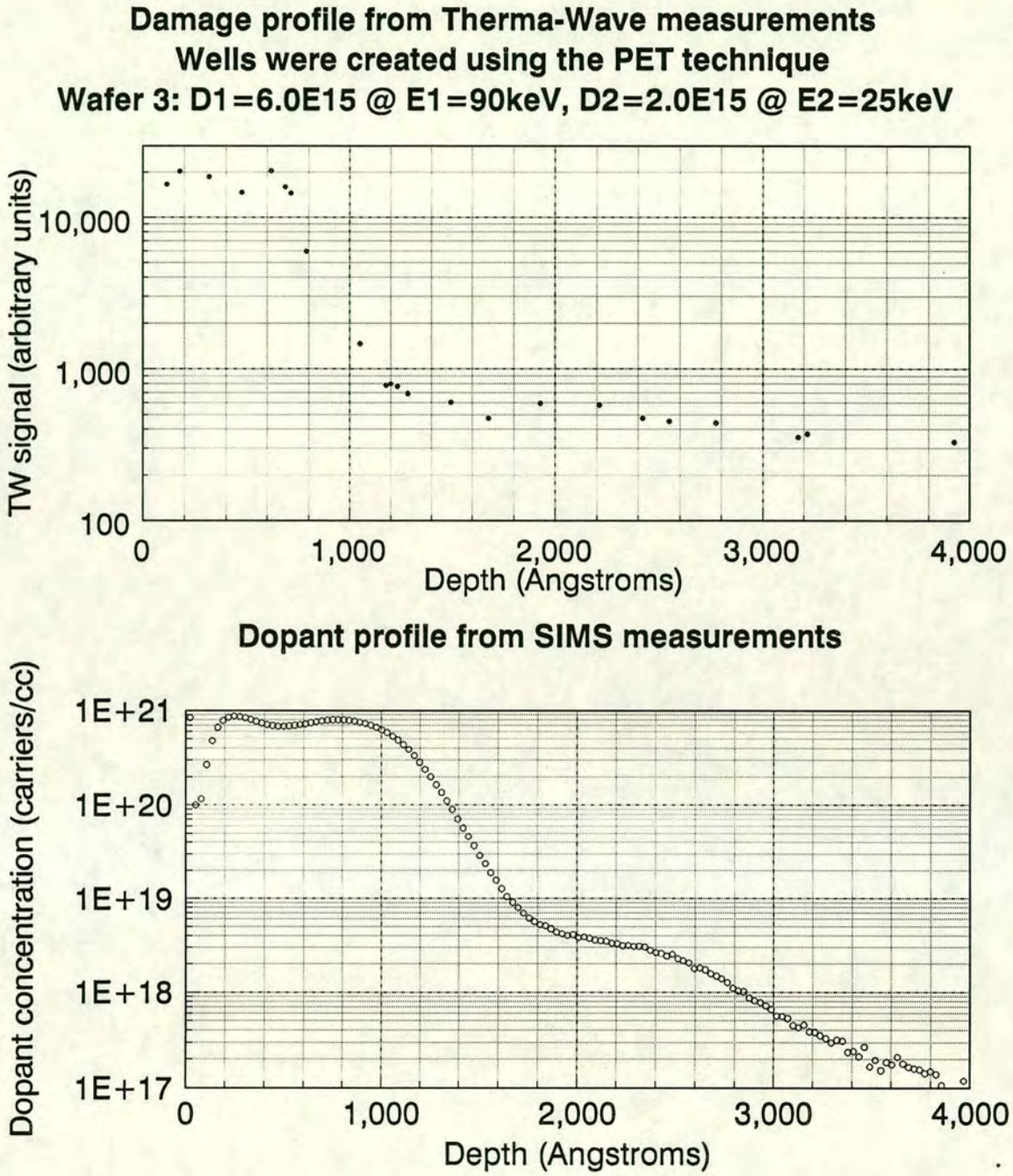

Figure 9–7: A comparison between the damage profile and the dopant profile for wafer # 3. Therma-Wave and SIMS measurements have been used.

The dose rates of both implants are an order of magnitude lower than the equivalent for wafer 1. As a result, both damage peaks appear clearly on the damage profile graph, as opposed to the damage profile of wafer 1. Therefore,

the dose rate value seems to be critical in the determination of the Therma-Wave upper sensitivity level. For high dose rates the Therma-Wave signal saturates.

The shoulder effect of the dopant concentration profile obtained by SIMS measurements, is depicted in fig. 9–7. As explained before it is due to the dissociation of the BF_2 ion just prior to impact with the target atoms. The boron dopant concentration at the shoulder, about 3×10^{18}ions/cm^2, is 10 times lower than the concentration of the equivalent "shoulder effect" region of wafer 1. This reduction of dopant concentration at 2000 Å may account for the reduced damage profile peak that was measured at this depth.

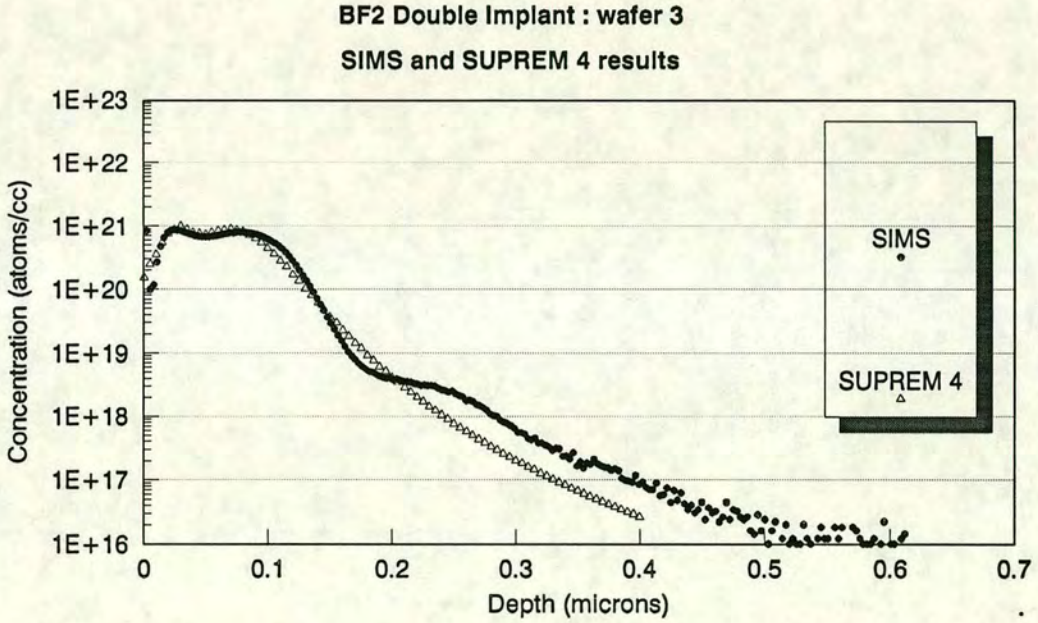

Figure 9–8: Suprem 4 doping profile simulation for wafer 3.

The simulated profile of fig. 9–8 reveals a deep dopant concentration peak at about 750 Å , very close to the 800 Å value of the experimental measurements. The 300 Å peak is, once again, deeper than the experimentally measured due to modelling inaccuracy for low energy implants.

9.4.1.3 SIMS measurements and simulation results.

The SIMS measurements were performed on a Cameca IMS-4f magnetic sector secondary ion mass spectrometer [7]. The SIMS measurements were performed on the three double implanted wafers described previously. The wafers were exactly similar to those used for the thermal-wave measurements and the PET technique has been used to create trenches of different depths on them. The trench dimensions were identical to those being probed by thermal waves (3mm by 1mm).

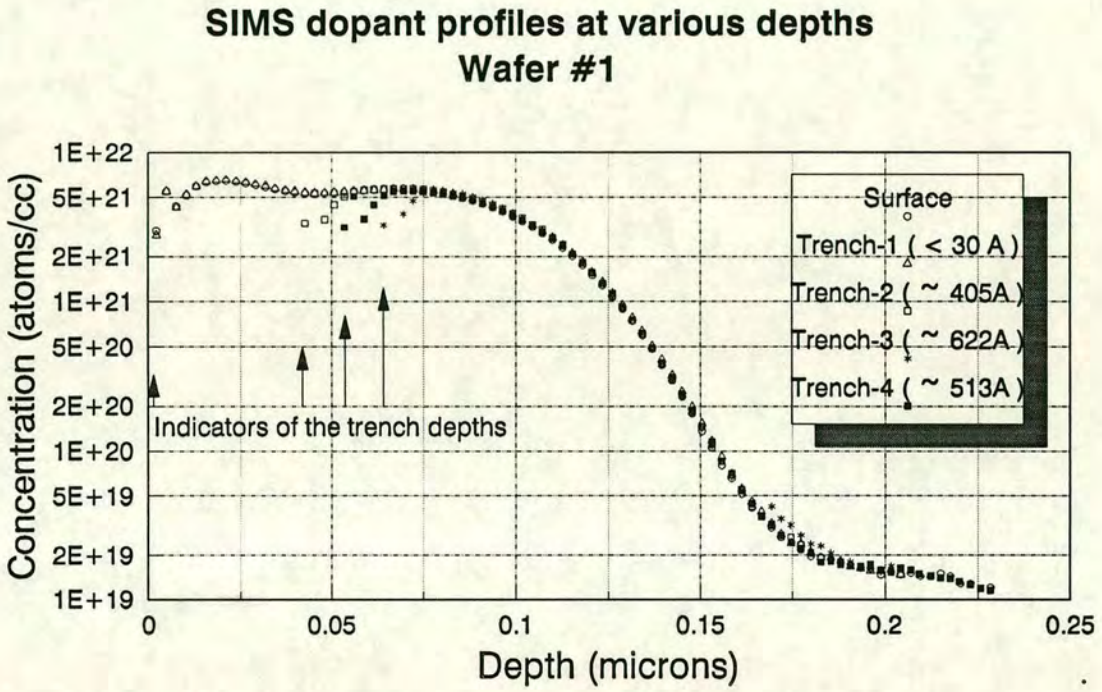

Figure 9–9: Dopant profiles have been extracted from various depths into Si. The trenches into which the profile extraction took place, have been patterned into Si by the PET technique.

In order to assess the effect of the RIE process step on the extracted dopant profile, SIMS analysis has taken place both at the surface of the wafer and inside the trenches. In fig. 9–9 the dopant profiles from wafer 1 indicate that there is no signal distortion due to the RIE step for the measurements extracted from the 4

[7]Measurements were performed in Cascade Scientific Ltd, Uxbridge, Middlessex, UK.

wells. The dopant concentration in each trench is lower than the respective surface dopant profile value at the same depth. This is not a PET technique artifact. It is solely due to the secondary ions depletion effect during the first 50 Å of each SIMS profile extraction. This effect is evident from the SIMS raw data results of fig. 9–10. The ion counts for B, F and ^{30}Si reveal a low secondary ion yield for the first few Å. As explained in chapter 5 this is due to the depletion of oxygen ions at that depth.

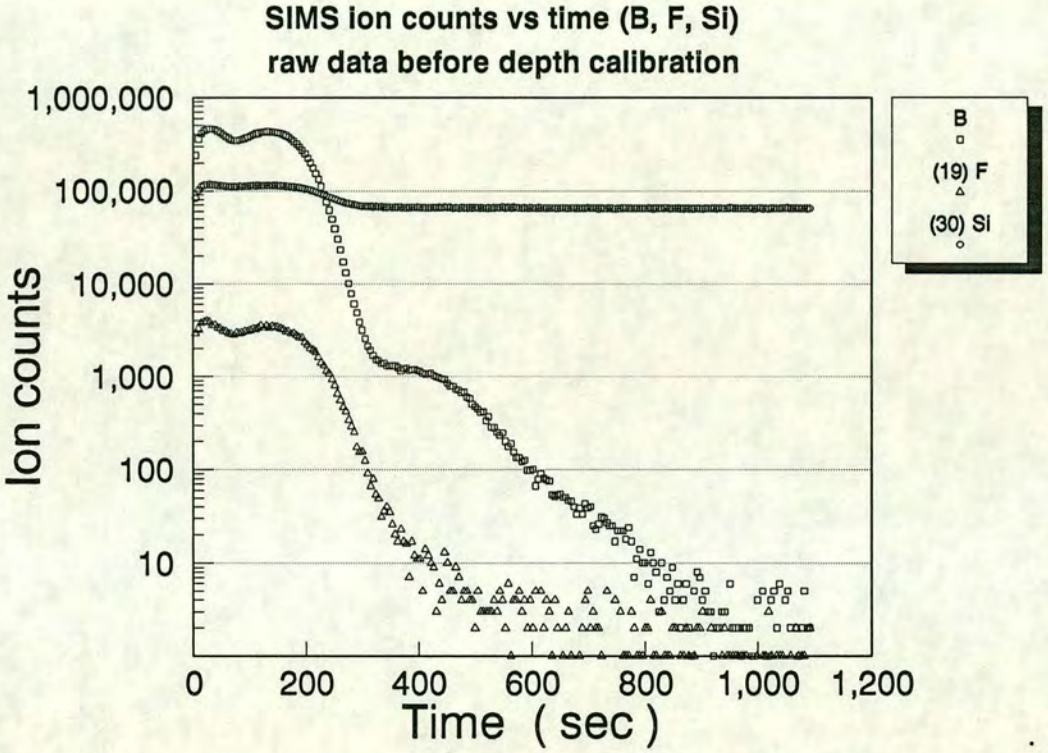

Figure 9–10: The ion counts versus time, for the dopant profile extraction for wafer 1. A slight decrease in the secondary ion yield near the surface can be observed in the Si calibration signal.

The full dopant profiles for the 3 double implanted wafers are displayed in fig. 9–11. The different doses used for the first implant at an energy of 90 keV result in a different state of amorphization of the wafer. This has an impact on the peak depth of the second implant, at 25keV. The higher the degree of amorphization, the closer to the surface the second implant peak should it be situated.

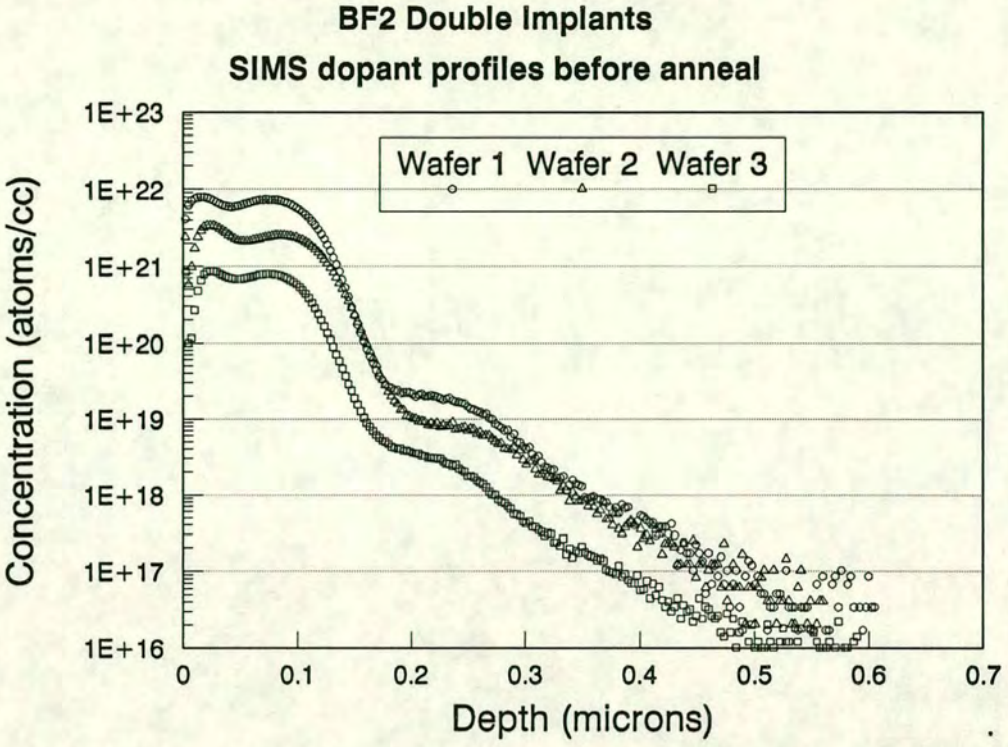

Figure 9–11: The SIMS dopant profiles for the 3 double implanted wafers.

The comparison between the SIMS and the SUPREM-4 simulated profiles for wafers 1 and 3 has been discussed in the previous section. In fig. 9–12 the simulation profile and dopant profile for wafer 2 is also displayed.

9.4.1.4 Variation of sheet resistance with time and temperature.

Due to the high dose and the BF_2 molecular mass employed for both implants, complete amorphization of the target takes place. According to the discussion in chapter 2, a low temperature anneal should be enough for a solid phase epitaxial regrowth and dopant activation. The RTA [8] was carried at 600 °C while the annealing time was varied. The average sheet resistance results for increasing annealing time and the corresponding sigma values are displayed in fig. 9–13.

---

[8] A Jipelec rapid thermal annealer in the isothermal mode has been used for the RTA.

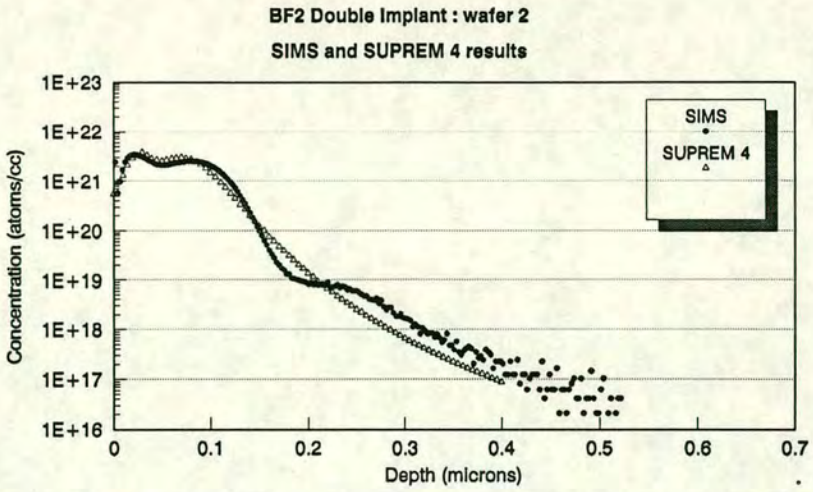

Figure 9–12: Suprem IV dopant profile simulation for wafer 2, as compared to the SIMS dopant profile.

From fig. 9–13 it is obvious that by increasing the annealing time, a rapid decrease in the sheet resistance non-uniformity across the wafer results. The best uniformity (lowest sigma value) is obtained after the 10 min furnace anneal. The drawback of the furnace anneal is the profile broadening due to increased carrier diffusion during the 950 °C for 10 min.

In order to compare the RTA sheet resistance results obtained at two different annealing temperatures, the above experiment was carried at 550 °C for the previous anneal times. The average sheet resistance results for increasing annealing time and the corresponding sigma values, are displayed in fig. 9–14. A comparison between the sheet resistance values after the two temperatures annealing indicates that the 550 °C leads to a much higher sheet resistance for the first 150 s as compared to the 600 °C results. This sheet resistance value is lowered significantly for longer annealing times.

The respective % σ values are higher for the lower temperature RTA. The furnace anneal severely lowers both the sheet resistance and % σ values.

Temperatures of 500 and 530 °C were not high enough to allow four point probe measurements, even though RTA times up to 150 s have been used.

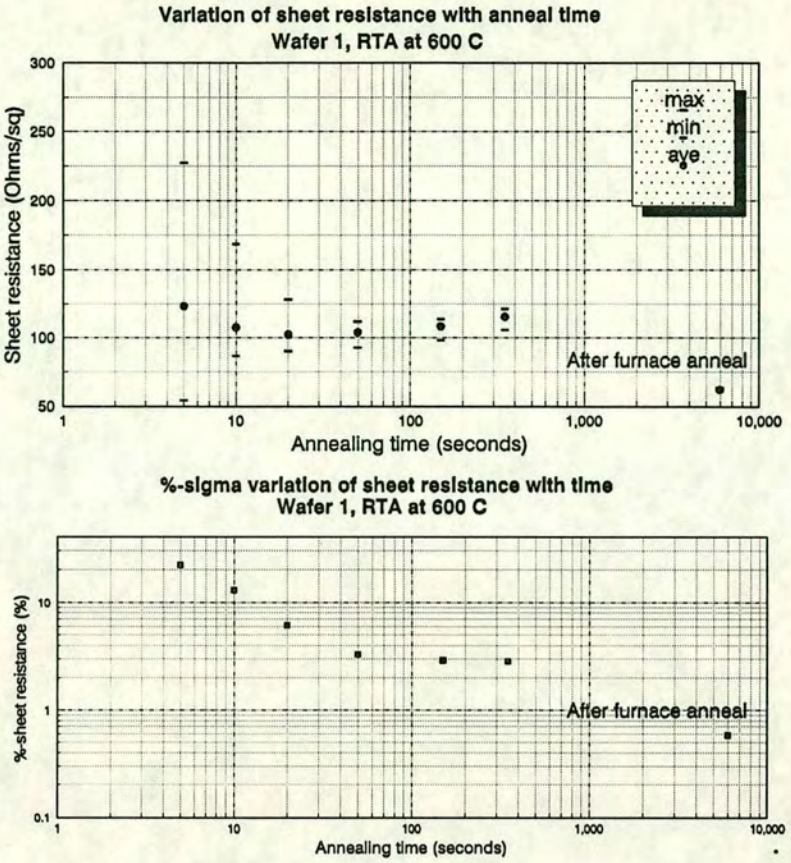

Figure 9–13: Variation of the average sheet resistance with anneal time for wafer 1. The measurements were performed over 69 points after anneal at 600 °C. The last measurement was performed after a 10min furnace anneal at 950°C. The $\%\sigma$ variation of the sheet resistance for the respective anneal times is displayed in the second chart.

The main conclusion that can be drawn from the above experiments is that the 600 °C is the most appropriate temperature for RTA anneal. Higher temperatures can minimize the number of dislocation loops but, as explained in chapter 2, they can lead in profile broadening.

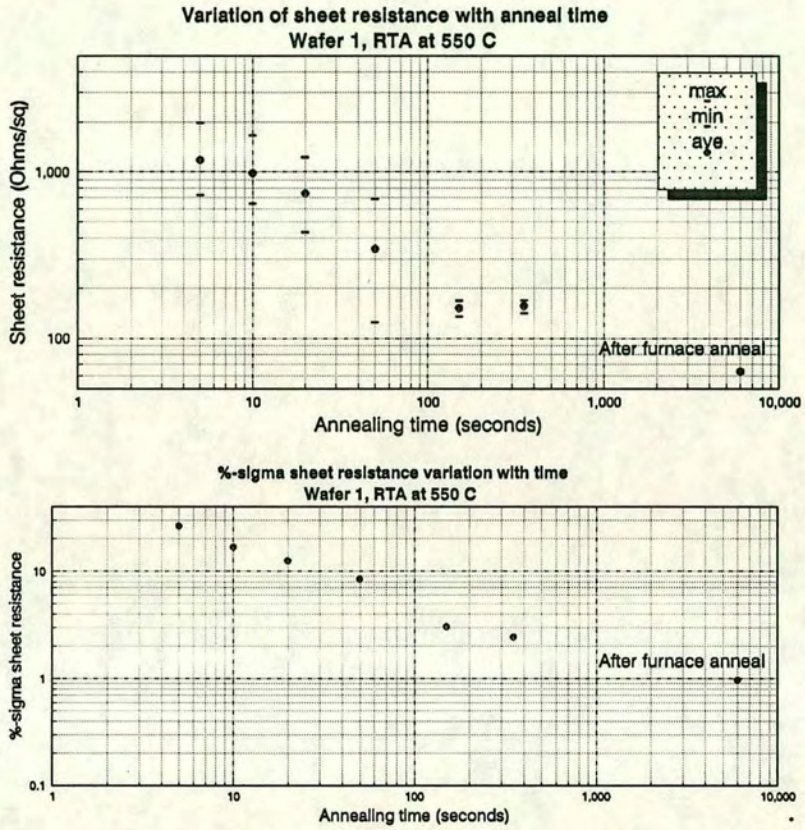

Figure 9–14: Variation of the average sheet resistance with anneal time for wafer 1. The measurements were performed over 69 points after anneal at 550 °C. The last measurement was performed after a 10min furnace anneal at 950°C. The % σ variation of the sheet resistance for the respective anneal times is displayed in the second chart.

9.4.2 Carrier concentration profiles

In order to investigate the shape of the carrier concentration profile after activation and to examine how well the damage and dopant concentration profiles correlate to the carrier concentration profile, both RTA and furnace anneal have been used. The two cases (profile shape after RTA anneal only and after RTA plus furnace anneal) will be discussed separately.

The optimized PET technique and the whole-wafer RIE-sectioning method of the previous chapters were used in combination with four point probe measurements for extracting the profiles. The two-dimensional wafer mapping of carrier profiles can be used as the benchmark for assessing the accuracy of the profile obtained from the measurements inside the PET structure trenches. The geometry of the PET trenches has been discussed in section 9.3.2.1. For the two-dimension sheet resistance wafer mapping, the measurements were performed over a 69 point rectangular array [9] and were averaged for each of the 9 rows. The RIE-induced depth non-uniformity has been taken into account in the results presented.

9.4.2.1 Wafer 1 after RTA at 600 °C.

Two-dimension RIE technique. The carrier concentration profile of wafer 1 after the 600 °C RTA anneal has been measured over the 69 points array. In figures 9–15, 9–16 and 9–17 the sheet resistance, carrier concentration and carrier mobility depth profiles are presented.

The average sheet resistance over each of the 9 wafer rows with increasing depth, is estimated from 5 measurements and is presented in fig. 9–15 (top graph). As the sheet resistance value increases with increasing depth into Si, so does the dispersion of measured values among the 9 rows. For example, the dispersion in average sheet resistance values among rows increases from a value of 0.1 % at the wafer surface to about 30 % at 2100 Å.

---

[9] The same array has been used and explained in the experiments of chapter 8.

The standard deviation, σ, of each curve is extracted for each individual row, at each measurement depth, from 5 sheet resistance measurements. The average plus 3σ and average minus 3σ sheet resistance curves are also depicted in fig. 9–15 as maximum (middle graph) and minimum (bottom graph) curves. The 6σ sheet resistance variation within each row at all depths, is smaller than the dispersion of average sheet resistance values between rows.

From the measured average, maximum and minimum sheet resistance curves of each row the respective carrier concentration and carrier mobility, depth profiles of figures 9–16 and 9–17 are extracted [10]

As it was also observed in the previous chapter, the largest carrier concentration variations among rows appear at the lower carrier concentration levels. Those regions are close to the wafer surface and the profile tail. The dispersion between the maximum and minimum curves for each individual row is, once again, smaller than the dispersion of curves among rows, for all the depths.

The actual shape of the carrier concentration curve indicates that further annealing is needed for complete activation of the dopant atoms in the 200 Å to 700 Å regime. A detailed analysis of the carrier profile shape can be found in section 9.4.2.3.

PET technique results. Fig. 9–18 shows the carrier concentration and sheet resistance for row 6. Each data point of the average (ave) curve represents the average value over the measurement points of the row [11]. The min and max curves represent the average minus 3σ and average plus 3σ sheet resistance measurements around the average sheet resistance curve. The carrier concentration curves that

---

[10]This extraction is performed by a dedicated FORTRAN program which is explained in more detail in chapter 4.

[11]The rows are positionned parallel to the wafer flat with row 1 closer to the flat. The wafer position inside the RIE etcher is the same as that of the previous chapter experiments.

are extracted from the respective sheet resistance curves are denoted as min and max respectively. Although an increase of the 6σ variation of the sheet resistance with depth, for row 6, can be observed in fig. 9–18, even at depths as deep as 2700 Å the 6σ variation does not exceed 9 %. Therefore, the dispersion between the minimum and maximum curves within each individual row is smaller than the dispersion between rows.

The measurements performed inside the PET structure trenches are also depicted in fig. 9–18. The PET sheet resistance measurements and the evaluated carrier concentration profile are well within the max and min limiting curves of row 6. Therefore, the measurements accuracy of the PET method is ensured.

Overall analysis and conclusions. The % σ value of the sheet resistance with depth can prove effective to predict the spread of the carrier concentration values at each depth for each row. The following conclusions can be drawn from fig. 9–19 and fig. 9–18:

1. The biggest σ variation in sheet resistance values can be found in the deepest depths, where high resistance values are being measured. The σ spread is reduced for shallower depths up to the surface, where it is a minimum. However, the % σ sheet resistance spread reaches its minimum value near the 200 Å depth value. This behaviour can be observed in fig. 9–19, where both the σ and % σ values of rows 6 and 9 are displayed. The existence of the minimum % σ in the proximity of the concentration peak is qualitatively expected. If a constant carrier concentration variation is allowed at all depths (due to the statistical nature of ion implantation), the high carrier concentration region, close to the peak, will be negligibly affected. However, the lower surface concentration and the much lower tail concentration will be affected. The lower concentration level of the tail will make it more susceptible to a higher σ variation.

2. It is the % σ spread behaviour, that determines the carrier concentration spread of the average, maximum and minimum carrier concentration curves

of fig. 9–18. An increased spread can be observed near the surface and the tail of the curve. This effect is entirely due to the sheet resistance spread discussed previously. Since the sheet resistance values are fitted by a cubic spline curve with user-specified knots, the same knots have been used for all the curves. This eliminates the software interference on the carrier concentration curves spread. Therefore the direct cause of the electrical profile curve variation, is the variation of the first derivative of the sheet resistance curves (which is due to the % σ spread).

9.4.2.2 Wafer 1 after RTA and furnace anneal at 950 °C.

Two-dimension technique. The same techniques have been used to investigate the effect of the 10 minutes furnace anneal of wafer 1, on its electrical profile characteristics just after the RTA. In figures 9–20, 9–21 and 9–22 the sheet resistance, carrier concentration and carrier mobility profiles are presented. For each row, the average, the average plus 3σ and the average minus 3σ sheet resistance values define the average, maximum and minimum sheet resistance curves of fig. 9–20. From those curves the respective carrier concentration and mobility average , maximum and minimum curves of figures 9–21 and 9–22 are extracted.

The conclusions that were drawn for the RTA anneal of wafer 1 are confirmed in the plots in figures 9–20, 9–21 and 9–22.

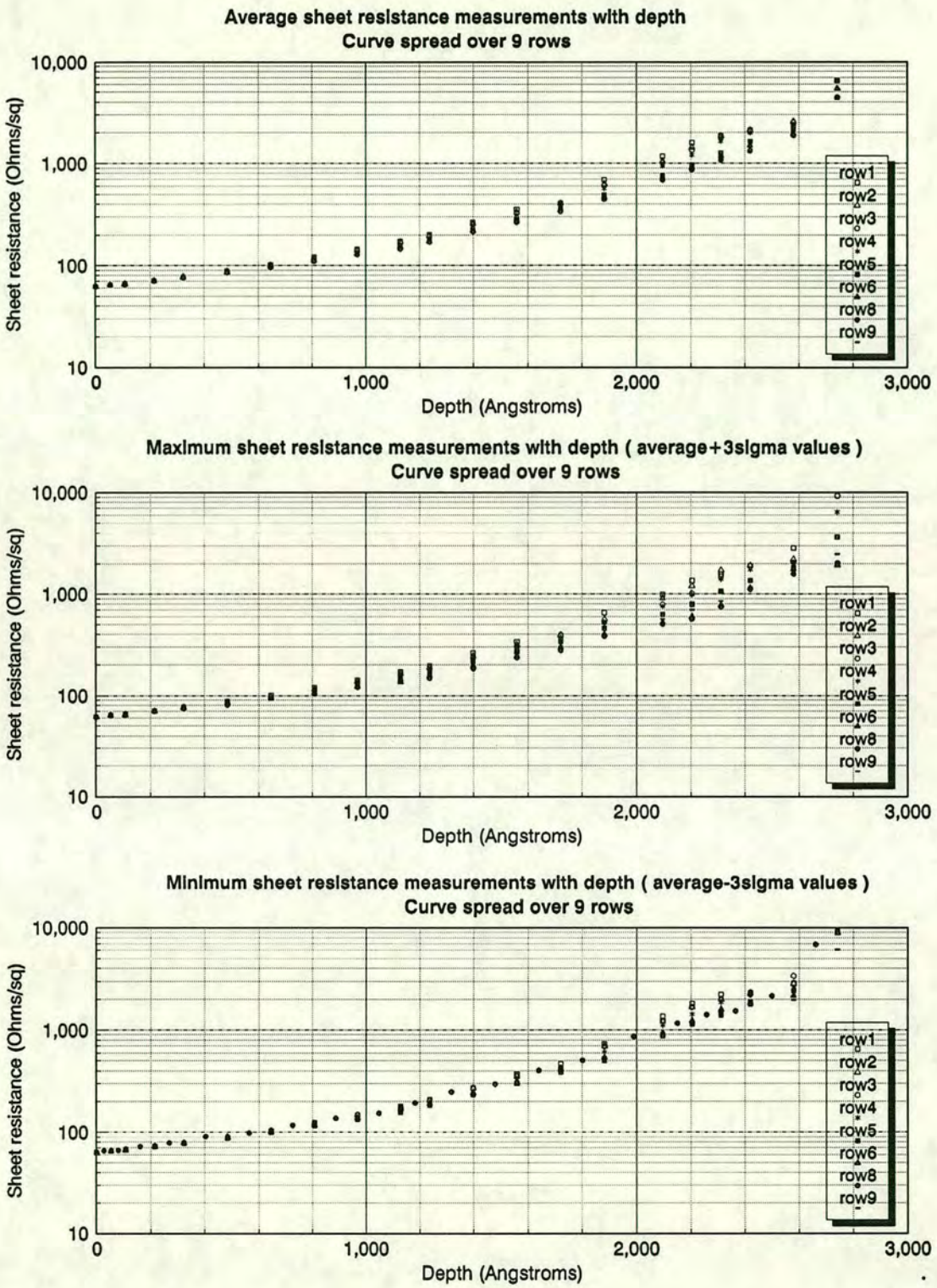

Figure 9–15: Sheet resistance variation with depth. Measurements were carried over an array of 69 points and averaged over the measurement sites of each row. At each site, at each depth 5 measurements were performed.

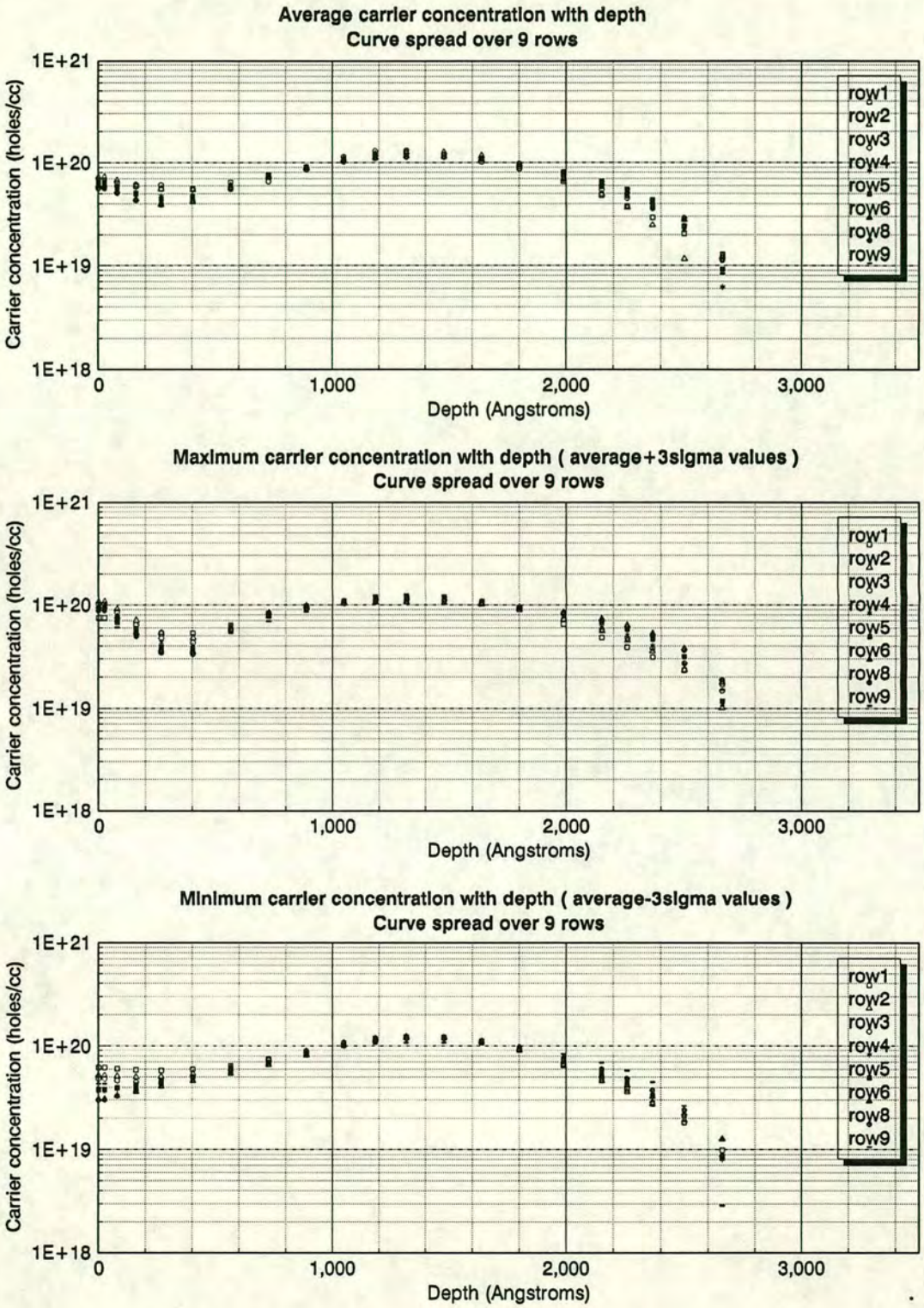

Figure 9–16: Carrier concentration variation with depth. The concentrations were evaluated from the respective sheet resistance average, maximum and minimum curve for each row.

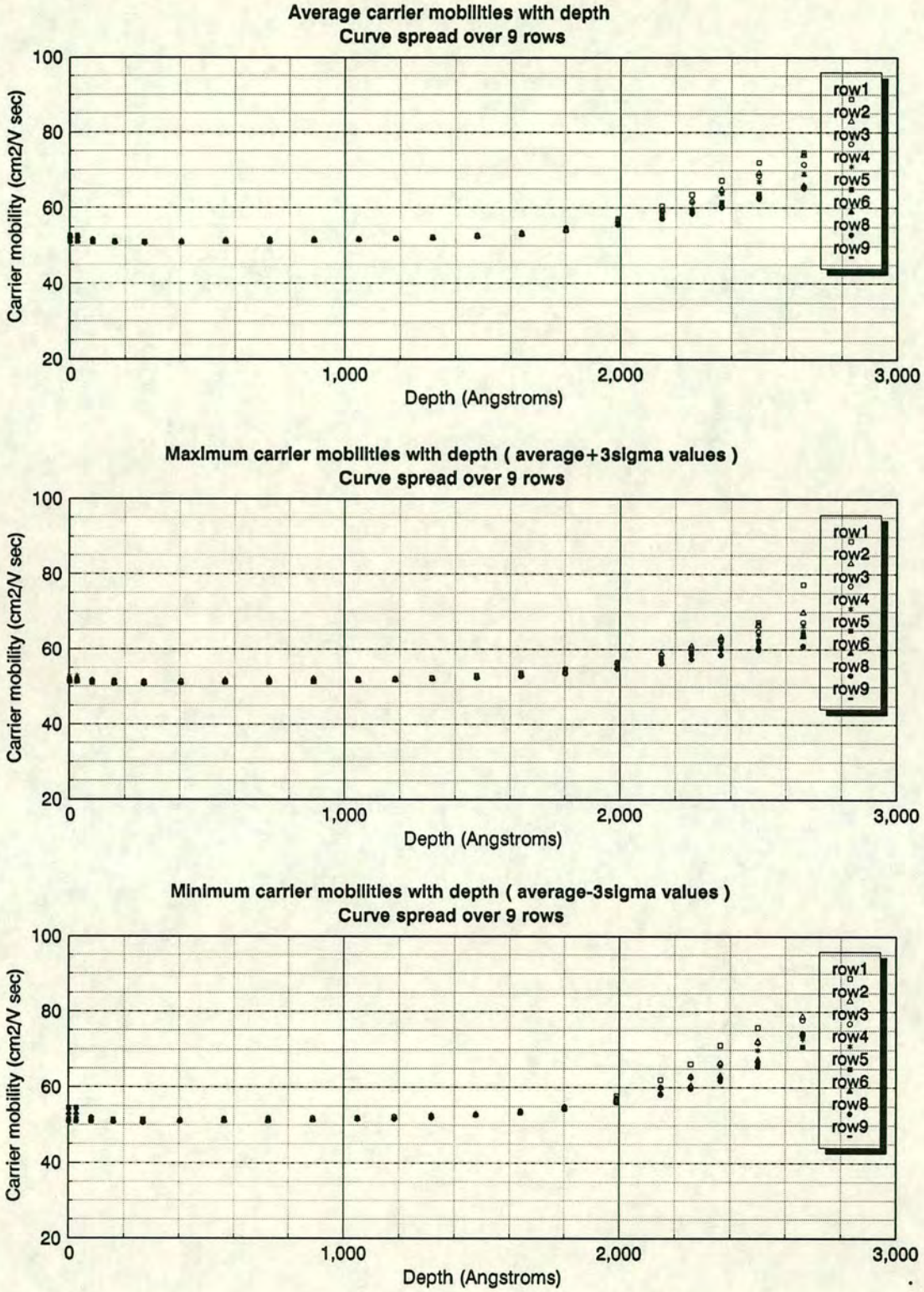

Figure 9–17: Carrier mobility variation with depth. The mobility values were evaluated from the respective sheet resistance average, maximum and minimum curve for each row.

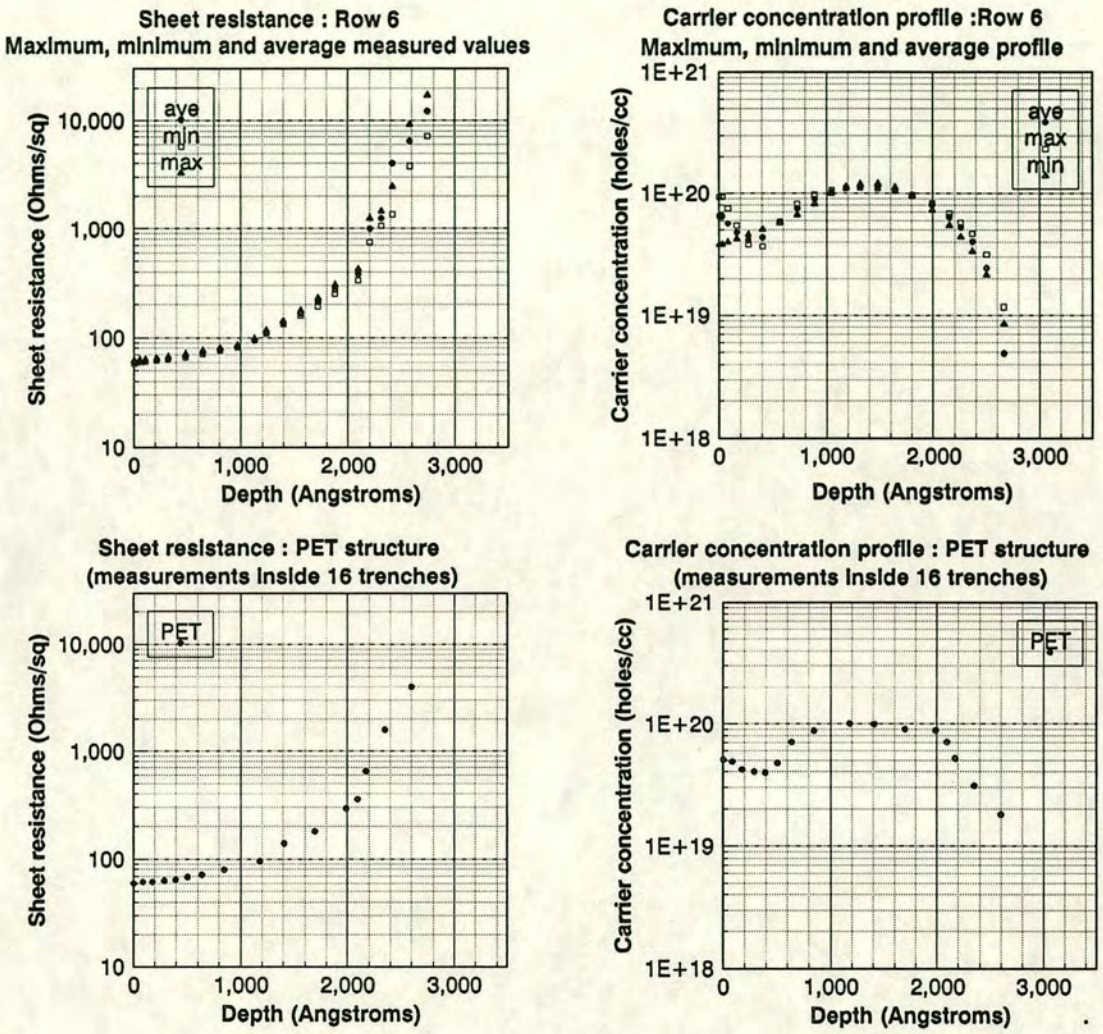

Figure 9–18: A comparison between the sheet resistance and carrier concentration profiles for rows 6 to the sheet resistance and carrier concentration profile obtained from the PET structure. The average, maximum (average + 3σ) and minimum (average - 3σ) curves for row 6 are also being displayed. The PET profile accuracy can thus be assessed

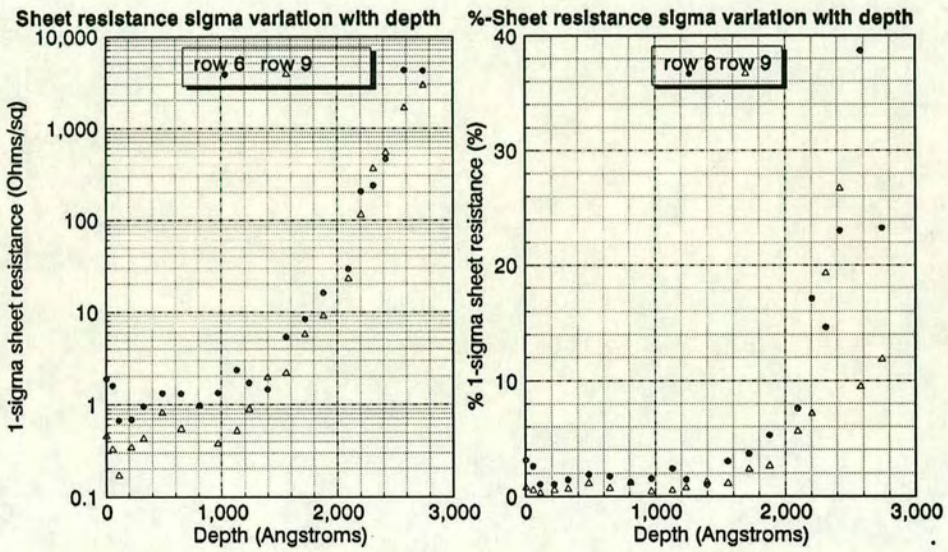

Figure 9–19: The σ and % σ values over the measured sheet resistance values, after each RIE step for rows 6 and 9. The σ value was extracted from the 9 points of each row.

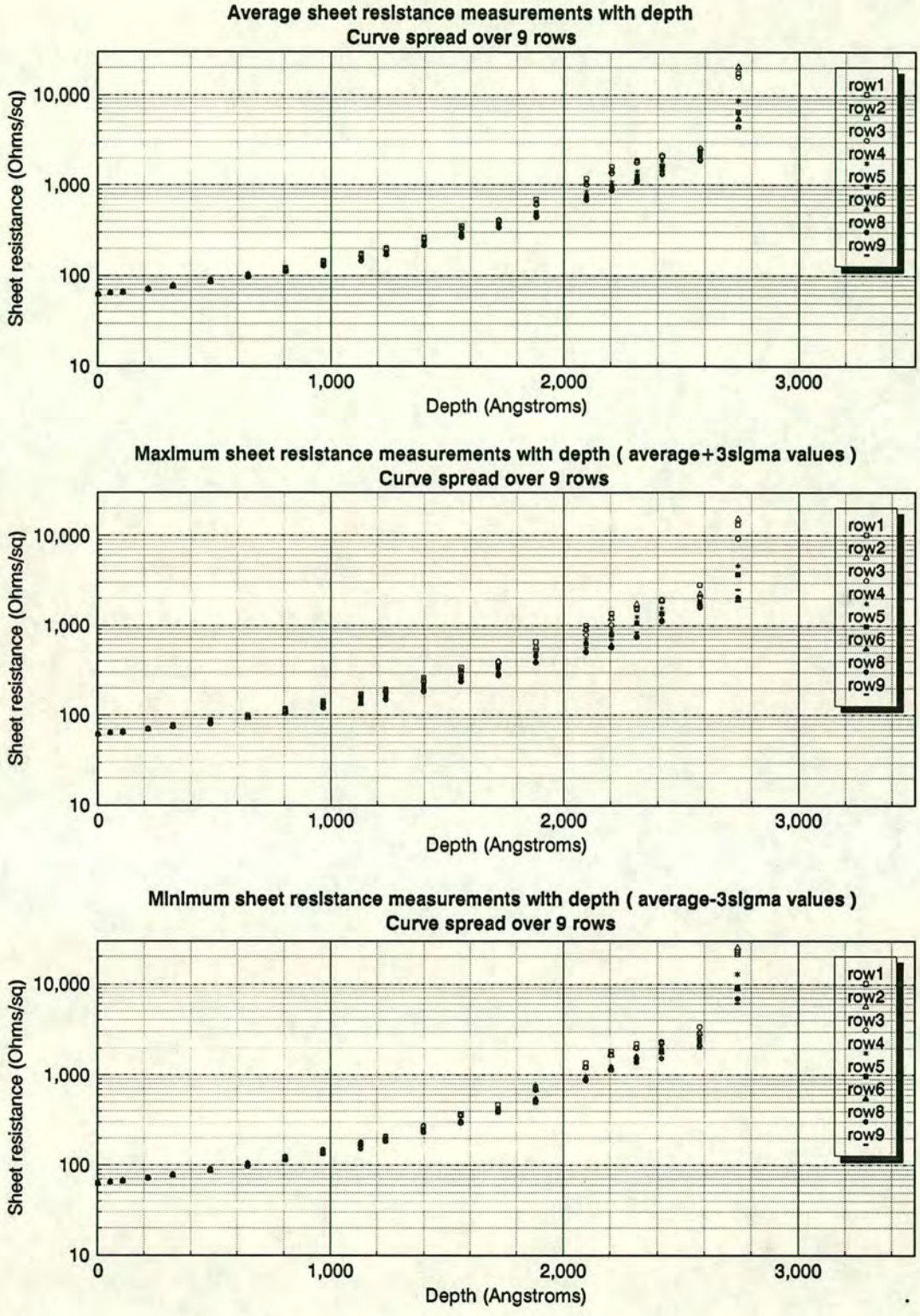

Figure 9–20: Sheet resistance variation with depth. Measurements were carried over an array of 69 points and averaged over the measurement sites of each row. At each site, at each depth 5 measurements were performed.

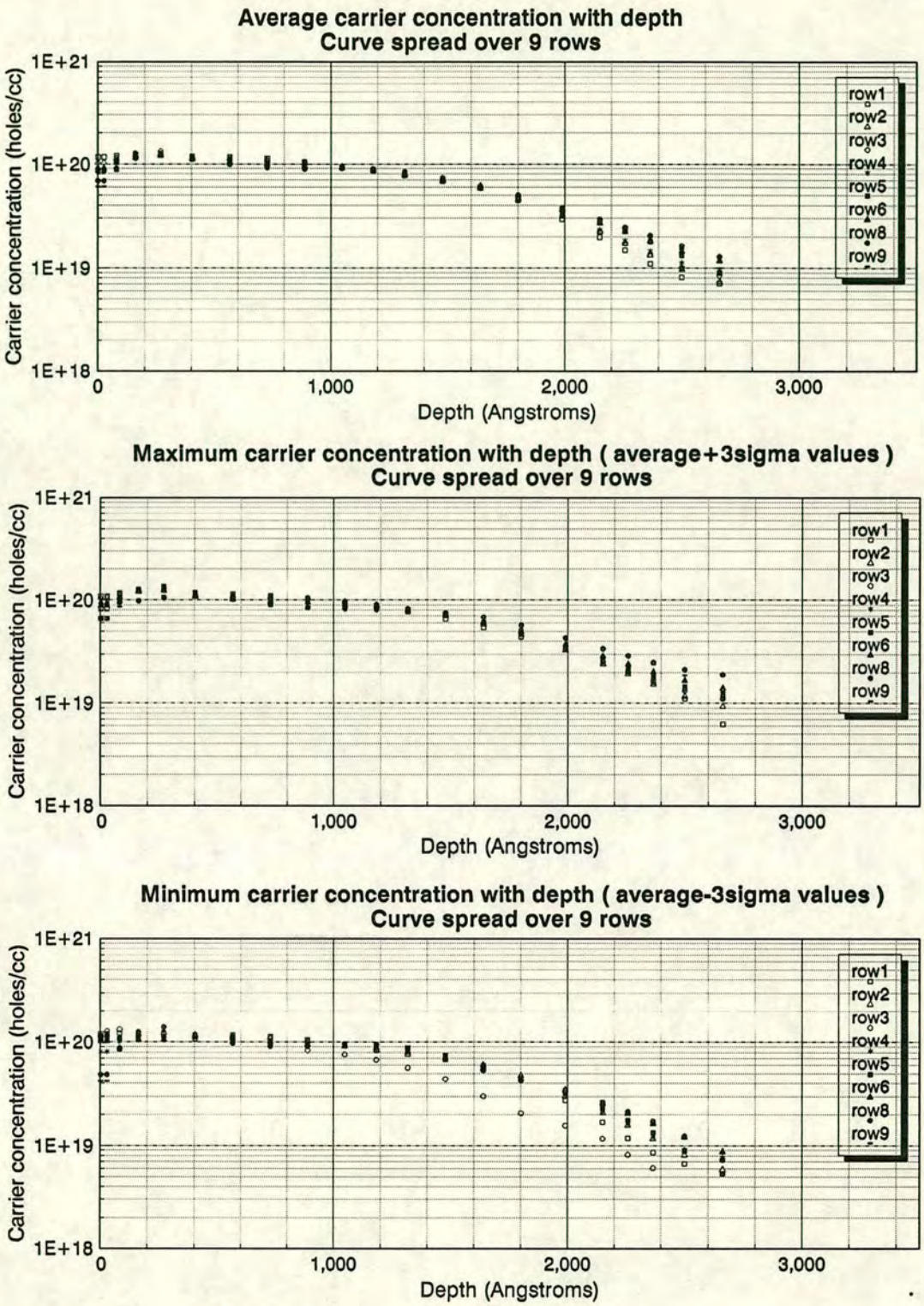

Figure 9–21: Carrier concentration variation with depth. The concentrations were evaluated from the respective sheet resistance average, maximum and minimum curve for each row.

PET technique results. In fig. 9–23 the sheet resistance and the carrier concentration depth profiles for row 5 from the 2-D results and from the measurements inside the PET structure trenches are displayed. The carrier concentration profile obtained from measurements inside the PET trenches is within the maximum and minimum carrier profile curves of row 5 (which are derived from the 3 σ limiting curves of the sheet resistance as explained earlier). Therefore, the accuracy of the method is ensured.

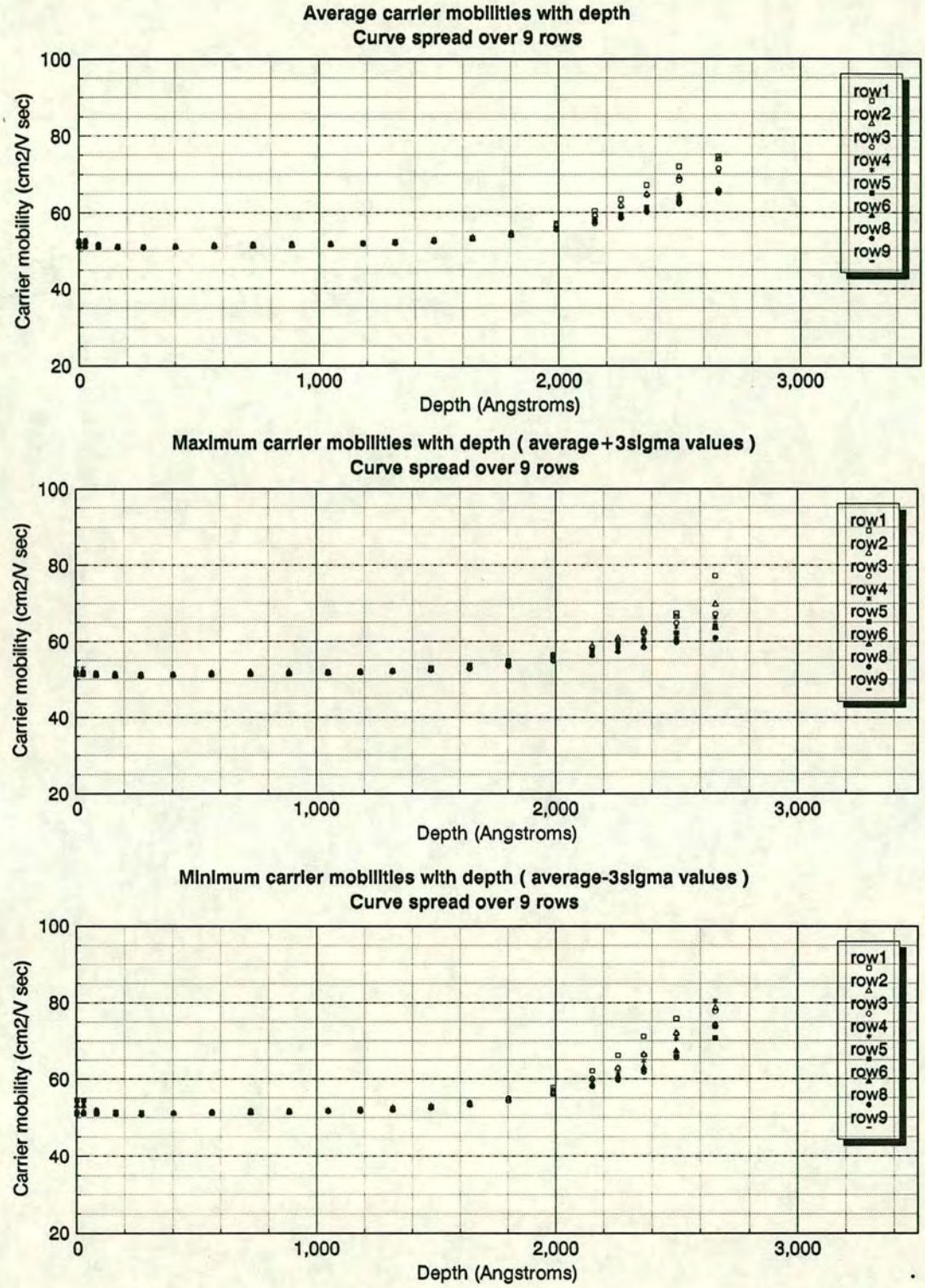

Figure 9–22: Carrier mobility variation with depth. The mobility values were evaluated from the respective sheet resistance average, maximum and minimum curve for each row.

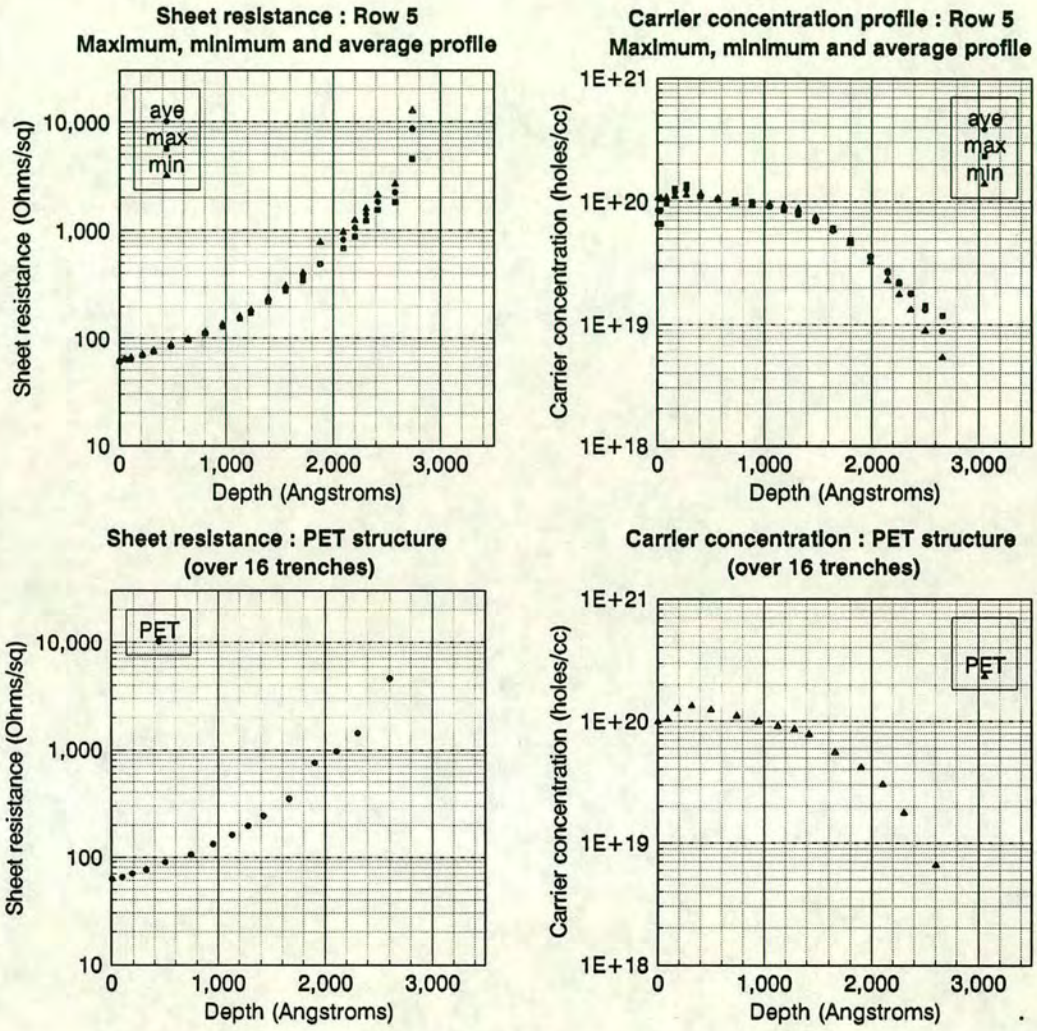

Figure 9–23: A comparison between the sheet resistance and carrier concentration profiles for row 5 to the sheet resistance and carrier concentration profile obtained from the PET structure. The average, maximum (average + 3σ) and minimum (average - 3σ) curves for row 6 are also being displayed. The PET profile accuracy can thus be assessed

9.4.2.3 Comparison between different implant profile types

A comparison among the damage, dopant and carrier concentration profiles of wafer 1 is displayed in a single graph in fig. 9–24. It explains the way the different types of profiles fit together. Such graphs can prove invaluable for the fast characterization of an implant and for reverse engineering purposes, when the cause of failure of a device is under investigation.

When BF_2 is used as the implant species, it is possible to obtain a near-surface amorphous layer (peak damage region) and a highly damaged but not amorphous subsurface region [13]. The distribution of both boron and fluorine exhibits different characteristics depending on the implant dose and the magnitude and distribution of the damage that remains after annealing [14]. During the low temperature recrystallization, boron is activated inside the amorphous region as discussed in chapter 2. The activation of boron implanted into the damaged (non-amorphous) crystalline region is due to the migration of thermally generated vacancies to interstitial B atoms. It is evident that the activation of those B atoms can be favored only if high temperature annealing steps are employed. The subsurface damaged region getters the fluorine atoms. This results in a fluorine peak below the boron peak.

The RTA anneal at 600°C for time intervals as long as 350 s shown in fig. 9–24, results in very low activation in the area of the two dopant peaks. This result appears to be in contradiction to the discussion in chapter 2, where it was mentionned that solid epitaxial regrowth and atomic activation are favored for high dose implants, even at temperatures as low as 600°C. However, for the 2 implants of $\mathbf{6.0x10^{15}}$ and $\mathbf{2.0x10^{15}ions/cm^2}$, inactive boron is found inside the recrystallized amorphous layer. At high concentrations the boron interstitials precipitate into cluster formations that are electrically inactive, [15]. The upper limit for the carrier concentration seems to be the boron solid solubility, which increases with annealing temperature. The value of $1.5 \times 10^{20}cm^{-3}$, of solid solubility for boron in silicon at 600°C is very close to the experimental results of fig. 9–24. In order to increase the boron activation, the maximum boron concentration must fall be-

low the solid solubility level. Therefore, the precipitates can dissolve only if an annealing temperature higher than 1000°C is employed.

The carrier profile confined in the first 1000 Å region (measured from the surface), is not activated during the low temperature RTA anneal. This is mainly due to the existence of a fluorine atom peak in that region. The as-implanted fluorine profile of fig. 9–10 does change during the RTA according to [16]. The amorphous and damaged crystalline regions strongly influence the fluorine redistribution during annealing. Since the fluorine atoms are not very mobile at 600°C, their redistribution is entirely due to accumulation at the amorphous-crystalline interface, as the latter moves from the damage peak to the surface. A comparison between the damage profile and the ANNEAL 1 electrical profile of fig. 9–24 justifies the previous arguments. The 250 Å carrier concentration local minimum is very close to the 210 Å damage peak. The 950°C furnace anneal leads to complete recrystallization, but the concomitant fluorine outdiffusion and redistribution greatly affect the carrier profile displayed as ANNEAL 2 in fig. 9–24. According to [16],the fluorine atoms preferentially migrate to defect-rich regions where a gettering effect takes place. After the 10 minute furnace anneal, boron activation occurs in the first 1000 Å region as fluorine outdiffuses. At the same time, a lowering of the boron activation level at the electrical profile tail region takes place. The damage profile indicates a damage peak in that area. Therefore, a fluorine migration to that defect-rich area is evident. The area is confined between 1000 Å and 1800 Å. As far as the electrical profile tail region inactivity is concerned, the end-of-range loops region feeds a damage level which is high enough to attract the fluorine atoms and reduce the boron activity level.

During the furnace anneal an as-expected broadening of the profile tail can be seen. This is due to the enhanced diffusivity of the interstitial boron atoms at the end-of-range-loops region of the implanted profile. During solid phase epitaxial regrowth no recrystallization takes place in that region and the furnace anneal temperature enhances boron diffusivity.

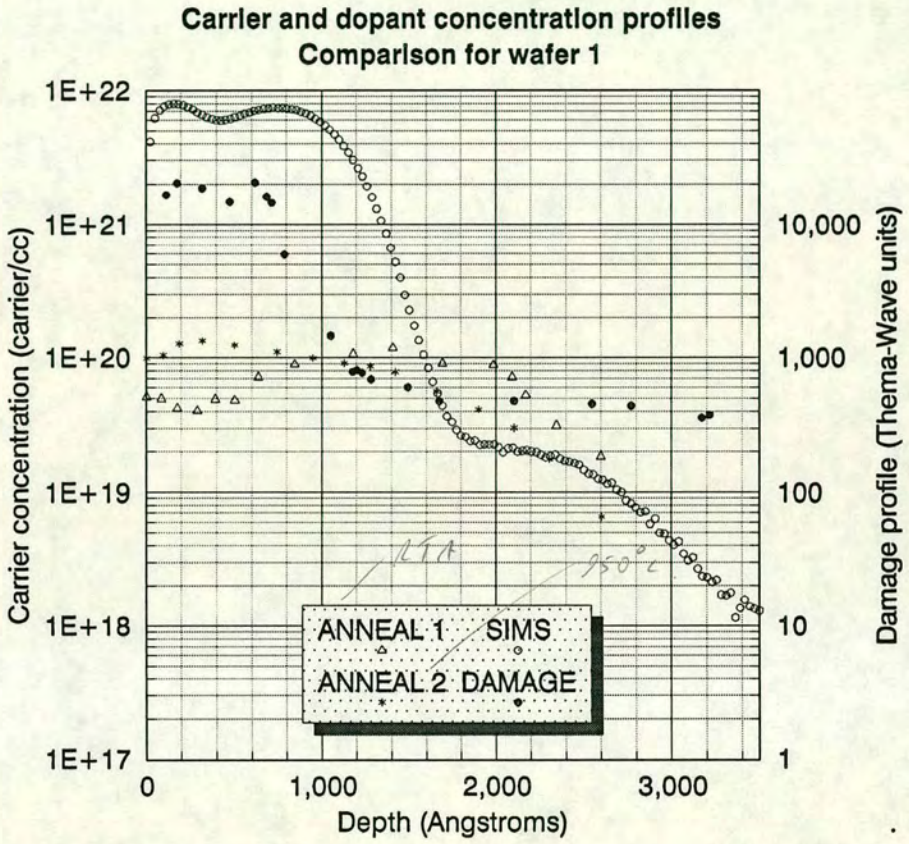

Figure 9–24: A comparison between carrier, dopant and damage profiles as obtained from PET combined with four point probe, SIMS and PET combined with thermal waves. Two different annealing conditions have been used.

9.4.3 Conclusions

By comparing dopant, damage and carrier profiles evaluated through the use of SIMS, the PET structure combined with Thermal-waves and four-point probe and RIE-sectionning combined with four point probe, the following conclusions can be drawn:

1. The 2-dimensional RIE sectioning technique has been proven to be both accurate and reliable for extracting wafer uniformity dopant profiles. It can be used as a useful tool to optimize a process, for reverse engineering purposes and as a benchmark for the profile obtained from a PET structure. The 6σ sheet resistance and carrier concentration limiting curves can prove useful for ensuring that the implantation and annealing steps are within specifications. They can be used to establish the upper and lower specification limit values for statistical process control purposes.

2. The PET structure and the RIE sectioning techniques give results which are consistent with dopant profile results (SIMS). The shape of the profiles conforms to theoretical predictions. Therefore, the PET technique can be used for on-line monitoring.

3. The ability to use most of the known characterization techniques inside the PET structure trenches offers a distinct flexibility for the on-line monitoring of the implant and annealing steps. The ability to controllably amorphize and characterize a crystalline material is important, since the outcome of the annealing step depends upon the crystal structural configuration just after implant. The PET structure combined with Therma-Wave measurements has been proved ideal for fast and accurate assessment for the degree of damage at various depths after implantation.

Bibliography

[1] J. Opsal, A. Rosencwaig, and D. L. Willenborg. Thermal-wave detection and thin-film thickness measurements with laser beam deflection. *Applied Optics*, 22(20):3169–3176, 1983.

[2] W. L. Smith, A. Rosencwaig, and D. L. Willenborg. Ion implant monitoring with thermal wave technology. *Applied Physics Letters*, 47(6):584–586, 1985.

[3] A. Rosenwaig, J.Opsal, W. L. Smith, and D. L. Willenborg. *Bulletin of the American Physics Society*, 30:374, 1985.

[4] J. Opsal and A. Rosencwaig. Thermal and plasma wave depth profiling in silicon. *Applied Physics Letters*, 47(5):498–500, 1985.

[5] W. L. Smith, A. Rosencwaig, D. L. Willenborg, J. Opsal, and M. W. Taylor. Ion implant monitoring with thermal wave technology. *Solid State Technology*, 29(1):85–92, 1986.

[6] B. J. Kirby, L. A. Larson, and R. Y. Liang. Thermal-wave measurements of ion implanted Si. *Nuclear Instruments and Methods in Physics research*, B21:550–553, 1987.

[7] W. L. Smith, A. Rosencwaig, D. L. Willenborg, J. Opsal, and M. W. Taylor. Ion implant monitoring with thermal wave technology. *Nuclear Instruments and Methods in Physics Research*, B21:537–541, 1987.

[8] J. R. Dennis and E. B. Hale. Amorphization of silicon by ion implantation. *Radiation Effects*, 30:219, 1976.

[9] J. Narayan and O. W. Holland. *Journal of the Electrochemical Society*, 131:2651, 1984.

[10] M. A. Wendman and W. L. Smith. Thermal wave implant dosimetry for process control on product wafers. *Nuclear Instruments and Methods in Physics research*, B21:559–562, 1987.

[11] P. Geraghty and W. L. Smith. Rie-induced damage to single crystal silicon monitored with non-destructive thermal waves. *Materials Research Symposium Proceedings*, 68:387–393, 1986.

[12] K. Ishikawa, M. Yoshida, and M. Inoue. Depth profiles of secondary defects of BF_2 and As implanted silicon measured by a thermal wave technique. *Nuclear Instruments and Methods in Physics Research*, B37/38:317–320, 1989.

[13] S. B. Kulkarni. Characterization of silicon epitaxial films. In *VLSI Electronics Microstructure Science, Volume 6: Materials and Process Characterization*, pages 74–145. Academic Press, 1983.

[14] R. G. Wilson. Boron, fluorine and carrier profiles for B and BF_2 implants into crystalline and amorphous Si. *Journal of Applied Physics*, 54:6879–6889, 1983.

[15] Comparison of impurity profiles generated by spreading resistance probe and secondary ion mass spectroscopy. In D. C. Gupta and P. H. Langer, editors, *Emerging Semiconductor Technology, ASTM Special Technical Publication 960 (ASTM STP 960)*, Philadelphia, PA, 1986. Fourth International Symposium on Semiconductor Processing, 1986, San Jose, California, ASTM.

[16] M. Y. Tsai, D. S. Day, and B. G. Streetman. Recrystallization of implanted amorphous silicon layers.II migration of fluorine in BF_2^+-implanted silicon. *Journal of Applied Physics*, 50(1):188–192, 1979.

Chapter 10

Conclusions

10.1 Project objectives

Ion implantation will unarguably continue to remain a crucial step in the fabrication of VLSI and ULSI circuits. There is no doubt that ion implanters become more sophisticated and incorporate self-diagnostic tools, automatic set-up and specialized hardware to minimize the sources error that were presented in chapter 3. However, the reduction in geometries and the increase in wafer diameters imposes stringent requirements for tighter tolerances. Therefore, the need for on-line monitoring of the implant and anneal steps becomes a challenging task. The objective of this project was to develop a novel approach to obtain fast and accurate implant profiles, suitable for on-line monitoring. There are three necessary steps to establish any new measurement technique. First, the measurement must be repeatable. Second, it must be possible to correlate the measurement with existing characterization techniques. Finally, the measurement must be accurate enough to be used for drawing conclusions about the structure under test. Therefore, the experimental work undertaken was also to verify that those three steps could be fulfilled.

10.2 Project achievements and limitations

10.2.1 Optimization of the PET technique

The traditional approach to ion implant profile extraction is to use a series of layer stripping and measuring steps. In the new approach, the Patterned Etch Transfer technique (PET), a fast method for creating trenches of increasing depth into Si was developed. A series of contradictory requirements had to be tackled to achieve the desired reproducibility, accuracy and control of the PET technique.

1. A low-γ photoresist has to be used in the PET technique since for low contrast values, any intensity variation across the exposure field has minimum impact on the remaining photoresist thickness uniformity. Therefore, for low contrast curves good depth uniformities across each trench can be achieved. However, such a requirement is in contradiction to the trend for higher contrasts for better resolution, which is sought by both photoresist manufacturers and users. From the other side, for a very low contrast curve the step heights between neighbouring trenches can be so small that depth overlap may occur between them due to depth variations inside each trench. Therefore, the lower limit of the γ value is imposed by the 3σ depth non-uniformity of the trenches.

2. Photoresist etch rate, etch rate uniformity and depth uniformity inside each trench were among the targets of the optimization experiments. When low temperature and short-time softbake and post-exposure bake steps were employed, an etch rate of 299 Å/min and a 12 % thickness non-uniformity inside each trench resulted. For higher temperatures, the non-uniformity was improved to 2 % while the etch rate was increased to 322 Å/min. High resist etch rates offer high selectivity of resist over Si during the RIE step. Since high selectivities reduce the depth non-uniformities inside the resist trenches and replicate shallower and more uniform trenches into Si, they

are desirable for the PET technique. At the same time, high post-exposure bake temperatures decrease the γ value. Increased softbake temperatures give better resist thickness uniformity but also increase the γ value of the resist/developer combination. A 1.41 selectivity value was obtained after the optimization experiments and was used for the experiments.

Therefore, several experiments were performed to obtain a balance between the contradicting requirements of the PET technique.

3. Increase in trench area, increases the depth non-uniformity of the trench. Therefore, depth differences between neighbouring trenches must be increased to avoid overlaps. An increase of the exposure time difference between the trenches (defined in the optical stepper exposure matrix file) is the best way to achieve that increase in step height difference. Therefore, the depth resolution of the PET technique deteriorates as the area of the trench increases. Since, the largest trenches were needed for the four point probe measurements, the worst trench depth non-uniformity occured for the 10x10 mm square trenches and gave a 3σ variation of 140 Å.

4. During the Reactive Ion Etching step we seek to minimize the damage on Si. The best way found to achieve it was to use low RF power levels and pressures in the 20 to 100mTorr range. However, both parameters affect the etch rate of Si, the selectivity and the depth non-uniformity of the trench in Si. Therefore, optimization experiments were carried out to identify the best levels of the RIE process par ameters.

5. The use of CF_4 as the etching gas in the RIE process step is most appropriate for obtaining a more isotropic, chemical assisted etch. Thus, the induced-damage by physical bombardment is reduced. The addition of oxygen in the etching gas chemistry increases the etch rate of both Si and resist and the selectivity of resist over Si.

6. The variation of the etch rate across a wafer deteriorates the control over trench depths. A linear etch rate variation with the radial chamber position

was measured by use of a test structure. Control over this etch rate variation was achieved through the RIE processing parameters, mainly RF power, total flow rate and pressure. For the optimum parameter levels a variation of less than 8 Å/min along a 3 inch wafer was achieved. No other appreciable etch rate variation has been found across any other direction on the wafer.

7. Repeatability of the PET technique requires a special RIE set-up which was described in section 6.3.4.3. Consistency between the various steps during the resist patterning and the RIE trench transfer processes is also a prerequisite.

For the optimised PET structure, 2x2 mm square trenches with step height differences of 90 Å and a 75 Å 3σ depth non-uniformity inside each trench were achieved.

10.2.2 RIE-induced damage

In chapters 7, 8 and 9 it was experimentally verified that due to the optimization experiments low induced-damage levels were obtained for the PET technique. Depending on the ion implant profile monitoring technique, special surface treatments were developed to further reduce the effect of damage or contamination on the measurements.

For sheet resistance monitoring, an oxygen ashing step is needed to clean the wafer from any organic contamination left over after the resist strip. Fuming nitric acid proves inefficient to completely remove resist that has been fluorinated during the RIE step of the PET technique. If ellipsometry is used to monitor the optical constants of the implanted material, the oxygen ashing step must be followed by an HF dip to etch off the thin layer of SiO_2 that is formed on the substrate. The optical contstants measurements must be performed immediately after the HF clean. The above treatments also increase the measurements repeatability for both techniques. The same surface treatment was also used for the samples that were monitored by thermal-waves.

Only after the above treatments can the sheet resistance, ellipsometry and thermal-wave measurements be free of RIE-induced damage errors. This was successfully demonstrated by monitoring the effect of the RIE etching time variation on the sheet resistance, the refractive index, the extinction coefficient and the thermal-wave signal of the implanted Si substrate. Only the thermal-wave technique showed a sensitivity to RIE time for etching times up to 8 minutes. The 300 thermal-wave units signal for an 8 minutes RIE is at least 10 times lower than the lowest thermal-wave signal obtained from the ion-implantation damage profile monitoring. Therefore, the measurements are not altered and the results are valid.

10.2.3 The use of implant profiling methods

Four point probe, ellipsometry, thermal-waves and SIMS measurements were performed on the flat bottom of the PET trenches. Due to the different resolutions of the above methods different trench sizes were used.

For all four point probe measurements there was a good agreement between the profiles obtained by the PET technique and the results of the differential Hall method. The depth accuracy was scrutinized by use of the etch rate variation across the wafer and the Dektak measurements. A careful experimental assessment gave sheet resistance measurement repeatability similar to the one obtained by the Hall technique. The carrier concentration profile spread due to x-y implant non-uniformities was also assessed by use of the two-dimensional RIE etching technique. The carrier concentration profiles were extracted at 69 points across the wafer. The 6σ profile variation curves were also evaluated. Those curves can be used to specify the upper and lower profile curve limits for a particular implant step. Fast on-line measurements after the implant and anneal steps can be performed by use of the PET technique. The obtained sheet resistance and carrier concentration curves can then be compared against the 6σ specifications. The success of the activation of the carriers along their full profile depth can thus be investigated. This method can reveal deviations from the process specifications at the tail of the profile, where conventional sheet resistance monitoring is inefficient.

Ellipsometric measurements inside the PET structure trenches can reveal the junction depth. A damage profile with depth can be obtained by both refractive index and extinction coefficient monitoring. Extinction coefficient monitoring with depth is also a very sensitive method to reveal if the annealing step has restored the crystallinity of the substrate for depths extending down to the junction. Its results can be correlated to the carrier concentration profile. A high sheet resistance variation at a certain depth can be due to incomplete activation. This would show up as an extinction coefficient peak at the same depth.

Thermal-wave measurements inside a PET structure are very sensitive in revealing the implant damage profile for the cases where self-annealing does not occur during the implant. Double, high dose implants showed excellent correlation between damage, dopant and carrier concentration profiles. They also agreed with simulation results and theoretical predictions. Due to its 3μm depth resolution, the thermal-waves technique is the most promising technique for a fast, on-line implant profile assessment.

The accuracy of all the above techniques was further assessed by use of SIMS and differential Hall measurements performed inside the PET trenches. No profile distortions were observed and the excellent profile matching for all depths reassured the PET technique reliability.

10.3 General remarks and suggestions for future work

The PET technique and the 2-dimensional RIE etching technique can provide a new insight into implant profile measurements. The PET method can prove a valuable tool for fast, on-line assessment of the implant and anneal steps. Its resolution is limited only by the characterization technique that is applied inside the PET trenches. Therefore, it meets the objectives set by this project. The 2-dimensional RIE etching method can provide information about the implant and anneal uniformity. Its depth resolution can be easily controlled by variation of

the RIE time for each stripping step, since a 215 Å/min etch rate was achieved. The etch rate non-uniformity across the wafer can be bypassed if a single-wafer etcher is used instead. However, a very accurate method for characterizing radial non-uniformity inside the etcher was presented and can be used for evaluating the etch rate at each position across the wafer for any type of etcher.

Some interesting areas were left out in the present work due to time and equipment constraints. Since the thermal-wave technique has become an industry standard, it would be very useful to extend those experiments for the whole range of dose and energy levels by using experimental design techniques. An area that needs more investigation is the effect of dose rate levels on the thermal-wave signal accuracy. If the thermal-wave signal saturation at high doses is dose-rate dependent, then by increasing the number of scans for a particular dose level we can extend the range of the technique for higher doses. Other techniques like spectroscopic ellipsometry and spreading resistance can also be used in combination with the two profiling techniques. The drawbacks of the spreading resistance have been explained in chapter 4. However, its high resolution is its only advantage against the four point probing method.

Deviations between apparent and true carrier profiles exist for all electrical characterization techniques. They are mainly due to spilling effect, surface states existence and depth scale errors. The software that was developed for the conversion of the sheet resistance measurements with depth into a carrier concentration made use of user adjusted cubic splines for the curve fitting. Incorporation of a correction routine for those three sources of error can improve the profile accuracy, especially for shallow implants.

A further reduction in RIE damage levels is very important since it can improve, by a factor of 10, the sensitivity of thermal-waves signals after annealing. A variety of techniques should be employed to fully analyze the damage. Junction current-voltage (I-V) measurements, Deep Level Transient Spectroscopy, Transmission Electron Microscopy and Rutherford Backscattering Spectroscopy are among the techniques that can be used to quantitatively assess the damage and the defect profile.

In summary, the two new profiling methods which were developed in this project offer a broad base of application of implant characterization techniques. The Pattern Etch Transfer technique can be particularly attractive to industry for implant profile monitoring due to its fast implementation and good accuracy. The two-dimensional Reactive Ion Etching method is capable of characterizing implant profile variations across the wafer and can give an insight into device problems that may arise from the spread of the implant profile tails across a wafer.

Appendix A

Calculating measurements errors of n(x)

The carrier concentration with depth is given by:

$$n_i(x) = -\frac{\Delta(\sigma_s)_i}{q\mu_i \Delta x_i} = -\frac{(\sigma_s)_i - (\sigma_s)_{i+1}}{q\mu(x_{i+1} - x_i)} \tag{A.1}$$

where Δ denotes a difference between consequent measurements. Let $(\sigma_\mu)_i$, $(\sigma_{\sigma_s})_i$ and $(\sigma_x)_i$ denote the standard deviations in carrier mobility, sheet conductance and measured depth and $(\sigma_n)_i$ the standard deviation in carrier concentration after the i-layer has been removed. If by $\delta\mu_i$, $\delta(\sigma_s)_i$ and δx_i we denote the uncertainties in the measurements of the respective quantities, then the uncertainty in the carrier concentration, δn_i , can be calculated from the relation:

$$\delta n_i = \left(\left(\frac{\partial n_i}{\partial(\sigma_s)_i} \delta(\sigma_s)_i \right)^2 + \left(\frac{\partial n_i}{\partial(\sigma_s)_{i+1}} \delta(\sigma_s)_{i+1} \right)^2 + \left(\frac{\partial n_i}{\partial x_{i+1}} \delta x_{i+1} \right)^2 + \left(\frac{\partial n_i}{\partial x_i} \delta x_i \right)^2 + \left(\frac{\partial n_i}{\partial \mu_i} \delta \mu_i \right)^2 \right)^{1/2} \tag{A.2}$$

If we assume that the standard deviation for the sheet conductance and the depth measurements for the different layers is identical ($\delta(\sigma_{\sigma_s})_i = \delta(\sigma_{\sigma_s})_{i+1}$ and $\delta x_i = \delta x_{i+1} \; \forall \, i$, where i denotes a Si layer) and that the same assumption holds for the respective uncertainties, then from A.1 and A.2 we finally get:

$$\sigma_n = \sqrt{\frac{2(\Delta x)^2\mu^2(\delta\sigma)^2 + 2(\Delta\sigma)^2\mu^2(\delta x)^2 + 2(\Delta x)^2(\Delta\sigma)^2(\delta\mu)^2}{(q\mu^2(\Delta x)^2}})^2 \tag{A.3}$$

In the previous calculations it has been assumed that the 3 uncertainties are independent and random. This is not true for the $\mu = \mu(\mathrm{n(x)})$ variable. However, since we can insert an uncertainty in μ larger than the actual one (obtained from the evaluation algorithm equations) the assumption can hold true.

In order to evaluate the contribution of each measurement uncertainty on the carrier concentration uncertainty, the fractional uncertainties for sheet conductance, depth and mobility defined by the equations:

$$s_n = \frac{\delta n}{n} \tag{A.4}$$

$$s_{\sigma_s} = \frac{\delta \sigma_s}{\sigma_s} \tag{A.5}$$

$$s_x = \frac{\delta x}{x} \tag{A.6}$$

$$s_\mu = \frac{\delta \mu}{\mu} \tag{A.7}$$

and the factors:

$$a_{\sigma_s} = \frac{\sigma_s}{\Delta \sigma_s} \tag{A.8}$$

$$a_x = \frac{x}{\Delta x} \tag{A.9}$$

$$a_\mu = \frac{\mu}{\Delta \mu} \tag{A.10}$$

are defined.

By substitution of equations A.3 and A.1 in A.4 we get:

$$a_n = \sqrt{2\left(\frac{\delta \sigma_s}{\Delta \sigma_s}\right)^2 + 2\left(\frac{\delta x}{\Delta x}\right)^2 + \left(\frac{\delta \mu}{\Delta \mu}\right)^2} \tag{A.11}$$

Therefore, by use of the above definitions we get:

$$a_n = \sqrt{2\left(a_{\sigma_s}^2 s_{\sigma_s}^2 + a_x^2 s_x^2\right) + a_\mu^2 s_\mu^2} \tag{A.12}$$

Appendix B

Model for RIE damage distribution in Si

The amount of residual damage in Si after the RIE process step is mainly determined by two competitive effects: damage accumulation and substrate etch rate. A simple model for estimating the time needed to reach a steady state in terms of damage production and etch rate should require that the effects of different ions on the Si substrate follow the superposition principle. The assumptions that damage creation and silicon etching occur simultaneously but independently and that damage and impurity profiles are close enough to coincide, are also required.

If we assume a gaussian type of profile for the distribution of impinging ions, the damage distribution for a time interval dt, n(x, t)dt, is:

$$n(x,t)dt = \frac{D}{\sqrt{2\pi}\Delta R_p} \exp\left[-\frac{1}{2}\frac{(x - st - R_p)^2}{\Delta R_p^2}\right] \tag{B.1}$$

where the initial Si surface is located at x = 0 and is etched with a rate s (velocity units). D denotes the dose rate per unit area (in square centimeters) and R_p and ΔR_p are the projected range and straggle of the impinging ions.

For a time interval t, the damage distributions can be summed and the total damage distribution is given by:

$$N(x,t)dt = \frac{D}{\sqrt{2\pi}\Delta R_p} \int_0^t \exp\left[-\frac{1}{2}\frac{(x - st - R_p)^2}{\Delta R_p^2}\right] \tag{B.2}$$

Equation B.2 can be rewritten, by use of the erf function as:

$$N(x,t)dt = \frac{D}{\sqrt{2\pi}s}\left[erf\left(\frac{x-R_p}{\sqrt{2}\Delta R_p}\right) - erf\left(\frac{x-st-R_p}{\sqrt{2}\Delta R_p}\right)\right] \qquad \text{(B.3)}$$

In the above equation the location is measured with respect to the initial surface. In order to easily evaluate the ion damage distribution for any point at any time, we would have to change system of coordinates. The etched surface coordinate system is the most appropriate and the linear transformation

$$x = x + st \qquad \text{(B.4)}$$

has to be used. The damage distribution for a point x, with respect to the actual surface, can therefore be evaluated from:

$$N(x,t)dt = \frac{D}{\sqrt{2\pi}s}\left[erf\left(\frac{x+st-R_p}{\sqrt{2}\Delta R_p}\right) - erf\left(\frac{x-R_p}{\sqrt{2}\Delta R_p}\right)\right] \qquad \text{(B.5)}$$

The damage distribution peak, $N_{max}(x,t)$, for a given distance x from the actual surface will have reached its maximum possible value [1] after a time t:

$$t \geq \frac{2.69\Delta R_p + R_p - x}{s} \qquad \text{(B.6)}$$

For such a simplistic model, effects such as diffusion of the injected impurities into Si are ignored.

---

[1] For this calculation the error function tables are used and the method can be found in J. Crank, "*The Mathematics of Diffusion,*" 2nd edition, Clarendon Press, Oxford,1975.